



Queen Mary  
University of London

Investigation of vibrations at the skin surface  
caused by the flow disturbance in stenosed  
tubes

Awais Yousaf

Blizard Institute

Queen Mary University of London

Primary Supervisor: Professor Steve Greenwald

Secondary Supervisor: Dr. Yi Sui

Submitted in partial fulfilment of the requirements of the

Degree of Doctor of Philosophy

## Acknowledgement

First and foremost, I would like to take this opportunity to thank my parents, siblings, and rest of the family for their continuous support throughout my education. Their prayers and sacrifices have given me the incentive and enabled me to pursue my goals. I would also like to acknowledge the enthusiasm and the drive shown by my friends and colleagues, and their encouragement throughout the project.

I would like to express my deepest gratitude to Professor Steve Greenwald (Queen Mary University of London) who has been an extraordinary mentor throughout the project. Steve's knowledge in the field and willingness to share has enabled me to make consistent improvements in my work. His patience, encouragement, and inspiration, up to the very last day, has provided me with a motivation which enabled the completion of the project.

I would like to take this opportunity to acknowledge the support given by my second supervisor, Dr. Yi Sui (Queen Mary University of London). A special thanks to Dr. Jonathan Reeves (post-doc at Queen Mary University of London) for his mentorship, sharing his insight about the subject area and his continual support in the lab. I would like to thank my colleagues in Clinical Physics, Blizard Institute and School of Engineering and Materials Science for their continuous support throughout the project.

Additionally, I would like to thank the Doctoral College Team for their support and arranging events throughout the course, which has helped me with my personal development. Finally, I would like to thank the Horizon 2020 team and Queen Mary University of London for providing the funding and a platform to conduct this study.

## Statement of Originality

I, Awais Yousaf, confirm that the research included within this thesis is my own work or that where it has been carried out in collaboration with, or supported by others, that this is duly acknowledged below and my contribution indicated. Previously published material is also acknowledged below.

I attest that I have exercised reasonable care to ensure that the work is original, and does not to the best of my knowledge break any UK law, infringe any third party's copyright or other Intellectual Property Right, or contain any confidential material.

I accept that the College has the right to use plagiarism detection software to check the electronic version of the thesis.

I confirm that this thesis has not been previously submitted for the award of a degree by this or any other university.

The copyright of this thesis rests with the author and no quotation from it or information derived from it may be published without the prior written consent of the author.

Signature:

Date: 20/07/2021

Details of collaboration and publications:

Funding: Horizon 2020 Framework Programme - Project: 644798 — CARDIS

Publication: Non-contact measurement of carotid artery pulse wave velocity: Neck phantom and preliminary in-vivo results - Summer Biomechanics, Bioengineering and Bio-transport Conference

Collaboration:

- Prof. Patrick Segers: Biofluid, Tissue and Solid Mechanics for Medical Applications-bioMMeda-Institute Biomedical Technology - IBiTech - Ghent University
- Prof. Emm Drakakis: Bio-inspired VSLI Circuits and Systems group - Department of Bioengineering, Imperial College).

## Abstract

An occlusion in an artery (a stenosis) induces disturbances in the downstream flow and those disturbances produce mechanical waves that impinge on the vessel wall causing it to vibrate. These vibrations then travel through the soft tissues to the skin surface where they can be detected, thus providing a possible method for the non-invasive diagnosis of the underlying disease. Hence, in this study, the potential of measuring those disturbances was explored.

Experiments were set-up to model the behaviour of carotid artery under different conditions. A 40:60 (by volume) glycerine-water solution was selected to simulate the viscosity of blood (approximately 4cP). A thin walled (250  $\mu$  m - 350  $\mu$  m wall thickness) latex Penrose drain tube, with an external diameter of 6.35mm and a Young's Modulus value of around 0.9MPa (for circumferential strains between 0.08 - 0.10), was used to mimic the carotid artery. Different severities (60%, 75% and 90% area reduction) of the stenoses, with a circular cross-section, were investigated. Two different types, axisymmetric and non-axisymmetric, were investigated to study the effects of asymmetry in the stenoses. The stenoses were 3D printed in an opaque VeroWhite material to mimic the occlusion. The stenosed artery was then embedded into a standardised neck phantom (filled with Parker Aquasonic 100 ultrasound gel) to mimic the soft tissues and the top of the phantom was sealed with a thin (50  $\mu$  m) polyurethane film (Platilon), with a stiffness value of approximately 21MPa, to simulate the skin.

To detect the disturbance on the phantom surface, different equipment (including accelerometers, and a Laser Doppler Vibrometer [LDV]) were tested. The LDV proved to be the most reliable under all conditions and was chosen as the standard measurement method for all the phantom experiments.

Having selected the appropriate materials and measurement techniques, the effects of flow rate, stenosis severity, stenosis symmetry and fluid viscosity were investigated. Both, steady and pulsatile flows were perfused through the phantom with flows ranging from 0-450ml/min for steady flow and 308-340ml/min for pulsatile flow. On modifying the viscosity of the fluid, it was seen that increasing the viscosity reduced the perturbations in the flow. This was expected due to the increased viscous forces in the flow, as the



viscosity of the fluid increased. Furthermore, the experiments showed that, on increasing the flow rate, the stenosis severity, and/or introducing asymmetry in the stenosis, the post-stenotic perturbations in the flow were amplified and their zone of origin moved nearer to the stenosis. These features were confirmed by conducting bare tube experiments as well as some ultrasound scans in a modified phantom. On further investigation it was found that along with the positional dependence of these perturbations, their range of frequencies was increased with increasing flow rate, stenosis severity and/or stenosis asymmetry.

In the phantom experiments the disturbances were barely detectable for an area reduction of 60% and were weakly present at 75%. However, strong disturbances were seen for the highly (90%) stenosed tube. A possible cause of the unexpectedly small effect of the 75% stenosis was speculated to be the stenosis symmetry: in-vivo, atherosclerotic plaques are invariably not symmetrical. To show this, experiments were conducted with an asymmetric stenosis where higher level of disturbances were detected (even with the 75% stenosis severity), hence, emphasising the impact of stenosis symmetry.

A preliminary computational simulation was also set-up to allow for future detailed modelling of the effects of changing the physical conditions on the signals arriving at the skin. The simulations (whose accuracy yet remains to be validated) showed similar effects of the increasing flow rates and the stenosis severity as the disturbances were amplified and moved nearer to the stenosis on increasing the value of either variable. Following this, an attempt was made to develop a fluid-structure interaction model to simulate the neck phantom and a sample simulation was set-up.

This study developed a novel method for detecting the disturbances in the post-stenotic region, and the experimental results from this study suggest the feasibility of using LVD to infer the presence of a stenosis at an early stage before the symptoms are evident.

# Table of Contents

Acknowledgement.....	2
Statement of Originality .....	3
Abstract .....	4
Table of Contents .....	6
List of Tables and figures.....	10
List of Symbols .....	25
List of Acronyms.....	26
Chapter 1 - Introduction .....	27
1.1. Cardiovascular diseases and their effect on the general population .....	27
1.2. Current diagnostic techniques.....	30
1.3. Impact of computational modelling on CVD .....	34
1.3.1. Fluid models to evaluate the flow physics in the arteries and how the flow affects the arterial walls .....	34
1.3.2. FSI models to simulate the interactions between blood, arterial walls, and the surrounding tissues.....	43
1.4. Scope of the study.....	47
2. Materials and Methods.....	50
2.1. Fluid Type.....	50
2.2. Arterial tubing.....	52

2.3.	Stenosis material and type .....	57
2.4.	Soft Tissue Models - Material Choices.....	61
2.4.1.	Agar gel.....	62
2.4.2.	Polyvinyl alcohol (PVA) gel.....	62
2.4.3.	Vegetarian gelatine gel.....	63
2.4.4.	Ultrasound gel .....	65
2.5.	Skin Model.....	66
2.6.	Preparation of Phantoms .....	68
2.7.	Control Hardware .....	72
2.7.1.	Pump .....	73
2.7.2.	Tap.....	74
2.7.3.	Header Tank .....	74
2.7.4.	Windkessel Chamber .....	74
2.8.	Sampling and Analytical Techniques .....	76
2.9.	Measurement Techniques .....	82
2.9.1.	Accelerometers.....	82
2.9.2.	Laser Doppler Vibrometer .....	83
2.9.3.	Pressure Transducer .....	88
3.	Steady flow - Flow inside a bare tube .....	93
3.1.	Detection of flow disturbances at tube surface (using accelerometers).....	93
3.2.	Detection of flow disturbances inside the tube (using Duplex Ultrasound) .	97
3.2.1.	Effects of flow rate.....	99

3.2.2.	Effects of stenosis severity.....	109
3.3.	Detection of flow disturbances at the tube surface (using LDV) .....	112
3.3.1.	Effects of fluid viscosity .....	112
3.3.2.	Effect of Stenosis Symmetry.....	129
3.4.	Conclusion .....	143
4.	Steady flow - Flow inside a tube embedded within a neck phantom.....	145
4.1.	Effect of stenosis severity and flow rate.....	145
4.2.	Effect of stenosis severity at high flow rates .....	159
4.3.	Effect of Frequency and Position.....	166
4.4.	Effect of stenosis symmetry.....	175
4.4.1.	Early-stage proof of concept work.....	175
4.4.2.	Tube embedded within the ultrasound gel neck phantom.....	179
4.5.	Conclusion .....	196
5.	Effect of superimposing pulsatile flow on the mean steady flow .....	197
6.	Errors & Uncertainties, conclusion & future work.....	209
6.1.	Errors & Uncertainties .....	209
6.2.	Conclusion .....	210
6.3.	Current limitations and Future Goals.....	214
7.	References .....	216
8.	Appendices.....	227
8.1.	Appendix A.....	227

8.1.1.	Computational fluid model .....	227
8.1.2.	Computational structural model.....	245
8.2.	Appendix B .....	258
8.2.1.	Visualisation of flow disturbances .....	258
8.2.2.	Homogeneous tissue models .....	258
8.2.3.	Platilon material properties .....	264
8.2.4.	Fitting for the phantom .....	265
8.3.	Appendix C .....	266
8.3.1.	Microphone Study .....	266
8.3.2.	Additional Duplex ultrasound scans from bare tube experiments .....	271
8.3.3.	Effect of flow rate .....	272
8.3.4.	Effect of flow rate (for steady flows) in 50-100Hz frequency range .....	283

# List of Tables and figures

## List of Figures

Figure 1: Development of plaque in the carotid artery and common methods for its detection (a) stenosed carotid artery (b) healthy vs unhealthy artery (c & d) laminar vs turbulent flow (e) ultrasound imaging (f) computed tomography angiography (g) magnetic resonance angiography (Sobieszczyk and Beckman, 2006).....	32
Figure 2: Geometric configurations for model stenoses .....	37
Figure 3: Comparison of pressure-drop data for axisymmetric and non-symmetric models (Young and Tsai, 1973b).....	37
Figure 4: Comparison of pressure-drop data for models with different area ratios (Young and Tsai, 1973b).....	38
Figure 5: Pressure distribution along wall of stenosis ( $z/Z_0 = 0$ indicates location of stenosis (Young and Tsai, 1973b)) .....	38
Figure 6: Post-stenotic flow separation zone (FSZ) in the 50% asymmetrical model at $t/t_p=0.275$ (a) 3-D surface plot, (b) Secondary flow (vectors) and FSZ (solid lines) at three different post-stenosis transverse planes (Long <i>et al.</i> , 2001).....	41
Figure 7: Schematic of three layers of an arterial wall (represent central axis of the cylindrical artery and R is its distance from each layer within the wall) (Khanafar and Berguer, 2009).....	46
Figure 8: Variation of the Von Mises wall stress across the wall of a descending aorta at various periods of the cycle (Khanafar & Berguer, 2009).....	47
Figure 9: Variation of viscosity in 40:60 (volume ratio) of the glycerine-water solution, with temperature [derived from (Segur and Oderstar, 1951; Trejo González, Longinotti and Corti, 2011)].....	51
Figure 10: Measurement of deformation in the tube to determine its Young's Modulus	53
Figure 11: An example image (top view) of the black latex rubber tube (midway along the tube length) captured at x6 magnifications during inflation test for pressures of 0mmHg (top) and 250mmHg (bottom).....	54
Figure 12: Stress-strain curve of a black latex rubber tube.....	56
Figure 13: Stress-strain curve of a Penrose latex tube from .....	57

Figure 14: A proof of concept non-axisymmetric stenosis (50% by area) formed in a silicone tube (5mm internal diameter) by tying a cotton thread around it .....	58
Figure 15: A planar view of a 75% axisymmetric stenosis (all dimensions are in mm).59	
Figure 16: Microscope image of 3D printed stenosis – cross-section view.....	60
Figure 17: Cross-section of axisymmetric and non-axisymmetric stenoses (x1 and x2, both 1mm offset from geometric centre), with (a) 75% and (b) 90% reduction in area, respectively .....	60
Figure 18: Reference values for speed of sound, attenuation, nonlinearity properties and mass density for a variety of human soft tissues (Mast, 2000) .....	61
Figure 19: PVA gel under tensile testing .....	63
Figure 20: Vegetarian Gelatine under compression testing .....	64
Figure 21: Stress-strain curve from a vegetarian gel sample, 23x23x20mm, using INSTRON 3342 machine).....	64
Figure 22: Stress-strain plot of Platilon material (Reeves and Greenwald, unpublished) .....	67
Figure 23: Weight loss of the phantom due to dehydration (Reeves and Greenwald, unpublished).....	68
Figure 24: A 2-D drawing of a deep neck phantom (for ultrasound gel) – tube centre located 22.5mm below the skin surface. Thickness of each of the acrylic panels is 6mm .....	71
Figure 25: Artificial neck phantom, using Penrose latex tube, ultrasound gel and Platilon to mimic carotid artery, soft tissues and the skin surface, respectively .....	72
Figure 26: Perfusion rig set-up (current set-up showing the LDV only) .....	72
Figure 27: Programmable piston pump.....	73
Figure 28: Windkessel effect on normally compliant arteries (Koeppen and Stanton, 2017) .....	75
Figure 29: Schematic of the Windkessel set-up .....	75
Figure 30: Pressure waveform without (top) and with (bottom) the Windkessel chamber, with same pump settings – one cycle shown between the red dotted lines.....	76
Figure 31: A sample schematic of the PowerLab hardware set-up.....	77

Figure 32: A cut-out sample of the time domain signal obtained with the LDV with pulsatile flow data set of 30 seconds.....	78
Figure 33: FFT of the signal corresponding to the time domain signal with 8K FFT size, 50% overlap with a Hann (cosine-bell) window.....	79
Figure 34: An exemplary plot showing a position-based comparison of FFT signals derived from the accelerometer data .....	79
Figure 35: An example plot showing the area under the curve of a FFT signal. ....	80
Figure 36: Frequency Spectra (top) and the Spectrogram (bottom) of the LDV time-domain signal .....	81
Figure 37: Sample placement of accelerometers on the phantom skin surface .....	83
Figure 38: Comparison between a reflective (right) and a retro-reflective (left) surface (Cole, 2016) .....	84
Figure 39: Neck phantom showing five retroreflective patches attached to the Platilon surface .....	85
Figure 40: Neck phantom placed under the LDV, measuring the displacements at two of the retroreflective patches .....	85
Figure 41: Power attenuation at 1.5cm downstream location, recorded using LDV .....	86
Figure 42: Power attenuation at 1.5cm downstream location, recorded using accelerometer .....	86
Figure 43: Power attenuation at 3.0cm downstream location, recorded using LDV .....	87
Figure 44: Power attenuation at the 3.0cm downstream location, recorded using an accelerometer .....	87
Figure 45: Pressure Transducer Calibrations (Channel 15 and Channel 16 correspond to two transducers) .....	88
Figure 46: Comparison between LDV data obtained at stenosis with (blue) and without (black) pressure transducer .....	90
Figure 47: Comparison between LDV data obtained at 1.5cm downstream of the stenosis - with (blue) and without (black) pressure transducer .....	90
Figure 48: Comparison between LDV data obtained at 3.0cm downstream of the stenosis - with (blue) and without (black) pressure transducer .....	91



Figure 49: Comparison between LDV data obtained at 6.0cm downstream of the stenosis - with (blue) and without (black) pressure transducer .....	91
Figure 50: Effect of introducing pressure transducer in the 75% stenosed tube.....	92
Figure 51: Stenosed bare tube, with accelerometers placed at four positions P1, P3, P4 and P5 to facilitate detection of the disturbances at the tube surface.....	93
Figure 52: Fourier spectra showing the effect of stenosis severity, flow rate and measurement position on a bare latex tube at four different positions: P1 (-3cm upstream), P3 (+1.5cm downstream), P4 (+3cm downstream) and P5 (+6cm downstream) .....	96
Figure 53: Duplex ultrasound set-up of a 90% stenosed tube.....	97
Figure 54: Flow velocity measurements (averaged across the tube diameter) obtained using Duplex ultrasound, at P1 (-3cm upstream) position in a water perfused 90% stenosed tube at (a) 200ml/min and (b) 345ml/min. ....	99
Figure 55: Variation of viscosity in 40:60 (volume ratio) of glycerine-water solution, with temperature [derived from (Segur and Oderstar, 1951; Trejo González, Longinotti and Corti, 2011)].....	113
Figure 56: Stenosed bare tube, with patches of retroreflective tape at four positions P1, P3, P4 and P5 to facilitate data collection using LDV device from axisymmetrically stenosed tubes .....	113
Figure 57: Ratios of area under the FFT curve (normalised to no flow) for a 90% stenosed tube, using water (blue) and glycerine-water solution (red) as the fluid medium, at P1 (b) P3 (c) P4 (d) P5 which are 3cm upstream, 1.5cm downstream, 3cm downstream, 6cm downstream of the stenosis, respectively .....	123
Figure 58: Area under the FFT curve (normalised to no flow) ratios with water, for 60% (blue), 75% (red) and 90% (green) bare stenosed tubes, at (a) P1 (b) P3 (c) P4 (d) P5, which are 3cm upstream, 1.5cm downstream, 3cm downstream and 6cm downstream, respectively .....	124
Figure 59: Area under the FFT curve (normalised to no flow) ratios with glycerine-water solution, for 60% (blue), 75% (red) and 90% (green) bare stenosed tube, at (a) P1 (b) P3 (c) P4 (d) P5, which are 3cm upstream, 1.5cm downstream, 3cm downstream and 6cm downstream, respectively .....	127
Figure 60: Means of averaged (0-150Hz) areas under the FFT curve (normalised to no flow), calculated from the combined downstream positions, showing the interactions between (a) flow rate & severity (b) flow rate & fluid type and (c) fluid type and severity .....	128

Figure 61: Cross section of axisymmetric and non-axisymmetric stenoses (x1 and x2, both 1mm offset from geometric centre), with 75% and 90% reduction in area, respectively .....	130
Figure 62: Stenosed bare tube, with patches of retroreflective tape at four positions P1, P3, P4 and P5 ensuring surface reflection of LDV beam from axisymmetrically and non-axisymmetrically stenosed tubes.....	130
Figure 63: FFT area ratios (normalised to no-flow) for 75% (a) axisymmetric and (b) non-axisymmetric cases tubes at P1 (-3cm upstream) position.....	131
Figure 64: Vector field plots for flow through a 80% stenosed in the femoral artery (axisymmetric (a) and non-axisymmetric (b)) (Padukkage and Barber, 2014) .....	133
Figure 65: FFT area ratios (normalised to no-flow) for 75% (a) axisymmetric and (b) non-axisymmetric cases at P3 (+1.5cm downstream) position .....	134
Figure 66: FFT area ratios (normalised to no-flow) for 75% axisymmetrically & non-axisymmetric stenosed bare tubes at P1 (-3cm), P3 (+1.5cm), P4(+3cm) and P5 (+6cm) .....	136
Figure 67: FFT area ratios (normalised to no flow) for 75% stenosed (axisymmetric (black) and non-axisymmetric (red). Data from bare tubes .....	137
Figure 68: FFT area ratios (normalised to no flow) for 75% & 90% stenosed (axisymmetric and non-axisymmetric) tubes .....	141
Figure 69: Means of averaged (0-600Hz) areas under the FFT curve (normalised to no flow), calculated from the combined downstream positions, showing the interactions between flow rate & severity, flow rate & symmetry, and symmetry & severity in bare stenosed tube .....	142
Figure 70: Stenosed embedded tube, with retroreflective patches placed at five positions, i.e., P1 (3cm upstream), P2 (vertically above the stenosis), P3 (1.5cm downstream), P4 (3.0cm downstream), and P5 (6cm downstream) to detect the surface level disturbances using LDV .....	146
Figure 71: Power spectra for non-stenosed stenosed tube (embedded in the phantom) perfused with glycerine-water solution at flow rate of 350ml/min.....	148
Figure 72: Power spectra for 60% axisymmetrically stenosed tube (embedded in the phantom) per-fused with glycerine-water solution at flow rate of 350ml/min .....	148
Figure 73: Power spectra for 75% axisymmetrically stenosed tube (embedded in the phantom) per-fused with glycerine-water solution at flow rate of 350ml/min .....	149

Figure 74: Power spectra for 90% axisymmetrically stenosed tube (embedded in the phantom) per-fused with glycerine-water solution at flow rate of 350ml/min – repeats shown in the Appendix C .....	149
Figure 75: Effect of flow rate on skin movement from a non-stenosed tube embedded in the phantom 6-8mm below the Platilon skin surface. (In this and subsequent figures, the zero position corresponds to a location in the middle of the stenosis.....)	150
Figure 76: Effect of flow rate on a 60% stenosed tube embedded inside the phantom	150
Figure 77: Effect of flow rate on a 75% stenosed tube embedded inside the phantom	151
Figure 78: Effect of flow rate on a 90% stenosed tube embedded inside the phantom – small errors bars at -3cm, 0cm, and 1.5cm show small differences between the two repeats .....	151
Figure 79: Instantaneous velocity vector fields at $\varphi = 0.5$ (peak inlet velocity) at $Re = 160$ (Hong <i>et al.</i> , 2017) .....	152
Figure 80: Comparison of FFT area ratios from all positions combined at (a) no stenosis, (b) 60% stenosis, (c) 75% stenosis and (d) 90% stenosis – Different scales on y-axis are shown to highlight the presence of small differences .....	156
Figure 81: Box and whisker plot to determine the outliers in the data (blue rectangles indicate the two middle quartiles and the small dark blue squares indicate the outliers, with the adjacent number identifying the number of the observation) – Different scales on y-axis are shown to highlight the presence of small differences .....	157
Figure 82: Power spectra, at the P3 position (1.5cm downstream of the stenosis) for axisymmetrically stenosed tube (embedded in the phantom) perfused with glycerine-water solution at flow rate of 350ml/min.....	160
Figure 83: Power spectra, at the P4 position (3cm downstream of the stenosis) for axisymmetrically stenosed tube (embedded in the phantom) perfused with glycerine-water solution at flow rate of 350ml/min.....	161
Figure 84: Power spectra, at the P5 position (6cm downstream of the stenosis) for axisymmetrically stenosed tube (embedded in the phantom) perfused with glycerine-water solution at flow rate of 350ml/min.....	161
Figure 85: Effect of stenosis severity at 350ml/min mean flow rate (0-50Hz) for axisymmetrically stenosed tube (embedded in the phantom) perfused with glycerine-water solution.....	163
Figure 86: Effect of stenosis severity at 350ml/min mean flow rate (50-100Hz) for axisymmetrically stenosed tube (embedded in the phantom) perfused with glycerine-water solution.....	163

Figure 87: Effect of stenosis severity at 450ml/min mean flow rate (0-50Hz) for axisymmetrically stenosed tube (embedded in the phantom) perfused with glycerine-water solution .....	164
Figure 88: Effect of stenosis severity at 450ml/min mean flow rate (50-100Hz) for axisymmetrically stenosed tube (embedded in the phantom) perfused with glycerine-water solution .....	164
Figure 89: FFT comparison of a 90% stenosed-embedded tube (for FFTs averaged for flow rates between 350-450ml/min) at the P5 (6cm of the stenosis) position .....	169
Figure 90: Combined effect of frequency and flow rate for 90% area stenosis .....	175
Figure 91: Cross-section of a 75% stenosed tube (with a 5mm original non-constricted inner diameter), using a cotton thread (black) tied around the outer surface .....	176
Figure 92: 75% asymmetrically stenosed tube (embedded in agar gel). Silver patches represent the accelerometers at P2 (0cm) and P3 (1.5cm) downstream of the stenosis	176
Figure 93: FFT of the accelerometer signal for flow measurements (at 1.5cm downstream position) from a non-symmetric & non-stenosed tube (embedded in agar gel) .....	177
Figure 94: FFT of the accelerometer signal for flow measurements (at 1.5cm downstream position) from a non-symmetric 75% stenosed tube (embedded in agar gel) .....	178
Figure 95: Effect of flow rate (in a 75% non-axisymmetrically stenosed tube) at low (0 - 98ml/min), medium (149ml/min - 199ml/min) and high (250ml/min - 375ml/min) flow rates .....	178
Figure 96: Area under the FFT curve, at P1 (-3cm upstream) for a 75% stenosed embedded tube (a) axisymmetric (b) non-axisymmetric .....	181
Figure 97: Area under the FFT curve, at P2 (0cm) for a 75% stenosed embedded tube (a) axisymmetric (b) non-axisymmetric .....	182
Figure 98: Area under the FFT curve, at P3 (+1.5cm) for a 75% stenosed embedded tube (a) axisymmetric (b) non-axisymmetric .....	183
Figure 99: Area under the FFT curve, at P4 (+3cm upstream) for a 75% stenosed embedded tube (a) axisymmetric (b) non-axisymmetric .....	184
Figure 100: Area under the FFT curve, at P5 (+6cm upstream) for a 75% stenosed embedded tube (a) axisymmetric (b) non-axisymmetric .....	185
Figure 101: Area under the FFT curve, at P1 (-3cm) for a 90% stenosed embedded tube (a) axisymmetric (b) non-axisymmetric .....	188

Figure 102: Area under the FFT curve, at P2 (0cm) for a 90% stenosed embedded tube (a) axisymmetric(b) non-axisymmetric.....	189
Figure 103: Area under the FFT curve, at P3 (+1.5cm) for a 90% stenosed embedded tube (a) axisymmetric (b) non-axisymmetric.....	190
Figure 104: Area under the FFT curve, at P4 (+3cm) for a 90% stenosed embedded tube (a) axisymmetric (b) non-axisymmetric.....	191
Figure 105: Area under the FFT curve, at P5 (+6cm) for a 90% stenosed embedded tube (a) axisymmetric (b) non-axisymmetric.....	192
Figure 106: Means of averaged (0-600Hz) areas under the FFT curve (normalised to no flow), calculated from the combined downstream positions, showing the interactions between flow rate & severity, flow rate & symmetry, and symmetry & severity in embedded stenosed tube.....	195
Figure 107: Pressure and Flow rate profile of a pulsatile waveform.....	198
Figure 108: Effect of stenosis severity with pulsatile flow amplitude of approximately 600ml/min and mean flow rate around 330ml/min.....	200
Figure 109: Effect of stenosis severity with a steady flow rate of 350ml/min .....	201
Figure 110: Comparison between steady (350ml/min) and pulsatile flow for a 75% stenosed tube at the P4 position, i.e. 3cm downstream of the stenosis.....	201
Figure 111: Effect of stenosis severity with the pulsatile flow within the 0-50Hz frequency band (mean flow rate between 310 and 340 ml/min and pulse-pressure between 30-40mmHg).....	204
Figure 112: Effect of stenosis severity with the pulsatile flow within the 50-100Hz frequency band (mean flow rate between 310 and 340 ml/min and pulse-pressure between 30-40mmHg).....	204
Figure 113: Averaged effect of stenosis severity across all positions shown by the estimated marginal means of the areas under the FFT spectra .....	205
Figure 114: Averaged effect of frequency and stenosis severity across all positions shown by the estimated marginal means of the areas under the FFT spectra .....	205
Figure 115: Averaged effect of frequency across all severities at downstream positions (Low Frequencies 0-300Hz, High frequencies 300-600Hz), shown by the estimated marginal means of the areas under the FFT spectra.....	206
Figure 116: Smooth stenosis with 60% diameter reduction (i.e. 84% by area).....	228

Figure 117: Linear trapezoidal stenosis with 50% diameter reduction (i.e. 75% by area) .....	228
Figure 118: Discretisation of the fluid domain (a) smooth bell shaped stenosis (b) linear trapezoidal stenosis .....	230
Figure 119: Fluxes around a finite volume (Müller, 2015).....	233
Figure 120: Velocity profiles showing development of flow (a) Entrance effect (b) Flow development (c) Comparison between analytical and numerical solution.....	236
Figure 121: Residuals from the flow solver for the three velocity components .....	237
Figure 122: Effect of downstream length on pre-stenotic flow .....	238
Figure 123: Effect of Reynolds number on the velocity field in the post-stenosed region (red shows regions of highest velocity and blue shows lowest) .....	239
Figure 124: Effect of decreasing the time steps from 0.005s down to 0.0000625.....	240
Figure 125: A 3-D model with a trapezoidal stenosis with 75% reduction in area .....	241
Figure 126: Effect of Reynolds number on post stenotic flow for Re values of 423, 740, 846 and 1481 .....	241
Figure 127: Time dependant velocity trace at a point 1mm before the exit of the tube (or 30D from centre of the stenosis) .....	242
Figure 128: Effect of stenosis severity.....	243
Figure 129: Velocity evolution at different positions for 50% Stenosis.....	244
Figure 130: Velocity evolution at different positions for 90% stenosis .....	244
Figure 131: Schematic of a tube embedded inside a gel.....	249
Figure 132: Distorted structure of a deformable tube .....	250
Figure 133: Solid mesh displacement for E=5MPa .....	251
Figure 134: Solid mesh displacement for E=1.8MPa .....	251
Figure 135: Ramping method to stabilise the solver (ANSYS, 2017).....	252
Figure 136: Displacement of the arterial wall (green shows high wall velocities and blue shows low wall velocities) .....	253

Figure 137: Introduction of a sinusoidal wave to allow gradual variations in velocities (a) inlet (b) inlet (red), outlet (green) and at the stenosis (blue) – y axis is velocity(m/s) and x axis is time(s). (Velocity= $0.2 \sin(\pi t) $ , with a period of 2 seconds) .....	253
Figure 138: Velocity contour showing velocity at which the arterial wall is deforming .....	254
Figure 139: Directional displacement of gel structure with dimension 37.5mm (height) 100mm (depth) and 287mm (length) (a) RMS Magnitude (b) X-Plane (c) Y-Plane (d) Z Plane.....	255
Figure 140: Flow visualisation of a post-stenotic disturbed flow .....	258
Figure 141: Vibrating bead set up. Vertical bead movement monitored by laser at top. Surface movement measured by video camera tracking movement of adherent reflective particles. Bead and camera position are adjustable (Reeves and Greenwald, unpublished) .....	259
Figure 142: Bead movement (blue), vertical surface movement (red) and horizontal surface movement (grey). Wave velocity calculated from phase lag between vertical bead and surface movements and gel dimensions. Middle bead, Excitation frequency 250Hz (Reeves and G .....	260
Figure 143: Wave velocity (blue bars, left hand scale) averaged for 5 gels. Surface/Bead displacement amplitude (red bars, right hand scale). Lower bead position 12.5 mm from gel base, middle at 25 and upper at 37.5. Note increased surface movement away from base.....	260
Figure 144: Time displacement relationship for agar gel subjected to a normal load showing creep from time zero to 45 hours, after which the load was removed. Note the permanent deformation revealing when the load was removed (Reeves and Greenwald, unpublished).....	260
Figure 145: Embedding magnet within the gel .....	261
Figure 146: Gel with an embedded cylindrical magnet (length = 4mm, diameter = 3mm, 0.35kg pull strength), placed vertically above a rotating magnet (connected to a motor) .....	263
Figure 147: 3D model of the magnet test rig set-up, with a cylindrical magnet hanging in the middle with a set of nylon strings (a) Side view (b) Top view .....	263
Figure 148: Typical properties of highly elastic polyurethane film - Plaitlon® (outlined in red) (Covestro, 2017) .....	264
Figure 149: A 2-D drawing of the fittings used in the neck phantom. Left side shows a lip of 15mm over which the latex tube slides (all dimensions are in mm).....	265

Figure 150: Schematic of the microphones set-up to detect disturbances in a 75% stenosed (embedded) tube (Drakakis Group) .....	267
Figure 151: Areas under the power signal at stenosis (0cm), +1.5cm and +3cm for flow rates of (a) 108ml/min, (b) 165ml/min, (c) 211ml/min, (d) 259ml/min, (e) 302ml/min and (f) 357ml/min .....	269
Figure 152: Area under the power signal at stenosis (0cm), +1.5cm and +3cm for flow rates of (a) 511ml/min and (b) 601ml/min.....	269
Figure 153: Positional comparison of area under the curve ratios for the normal (<360ml/min) and high (>500ml/min) flow rates .....	270
Figure 154: 90% Stenosis - 1.5cm position - Middle band of 2.0mm .....	271
Figure 155: Effect of flow rate in a stenosed (embedded) tube in a 0% stenosed case at the P1 position (-3cm upstream of the stenosis) .....	272
Figure 156: Effect of flow rate in a stenosed (embedded) tube in a 0% stenosed case at the P2 position (vertically above the stenosis).....	273
Figure 157: Effect of flow rate in a stenosed (embedded) tube in a 0% stenosed case at the P1 position P3 position (1.5cm downstream of the stenosis).....	273
Figure 158: Effect of flow rate in a stenosed (embedded) tube in a 0% stenosed case at the P4 position (+3cm downstream of the stenosis) .....	274
Figure 159: Effect of flow rate in a stenosed (embedded) tube in a 0% stenosed case at the P5 position (+6cm downstream of the stenosis) .....	274
Figure 160: Effect of flow rate in a stenosed (embedded) tube in a 60% stenosed case at the P1 position (-3cm upstream of the stenosis) .....	275
Figure 161: Effect of flow rate in a stenosed (embedded) tube in a 60% stenosed case at the P2 position (vertically above the stenosis).....	275
Figure 162: Effect of flow rate in a stenosed (embedded) tube in a 60% stenosed case at the P3 position (1.5cm downstream of the stenosis).....	276
Figure 163: Effect of flow rate in a stenosed (embedded) tube in a 60% stenosed case at the P4 position (+3cm downstream of the stenosis) .....	276
Figure 164: Effect of flow rate in a stenosed (embedded) tube in a 60% stenosed case at the P5 position (+6cm downstream of the stenosis) .....	277
Figure 165: Effect of flow rate in a stenosed (embedded) tube in a 75% stenosed case at the P1 position (-3cm upstream of the stenosis) .....	277



Figure 166: Effect of flow rate in a stenosed (embedded) tube in a 75% stenosed case at the P2 position (vertically above the stenosis).....	278
Figure 167: Effect of flow rate in a stenosed (embedded) tube in a 75% stenosed case at the P3 position (1.5cm downstream of the stenosis).....	278
Figure 168: Effect of flow rate in a stenosed (embedded) tube in a 75% stenosed case at the P4 position (+3cm downstream of the stenosis) .....	279
Figure 169: Effect of flow rate in a stenosed (embedded) tube in a 75% stenosed case at the P5 position (+6cm downstream of the stenosis) .....	279
Figure 170: Effect of flow rate in a stenosed (embedded) tube in a 90% stenosed case at the P1 position (-3cm upstream of the stenosis) .....	280
Figure 171: Effect of flow rate in a stenosed (embedded) tube in a 90% stenosed case at the P2 position (vertically above the stenosis).....	280
Figure 172: Effect of flow rate in a stenosed (embedded) tube in a 90% stenosed case at the P3 position (1.5cm downstream of the stenosis).....	281
Figure 173: Effect of flow rate in a stenosed (embedded) tube in a 90% stenosed case at the P4 position (+3cm downstream of the stenosis) .....	281
Figure 174: Effect of flow rate in a stenosed (embedded) tube in a 90% stenosed case at the P5 position (+6cm downstream of the stenosis) .....	282
Figure 175: Effect of Flow Rate in a 60% stenosed tube embedded within a phantom (50-100Hz) - 200ml/min outlier at -3cm position filtered out on y-axis.....	283
Figure 176: Effect of Flow Rate in a 75% stenosed tube embedded within a phantom (50-100Hz).....	284

## List of Tables

Table 1: Classification of atherosclerosis lesions - American Heart Association (adopted from (Stary <i>et al.</i> , 1995) .....	29
Table 2: Classification of plaque vulnerability (Stary <i>et al.</i> , 1995; Bentzon <i>et al.</i> , 2014) .....	29
Table 3: Inflation data at 15cm from the inlet of the black latex rubber tube .....	55
Table 4: An extract from inflation data at 15cm from the inlet of the Penrose latex tube .....	56
Table 5: Comparison between candidate materials for the arterial tubing material .....	57

Table 6: Material properties of VeroWhite material for the 3D printed stenoses.....	60
Table 7: Properties of the ultrasound gel (Parker Laboratories, 2011) .....	65
Table 8: Comparison between candidate materials for the soft tissues mimicking material .....	66
Table 9: Manufacturer specifications of the ADXL337 accelerometers (ADInstruments, 2019) .....	83
Table 10: Flow mapping, using Duplex ultrasound, of a 90% stenosed tube at different positions along the circumferential and longitudinal direction (at flowrate of 345ml/min) .....	101
Table 11: Flow mapping, using Duplex ultrasound, of a 90% stenosed tube at different positions along the circumferential and longitudinal direction (at flowrate of 200ml/min) .....	105
Table 12: Flow mapping, using Duplex ultrasound, of 60%, 75% and 90% stenosed tubes at 1.5cm downstream of the stenosis at a flow rate of 345ml/min.....	110
Table 13: Flow mapping, using Duplex ultrasound, of 60%, 75% and 90% stenosed tubes at 3cm downstream of the stenosis at a flow rate of 345ml/min.....	111
Table 14: Bare tube run with water - FFT spectra obtained from LDV data at P1 and P3 .....	116
Table 15: Bare tube run with water - FFT spectra obtained from LDV data at P4 and P5 .....	117
Table 16: Bare tube run with glycerine-water solution - FFT spectra obtained from LDV data at P1 and P3 .....	118
Table 17: Bare tube run with glycerine-water solution - FFT spectra obtained from LDV data at P4 and P5 .....	119
Table 18: Regression analysis of effect of flow rate in a bare stenosed tube, with water as perfusing liquid at P1 (-3cm upstream), P3 (+1.5cm downstream), P4 (+3cm downstream) and P5 (+6cm down-stream) positions – green (highly significant), and red (insignificant) .....	125
Table 19: Regression analysis of the effect of flow rate in a bare stenosed tube, with glycerine-water solution as perfusing liquid at the P1 (-3cm upstream), P3 (+1.5cm downstream), P4 (+3cm downstream) and P5 (+6cm downstream) positions – green (highly significant), yellow ( $0.1 > p > 0.5$ ), and red (insignificant) .....	125

Table 20: Regression analysis of effect of the flow rate in a 75% bare stenosed (axisymmetric and non-axisymmetric) tube, with water as perfusing liquid, at P1 (-3cm upstream), P3 (+1.5cm downstream), P4 (+3cm downstream) and P5 (+6cm downstream) positions .....	133
Table 21: Regression analysis of effect of flow rate in a 90% bare stenosed (axisymmetric and non-axisymmetric) tube, with water as perfusing liquid, at P1 (-3cm upstream), P3 (+1.5cm downstream), P4 (+3cm downstream) and P5 (+6cm downstream) positions .....	138
Table 22: FFT area ratios (normalised to no-flow) for 90% axisymmetrically & non-axisymmetrically stenosed bare tubes at P1 (-3cm), P3 (+1.5cm), P4(+3cm) and P5 (+6cm).....	139
Table 23: Sample normality test for the effect of flow rate for all stenosis severities. Figures highlighted in orange indicate significant deviation of the data from the normal distribution .....	158
Table 24: One-way ANOVA – (p-value analysis to assess the effect of flow rate) - Green shading indicates a significant difference .....	159
Table 25: ANOVA (effects of stenosis severity within each flow rate) .....	165
Table 26: p- values from ANOVA showing statistical significance of effect of stenosis severity at two flow rates .....	166
Table 27: p-values related to the effect of position (Tukey post-hoc test).....	167
Table 28: p-values signifying the effect of frequency (post-hoc Tukey analysis) at three positions 1.5cm (top) 3.0cm (middle) and 6cm (bottom) .....	168
Table 29: Interaction effect of flow rate and stenosis severity (x=6, y=36) .....	170
Table 30: Interaction effects between stenosis severity and flow rate determined by two-way ANOVA.....	172
Table 31: Regression analysis of effect of flow rate in a 75% embedded stenosed (axisymmetric and eccentric) tube, with glycerol-water solution as perfusing liquid, at P1 (-3cm upstream), P2 (0cm), P3 (+1.5cm downstream), P4 (+3cm downstream) and P5 (+6cm downstream) positions – green (highly significant), yellow (0.1 > p >0.5), and red (insignificant).....	186
Table 32: Regression analysis of effect of flow rate in a 90% embedded stenosed (axisymmetric and eccentric) tube, with glycerol-water solution as perfusing liquid, at P1 (-3cm upstream), P2 (0cm), P3 (+1.5cm downstream), P4 (+3cm downstream) and P5 (+6cm downstream) positions – green (highly significant), yellow (0.1 > p >0.5), and red (insignificant).....	193

Table 33: Significance (p-values) of the effect of stenosis severity in Pulsatile Flow (between 0-600Hz), where statistically significant results are highlighted in green ....202

Table 34: Significance of the effect of frequency in Pulsatile Flow - Each number (x) represents a band of 50Hz from (x-50)Hz to xHz. The mean difference is significant at the 0.05 level. ....207

Table 35: Flow rates and their corresponding Reynolds numbers .....234

## List of Symbols

Symbol	Quantity
Re	Reynolds number
$\mu$	Viscosity
$pH$	Potential of Hydrogen
$dB$	Decibels
$V$	Voltage
$div$ or $\nabla$	Divergence Operator
$\rho$	Density
$p$	Pressure
$E$	Young's Modulus
$G$	Shear Modulus
$M$	Structural Mass Matrix
$C$	Damping Matrix
K	Stiffness Matrix
$\tau$	Shear Stress
$\sigma$	Normal Stress
u or v	Velocity
$U$	Velocity Vector
$F(t)$	Time-dependent applied load
t	Time
$t$	Traction vector
$N$	Total Grid Nodes
$N_{min}$	Minimum number of coupling iterations

## List of Acronyms

Acronyms	Full Form	Acronyms	Full Form
ABS	Acrylonitrile Butadiene Styrene	LDV	Laser Doppler Vibrometer
ADINA	Name of software	MRA	Magnetic Resonance Angiography
ANOVA	Analysis of Variance	NHLBI	National Heart, Lung, and Blood Institute
CFD	Computational Fluid Dynamics	NHS	National Health Service
CIMT	Carotid Intima-Media Thickness	PCB	Programmable Circuit Board
CNC	Computer Numerical Control	PE	Polyethylene
CTA	Computed Tomography Angiography	PLA	PolyLactic Acid
CVD	Cardiovascular Disease	PVA	Polyvinyl Alcohol
DSA	Digital Subtraction Angiography	PWV	Pulse Wave Velocity
DUS	Duplex Ultrasonography	RAM	Random Access Memory
EMM	Estimated Marginal Means	RMS	Root Mean Square
FFT	Fast Fourier Transform	SEM	Scanning Electron Microscope
FSI	Fluid-Structure Interaction	SIMPLE	Semi-Implicit Method for Pressure-Linked Equations
HPC	High Performance Computing	SIOS	Name of company
IQR	Inter Quartile Range	WSS	Wall Shear Stress

# Chapter 1 - Introduction

The introductory chapter of this thesis outlines the necessity of finding a suitable screening method for early-stage detection of cardiovascular diseases. Current diagnostic techniques, which come with their limitations, are presented, and the potential of computational modelling in this field is discussed. Finally, the aims and objectives of this study are defined.

## 1.1. Cardiovascular diseases and their effect on the general population

Cardiovascular diseases (CVD) are the leading cause of death in the western world and a rapidly increasing problem elsewhere. In 2013, 31% of global deaths (accounting for 17.3 million) were due to CVD, and according to (Benjamin *et al.*, 2019), this number is predicted to grow to 23.6 million by 2030. Cardiovascular diseases are disorders of the heart and/or blood vessels, and these can be divided into a few main categories: coronary artery disease, peripheral artery disease, carotid artery disease, and aortic disease (Safar, O'Rourke and Frohlich, 2015).

In general, most types of CVD are associated with reduced or zero blood flow to downstream sites. Coronary artery disease is caused by a lack of oxygenated blood to the heart, of which chest pain (angina) is a frequent symptom. In peripheral artery disease, blood flow to the limbs is impaired, leading to pain in the limbs. Likewise, carotid artery disease results in reduced blood supply to the brain (Figure 1a). In extreme cases, the symptoms can be unresponsiveness of body, face, arms, speech, etc. (NHS, 2017). Aortic disease, such as an aneurysm, can occur when the atherosclerotic plaque builds up, leading to weakening of the arterial wall over time. The arterial wall bulges due to constant pressure from the blood, especially due to an untreated high blood pressure condition. Other conditions that can lead to such aortic disease include hypertension, genetic conditions (such as Marfan syndrome), connective tissue disorder, untreated infections, and any traumatic injury. Aneurysms can be extremely dangerous as the affected area of the arterial wall can rupture and cause substantial internal bleeding (Hopkins, 2017).

A critical pathology that underlies most arterial diseases is arteriosclerosis, which is

thickening and stiffening of arterial walls or atherosclerosis (sometimes used interchangeably with arteriosclerosis) due to localised build-up of plaque, containing lipids, fatty and calcium deposits (Figure 1b). This pathology is caused by several factors, including and not limited to chronically elevated blood pressures, generalised calcification of arterial walls (elastocalcinosis) or metabolic imbalances such as type II diabetes (which is associated with the adoption of western diet and obesity). (Abedin, Tintut and Demer, 2004)

Atherosclerotic plaques usually develop in elastic and medium-large muscular arteries, such as the femoral and popliteal arteries in the leg (Stary, 2000). The margin of the arterial wall in contact with the blood is generally very smooth at an early age, allowing the blood to flow without adhering to the endothelium (the cells lining the inner wall of the vessel). However, over time, the endothelial cells begin to produce cell surface adhesion molecules. The endothelial cells also start deforming, and the gaps between them allow permeability to fluids, lipids, and leukocytes (white blood cells). Lipoprotein particles enter the arterial wall and undergo oxidation due to their exposure to nitric oxides and macrophages. Macrophages retain the lipid they have taken up, and those lipid-laden macrophages are referred to as foam cells. Fatty streaks are these lipid-containing foam cells that lie in the arterial wall just below the endothelial layer (LaMorte, 2016). In time, these fatty streaks can form a plaque in the arterial wall (between the endothelium and the arterial media). In several cases, these cells will continue to absorb cholesterol. They may progress into *atherosclerotic plaques*, consisting of fat engorged foam cells, smooth muscle cells that have migrated from the middle of the vessel wall and proliferated, where they synthesise connective tissue proteins (mainly collagen). The lesion formed is called an atheromatous plaque. It enlarges and with time, becomes calcified and progresses to form a stenosis resulting in gradual occlusion of the lumen and thus increasingly impeding the blood flow and giving rise to detectable symptoms. The disease caused by this process is called atherosclerosis and can progress in a couple of different ways.

Firstly, the plaque may grow and strengthen with time. In the carotid arteries, which carry oxygenated blood to the brain, the build-up of plaque inside them narrows the local lumen, forming a stenosis. If the stenosis is severe enough, the blood supply to the brain is inhibited, which can cause cells to die, impairing brain function. It can also lead to other clinical complications such as ischemic attacks (due to occlusion in the cerebral vessels caused by unstable plaque, as discussed below) resulting in neurological deficits,



which can be a precursor to an ischaemic, or if the plaque sheds a blood clot, an embolic stroke. Similarly, in coronary arteries, if the plaque causes a 70% reduction by area in the lumen, patients may start to experience symptoms such as chest pain (angina) resulting from acute or chronic shortage of oxygen to the myocardium (Urman and Caren, 2007).

Table 1: Classification of atherosclerosis lesions - American Heart Association (adopted from (Stary *et al.*, 1995)

Histological Classification	Description	Progression Mechanism	Clinical Correlation
Type I	Isolated macrophage foam cells	By lipid accumulation	Silent
Type II	Intracellular lipid accumulation		
Type III	Type II changes and formation of small extracellular lipid pools		
Type IV	Type II changes and formation of extracellular lipid core		
Type V	Lipid core and fibrous cap, or multi-cap/core, or mainly calcific, or mainly fibrotic	Accelerated smooth muscle and collagen increase	Silent or Overt
Type VI	Surface defect, ulceration, haemorrhage, thrombus	Thrombosis, haematoma	

Secondly, if the plaque does not stabilise, a more vulnerable plaque starts to form. This can spontaneously rupture and damage the underlying layer of endothelial cells, exposing the blood to the collagen which stimulates the formation of blood clots. If the clot breaks and shreds, small fragments may travel downstream with the blood flow and lodge into smaller vessels, leading to myocardial infarction (heart attack) due to lack of oxygen to a region of tissue and its localised death. A larger fragment of the clot can block a major coronary artery disrupting blood to a large region of the heart, and a fatal heart attack can ensue. Similarly, if a fragment of the clot from the carotid artery travels downstream and completely blocks a cerebral artery, it can lead to a stroke (NHLBI, 2015).

According to the American Heart Association’s classification, atherosclerotic lesions can be divided into six types Table 1. Types I-III are usually referred to as stable or clinically silent, and from type IV onwards, they start to become more prominent and/or vulnerable (Stary *et al.*, 1995). Plaque vulnerability can be characterised using several features. Pathological markers of vulnerable plaques include (and are not limited to) thrombus, carotid artery intima/media thickness, calcification, ulceration and thin fibrous cap. Plaque vulnerability is summarised morphologically in Table 2 (Stary *et al.*, 1995).

Table 2: Classification of plaque vulnerability (Stary *et al.*, 1995; Bentzon *et al.*, 2014)

<b>Vulnerable Plaque</b>	<b>Stable Plaque</b>
Soft	Hard
Thin fibrous cap	Thick fibrous cap
Large lipid pool	Small or no lipid pool
High collagen content	Low collagen content
Intra-plaque haemorrhage	Minimum or no erythrocytes
Positive remodelling	Concentric vessel
Disrupted cap	Intact cap
Thrombosis	No thrombosis
Endothelial damage	Intact endothelium
Sparse or no calcification	Extensive calcification
>75% area stenosed	<60% area Stenosed
High plaque strain	Low plaque strain

While these diseases may remain undetected when carrying out normal day to day activities, they might become apparent when oxygen demand is increased, such as during exercise or in a state of stress. Since the inconspicuous nature of atherosclerosis in its early stages allows its development to a rather mature state before clinical symptoms are evident, much effort is currently being invested in developing safe, non-traumatic and non-invasive methods for diagnosing this disease in its early stages. Since these diseases affect a large fraction of the population, many of whom have a high risk of suffering the acute effects of the disease (such as stroke or myocardial infarction), it is critical to identify any opportunities to identify those at risk (Klabunde, 2007).

## 1.2. Current diagnostic techniques

“Given the fact that atherosclerosis is a complex, chronic disorder involving inflammatory and proliferative cells and signalling pathways, it is generally thought that imaging of events during all stages of its pathogenesis could contribute to better and earlier diagnostic assessment, risk estimation, and measurement of treatment effects” (Kaufmann, 2009).

One of the prime events in arteriosclerosis is the stiffening of arterial walls. A generalised increase in conduit arterial stiffness is now regarded as a marker of cardiovascular ageing, and it can be used to predict cardiovascular events in the general population (Shirwani and Zou, 2010). Since the measurement of arterial stiffness is such an important indicator of CVD, it is critical to identify any opportunities and strategies that can assist in measuring arterial stiffness and hence identify those at risk, ideally before symptoms become severe.

In carotid atherosclerosis, the local narrowing of the artery leads to instabilities in the flow. Figure 1 (c) & (d) show that generally, the flow in a non-constricted tube is laminar (the case in most arteries under physiological flow conditions). However, once as the blood flows through the stenosis, it accelerates and tends to separate from the arterial walls, just downstream of the stenosis, and as a result, an unsteadiness can then be observed in the post-stenotic region.

This disturbance causes a characteristic sound called a bruit, which can sometimes be heard with a stethoscope. A drawback to this technique is its dependence on the operator's skill since the incorrect placement of the stethoscope, or slightly high localised pressure can potentially provide false results.

The patient is often recommended to take an imaging test to determine whether a stenosis is present. Frequently, an ultrasound scan (Figure 1e) is recommended as the first line of evaluation for superficial arteries as the carotid (Saha, Whayne and Mukherjee, 2010), though digital subtraction angiography (DSA) is still considered the gold standard (Adla and Adlova, 2014). The gold standard for the less superficial coronary arteries is X-ray angiography (Sobieszczyk and Beckman, 2006).

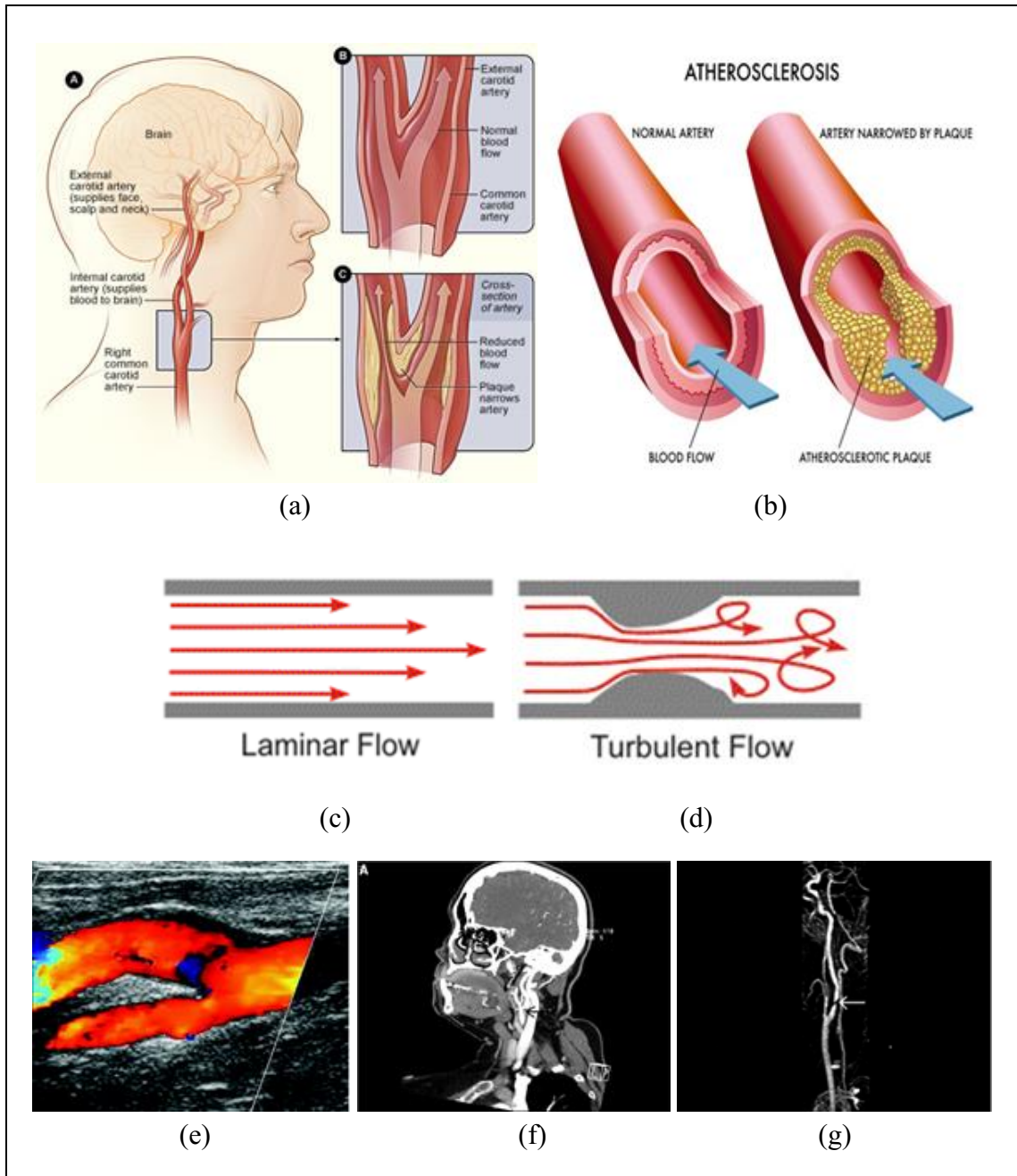


Figure 1: Development of plaque in the carotid artery and common methods for its detection (a) stenosed carotid artery (b) healthy vs unhealthy artery (c & d) laminar vs turbulent flow (e) ultrasound imaging (f) computed tomography angiography (g) magnetic resonance angiography (Sobieszczyk and Beckman, 2006)

Atherosclerotic lesions can be visualised as protrusions of the intima-media, with anatomical B-mode ultrasound imaging (Steinl and Kaufmann, 2015). Duplex ultrasonography (DUS) is also sometimes used as it uses B-mode to image the vessel under investigation and Doppler to evaluate the direction of blood flow and its velocity. The high temporal and spatial resolution of carotid ultrasound allows accurate measurement of the distance from the luminal surface to the intima-media boundary, termed carotid intima-me-

dia thickness (CIMT), even before the development of significant atherosclerosis. “Ultrasound imaging is widely available and can be used for high-throughput screening at low cost, and therefore compares favourably with other imaging techniques when being considered as a screening tool in large populations at risk for atherosclerotic events” (Kaufmann, 2009). A drawback to ultrasound can be its dependence on the operator's skill; otherwise, this technique appears to be the most researched and readily used in the assessment of carotid plaques and strokes (Brewin, 2010), although its use in the diagnosis of coronary stenosis is limited due to the smaller size and greater depth below the skin of these vessels.

Other tests used for this purpose, especially for coronary vessels are catheter-based angiography, computed tomography angiography (CTA) (Figure 1f) and magnetic resonance angiography (MRA) (Figure 1g). In these techniques, a contrast medium is often injected into the patient to capture detailed high resolution images of the arteries, allowing reliable determination of stenosis severity and position and guide possible treatment (Sobieszczyk and Beckman, 2006). CTA or MRA is sometimes used following the DUS when the disease is severe or if results from the ultrasound are inconclusive. Furthermore, these techniques have the added advantage of imaging the intracranial circulation (Brewin, 2010). Many centres have found that a combination of ultrasound and CTA is sufficient to quantify the severity of severely stenosed arteries (Herzig *et al.*, 2004). Despite their benefits, these techniques are expensive and are not usually used at the first point of screening. Furthermore, the injection of the contrast medium makes them invasive and is itself a procedure not without risk.

With the current methods available for detecting of stenoses, the experience can be traumatic for patients. The expense, late-stage screening and technical complexity of these methods make them unsuitable for widespread use. Furthermore, there are added risks of infections, damaged blood vessels and/or allergic reactions from contrast media (Andreucci, Solomon and Tasanarong, 2014). As mentioned, the number of global deaths due to CVD is expected to grow to 23.6 million per year by 2030 (Benjamin *et al.*, 2019). Therefore, there is an urgent need to develop easy-to-use, reliable non-invasive methods for screening large populations at an early age of the disease.

### 1.3. Impact of computational modelling on CVD

With a new generation of computational resources, computer-aided modelling has become a powerful tool to understand complex structural mechanics and flow dynamics. The models are not limited to flow analysis anymore and can simulate complex cardiovascular events and their impacts. While a simplistic model to compute the wall shear stress of arteries can be set up, more complex models can also be used to investigate the heart's function, for instance after cardiac resynchronisation therapy (Hu *et al.*, 2014). In the cardiovascular system, computational modelling allows the investigation of flow fields and pressure at resolutions unachievable by experimental methods and allows the generation of additional data to provide an in-depth understanding of cardiovascular pathophysiology non-invasively. In the last few decades, computational modelling has greatly increased our knowledge of haemodynamics and has opened a gateway to numerous opportunities. Some examples of the recent contributions towards the advancement of understanding cardiovascular physiologies are discussed in this section.

#### 1.3.1. Fluid models to evaluate the flow physics in the arteries and how the flow affects the arterial walls

##### i. Flow parameters and geometrical features affecting the flow

##### *Stenosis geometry & effect of Reynolds number*

Stenosis geometry plays an important role in the flow proximal to a stenosis. Shape, severity, and symmetry are three of the main geometric features of a stenosis. Several studies have investigated the effects of these features on the pre- (upstream) and post (downstream)-stenotic flow. Similarly, the tube diameter and the fluid viscosity (as expressed by Reynolds number) have a strong effect on the flow features.

Young and Tsai, 1973 conducted an experimental study of flow characteristics in axisymmetric and non-symmetric stenoses, which motivated many subsequent computational investigations. They showed that with an increase in Reynolds number, the disturbances in the post-stenotic flow moved closer to the stenosis, and the line of flow separation was extended further downstream (Figure 2). They also indicated how the pressure losses and flow transitions (from laminar to turbulent) are dependent on geometry (Figure

3). The pressure losses increased with the increase in the severity of stenosis. Additionally, they showed that the location downstream at which the disturbances first become detectable was dependent on the geometry of the stenosis. It was further highlighted how the pressure losses in non-symmetric/eccentric models were higher when compared to axisymmetric models and that the pressure drop started further upstream of the stenosis (Figure 4 & Figure 5). They further investigated that, although pressure losses are dependent on Reynolds number, once the Reynolds number reaches a critical value (depending on the geometry), the turbulent losses are dominant and the pressure drop becomes independent of the Reynolds number, which means that the reattachment point will also become independent.

(Ghalichi *et al.*, 1998) conducted a similar computational study to analyse the turbulent flow (using the standard  $k-\varepsilon$  model) distal to arterial stenosis, where they used three different models with area reductions of 50%, 75% and 86%, and Reynolds numbers up to 2000. They also looked at vortex lengths in post stenotic flow within the laminar flow regime. They identified the critical Reynolds number for their geometry to be 1100, 400 and 230 for the severities of 50%, 75% and 75%, respectively. These values lay within 10% of the experimental results reported (Yongchareon and Young, 1979).

#### *Stepped vs smooth stenosis*

A computational study was conducted (Hyun, Kleinstreuer and Archie, 2000) to analyse the difference in flow fields past a 90-degree backward-facing stepped stenosis and a smooth stenosis. The numerical calculations were carried out with the SIMPLEC algorithm for the pressure correction, using a validated finite volume-based algorithm CFX 4.2. The study concluded that the smooth configuration induced less disturbance in the flow. They also observed that the exit of the stenosis (expansion region) is a region that is susceptible to the deposition of particles carried by the flowing blood, and that the flow profiles demonstrated that it is more likely for the particles to be trapped in the stepped stenosis in comparison to the smooth configuration. One of the important features that make particular sites more prone to arterial diseases is low wall shear stress (WSS), and an atherosclerotic plaque can be expected in these regions due to thrombotic particle aggregation and wall deposition. Therefore, stenoses with sharply defined edges are more susceptible to arterial diseases such as atherosclerosis.

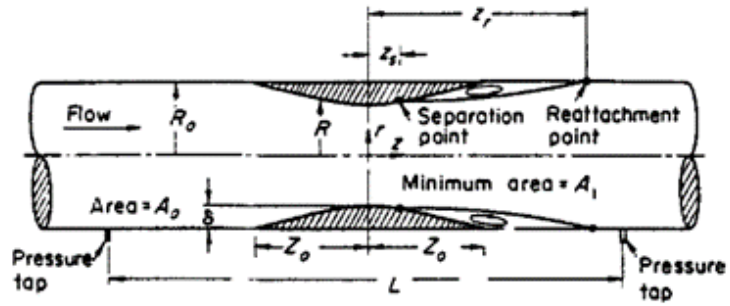
### Pulsatile vs steady flow

Fluid dynamical analysis can be readily applied to understand local pressures and velocities inside arteries of various geometries and under various physiological or pathological conditions. Therefore, this understanding can help provide better guidelines for the diagnosis and to find faster acting remedial measures. Blood flow comprises two parts, a pulsatile component, also referred to as Womersley flow (Kundu, Cohen and Dowling, 2011), which is a flow with periodic variations super-imposed onto the steady flow. For the most part, blood flow is generally laminar, but its periodically unsteady nature and narrowing or other irregularities in the arteries can lead to turbulence. The flow rate in arteries can reach high peak values during pulsatile flows whereas mean flow rates may remain low. It is interesting to compare the effect of steady flow with that of pulsatile, on the flow field. (Ahmed and Giddens, 1984) mentioned in their experimental study that by introducing a pulsatile component, flow distal to the stenosis became more disturbed, and the permanent recirculation regions that appeared in steady flow conditions did not exist when the flow was pulsatile.

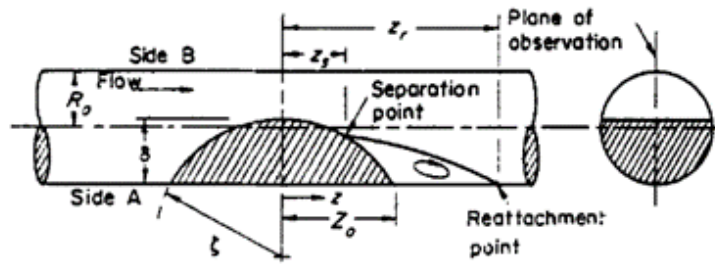
(Razavi, Shirani and Sadeghi, 2011) conducted a study on 30-60% axisymmetric stenosis under unsteady flow condition for Newtonian and six non-Newtonian (modified Casson, generalised power law, Carreau, Carreau-Yasuda, power law and Walburn-Schneck) viscosity model. Separation lengths of the recirculation zones at different points of the cardiac cycle were investigated. High values of WSS were observed at the stenosis when the flow was maximal and when flow at the inlet decelerated, WSS decreased, and recirculation zones were formed downstream of the stenosis, thereby providing a suitable location to intensify plaque formation. The disturbed distribution of radial velocity, and thus the generation of the recirculation zones in the post-stenotic region, reiterates the importance of incorporating the pulsatile component of the flow.

(Liao, Lee and Low, 2004) conducted a study to investigate the characteristics of the flow by simulating three different types of pulsatile flows (a physiological flow, an equivalent pulsatile flow, and a pure sinusoidal flow) through a bell-shaped stenosis. The analysis with the physiological flow showed distinct differences to the other two (the flow patterns of which were similar to each other). The characteristics of the three different types of pulsatile flow showed similar patterns at the peak forward flow, however, differ-





(a) Axisymmetric



(b) Nonsymmetric

$$\frac{R}{R_0} = 1 - \frac{\delta}{2R_0} \left( 1 + \cos \frac{\pi z}{Z_0} \right)$$

for  $-Z_0 \leq z \leq Z_0$

Figure 2: Geometric configurations for model stenoses

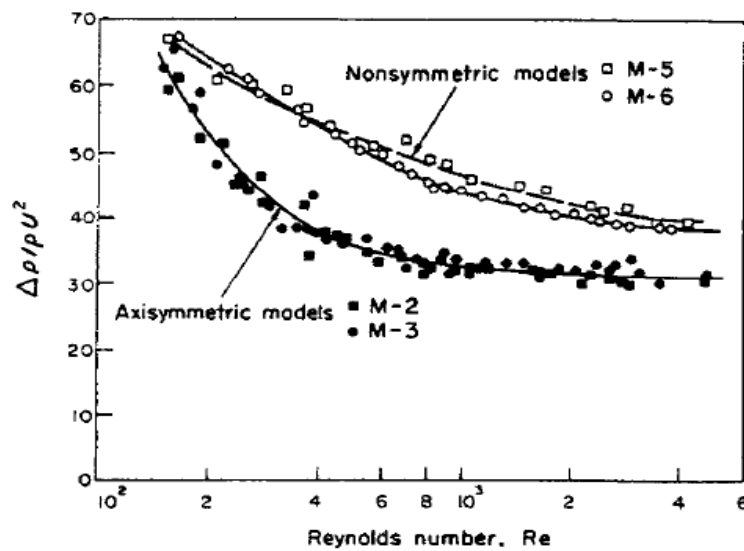


Figure 3: Comparison of pressure-drop data for axisymmetric and non-symmetric models (Young and Tsai, 1973b)

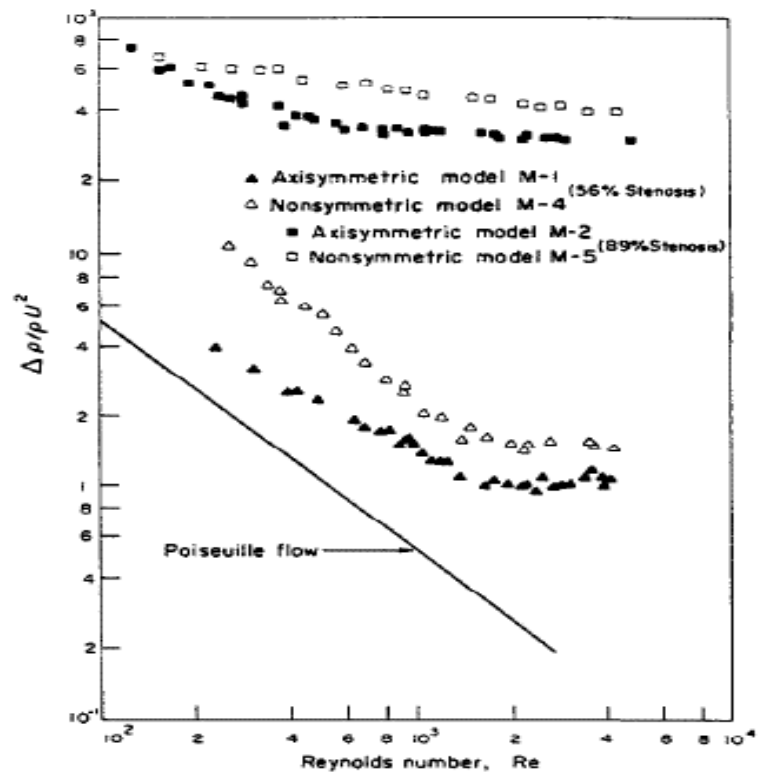


Figure 4: Comparison of pressure-drop data for models with different area ratios (Young and Tsai, 1973b)

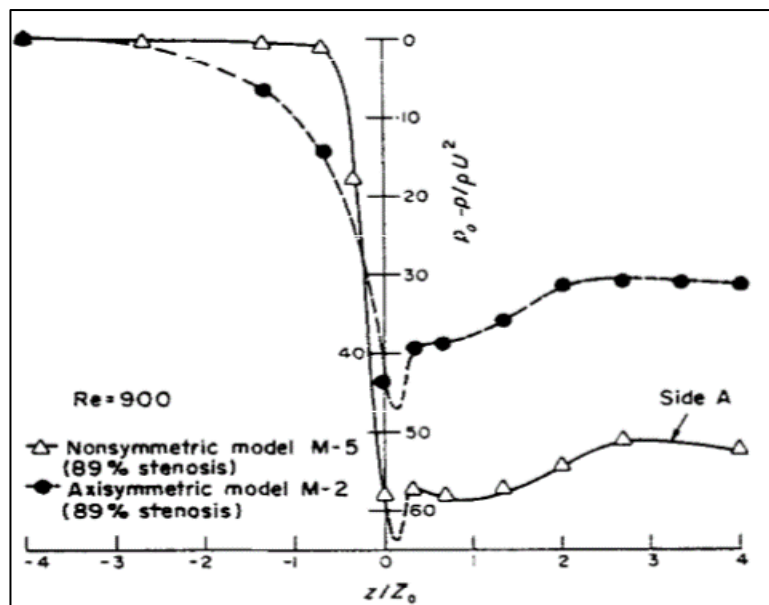


Figure 5: Pressure distribution along wall of stenosis ( $z/Z_0 = 0$  indicates location of stenosis) (Young and Tsai, 1973b)

ences were seen at the peak backward flow rate. The study further identified the effect of Womersley number (pulsatile flow frequency relative to viscous effects) on the flow field. It was firstly found that the pressure drops become higher across the stenosis with increasing Womersley number. Furthermore, in pulsatile flow during systole, the reattachment length of the flow decreases with the increasing Womersley number, and during the deceleration phase of systole, it is likely that vortices may continue to grow and move downstream.

A similar study (Hasan and Das, 2008) simulated 45% trapezoidal stenosed (by area) artery with peak Reynolds number of 1000, using a sinusoidal pulsatile flow. Viscous, incompressible, and Newtonian assumptions were made for the fluid and the effects of stenosis severity, pulsation, Reynolds number and Womersley number were investigate. It was shown that the pulsatile nature of the flow disturbs the flow field and generates recirculation zones in the post-stenotic region. For the effects of stenosis severity, the study showed that the peak wall shear stress for the 65% severity was 1.3, 2.2, and 3 times higher than the 55%, 45% and 30% stenoses severities, respectively. The peak wall vorticity increased with the increasing stenosis severity and Reynolds number. Finally, the Womersley numbers studied (5, 7.75 and 10, and 12.5) did not significantly affect the instantaneous wall vorticity, however, the recovery process of wall vorticity across the constriction was very slow for low Womersley numbers. The above studies emphasise on the importance and accurate modelling of the pulsatile component of the flow in such studies.

## ii. Wall shear stress

As implied above, wall shear stress is another important feature that plays a role in the development and progression of vascular disease. It is quite difficult to measure wall shear stress experimentally; however, a CFD model can compute these results without the need for invasive measurements and generate a mapped distribution of WSS along the lumen. (Leondes, 2001) studied WSS for varying flow rates and observed that WSS increased just upstream of the narrowest section of the stenosis, with increasing flow rates as expected. Using the Ansys Fluent® CFD package, (Zhang *et al.*, 2012) mapped the WSS throughout the surface of the lumen, which would be impossible to measure in practice. The study where WSS for varying stenosis severity and shapes in the carotid artery

was investigated provided a similar conclusion (Srivastava, 2014). Several experimental and theoretical studies have been conducted to investigate the effects of stenosis on the flow fields. (Deplano and Siouffi, 1999) used Doppler ultrasound to measure velocity in a 75% stenosed artery and also conducted transient simulations using a finite element package to study the evolution of wall shear stress through time. They concluded that the presence of a stenosis induced high shear stress values at the arterial wall in close proximity to the stenosis, which can imply more damage such as plaque disruption. Furthermore, the presence of a stenosis induced oscillating and low wall shear stresses, which can also encourage the disease to progress.

(Ahmed and Giddens, 1984) conducted an experimental study with symmetrical stenoses having severities of 25%, 50%, and 75% and entrance lengths of 96 tube diameters to ensure fully developed upstream flow. The velocity measurements were made with a Laser Doppler Velocimeter. A thin separation line was observed towards the exit of the 50% stenosis, and dominating turbulence was observed for the 75% stenosis. Furthermore, they determined the wall shear rates from near-wall velocity profile gradients and similar to other studies, high shear stresses were observed near the throat of the stenosis, and lower stress values were found in the post stenotic regions.

(Long *et al.*, 2001) simulated pulsatile flow in three straight axisymmetric and asymmetric stenosed tube models, with area reductions of 25%, 50% and 75%, and a measured human carotid artery blood flow waveform (corresponding to a mean Reynolds number of 300) was used. The focus of this study was to investigate the flow separation zones for all these models. They found that post stenotic flow in axisymmetric stenoses is more sensitive to changes in the degree of stenosis than in asymmetric models. Furthermore, their study showed flow separations zones to be circumferentially uniform with a changing length and thickness with respect to location and time, and that they tend to be more stable. However, “ring-type” flow separation zones were seen in asymmetric models for a limited period only, and that too, mostly at the downstream segment of the stenosis where jet flow had become parallel to the tube axis (Figure 6).

(Liao, Lee and Low, 2004) reproduced the same results regarding the stenosis severity, i.e., that the structure of the flow fields does not undergo any significant changes other than that with increasing severity, the scale and strength of vortices increase and that with

pulsatile flow, the severity of stenosis also affects the variations in wall vorticity and its peak value.

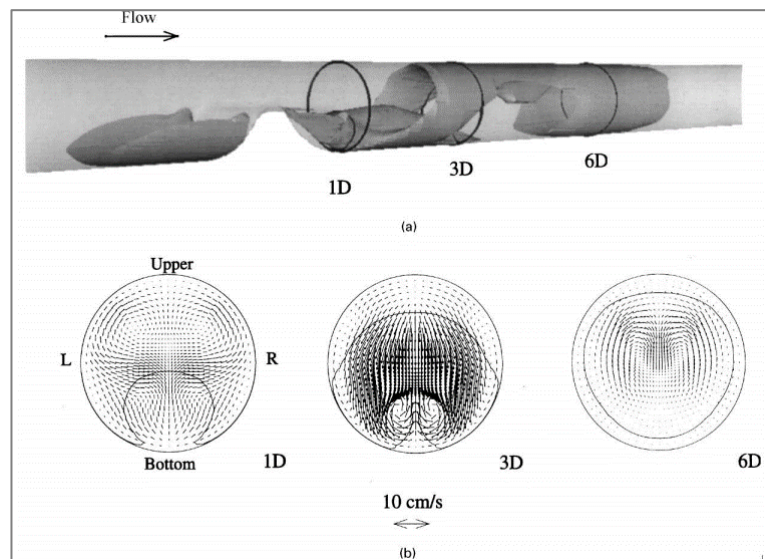


Figure 6: Post-stenotic flow separation zone (FSZ) in the 50% asymmetrical model at  $t/t_p=0.275$  (a) 3-D surface plot, (b) Secondary flow (vectors) and FSZ (solid lines) at three different post-stenosis transverse planes (Long *et al.*, 2001)

### Rheological Models

Several investigations have been carried out to study flow in arteries by assuming blood is a Newtonian fluid (Biyue and Tang, 2000), but this assumption is not valid when the shear rate is low. A study was carried out by (Mekheimer and Kot, 2008), where blood flow through a tapered artery with a stenosis was investigated. The study was conducted using a micropolar model to describe the non-Newtonian behaviour of blood. Micropolar fluids are a subclass of microfluids where fluid microelements are considered to be rigid “to support couple stresses & body couples and exhibit micro-rotational and micro-inertial effects”). The study found that the resistance impedance for a micropolar fluid was higher than that for a Newtonian fluid model.

The instantaneous shear rate over a cardiac cycle varies from zero to approximately  $1000\text{s}^{-1}$  in several large arteries (Cho and Kensey, 1991). Over a cardiac cycle, there are time periods where the blood exhibits shear thinning behaviour. In addition to low shear time periods, low shear exists in some regions such as near bifurcations, stenoses, and aneurysms. Blood in those regions appears to have non-Newtonian properties.

The pulsatile flow of blood through a mildly stenosed artery was studied by (Sankar and Lee, 2009). Casson fluid and Herschel–Bulkley fluid models were used by (Iida, 1978; Kapur, 1985) in blood flow studies to analyse the effect of arterial constriction on the blood flow characteristics. A non-Newtonian blood flow through a tapered overlapping stenosed artery was considered by (Ismail *et al.*, 2008). (Tu and Deville, 1996) simulated blood flow through the stenosis incorporating Herschel-Bulkley, Bingham and power-law fluids in a partially occluded circular tube and highlighted that the rheological properties of blood can alter the flow behaviour. While simulating pulsatile flow through a 75% occlusion (by area) with a Womersley number of 1.25, they determined that the vortex formation effects are stronger in Herschel-Bulkley than in the Newtonian model. (Sankar and Lee, 2009) numerically solved flow through a mildly stenosed artery using the Herschel-Bulkley model and concluded that this model could be more useful than the Newtonian model to investigate blood flow through stenosed tubes.

Carreau and power-law models were compared with the Newtonian model while simulating flow through a 45% (by area) axisymmetric trapezoidal stenosis in a fluid-structure interaction study (Chan, Ding and Tu, 2007). The results showed that the Carreau model had very small differences along the centreline axial velocities, and it mostly followed the velocity profiles of the Newtonian model except for at lower velocities. However, the Power Law model showed a marked decrease along the centreline velocities and significant vortices with lower wall shear stress values than the Newtonian model. Despite this, it was mentioned that although the Power Law model highlighted more dominant non-Newtonian effects, it may produce excessive values of  $I_G$  (a non-Newtonian importance factor, mentioned below), which means that this model needs further investigation.

(Shaw *et al.*, 2009) simulated pulsatile Casson fluid through a stenosed bifurcated artery and noticed that although the variation of axial velocity in both the coronary and femoral arteries is uniform, the flow in the daughter artery experiences more oscillations with the Casson model fluid as compared to the Newtonian one. Furthermore, they distinguished that the velocity profile in the daughter artery experienced a greater effect of flow rheology and flow rates, and that the axial velocities were higher in the femoral artery than in the coronary artery.

(Razavi, Shirani and Sadeghi, 2011) numerically investigated symmetric stenoses in a common carotid artery under unsteady flow conditions for six different non-Newtonian models and compared them with the Newtonian model. The trends in WSS and radial velocity were found to be similar in all the models. However, there were differences in their magnitudes. These differences were found to be more marked at low inlet velocities, but for the power law and Walburn-Schneck models, they were significant even for high inlet velocities. A global non-Newtonian importance factor “IG” was introduced by (Johnston *et al.*, 2004), which can be defined as in equation 1 and the study conducted by (Razavi, Shirani and Sadeghi, 2011) concluded that the power law model overstated the non-Newtonian behaviour whereas the modified power law model and the generalised Casson model underestimated it. Therefore, Carreau and Carreau-Yasuda models were the ones suggested as the most suitable.

$$IG = \frac{1}{N} \frac{[\sum_N(\mu - \mu_\infty)^2]}{\mu_\infty} \quad (1)$$

Where N is the total number of grid nodes. The importance factor IG is evaluated at each node on the surface of the artery and expresses the relative departure from the Newtonian value for each value of molecular viscosity ( $\mu$ ).

The pulsatile nature of flow highlights the direct relation between varying inlet velocity profile and the wall shear stress. As expected, the highest WSS occurs at the throat of the stenosis when flow velocity through the artery is maximal. Furthermore, when the flow at the inlet is decelerating, WSS decreases downstream of the stenosis and recirculation zones start to form, thus making that region more susceptible to plaque formation. (Razavi, Shirani and Sadeghi, 2011) found a similar trend regarding stenosis severity as others, such that with increasing stenosis severity, the recirculation zone downstream of the stenosis becomes larger and the throat of the stenosis experiences a higher WSS.

### 1.3.2. FSI models to simulate the interactions between blood, arterial walls, and the surrounding tissues.

The study of blood flow through stenosed arteries is of great clinical interest, as mentioned earlier. A number of studies have been conducted to investigate flow characteristics through a stenosed artery and their interaction with the stenosed tube. A numerical

study was conducted by (Lee and Xu, 2002) where they investigated unsteady blood flow through a distensible stenosed tube. Their simulations were a follow up of an earlier experiment conducted by (Ojha *et al.*, 1989), and in their simulations they chose an isotropically elastic solid to represent the mechanical behaviour of a blood vessel wall. Velocities and wall shear stresses were calculated, while assuming blood to be Newtonian fluid and expansion of ‘artery’ was observed due to the internal pressure. (Chan, Ding and Tu, 2007) further continued the study carried out by (Lee and Xu, 2002) and considered non-Newtonian models for the blood flow including the power law and Carreau models. (Li *et al.*, 2007) investigated vessel wall mechanics incorporating pulsatile flow, with varying degrees of stenoses. Their study pointed them towards the same conclusion as highlighted earlier that increasing severities resulted in increased blood velocities and higher wall shear stresses, which may contribute to development and rupture of plaques.

(Tang *et al.*, 2001) carried out a fluid-wall interaction study where fluid was passed through thick-walled stenosis. Their results indicated that increasing stenosis severity increased the compressive stress within the tube wall. They also observed that the stress distribution was localised, and maximum compressive and tensile stresses were found inside the stenotic section, which can lead to conditions such as plaque rupture and thrombus formation. However, these key features are subject to change based on stenosis severity and geometry (as discussed earlier), plaque stiffness and pre-stretch in the arterial wall.

(Bressloff, 2007; Nguyen *et al.*, 2008) conducted a FSI study on parametric model of human carotid artery and considered five geometrical features; sinus bulb (stenosis) width, angles, and outflow diameters of both internal and external carotid artery. They concluded that sinus bulb width (which essentially controls severity of stenosis) had the most dominant effect on the time averaged shear stress.

(Perktold and Rappitsch, 1995) simulated pulsatile flow in a compliant 3-D human carotid bifurcation model, using a non-Newtonian blood rheology model and the artery was assumed to be linearly elastic within the systolic and diastolic pressure range. They compared the results with a rigid tube model and agreed that distensibility of the vessel wall affected the flow field, in essence by reducing wall shear stresses.



A similar fluid-structure interaction study was carried out by (Tang *et al.*, 1999) and (Tang *et al.*, 2001) where they simulated a thick and thin-walled artery to investigate wall stresses, strain distributions and flow fields using ADINA software. The tube wall was modelled to be hyper-elastic, homogeneous, isotropic, and incompressible, and the model was run both for symmetrical and asymmetrical stenoses and for multiple stenosis severities. They found that the presence of a stenosis caused considerable compressive stresses in tube wall and suggested that a severe stenosis might cause the tube walls to collapse due to negative transmural pressure. Furthermore, in the thick-walled model, they found that the maximum shear stress in an asymmetric stenosis was 20% lower than that in its symmetric counterpart due to wall contraction and reduced flow. This shear stress was considerably lower than that from the thin-walled model due to increased thickness (hence stiffness) of asymmetric stenosis. From this they deduced that stiffer stenosis might be less dangerous than softer ones, and this was consistent with their clinical observations.

(Mittal, Simmons and Najjar, 2003) conducted a study in which they investigated large-eddy simulations of pulsatile flow for varying Reynolds numbers. They found that fluctuations in wall pressures were related to a vortex flow region for Reynolds numbers of 1000 and higher.

(Mortazavinia, Zare and Mehdizadeh, 2012) conducted a somewhat similar study comparing a healthy and a stenosed right renal artery. The healthy model was constructed from a patient-specific model of arteries from CT images, and an axisymmetric trapezium shape stenosis (45% area reduction) was introduced to model the unhealthy case. Pulsatile non-Newtonian blood flow was simulated while incorporating the FSI. The effects of renal arterial stenosis on the wall shear stress and displacement of vessel wall were investigated. On comparing a healthy and diseased artery, the model revealed that though the flow velocity in the stenotic region increases due to the reduction in the cross-sectional area, the stenosis causes a decrease in the velocity within the post-stenotic region. Furthermore, it is found that the wall shear stress increased as the cross-sectional area decreased suddenly, and the flow direction changed in the entrance region of the stenosis. Immediately after that, the wall shear stress suddenly dropped.

It was also observed that the vessel wall in the stenosed model experienced lower shear stresses than the unobstructed ones. Though it was seen that peak wall shear stress did not reach 40Pa (the critical value above which endothelial damage ensues) with a 45% stenosis severity, higher flow rates or severities may increase the likelihood of lesions occurring. Finally, the time-dependent study of the vessel displacement revealed that the wall displacement during systole was higher than that during diastole, and that the wall displacement in the stenosed artery was much lower than in the healthy one due to the wall stiffness in the stenotic region.

In another study of asymmetric stenoses (Tang *et al.*, 2003), the effects of stenosis severity, eccentricity, and pressure conditions on blood flow and artery distension were quantified. They found that for the same severity, i.e., 70%, introducing a 50% eccentricity caused a 100% increase in compressive stress (artery compression) and 40% variation in shear stress distribution and some considerable changes in the flow field. They concluded that severity and eccentricity have considerable effects on the flow profile and stress-strain distribution along the tube wall, and the increase in eccentricity leads to an increase in buckling pressures which leads to collapsing of the tube and may be related to the rupture of the atherosclerotic plaque causing the stenosis.

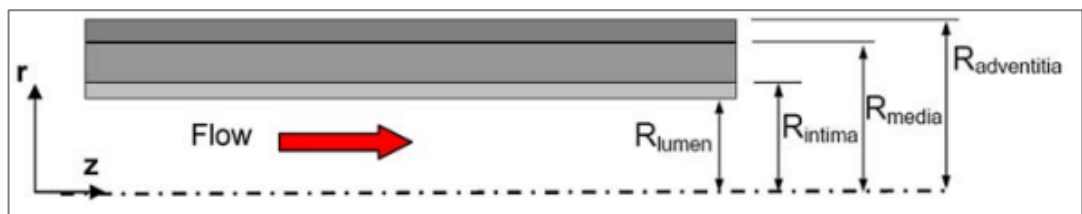


Figure 7: Schematic of three layers of an arterial wall (represent central axis of the cylindrical artery and R is its distance from each layer within the wall) (Khanafar and Berguer, 2009)

(Khader *et al.*, 2014) created a 3D FSI model (using ANSYS 13.0) of an eccentrically stenosed tube to study the effects of increasing severity. Blood flow was modelled as pulsatile, and pressure and velocity distributions in the tube were investigated along with wall shear stresses. The post-stenotic wall shear stress and WSS were maximum during peak systole, and wall collapsibility was observed during early diastole. They observed a significant pressure drop and a complex deformation in the post-stenotic region as the stenosis severity increased. Moreover, the wall deformation in the 95% stenosed tube caused extended deformation along the entire downstream length when compared to partial deformation in the case of 66% stenosed tube.

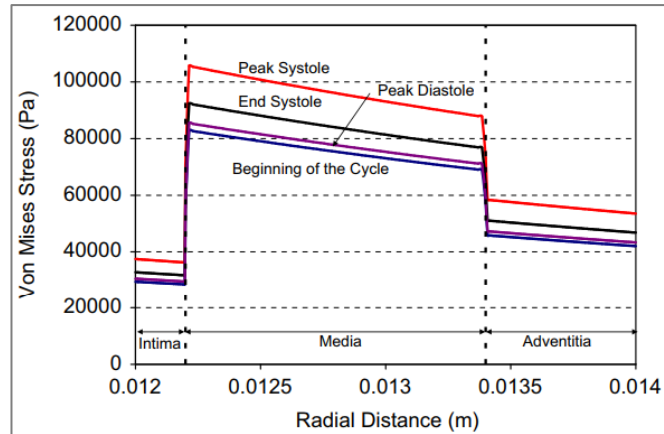


Figure 8: Variation of the Von Mises wall stress across the wall of a descending aorta at various periods of the cycle (Khanafer & Berguer, 2009)

(Khanafer and Berguer, 2009) studied wall mechanics in an axisymmetric three-layered wall model of a descending aorta, exposed to pulsatile flow. The three layers were intima, media and adventitia, as depicted in Figure 7. ADINA software was used to perform a fully coupled FSI analysis, where Von Mises stresses were calculated. The Von Mises comparison of the three layers is shown in Figure 8. According to their results, the peak wall stress and maximum shear stress were observed in the medial layer of the blood vessel wall.

#### 1.4. Scope of the study

In this project, in which we are a part of an EU consortium (CARDIS), we are working towards building a non-contact device to determine carotid artery PWV and the detection of disturbed flow due to atherosclerosis. The novelty of the device is to use laser Doppler interferometry to measure displacements at the skin surface, due both to pulse waves and stenosis-induced turbulence. A neck phantom consisting of a soft tissue-mimicking gel with an embedded compliant tube (stenosed or un-stenosed) will be constructed, and flow (steady or pulsatile) will be passed through the tube. Laser interferometry will then measure displacement at the gel surface.

The original emphasis of my part of the research was to develop a computational fluid-structure interaction (FSI) model, along with experimental validation of how energy is transferred from the disturbed post-stenotic flow to the arterial wall and thence through the soft tissue to the skin surface. Some early-stage numerical investigation of fluids models (to study the effects of Reynolds number, stenosis shape and severity) was conducted

using ANSYS, and an initial FSI model was attempted. However, due to the unavailability of computational resources, the computational part of the research was discontinued. Preliminary results from the computational study are presented in the Appendix A (section 8.1), though their accuracy remains to be validated.

Therefore, the focus of the research was redirected towards a more experimental study. The revised aims, with which the majority of the work in this thesis is concerned, were twofold:

- To develop and experimentally validate a fluid model to investigate the flow disturbances in post-stenotic flow.
- To construct a simplified neck phantom and measure the vibrations generated at the skin surface due to the post-stenotic flow-induced disturbances (which travel through the arterial wall and thence through the soft tissue-mimicking gel to the skin surface).

To meet these aims, the following objectives had to be met:

- Conduct a design study to identify suitable materials to model the carotid artery, the perfusing fluid, the stenosis, soft tissues and the skin.
- Identify suitable methods to visualise the disturbances within the flow and measure them at the tube surface and the neck-phantom surface level.
- Identify the parameters affecting the flow (flow rate, stenosis symmetry, stenosis severity, fluid viscosity, and positioning of the stenosis)
- Conduct experiments in which fluid flows through bare stenosed and non-stenosed tubes to determine displacements of their walls.
- Create a physical model containing a compliant tube (with and without stenosis) embedded in a tissue-mimicking gel covered with a skin-mimicking surface. This model is used as a simple representation of the neck in which pressure and flow within the tube and associated disturbances at the skin surface are measured.
- Conduct experiments to measure disturbances at the neck-phantom surface due to locally induced vibrations, i.e., disturbances from the stenosed flow.

In this thesis, a design study will first be presented in Chapter 2, where suitable materials, methods, and hardware for conducting the experiments will be discussed. Then experimental investigations of the steady flow inside a bare tube will be presented in Chapter 3, where effects of flow rate, stenosis symmetry, stenosis severity, fluid viscosity, and positioning of the stenosis (disturbances at different positions w.r.t. the stenosis) will be discussed. This investigation will then be expanded in Chapter 4, focusing on these effects for a steady flow inside the tube embedded within a neck phantom. Finally, in Chapter 5, the effects of imposing a pulsatile flow will be discussed.

## 2. Materials and Methods

This chapter focuses on the preliminary work conducted to obtain a final experimental setup to mimic a physiological model of a carotid artery embedded inside the neck. This chapter will include the investigation of different mediums used, such as fluid types, arterial materials, soft tissue models, and different methods to produce the disturbances in the model and investigate their responses.

Before studying the displacements at the skin surface, the initial focus was to study the origin of the disturbance, which is the embedded artery. There are two things to consider here: the arterial wall through which the energy is being transferred, and the other is the fluid inside the tube where the flow-induced disturbances originate (caused by the emergence from a narrowed path).

Firstly, we will be looking at the fluid in the tube to identify properties that could be used to mimic the behaviour of the blood. As discussed earlier, Reynolds number is an important parameter that reflects the behaviour of flowing fluids and changing the viscosity can have a significant effect on the Reynolds number and hence the flow profile within an artery.

### 2.1. Fluid Type

Before replicating a physiological scenario, the objective was to understand and provide a proof of concept of detection of flow disturbances at varying flow rates. Assuming negligible changes in density and diameter, the adjustable variables were the viscosity and flow rate, through which the effects of changing Reynolds number would be investigated. Hence, before using a blood-mimicking fluid, a fluid with a different viscosity to that of blood was investigated to identify and understand the disturbances in the flow profile at varying flow rates.

A suitable blood-mimicking fluid is required to mimic blood flow in human arteries. The main criterion set to identify the suitability was the viscosity of the fluid. It was important to maintain the fluid viscosity close to 4cP (along with controlling other parameters discussed later in this chapter) to keep the Reynolds number in the physiological range. Another desired property was the transparency of the fluid, with the objective of

visualising the flow disturbances when injecting a dye into it, as shown in Appendix B (section 8.2.1).

De-ionized water (with dynamic viscosity of around 1cP) was the initial choice of fluid due to ease of handling and availability in the lab. Having water as the perfusing fluid meant that a high Reynold's number would be achieved at a lower velocity than the physiological conditions, as the viscosity of the blood is approximately four times that of water. This would better allow us to visualise the effects of the increasing flow rate (and hence Reynolds number).

Although there were benefits identified earlier, using water would mean that high disturbance would be potentially visible despite the lower flow rate, especially in the post-stenotic region. Furthermore, a higher Reynolds number (due to low viscosity) would incur more computational time and costs to obtain fully converged results on the computational side.

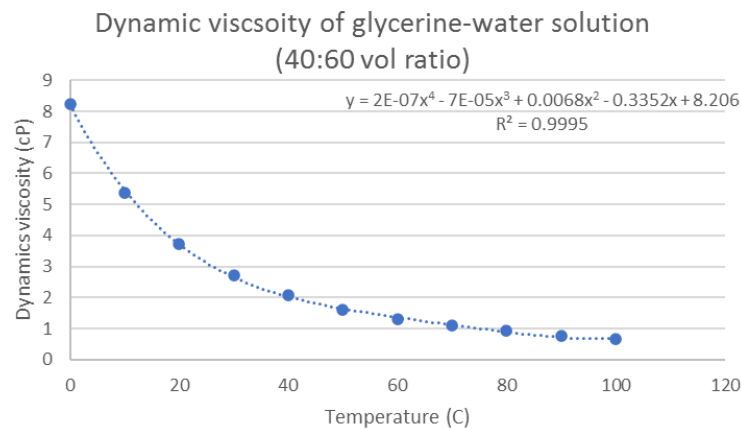


Figure 9: Variation of viscosity in 40:60 (volume ratio) of the glycerine-water solution, with temperature [derived from (Segur and Oderstar, 1951; Trejo González, Longinotti and Corti, 2011)]

Following the early-stage proof of concept experiments, the experimental set-up was tested and scrutinised for both steady and pulsating flows with de-ionized water. Following this, a suitable material to mimic blood behaviour was identified. A solution of vegetable-based glycerine and de-ionized water was chosen due to its transparency and adjustable viscosity (by glycerine-water ratio and the solution temperature). For the final set-up, a 40:60 (by volume) solution of glycerine in de-ionized water was used to achieve a resulting dynamic viscosity ( $\mu \approx 3.83cP - 4.15cP$ ) interpolated between 17°C and 19°C respectively as illustrated in Figure 9, corresponding to the ambient conditions at

which experiments were conducted) (Segur and Oderstar, 1951; Yousif, Holdsworth and Poepping, 2009).

## 2.2. Arterial tubing

Carotid arteries, being major blood vessels, play a significant role in the blood supply to the brain. As discussed earlier in Chapter 1, increased arterial stiffness is closely associated with most arterial diseases. Therefore, it is important to ensure that arterial tubing closely replicates its elastic properties to mimic a human carotid artery. The main material criterion to be considered was Young's modulus ( $E$ ) of the tube. Tube thickness was considered for distensibility purposes. Tube translucency was desirable in the experiments to help in the apparatus set-up and visualise the flow profile.

As mentioned in section 2.1, the initial objective was to provide a proof of concept and visualize the flow fields in the vicinity of the stenosis at varying flow rates. For this, a readily available translucent silicone rubber tube was used. Despite Young's modulus value very much greater than that of an artery, this tube was used to detect disturbances in the stenosed flow, although no elasticity measurements were performed. An exploratory study then followed the proof of concept to find a tubing material with a physiological modulus value close to the ones cited in the literature, along with transparency.

The walls of conduit arteries such as the carotid have three distinct layers: tunica intima nearest to the vessel lumen, tunica media, and tunica adventitia (Khamdaeng *et al.*, 2012a; Miura, 2020). The tunica media and adventitia are predominantly responsible for the arteries' mechanical behaviour at lower and higher-pressure levels, respectively. Measurements of Young's modulus for both these layers in the human carotid artery averaged  $0.9 \pm 0.25$  MPa (for circumferential strain in the range of 0.04-0.08), and this was set as the reference value for this study (Khamdaeng *et al.*, 2012a). The study by (Riley *et al.*, 1992) provided a maximum value of Young's modulus of around 1.54MPa for a systolic pressure of around 140mmHg, in a 60-64 year old (male) age group. Arterial properties vary among patients due to various factors, including gender, age, disease state and cardiac dynamics (Riley *et al.*, 1992; Aggoun *et al.*, 2000; Łoboz-Rudnicka *et al.*, 2018).

Following the literature review showing a range of values for the internal lumen diameter, a value of 6.35mm was chosen to replicate the carotid artery embedded in the phan-



tom, this being within the physiological range (Krejza *et al.*, 2006; Khamdaeng *et al.*, 2012a). This value was set as the reference value to be used for the final iteration of the experiments. A black latex rubber tube and a translucent Penrose latex tube were investigated by material testing and observations regarding their suitability to mimic a carotid artery.

A black latex rubber tube with an internal diameter of 6.25mm, a wall thickness of 0.65mm, and a length of 305mm was investigated. An inflation test was used to determine the mechanical properties of the tube. The tube was placed under a digital camera (Figure 10) fitted with a macro lens, giving a magnification of x6 and producing a resolution of 117 pixels/mm. The tube was closed at one end, and the other end was inflated with air (using a sphygmomanometer). The tube was marked along its length at six regular positions 5cm apart and was inflated to pressures increasing from 0 – 250 (mmHg) in increments of 50mmHg. For each pressure value, the diameter was recorded from the camera image (an example of which is provided in Figure 11).

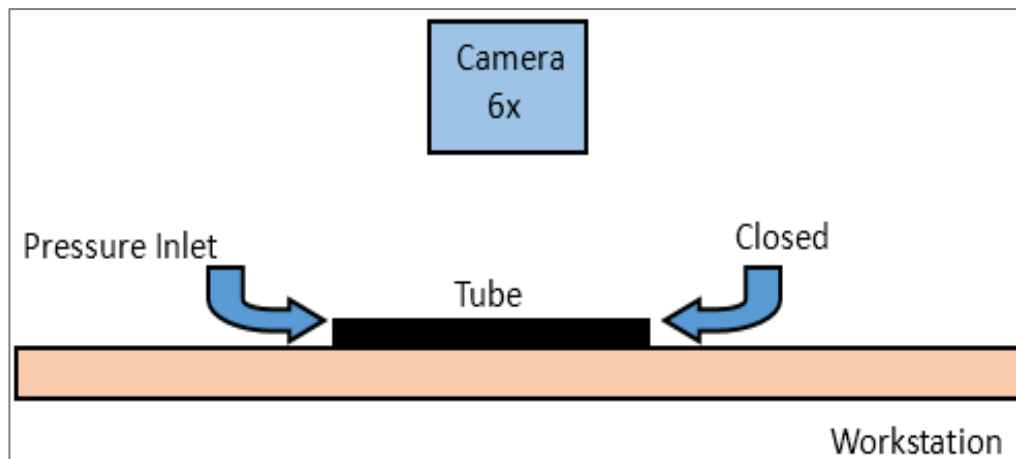


Figure 10: Measurement of deformation in the tube to determine its Young's Modulus

Constant wall volume and incompressibility were assumed to determine hoop stress ( $\sigma_H$ ). According to (Bai and Bai, 2018), the mid-wall hoop stress for a thick-walled tube ( $D/t$  of 9.6) under a pressure  $\Delta P$  with external diameter ( $D$ ) and wall thickness ( $t$ ) can be determined by:

$$\sigma_H = \frac{\Delta P(D_e - t)}{2t} \quad (2)$$

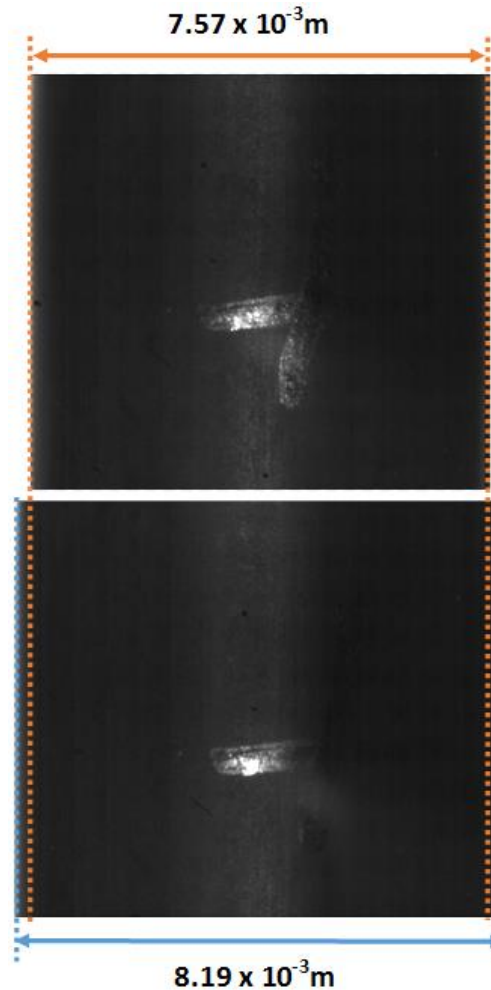


Figure 11: An example image (top view) of the black latex rubber tube (midway along the tube length) captured at x6 magnifications during inflation test for pressures of 0mmHg (top) and 250mmHg (bottom)

The hoop stress values and strains were then used to calculate Young's modulus (E) of the tube. A sample data set obtained from the middle of a 305mm long tube, and its corresponding calculations are shown in Table 3. A linear trend was observed between hoop stress and strain, as shown in Figure 12, which provided an average E value of 2.10MPa.

Compared with the mean (0.9MPa) and the maximum (1.54MPa) physiological values specified earlier, the measured Young's modulus for the black latex rubber tube was higher with a value of 2.10MPa. Furthermore, this stress increased linearly with the strain, which is not comparable to a human artery – where the stress increases with increasing strain. Furthermore, with the added disadvantage of lack of transparency, the material was not deemed suitable, and flow experiments with the silicone rubber were continued until a better alternative was found.

The final tube that was investigated was a Penrose latex tube. A tube of length 305mm,

Table 3: Inflation data at 15cm from the inlet of the black latex rubber tube

Pressure (mmHg)	Width/Diameter (m)	Strain	Hoop Stress (Pa)	Inner Diameter (m)	Wall thickness (m)
0	7.57E-03	0.00E+00	5.66E+02	6.25E-03	6.58E-04
50	7.65E-03	1.09E-02	2.87E+04	6.33E-03	6.59E-04
100	7.77E-03	2.75E-02	6.02E+04	6.48E-03	6.46E-04
150	7.89E-03	4.26E-02	9.42E+04	6.62E-03	6.35E-04
200	8.04E-03	6.22E-02	1.33E+05	6.79E-03	6.21E-04
250	8.19E-03	8.21E-02	1.75E+05	6.97E-03	6.08E-04

with a measured diameter and thickness of approximately 6.35mm and 225  $\mu\text{m}$ -325 $\mu\text{m}$ , respectively, was used. The density of this material was calculated by cutting and submerging a rectangular patch of the tube (0.9cm x 1.2cm) into a water-ethanol mixture. The ratio of ethanol to water was adjusted (up to 49.6%) until the patch became neutrally buoyant. Therefore, at this point, the density of the Penrose tube was taken to be the same as that of the mixture, which was measured as 895  $\text{kg}/\text{m}^3$  (+/- 3.5%).

The Young's modulus of the tube was determined in the same way as that of the black latex rubber tube, the only difference being that thin-wall assumption was used in this case (with a mean D/t ratio of 23. Hoop stress, under pressure  $\Delta P$ , with an external diameter (D) and wall thickness (t) was now determined by:

$$\sigma_H = \frac{\Delta P(D_e)}{2t} \quad (3)$$

The hoop stress values and strains were then used to calculate Young's modulus (E) of the tube. An extract from one of the data sets obtained from 15cm (mid-way of a 30cm long tube) and its corresponding calculations are shown in Table 4. An increase of hoop stress was seen with increasing strain, as shown in Figure 13. This yielded a range of Young's modulus values between 0.88-2.36 MPa (between strain values of 0.08-0.25), after which the modulus value started to decrease.

The minimum value calculated here is within the earlier specified physiological average of 0.9 +/- 0.25 MPa (for circumferential strain in the range of 0.04-0.08). Since the circumferential strains under physiological conditions are below 0.1 (Khamdaeng *et al.*,

2012b; Rosenberg *et al.*, 2018), the Penrose latex tube provided a close approximation of the carotid arterial stiffness within this range of strains. Several other studies have also used this material for arterial tubing (Binns and Ku, 1989; A. Scroggs, 2001; Yazicioglu *et al.*, 2005). Furthermore, its semi-transparent properties would serve well in the experimental set-up and allow visualising of the flow field inside the tube. Therefore, the Penrose latex tube was chosen as the most suitable (based on criterion summarised in Table 5) for conducting the final set of experiments, the results of which are discussed in chapters 3, 4, and 5.

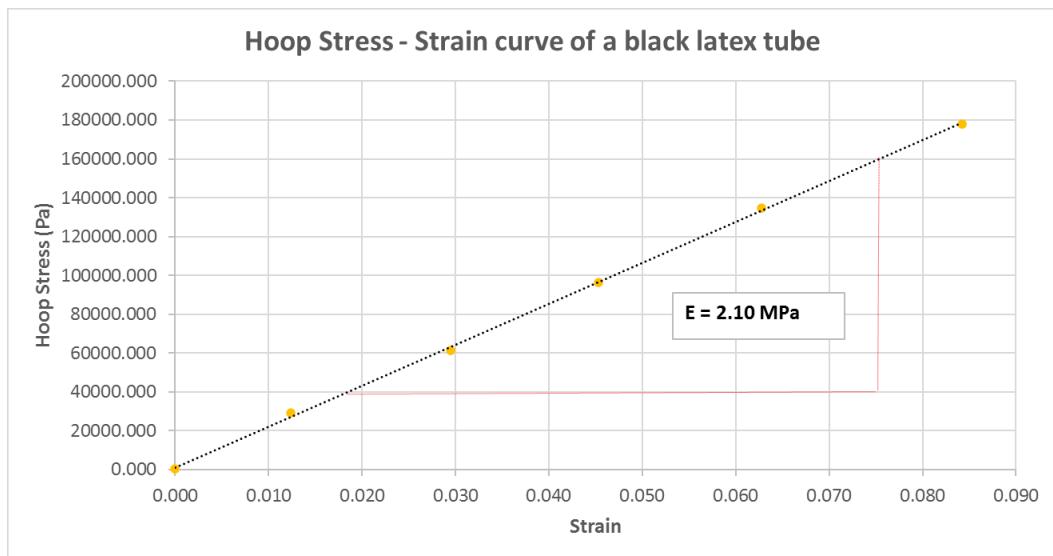


Figure 12: Stress-strain curve of a black latex rubber tube

Table 4: An extract from inflation data at 15cm from the inlet of the Penrose latex tube

Pressure (mmHg)	Width/Diameter (m)	Strain	Hoop Stress (Pa)	Inner Diameter (m)	Wall thickness (m)
0	6.50E-03	0.00E+00	0.00E+00	0.00E+00	5.90E-03
20	7.16E-03	1.03E-01	2.67E+03	3.28E+04	6.63E-03
40	7.27E-03	1.19E-01	5.33E+03	6.77E+04	6.74E-03
60	7.43E-03	1.43E-01	8.00E+03	1.07E+05	6.91E-03
80	7.55E-03	1.62E-01	1.07E+04	1.47E+05	7.04E-03
100	7.65E-03	1.77E-01	1.33E+04	1.89E+05	7.14E-03
120	7.78E-03	1.98E-01	1.60E+04	2.36E+05	7.29E-03
140	7.93E-03	2.20E-01	1.87E+04	2.87E+05	7.44E-03
160	8.06E-03	2.41E-01	2.13E+04	3.41E+05	7.59E-03
180	8.27E-03	2.73E-01	2.40E+04	4.05E+05	7.81E-03

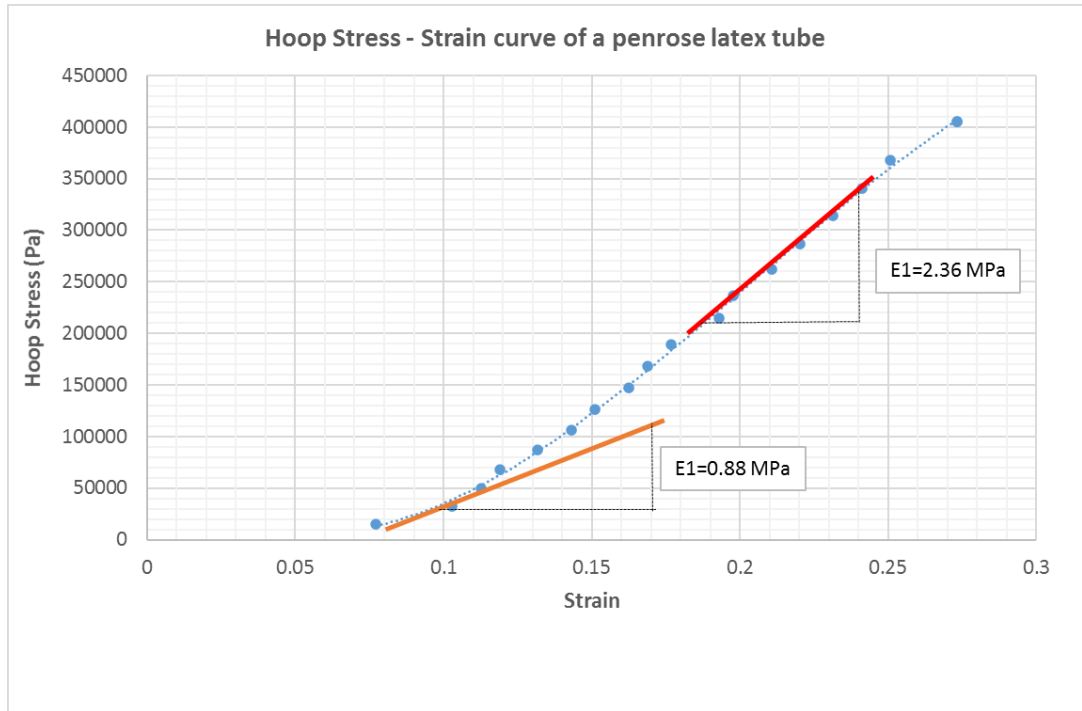


Figure 13: Stress-strain curve of a Penrose latex tube from

Table 5: Comparison between candidate materials for the arterial tubing material

	Stiffness	Transparency	Tube thickness
Silicone rubber tube	✗	✓	✗
Black latex rubber tube	✗	✗	✗
Penrose latex tube	✓	✓	✓

### 2.3. Stenosis material and type

This study focuses on identifying carotid artery disease at an early stage, which ties in with detecting flow-induced disturbances (due to the presence of stenosis). Therefore, a stenosis needs to be introduced in the arterial tubing to induce these disturbances. In vivo, a few parameters determine the characteristics of stenoses. These include stenosis symmetry, severity (reduction in lumen area), geometric shape (uniformity) and stenosis length. For an early-stage diagnosis, the effect of stenosis severity was critical to understand. The second parameter to be investigated in combination with the severity was the

stenosis symmetry. The idea was to understand and localise the stenosis based on the disturbances detected from the presence of different severities and asymmetry.

For the early-stage proof of concept mentioned in section 2.1, a moderate narrowing (50% by diameter or 75% by area) was introduced. A narrowing was created by introducing a cylindrical rod (of half the inner tube diameter) inside the tube to define the diameter of the stenotic neck, and a cotton thread (with a diameter of around 150 microns) was firmly tied around the outer surface (halfway along the length of the tube) until the rod could not slide freely inside. The rod was then carefully pulled out, leaving behind a constricted tube with a minimum diameter close to that of the rod and cross-sectional profile, as shown in Figure 14. It can be seen from the figure that once the rod was removed, the inner perimeter of the tube was not circular anymore. The non-circular cross-section can be explained by how two edges of the thread were pulled before the double overhand stopper knot was made.

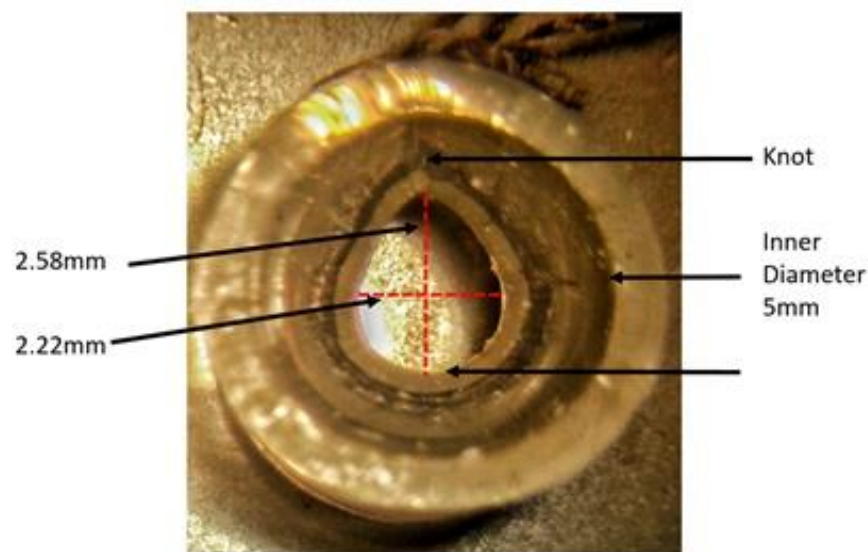


Figure 14: A proof of concept non-axisymmetric stenosis (50% by area) formed in a silicone tube (5mm internal diameter) by tying a cotton thread around it

Following the proof-of-concept study, a robust method of introducing a narrowing was required, which offered repeatability and allowed the control of the geometric features of the stenoses, including severity, symmetry, shape, and length. 3-D printing was therefore adopted so that these variables could be specified and controlled. In addition to its cost-effectiveness and quick turn-round time, it also allowed freedom of design.

Stenoses (which would later be inserted into arterial tubing) were 3-D printed in an opaque VeroWhite material (Stratasys Ltd, Standford Marsh, Derby, UK, properties listed in Table 6 with a print resolution of 100 microns. A range of stiffness was provided for this material, which could be due to variation in the size of the microscopic particles in the resin and/or the orientation of the print). A cross-section of a 75% severity stenosis (50% reduction in diameter) is shown in Figure 15. The total of length of 10mm shown in Figure 15 was maintained constant across all the stenosis severities.

The printed stenoses were measured and checked against 2-D drawings. Furthermore, a quick study was conducted to investigate the effect of the printing resolution on the flow (as flakes due to inconsistencies in printing shown in Figure 16 were suspected to disturb the flow). It was concluded that the disturbances (if any) due to this were hidden in the larger disturbances due to the presence of the stenosis itself and did not have any significant effect on the resulting system.

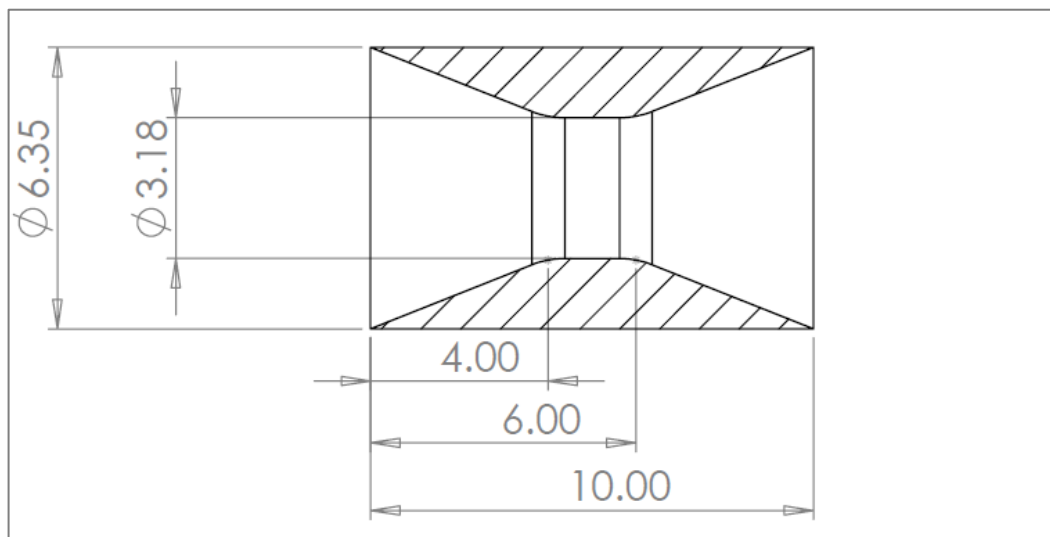


Figure 15: A planar view of a 75% axisymmetric stenosis (all dimensions are in mm)

Therefore, for the final set of experiments, a set of 3-D printed stenoses were made, simulating axisymmetric carotid artery stenoses of 60%, 75% and 90% reductions in the area. For a non-stenosed control, an empty tube was used with no stenosis inserted. To study the effect of stenosis symmetry, two eccentric stenoses with severities of 75% and 90% were printed where the narrowing was offset by 1 mm from the centre). 2-D drawings for these stenoses are presented in Figure 17.

Table 6: Material properties of VeroWhite material for the 3D printed stenoses.

Tensile Strength (MPa)	Elongation at Break (%)	Modulus of Elasticity (MPa)	Flexural Strength (MPa)	Water Absorption (%)
50 – 65	10 – 25	2,000 – 3,000	75 – 110	1.1 – 1.5

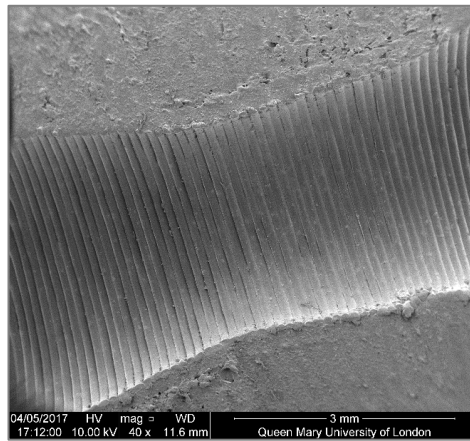


Figure 16: Microscope image of 3D printed stenosis – cross-section view

Severity	Axisymmetric	Non-axisymmetric
75%		
90%		

Figure 17: Cross-section of axisymmetric and non-axisymmetric stenoses ( $x_1$  and  $x_2$ , both 1mm offset from geometric centre), with (a) 75% and (b) 90% reduction in area, respectively

Having defined the design criteria for fluid type, arterial tubing material and the stenoses, it was then possible to start experiments with the bare tube, either unobstructed or



fitted with stenoses. The tube would later be embedded in neck models (neck-phantoms), before which a suitable material to mimic the soft tissues around the arterial tubing was investigated.

## 2.4. Soft Tissue Models - Material Choices

In addition to the vertebrae, the neck consists of various soft tissues, including tendons, ligaments, and muscles. The stiffness value for these soft tissues usually lies between  $10^4$  -  $10^6$  Pa (Akhtar *et al.*, 2011; Wells, 2013). The presence of these soft tissues allows the transmission of the energy from the carotid artery (embedded within the soft tissues) to the skin surface. Therefore, the speed of sound in the material is another parameter to be considered when making a phantom from a tissue-mimicking material (TMM). While the speed of sound in soft tissues is usually in the range of 1400-1650m/s (Anderson and Trahey, 1998), speed of sound in-vivo is typically assumed to be around 1540m/s (Lee *et al.*, 2019). An example of speed of sound for different tissues is shown in Figure 18.

Tissue Type	Speed (mm/ $\mu$ s)	Density (g/cm <sup>3</sup> )	Atten. Coef. @ 1 MHz (dB/cm)	Nonlin. Param. (B/A)
Connective <sup>1</sup>	1.613	1.120	1.57	—
Muscle <sup>1</sup>	1.547	1.050	1.09	—
Fat <sup>1</sup>	1.478	0.950	0.48	—
Adipose <sup>2</sup>	1.450	0.950	0.29	10.0
Blood <sup>2</sup>	1.584	1.060	0.20	6.1
Brain <sup>2</sup>	1.560	1.040	0.60	7.1
Breast <sup>2</sup>	1.510	1.020	0.75	—
Eye: lens <sup>2</sup>	1.645	1.070	0.80	—
Eye: vitreous <sup>2</sup>	1.528	1.010	0.1	—
Kidney <sup>2</sup>	1.560	1.050	1.0	7.4
Liver <sup>2</sup>	1.595	1.060	0.50	6.6
Muscle, cardiac <sup>2</sup>	1.576	1.060	0.52	7.1
Muscle, skeletal <sup>2</sup>	1.580	1.050	0.74	6.6
Skin <sup>2</sup>	1.615	1.090	0.35	7.9
Fatty <sup>2</sup>	1.465	0.985	0.40	8.5
Non-fatty <sup>2</sup>	1.575	1.055	0.60	7.0
Blood cells <sup>3</sup>	1.627	1.093	0.28	—
Blood plasma <sup>3</sup>	1.543	1.027	0.069	—
Eye: cornea <sup>3</sup>	1.586	1.076	—	—
Spinal cord <sup>3</sup>	1.542	1.038	—	—
Spleen <sup>3</sup>	1.567	1.054	0.4	7.8
Testis <sup>3</sup>	1.595	1.044	0.17	—
Mean	1.561	1.043	0.54	7.5
St. Dev.	0.051	0.042	0.37	1.1

Figure 18: Reference values for speed of sound, attenuation, nonlinearity properties and mass density for a variety of human soft tissues (Mast, 2000)

Other parameters of interest are manufacturing times, ease of handling/processability and some degree of transparency (to enable controlled placement of the tube with known location and orientation of the stenosis, visualisation of any leakages, local twist/collapse of the tube and/or swelling as a result of any weakening of the tube due to over-inflation).

Candidate materials chosen to mimic the soft tissues were agar, polyvinyl alcohol (PVA), vegetarian gelatine and Parker Aquasonic 100 ultrasound gel.

#### 2.4.1. Agar gel

Agar gel was prepared by adding granulated, purified agar to deionised water at 96°C in the ratio of 3:97 by weight. The mixture was cooled for 2 -3 hours to 47°C, poured into moulds and allowed to solidify at room temperature. Three different techniques were used in this study to determine the modulus. Firstly, a known compressive load was applied to a cuboidal sample of the gel, and a travelling microscope monitored the deformation. Secondly, a compressive load was applied to a cylindrical sample of the gel, and a laser displacement sensor measured the displacement. Finally, stress-strain measurements were repeated with an INSTRON machine, where force generated by the known displacements was measured. Young's modulus, measured on freshly prepared specimens from all these methods was in the order of  $10^5$  Pa (Brewin *et al.*, 2015).

To prevent dehydration, specimens were stored in deionised water at room temperature, after which Young's modulus increased from  $1.0 \times 10^5$  Pa to  $1.5 \times 10^5$  Pa. Before this project, the propagation of shear waves and viscoelastic creep had been investigated in our laboratory. The material has viscoelastic properties but, in some respects, behaves as a highly viscous fluid, undergoing steady creep when loaded for periods up to 1 week. The sound speed measured corresponded to Young's modulus value of  $10^5$  Pa, which agrees with the value obtained from the above testing (Banks *et al.*, 2013). Further details of these dynamic measurements are presented in Appendix B (8.2.2). The gel, however, did not have the desired optical properties due to its opaque nature.

#### 2.4.2. Polyvinyl alcohol (PVA) gel

PVA gel was prepared by dissolving granulated PVA in deionized water, and ethylene glycol was added to lower the freezing point of the solution, thus avoiding the formation of ice crystals during the freeze cycle. The aqueous solution was warmed up well above 70 °C for dissolution to occur and then combined with PVA powder while stirring to break any PVA aggregate. The resulting liquid was cooled down to room temperature to ensure the formation of a homogeneous gel and is then poured into the appropriate moulds. The liquid was allowed to rest (covered to minimise dehydration) at room temperature to

let air bubbles rise to the surface. The mould was then placed in a freezer at -20 °C for at least 12 hours, since the freeze time and the thaw time depend on the size of the mould. At the end of the thaw cycle, the gel can undergo additional freeze-thaw cycles if needed, as explained below.

High-grade polyvinyl alcohol in an aqueous solution can be permanently cross-linked through repeated freeze-thaw cycles to obtain a tissue-mimicking hydrogel whose mechanical properties are highly stable (>6 months) and appropriate to the tissue to be modelled. The stiffness is affected mainly by two factors: the number of freeze-thaw cycles and PVA concentration in the aqueous solution. The number and stability of PVA crystallites are increased as the number of freeze-thaw cycles, or the PVA concentration is increased, leading to a wide achievable range of mechanical properties. Compressional and tensile tests on PVA samples (Figure 19) found that the stiffness of a 10 wt% PVA gel can vary between  $10^4$  and  $10^5$  Pa, depending on the number of freeze cycles. (Fromageau *et al.*, 2007)

Although PVA gel offers a range of stiffness values, allowing the wave propagation speed to be controlled, it is time-consuming to prepare, and its lack of transparency makes it difficult to visualise the embedded tube and the precise position of the stenosis within it.



Figure 19: PVA gel under tensile testing

#### 2.4.3. Vegetarian gelatine gel

Vegetarian gelatine gel was prepared by adding 6.5g of granulated vegetarian gelatine substitute (Dr. Oetker's Veg Gel containing Dextrose, Gelling agents: Carrageenan, Locust bean gum; Acidity regulators: Calcium acetate, Potassium chloride) to 190ml of deionised water at room temperature and stirred until the granules were dissolved. The mixture was heated to its boiling point while stirring and then immediately taken off the heat. It was then cooled at room temperature for 10 minutes, poured into the mould and allowed

to solidify at room temperature for 4-5 hours. Once the gel was set, it was taken out of its mould and refrigerated (at 4° C) for later use.

To measure the gel's stiffness, a freshly prepared sample of dimensions 23x23x10mm was placed on the compression plate (of an Instron 3342 universal testing system) and compressed at a rate of 1mm/min (Figure 20). Compression stress values for a range of strains were recorded and plotted as shown in Figure 21.



Figure 20: Vegetarian Gelatine under compression testing

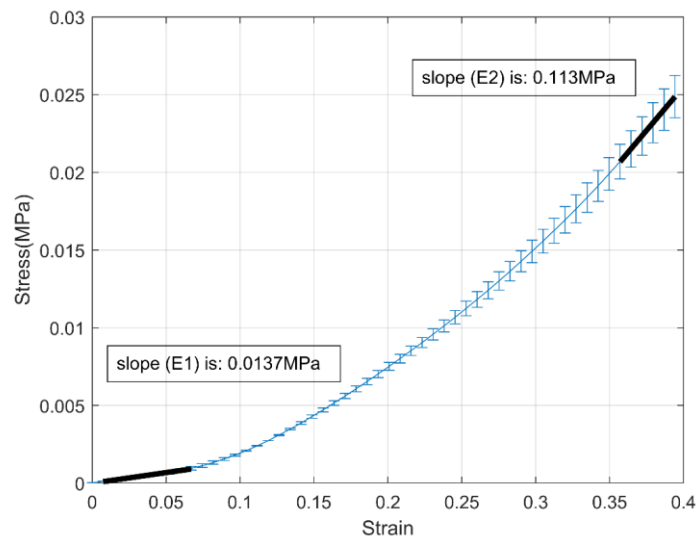


Figure 21: Stress-strain curve from a vegetarian gel sample, 23x23x20mm, using INSTRON 3342 machine)

The Young's modulus, measured on freshly prepared specimens under compression, was in the order of  $10^4$  -  $10^5$  Pa (between strains of 0-0.4). However, since the gel would

not be under strains as large as 0.4 during the experiments, the Young’s modulus of the gel was towards the lower end of the range (i.e. in the order of  $10^4$  Pa) thus the material was not considered ideal for replication the elastic properties of human tissues (Akhtar *et al.*, 2011; Wells, 2013).

Besides the measured mechanical properties and the optical transparency, the reduced preparation times of the mould makes this gel a viable candidate for a TMM. An attempt to investigate controlled shear wave generation inside this gel was also made by embedding a magnet with a gel and inducing a spin through an external magnet. The poor structural integrity of the gel prevented the further development of this study. Further details of this study are presented in Appendix B (section 8.2.2).

#### 2.4.4. Ultrasound gel

In addition to the three types of gels specified earlier, which were made in-house and inserted into the moulds while still in liquid form, the possibility of using a commercially available ultrasound gel was also explored. The potential added benefits were not only a closer replication of soft tissue acoustic properties but also meant the lead times between the experiments were reduced as the gel did not have to be frozen again for experiments within the same week as long as the phantom was covered to minimise dehydration of the gel (details in section 2.5). It was observed that the weight loss through the Platilon “skin” (see section 2.5) over a period of one week was less than 3%, which meant that the gel could be repeatedly used for the experiments, before it had dehydrated and changes its properties (Table 7). The speed of sound in the Konix® gel (substantially equivalent to the Parker Aquasonic 100 ultrasound gel) was reported to be 1518 m/s (Amen, 2014).

Table 7: Properties of the ultrasound gel (Parker Laboratories, 2011)

Physical State	Viscous, Aqueous
Colour	Clear Blue
Specific Gravity	1.02
Viscosity (cps)	130,000-185,000
pH	6.50-6.95
Solubility in Water	Soluble

Parker Aquasonic 100 ultrasound gel, in addition to being readily available, closely mimicking the speed of sound in the material, and minimizing the phantom preparation time, also offers a degree of transparency which is one of the key properties required of the phantom. Based on the design criteria summarised in Table 8, Parker Aquasonic 100 ultrasound gel was deemed the most suitable candidate for the final iteration of the experiments.

Table 8: Comparison between candidate materials for the soft tissues mimicking material

	Stiffness	Speed of sound	Ease of handling / processability	Preparation Time	Transparency
Agar	✓	✓	✓	✗	✗
PVA	✓	-	✗	✗	✗
Vegetarian gelatine	✗	-	✓	✗	✓
Parker Aquasonic 100	-	✓	✓	✓	✓

## 2.5. Skin Model

Alongside the choice of the materials for simulation of arteries and soft tissues, the skin was an important organ to be accounted for. Besides physiological importance, a skin surface was needed to hold the ultrasound gel in a well-defined shape (due to its viscous nature) and provide a surface to facilitate displacement measurements. The agar, vegetarian gelatine, and PVA gels discussed in section 2.4 did not require a skin surface due to their solidity which provided a solid surface to facilitate the measurement.

The criteria set for the skin mimicking material (SMM) was that its stiffness value lay within the broad physiological range (varying greatly due to skin site, age, thickness, body mass index and hydration, amongst other factors) of 0.005 – 140 MPa (Pawlaczyk, Lelonkiewicz and Wieczorowski, 2013; Kalra and Lowe, 2016). Like the gels, some transparency was also required, as mentioned in section 2.4. Furthermore, the dehydration of gel had to be minimised.

Polyurethane is usually used for artificial skin models, simulating the epidermis, for training in medical areas (Dabrowska *et al.*, 2016; Shimizu and Nonomura, 2018). A polyurethane film material, Platilon® (Covestro, 2017) was selected as a suitable SMM. Before starting this work, a similar experiment was carried out by J. Reeves in the Greenwald group (unpublished), where a 120  $\mu\text{m}$  - 200 $\mu\text{m}$  thick layer of polyurethane material was used to mimic the skin. The material's elastic modulus was measured by performing a tensile test on a dog-bone specimen using an Instron 3342 universal testing system. A 31mm long specimen with a width and thickness of 6.3mm and 0.12mm was used, and the sample was stretched at a rate of 50mm/min. The resulting stress-strain curve is plotted in Figure 22 and, as discussed later in section 2.6, the biaxial strain applied to the Platilon in the phantom was around 0.01. The resulting Young's modulus, determined by the gradient at this strain (Figure 22), was 20.13 MPa which is within the range specified above. Further properties of Platilon are detailed in Appendix B (section 8.2.3)

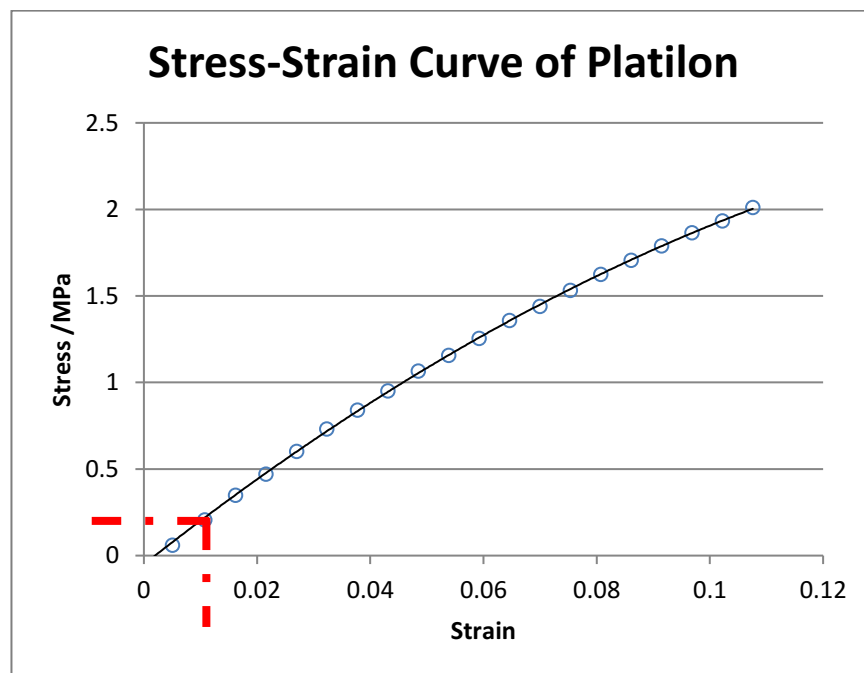


Figure 22: Stress-strain plot of Platilon material (Reeves and Greenwald, unpublished)

A study was carried out to assess the ability of the Platilon to prevent dehydration of the ultrasound gel, where a cylindrical container (approximate diameter 50mm and volume 30 ml) was filled with the gel and covered with Platilon, secured tightly round the edges with elastic bands. The experiment was repeated with a tightly fitting impermeable lid and again, with no covering over the gel. For each set-up, the container was weighed

periodically for a few weeks (results in Figure 23) to assess dehydration, and as mentioned in section 2.4.4, the weight loss observed within one week (due to dehydration) was less than 3%, after which the phantom would be topped up. Furthermore, Platilon also offered transparency, making it a suitable choice for a skin mimicking material.

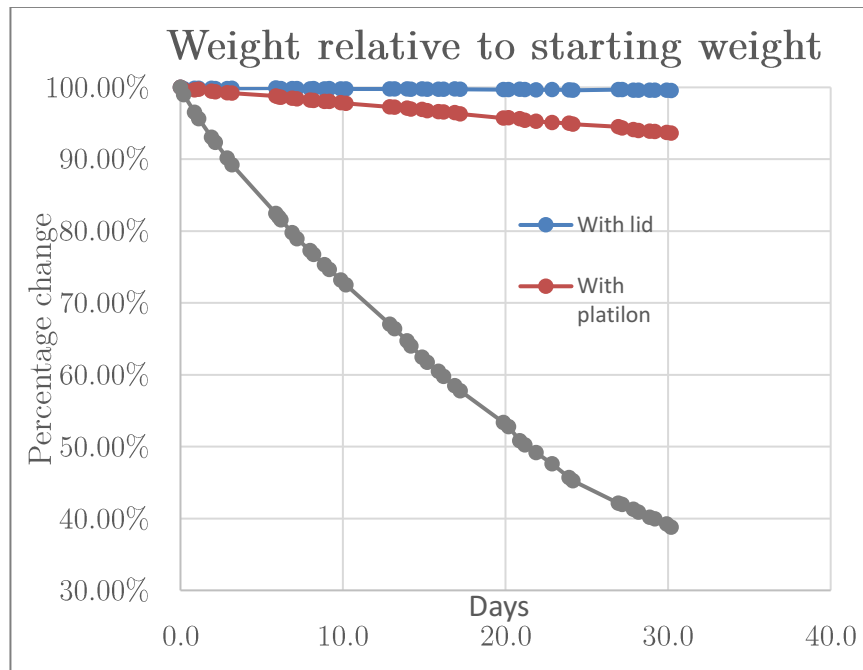


Figure 23: Weight loss of the phantom due to dehydration (Reeves and Greenwald, unpublished)

## 2.6. Preparation of Phantoms

According to the different states of the gels, two different approaches were taken to prepare the phantoms. All but the ultrasound gels discussed in section 2.4 were prepared in the liquid form, poured into pre-assembled cuboidal moulds (with an embedded tube) and removed from the moulds on solidification. However, the ultrasound gel was simply poured into a pre-assembled mould, hence taking the mould's shape due to its viscous nature, and the top surface of the mould was covered by the SMM.

The initial proof of concept study was conducted with a cuboidal phantom of agar gel (287mm x 100mm x 37.5mm). However, due to the complexity of the surrounding tissues (or the phantom boundaries in this case) there was a potential of wave reflections and their interactions with the surrounding structure. Therefore, when moving to the final set-up with the ultrasound gel, wave reflections were taken into consideration, and the phantom dimensions were increased to minimise these (as the waves would have to travel



further, hence dissipating more energy). The dimensions for one of the simplified neck phantoms are shown as a plan view in Figure 24.

A critical dimension was the depth of the embedded tube. Figure 24 shows that the latex tube was positioned centrally with respect to the height of the mould, resulting in 19.3mm (considering 6.35mm tube diameter) gap between the tube's upper surface and the skin surface. The idea was to test two different depths of the tube, one shallow (7mm below skin) and one at a greater depth (12mm), to identify the effect of the depth of the artery on the detection of the signal.

A plan was in place to test the shallow depth first for different stenosis severities and physiological mean flow rates, and if there was a significant difference in power of the signal due to the stenosis, then the deeper version would be investigated. Due to no detectable disturbances in the 12mm version, the 19.3mm version was also disregarded, and studies continued with the shallow depth phantom.

#### *Standardisation of the phantoms*

To ensure consistency across different phantoms, a standardisation process was followed for each mould. The phantom, as can be seen, is an assembly of different components (Figure 25). Each of these panels was made of 6mm thick acrylic and was cut to the required dimensions using a CNC machine (with a tolerance of +/- 100 microns). All the panels apart from the top and bottom were screwed together, and the edges were sealed using silicone to minimise leaks and dehydration.

The tube fittings (dimensions detailed in Appendix B (section 8.2.4) were inserted in the phantom from both ends, as shown in Figure 25, and each fitting was secured in place by a nut. A non-stretched length of 305mm (330mm when stretched, yielding a 7.5% strain) of the Penrose latex tube was used in all experiments. The (stenosed/non-stenosed) tubes were secured to the fittings by tying a thin cotton thread, and a rubber O-ring was fitted around the outside of the tube as an added insurance against leaks, especially during pulsatile flow.

Once the tube was fixed in place, the top surface of the phantom was covered with Platilon, which was stretched bi-axially to maintain a strain of 0.01 in each direction.

Platilon was secured to the phantom using a double-sided adhesive tape around the interfacing edges. Following this, the top panel with the central cut-out as shown in Figure 25, was secured above it, leaving most of the skin exposed.

The phantom was then placed upside down, so that the ultrasound gel could be poured into the mould. Before adding the gel, two important steps were carried out. Firstly, a solid rod (5mm in diameter) was lubricated with distilled water and passed gently into the tube from each end, meeting in the middle (at the stenosis). The ends of the two rods were keyed so that they locked together where they met, thus preventing the tube from collapsing and sagging when the gel was poured in. Secondly, the opening in the top plate was temporarily closed with a snugly fitting acrylic plate (with same thickness of 6mm), to prevent sagging of the Platilon film due to the weight of the gel.

Each phantom was filled with 2500 grams of ultrasound gel and placed in a vacuum chamber for 15-20 minutes. The pressure inside the chamber was brought down to 0.05atm to facilitate removing any air bubbles trapped within the gel. The phantom was then left overnight (for approximately 12 hours) and partially covered to allow escape of any remaining smaller air bubbles. On the following day, any remaining bubbles close to the skin or the tube were manually removed with a syringe connected to a fine tube, and the phantom was closed and sealed off with a silicone rubber compound (RS, 2016). Finally, the phantom was inverted (with the top plate facing upwards), and the solid rods inserted previously were gently removed from the tube.

The phantom was weighed at various times throughout the week. For mass losses (due to dehydration of the gel) between 5%-10% the phantom was topped up, through the opening on the side shown in Figure 25. For mass loss of over 10% the phantom was reopened, and the gel was replaced.

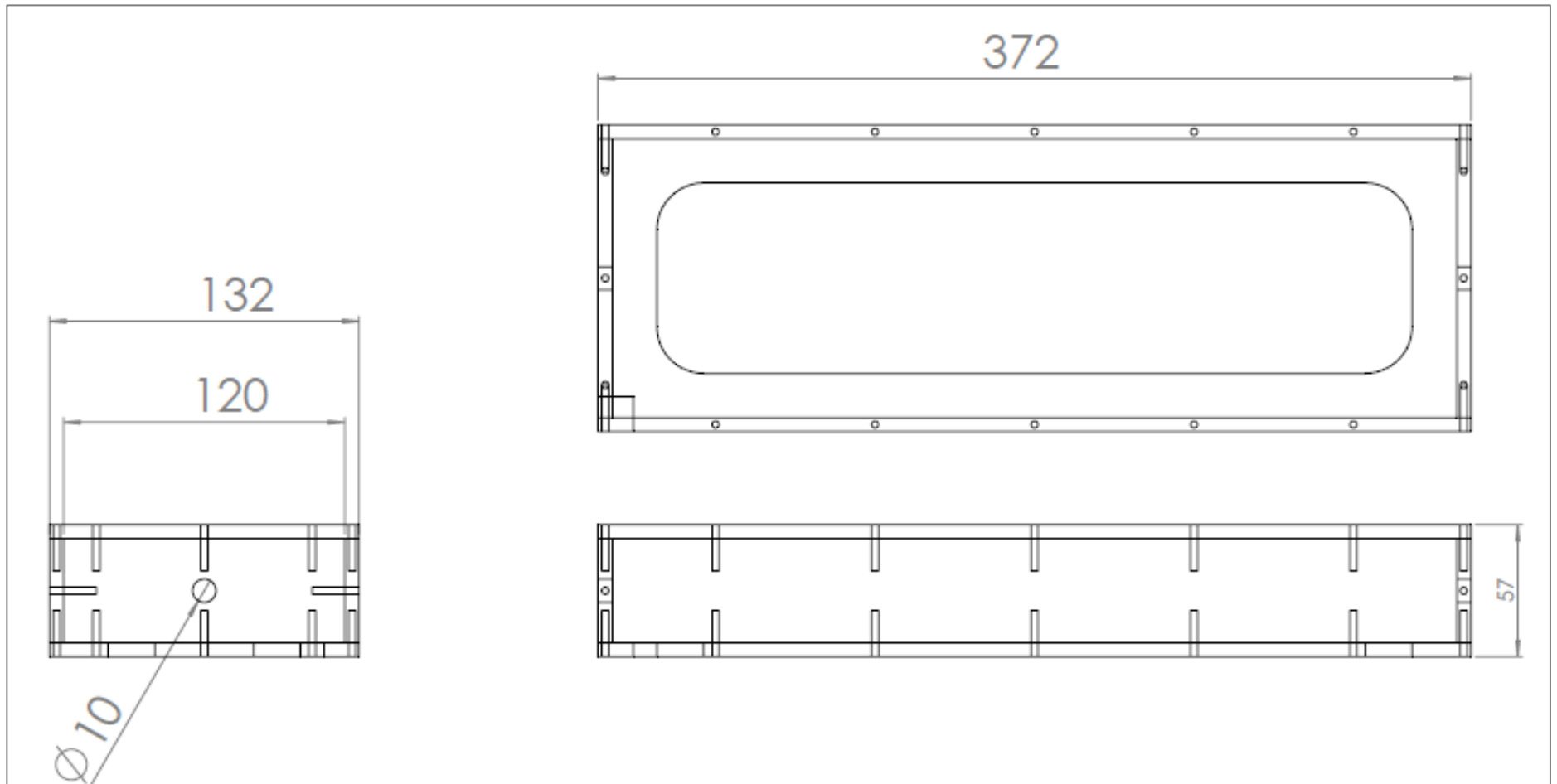


Figure 24: A 2-D drawing of a deep neck phantom (for ultrasound gel) – tube centre located 22.5mm below the skin surface. Thickness of each of the acrylic panels is 6mm

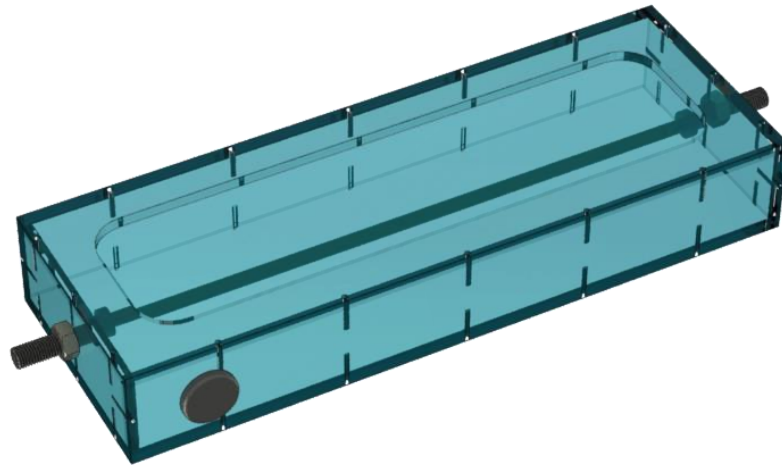


Figure 25: Artificial neck phantom, using Penrose latex tube, ultrasound gel and Platilon to mimic carotid artery, soft tissues and the skin surface, respectively

## 2.7. Control Hardware

A continuous flow circuit was built as shown in Figure 26. The fluid flows from within the reservoir driven by a constant pressure head (with a maximum of 12% reduction as the tank empties) and flows into a programmable piston pump. As the fluid exits the pump, it flows through a cannulating flow probe (model T403, Transonic Systems, Europe B.V., Maastricht- The Netherlands) and then enters the latex tube (bare or embedded within a phantom) specified in the section 2.2.

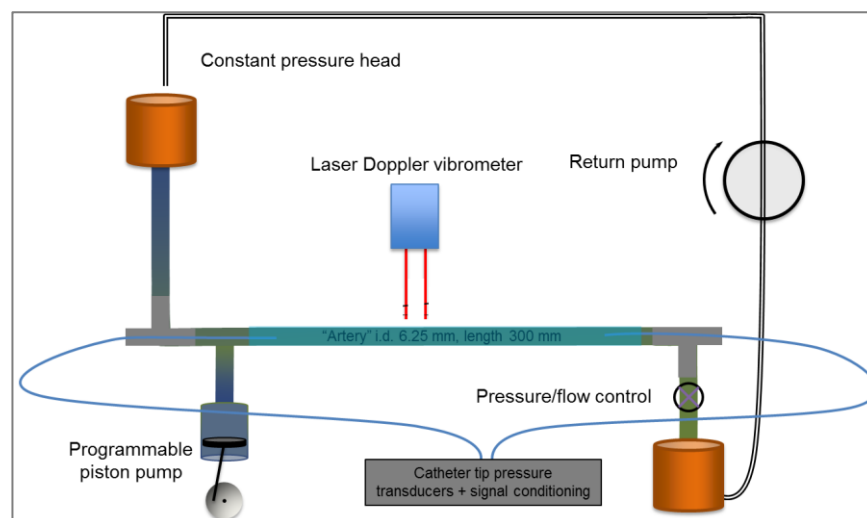


Figure 26: Perfusion rig set-up (current set-up showing the LDV only)

Vertically above the latex tube is either a set of accelerometers or a two-beam laser Doppler Vibrometer (Sios Messtechnik, Ilmenau, DDR) which collects vibration data

(over a wide range of frequencies) at the tube/phantom surface. In addition to the measuring the disturbances on the surface, two catheter-tip pressure transducers are also inserted (one from each end of the tube) to record pressure perturbations inside the tube. Once the fluid leaves the tube, it flows into a collector tank (at atmospheric pressure) whence it is returned (through a diaphragm pump) to the reservoir. More details on the individual components follow:

### 2.7.1. Pump

A custom-made programmable piston pump (H. Denyer, Consultant Engineer, Greatham, UK) was used to generate pulsatile flow, thus simulating the left ventricle of a human heart. For the steady flow cases, the valves were left open and the fluid was allowed to flow freely driven by the pressure head, without operating the pump. However, for the pulsatile flow, once the piston started generating a pulse, the backflow of the fluid was controlled by programmable valve to mimic the behaviour of the mitral valve (Figure 27). The stroke volume, stroke rate, outflow & inflow time and all other parameters are controlled by means of in-house software developed by our group in collaboration with T.J. Haslam (a programmer working with Denyer).

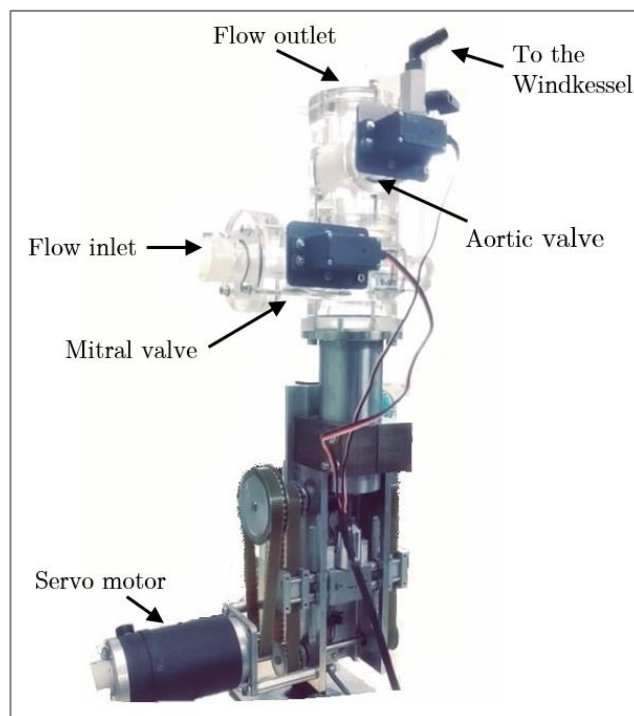


Figure 27: Programmable piston pump

### 2.7.2. Tap

The flow rate was adjusted by varying the outflow resistance of a manual screw valve tap. The importance of placing the tap downstream of the stenosed region was identified since it played a critical role in controlling the resistance and hence the mean pressure of the system. This prevented the tube from collapsing at low flow rates which would have occurred if the tap was positioned upstream.

### 2.7.3. Header Tank

The inflow pipe originated from a header tank, containing either water or the glycerol/water solution, positioned at an enough height (typically 1.3 m above the tube (bare or embedded in the phantom)) to produce an adjustable, constant flow rate up to approximately 400-450 ml/min. The outlet drained water into a receiving reservoir (open to the atmosphere), from which it was returned to the header tank by an electric diaphragm pump (Xylem Flojet RLFP122202D - positive displacement pump). A constant pressure head was maintained by a level switch in the header tank controlling the pump. The pump was switched off during the data recording to minimize electrical noise. In a typical recording period, this resulted in a level drop of approximately 18cm corresponding to 8-10 % reduction in the pressure.

### 2.7.4. Windkessel Chamber

An extra piece of equipment was introduced in the later part of the experiments. Large elastic arteries such as the aorta and its main branches contain elastic tissues in their walls which confer distensibility and the ability to recoil elastically. Considering that the heart ejects around 60-70ml of blood during each beat, the distensibility of the arteries allows the accommodation of that stroke volume (in a healthy arterial system) with a 30-40mmHg increase in pressure within the arteries near the heart. Due to this property of the walls, part of the energy is stored within them as potential energy, and during diastole, when the filling of the system by the heart has ended, the stretched elastic walls of the aorta recoil (Figure 28) and the stored potential energy is transferred to the blood hence ensuring diastolic flow. In other words, the elastic recoil of the large elastic arteries acts

as a subsidiary pump to maintain a blood flow during diastole whilst reducing the fluctuations in pulse pressure that would occur in a less distensible system. This elastic reservoir is referred to as a Windkessel chamber (Lip, 2007; Muir and Hubbell, 2009).

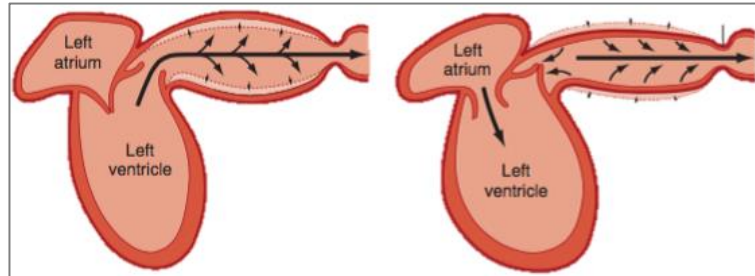


Figure 28: Windkessel effect on normally compliant arteries (Koeppen and Stanton, 2017)

Due to the importance of the Windkessel effect on haemodynamics, it was crucial to integrate this into our models for pulsatile flow. This was achieved by introducing an airtight chamber in parallel with the programmable piston pump (Figure 29). Although the Windkessel was placed in parallel and not in series, a recoil effect was still achieved due to the pressurised chamber and a dampened waveform. The pump was allowed to run for some time until a stable pulse pressure waveform was achieved. The damping effect of the Windkessel was controlled by adjusting the amount of air inside the chamber.

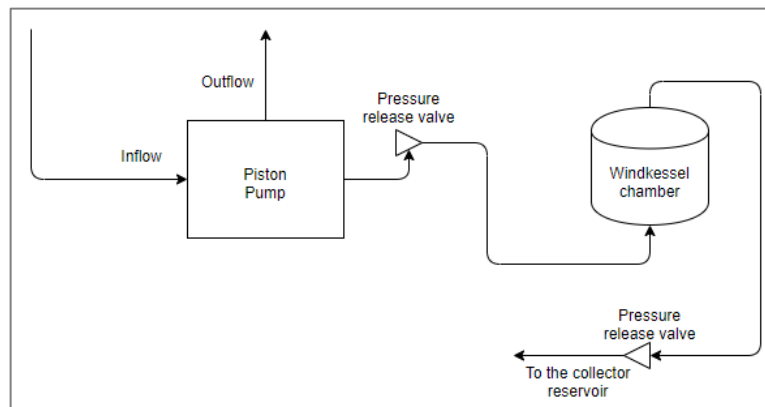


Figure 29: Schematic of the Windkessel set-up

A pulse pressure of 35-45mmHg was maintained during the pulsatile flow experiments and a typical waveform with and without the Windkessel chamber (with the same pump settings) is shown in Figure 30. It can also be seen from the figure that, with the use of the Windkessel chamber, the lower limit of the pressure waveform is now higher, and a higher positive mean pressure is maintained in the system throughout every cycle.

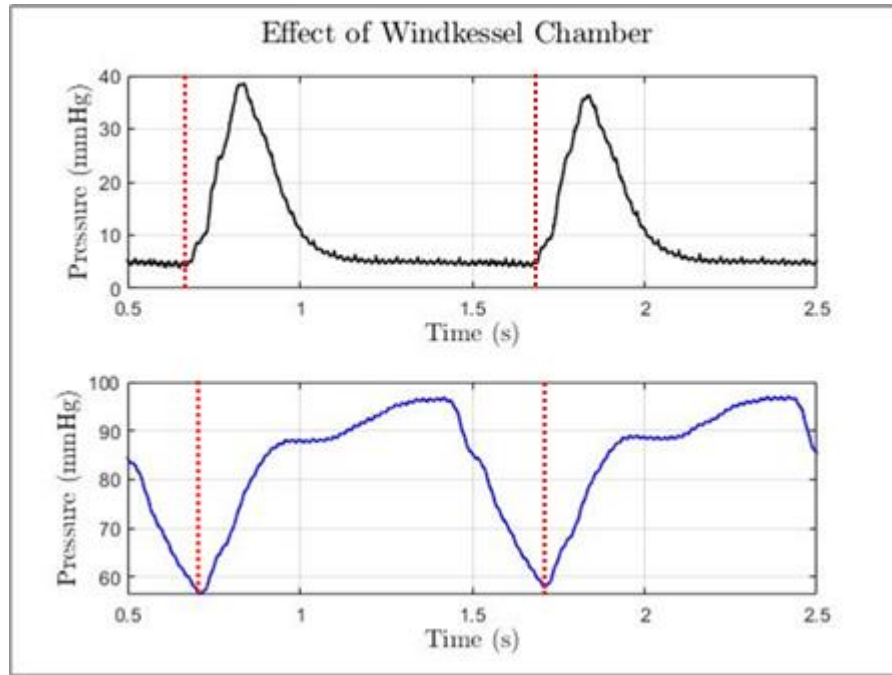


Figure 30: Pressure waveform without (top) and with (bottom) the Windkessel chamber, with same pump settings – one cycle shown between the red dotted lines

## 2.8. Sampling and Analytical Techniques

The signals from all sensors were digitised using a PowerLab 16/35 system (AD Instruments, Oxford, UK). The system comprised a recording unit containing 16 single/dual-ended analogue amplifiers and a 16 channel A to D converter. This was interfaced (USB) to a standard PC running dedicated software (LabChart, v8, AD Instruments) that allowed recording, real-time display and real-time or off-line analysis of the data. The system has a 16-bit resolution and can record at speeds of up to 200,000 samples per second. The 16 input channels allow recording data from multiple instruments simultaneously, i.e., flow meter, pressure transducers, LDV and multiple accelerometers (Figure 31). The unused channels can be used to apply several functions, e.g. filtering, arithmetic processing and smoothing to the live signals from the other channels, if necessary (ADInstruments, 2014).

Typically, the recording sessions in this study were run for 30 seconds at a sample rate of 10kHz and displayed as amplitude versus time plots in real-time using the LabChart software. The data from the measuring devices (discussed in section 2.9) were transformed to the frequency domain to identify the signal strength of the fluctuations and their



corresponding frequencies. The conversion was done using the fast Fourier Transform (FFT).

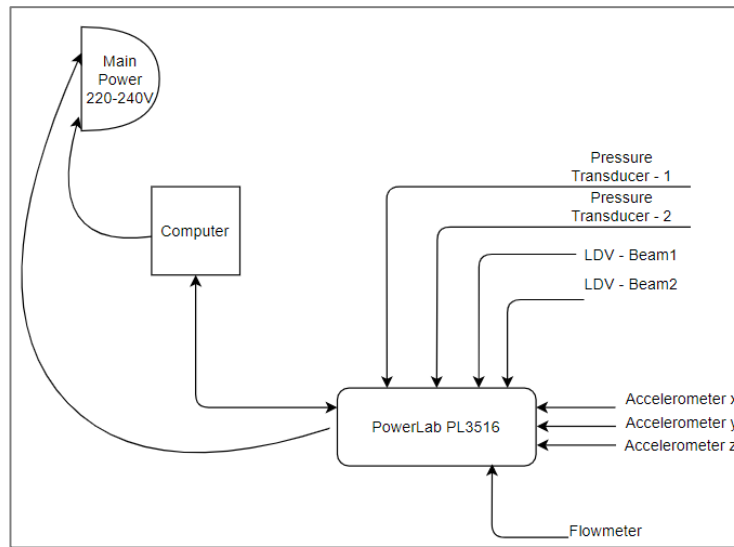


Figure 31: A sample schematic of the PowerLab hardware set-up

“The Fast Fourier Transform works on a certain number of data points at a time over the selection of data to be analysed. The larger that number, the greater the frequency resolution (the number of frequency bins into which the signal is resolved). Smaller FFT sizes give higher amplitude accuracy, but lower frequency resolution” (NIInstruments, 2019). For our steady and pulsatile flow studies, the FFT sizes chosen were 4000 and 8000, respectively.

Another important aspect while conducting a FFT is the data window and the concept of overlap. Data windows reduce the influence of the edges at the start and end of the data segments, which tends to produce false peaks at high frequencies. In this study, the window type used was the Hann (cosine-bell) window. This has a sinusoidal shape and results in a wide peak but low sidelobes, touching zero at both ends, hence minimising discontinuity (NIInstruments, 2019).

Overlap analysis, as the name suggests, means that consecutive blocks of the time data are overlapped by a designated percentage of their duration. The purpose of overlapping is to reduce the effect of windowing and to improve the resolution of the transform. When a windowing function drops to 0 near the frame edge, some important information on the edges can get lost, hence, affecting the FFT results. A 50% window overlap was used in

our analyses, which means that each successive FFT overlaps with the previous one by 50%. It follows that the number of FFTs is doubled, resulting in a better frequency representation of the time domain signal by avoiding the loss of components that may coincide with the zeros imposed by the windowing function at the edges of the period covered by the FFT (NIInstruments, 2019).

For example, in a sample of 300,000 time points processed with an FFT size of 8,000 points and no overlapping, the sample would be divided into segments of the form 1-8000, 8001-16000, 16001-24000 and so on. However, when 50% overlapping is used, the points are divided into segments of the form 1-8000, 4000-12000, 8001-16000, and so on. Hence with a 50% Overlap, the result will be an average of 75 FFTs instead of 37.5, giving a better frequency resolution as well as improved handling of the start and finish of the data.

The FFT spectra are presented in terms of Power Attenuation, which gives a wide range of powers. This power is expressed in dB, relative to the reference power (attenuation =  $10 * \log(\text{power} / \text{reference power})$ ). A default value of 0.001 was used to provide a reference value to the power (ADInstruments, 2015). Attenuation generally refers to the loss in signal, so the closer the power attenuation is to 0, the lower the signal loss. An example of a signal in the time domain and its corresponding FFT is shown in Figure 32 and Figure 33, respectively, and since the main focus of this study is to investigate high amplitude low-frequency oscillations, only the frequency range under investigation is 0-500Hz (unless specified otherwise).

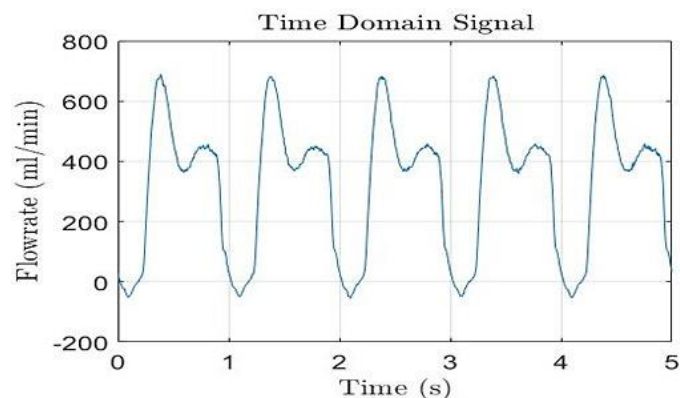


Figure 32: A cut-out sample of the time domain signal obtained with the LDV with pulsatile flow data set of 30 seconds

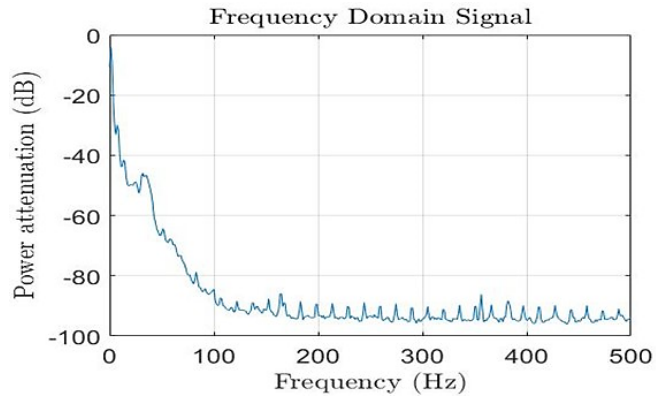


Figure 33: FFT of the signal corresponding to the time domain signal with 8K FFT size, 50% overlap with a Hann (cosine-bell) window.

Once the Fourier transforms of the signals have been obtained, the next step is to investigate the effect of changing variables such as flow rate, position, and stenosis severity. In the attempt of plotting some of the parameters, it was noticed that the comparison was cumbersome. For instance, a comparison was made to study the effect of the disturbances at different positions, using the accelerometer data. An example FFT plot (within the 0-150Hz band) in Figure 34 shows that differences in the signal are difficult to identify in their current form, therefore, further processing of this data was required.

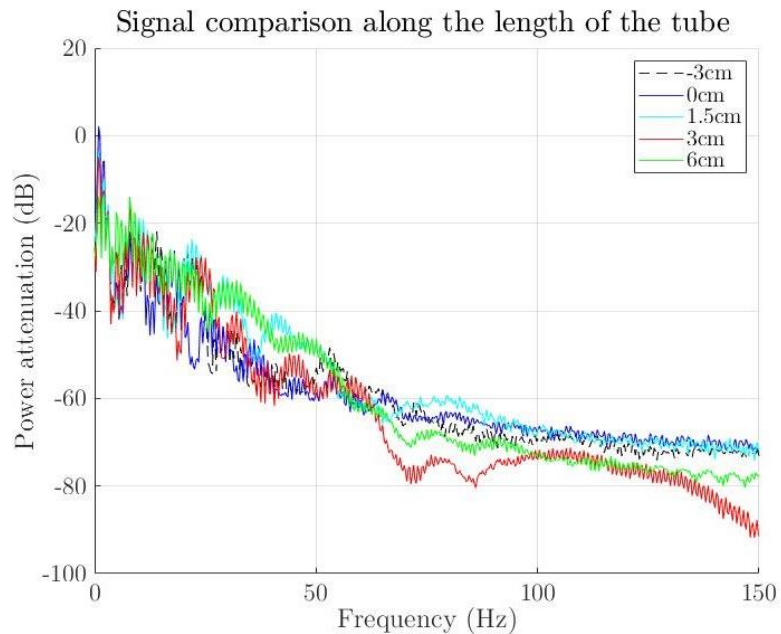


Figure 34: An exemplary plot showing a position-based comparison of FFT signals derived from the accelerometer data

The areas under the FFT curves were calculated over 50Hz intervals in the range 0 – 500Hz. Despite the averaging effects on the signal, the chosen 50Hz band provided a

good compromise and allowed the identification of meaningful trends (Mancini, Tommasin, *et al.*, 2019). In the results section, these are shown alongside the FFT plots. The areas under the curves for each 50Hz frequency band were obtained numerically using the trapezoidal method with unit spacing. Figure 35 below is an example of this analysis where dotted vertical lines show the boundaries between the 50Hz frequency bands, and the value inside each band represents the area under the curve (with -100dB as the horizontal reference axis).

A final technique that was reviewed for the analysis was the spectrogram. The spectrogram's added benefit is that it shows how the frequency response changes with time, making it possible to identify any time-dependent patterns embedded within the signal. The FFT spectra and a spectrogram of a sample signal are depicted in Figure 36. The spectrogram can show changes of frequency (y-axis) with time (x-axis), where the colour scale represents signal power. It can be seen that the yellow bars (corresponding to a high signal power) just below 2Hz are present in every one-second interval on the x-axis. These high-power readings correspond to the 1Hz pulse generated by the pump, the discrepancy between this derived frequency and the true 1Hz value is because of the limited frequency resolution of the FFT (discussed earlier in this section). Similarly, the FFT spectra themselves make it possible to identify other recurring patterns otherwise hidden within the signal.

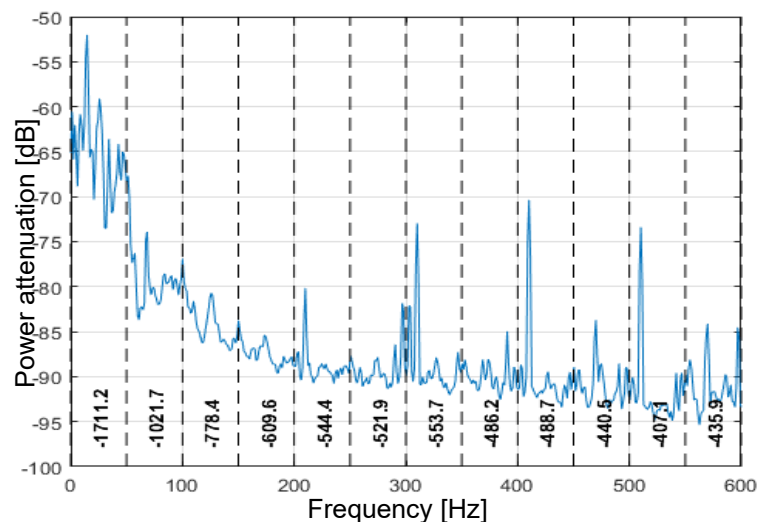


Figure 35: An example plot showing the area under the curve of a FFT signal.

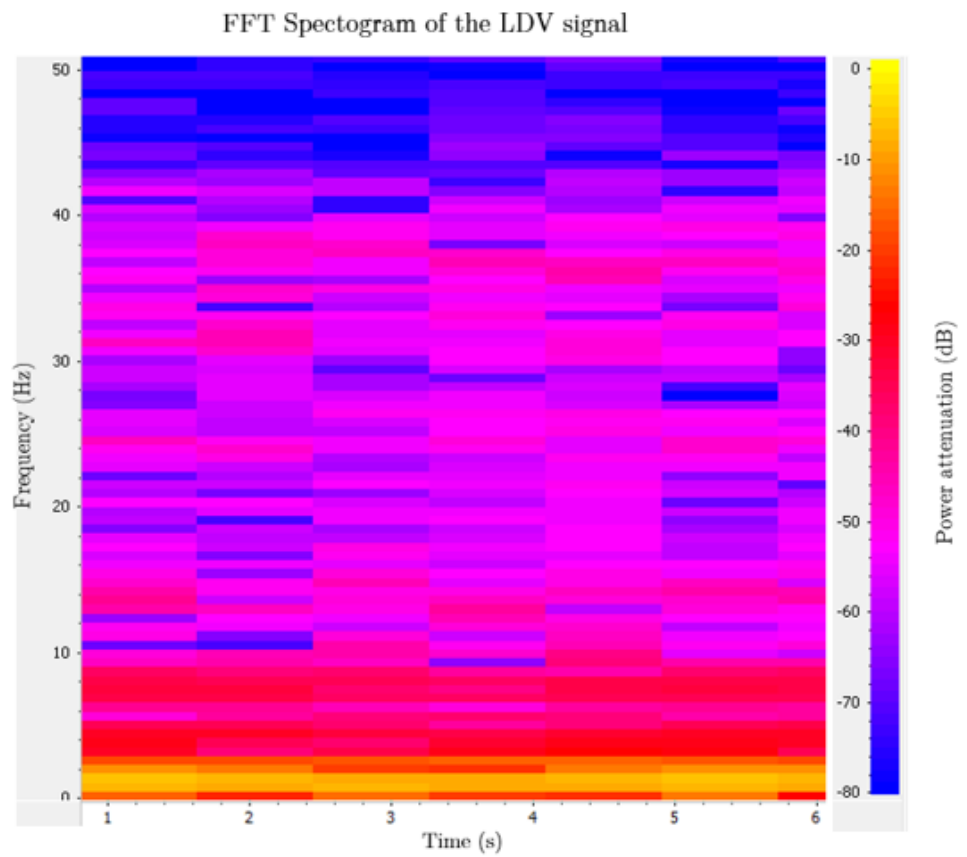
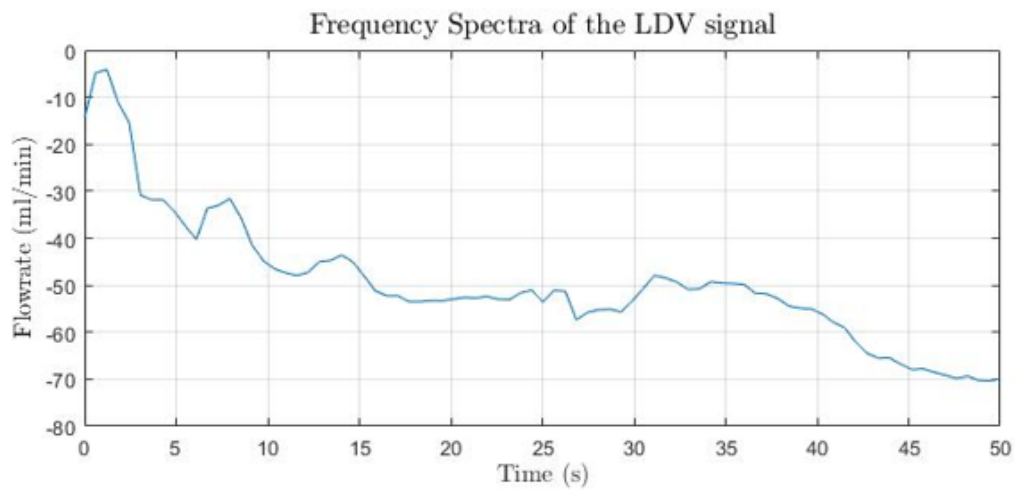


Figure 36: Frequency Spectra (top) and the Spectrogram (bottom) of the LDV time-domain signal

## 2.9. Measurement Techniques

The transmission of energy from the fluid, through the tube and the gel, to the skin surface, induces vibrations at the skin surface. A suitable method was required to measure these vibrations and potentially the perturbations within the flow.

The main criterion for choosing a suitable method was the repeatability, ease of use and most importantly, its sensitivity. The device was preferred to be non-contact based so that it does not significantly affect the vibrations produced (e.g., placement of ultrasound probe on the neck can produce local narrowing of the artery if incorrectly placed). Two candidates explored for these investigations were accelerometers, and a laser Doppler Vibrometer (LDV).

In addition to measuring the vibrations at the skin surface, the possibility of identifying the flow disturbances at their source (i.e., inside the tube) was also explored by using catheter-tip pressure transducers.

A supplementary technique (Duplex ultrasound) was used to visualise the flow features, details on this technique are presented in section 3.2. Furthermore, the possibility of using microphones (placed on a skin) surface to detect the murmurs resulting from flow disturbances in the underlying stenosed tube is under investigation as specified, details of this which are presented in Appendix C (section 8.3.1). In this current section, Accelerometers and LDV were compared for skin level vibrations and the use of pressure transducers was studied to identify the flow disturbances inside the tube.

### 2.9.1. Accelerometers

Accelerometers are devices that convert mechanical motion into electrical signals. Small, low power, 3-axes accelerometers (ADXL337, Analog Devices, Norwood, MA, USA) were soldered onto a small, printed circuit board (PCB) and were connected to the data acquisition units (section 2.8) via a set of fine flexible wires. The accelerometers were then positioned directly above the tube/skin surface (Figure 37) and were placed at several positions along the length of the tube, i.e., P1 (3cm upstream of the stenosis), P2 (vertically above the stenosis), P3 (1.5cm downstream of the stenosis), P4 (3cm downstream of the stenosis), and P5 (6cm downstream of the stenosis).

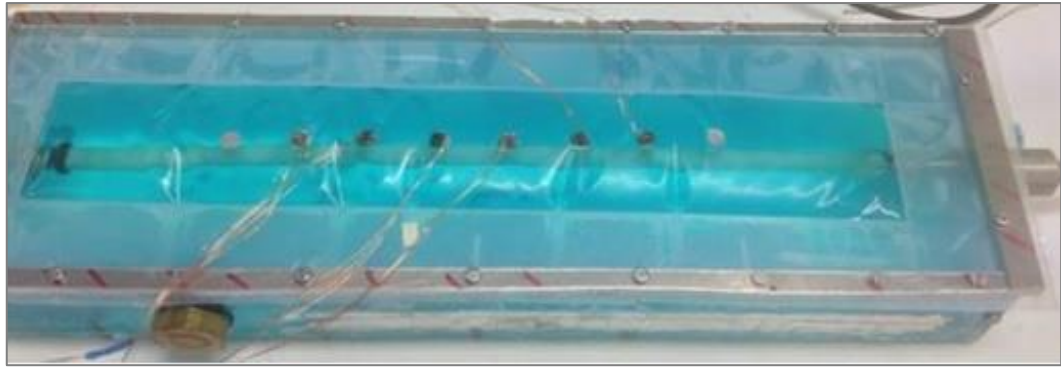


Figure 37: Sample placement of accelerometers on the phantom skin surface

Various methods were explored to attach the accelerometers to the skin. Thin double-sided tape provided the best adhesion in comparison with superglue and ultrasound gel, both of which revealed a visible movement of the accelerometers with respect to the skin surface. The performance of the accelerometers (manufacturer data) is presented in Table 9.

Table 9: Manufacturer specifications of the ADXL337 accelerometers (ADIInstruments, 2019)

Operating voltage range	1.8 - 3.6 V
Measurement Range	+/- 3.6 g*
Sensitivity (x, y and z axes)	270 - 330 mV/g
Frequency response (x and y)	1600 Hz
Frequency response (z)	550 Hz
Operating temperature range	-40 to +85 °C
Mass	0.28 ±1 gram
* In this context “g” represents sea-level gravitational acceleration, i.e., 9.81 ms <sup>-2</sup> .	

### 2.9.2. Laser Doppler Vibrometer

A laser Doppler Vibrometer allows non-contact velocity and displacement measurements (with a high resolution) of a vibrating surface in a direction normal to the laser beams (in this study, normal to the skin surface). The scan head usually consists of one or more laser beams of precisely known frequency and wavelength, which cause a Doppler shift when reflected by a moving surface. This Doppler shift can be measured using

a laser interferometer. The output is a voltage reading proportional to the velocity of vibrations and can be integrated to get the displacement amplitude of the vibrations (Polytech, 2019). However, the device used in this work, a dual-beam instrument (SIOS SP12-DS, SIOS Meßtechnik, Ilmenau, Germany), gives a displacement output directly with a resolution of 0.1nm (SIOS, 2015). The sensitivity of the LDV was measured to be 0.99mV/microns.

For the interferometer to function correctly, the reflected beam must be returned along a path close to that of the incident beam. In practice, this is difficult to achieve with a specular reflective surface, however high the reflection coefficient. With the use of retroreflective patches containing glass or plastic micro-beads, total internal reflection makes it possible to capture the incident beam from a range of incidence angles (typically  $\pm 5 - 10^\circ$ ) and reflect it in the same direction, as shown in Figure 38, thus allowing reflected light to be detected without the need to ensure that the beam is perfectly normal to the moving surface.

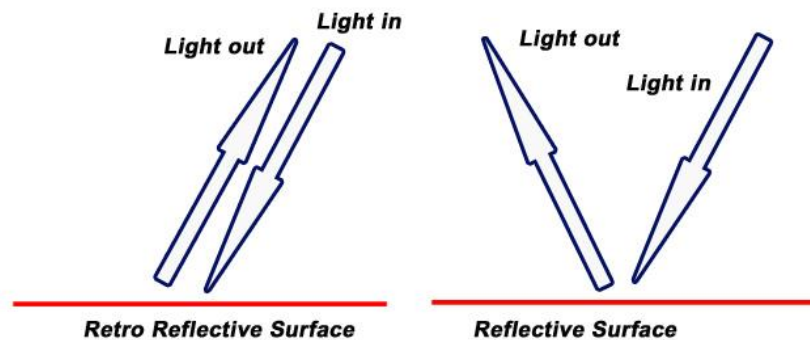


Figure 38: Comparison between a reflective (right) and a retro-reflective (left) surface (Cole, 2016)

To obtain data from the phantom, patches of retroreflective tape (3M® 7610 High Gain Reflective Tape) were placed at the same positions on the skin surface as those chosen for the accelerometers ( i.e. P1, P2, P3, P4 and P5), and the phantom was then placed directly underneath the device (separated by a vertical distance of approximately 18-20cm) such that one of the two laser beams was directed at the centre of the patch Figure 39 and Figure 40.

Data from two identical phantoms were sequentially tested to compare the signals from accelerometers and LDV. Two repeat measurements were carried out where 40:60 gly-



erol-water solution (as detailed in section 2.1) was passed through a 75% stenosed (ax-  
isymmetrically) Penrose latex tube embedded within the shallow phantom (as detailed in  
section 2.6).

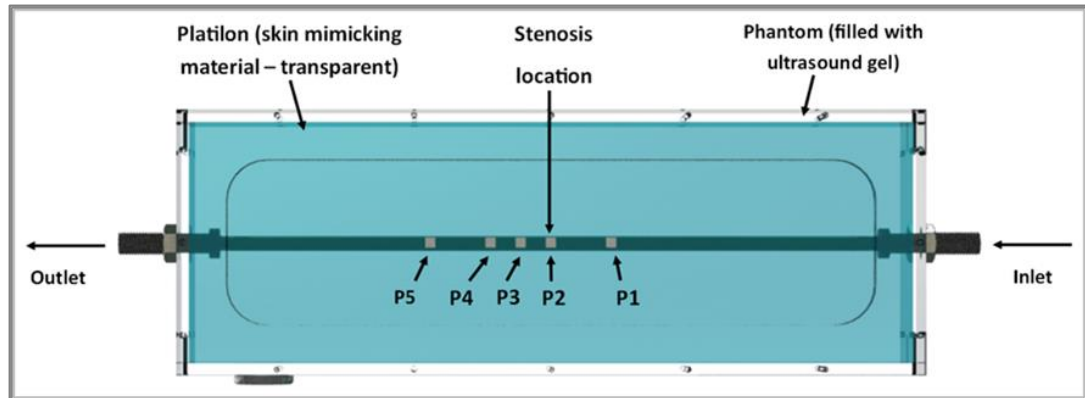


Figure 39: Neck phantom showing five retroreflective patches attached to the Platilon surface

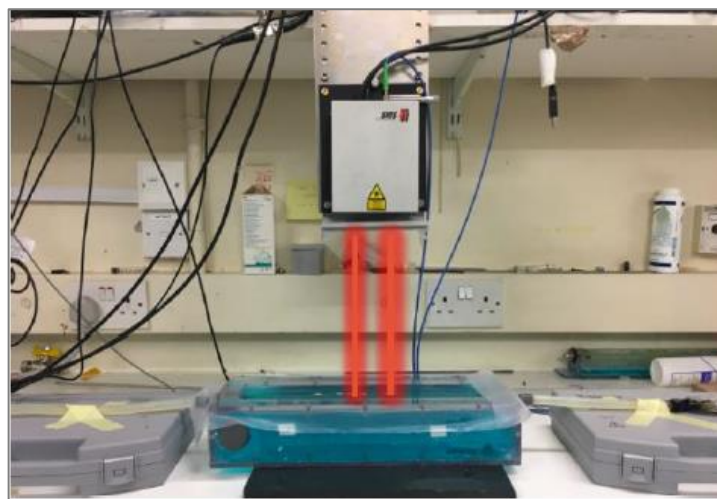


Figure 40: Neck phantom placed under the LDV, measuring the displacements at two of the retroreflective patches

The results indicated higher reliability with the LDV in comparison to the accelerometers. The data were recorded at two positions, 1.5cm (Figure 41 and Figure 42) and 3.0cm (Figure 43 and Figure 44), downstream of the stenosis location. It can be seen that at both positions that in the case of LDV, both positions showed a stronger signal as the flow rate increased, especially above 350ml/min within the first 100Hz band, whereas there was no visible trend in the accelerometer data. Repeats for accelerometer data were not recorded due to lack of any trends (with increasing flow rates) and hence reliability of the signal. The absence of trend can be explained by the fact that although the double-sided tape provided good adhesion, there were still small areas where a perfect contact between

the accelerometer and the skin was not achieved, which may be due to the irregular surfaces of both the skin and the accelerometers. Furthermore, despite the effort to keep the wires fixed, the slight pull from the wires of the accelerometers could also have perturbed the accelerometer readings by loading the skin surface.

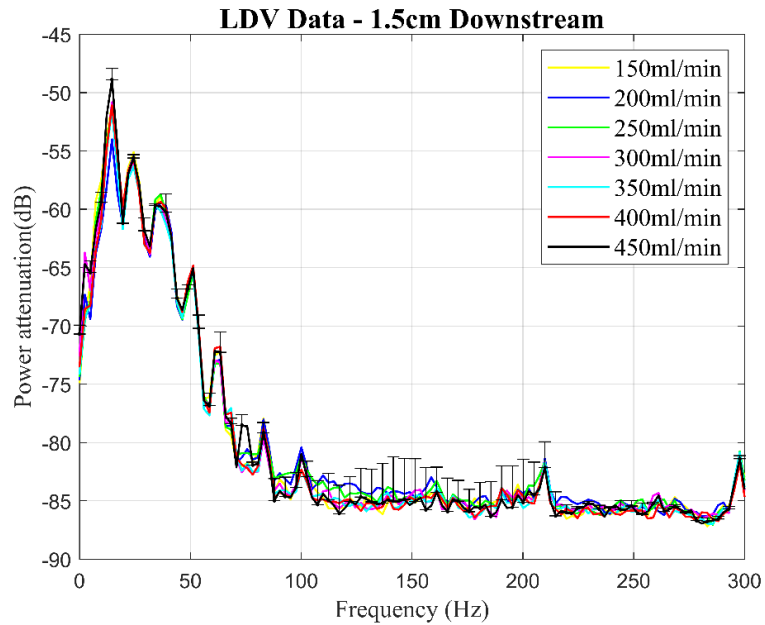


Figure 41: Power attenuation at 1.5cm downstream location, recorded using LDV

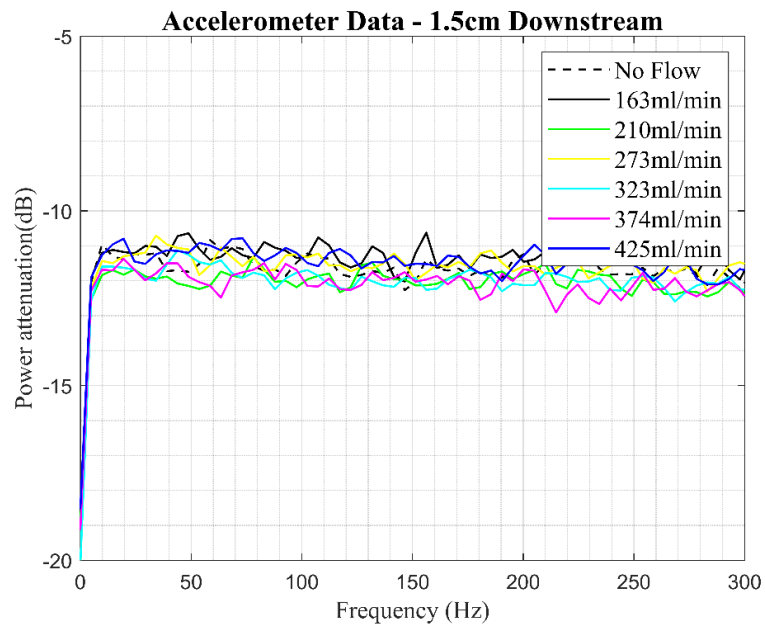


Figure 42: Power attenuation at 1.5cm downstream location, recorded using accelerometer

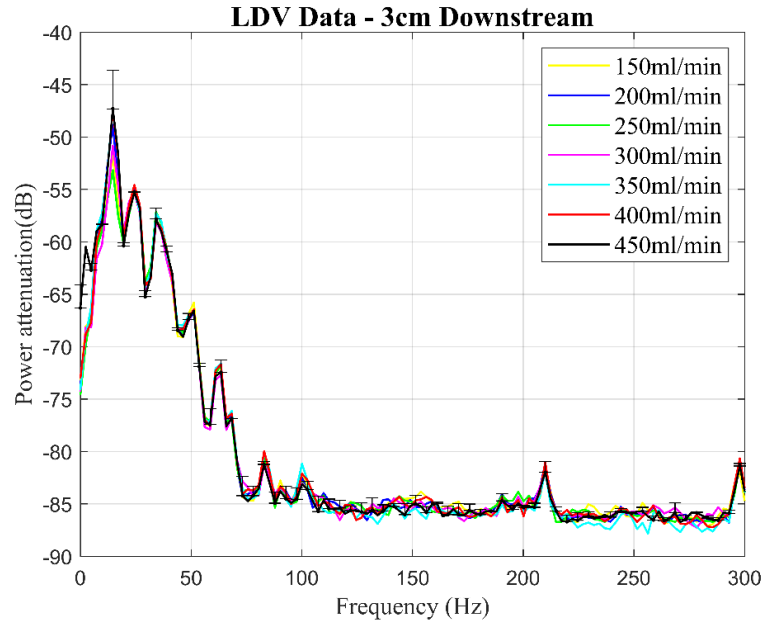


Figure 43: Power attenuation at 3.0cm downstream location, recorded using LDV

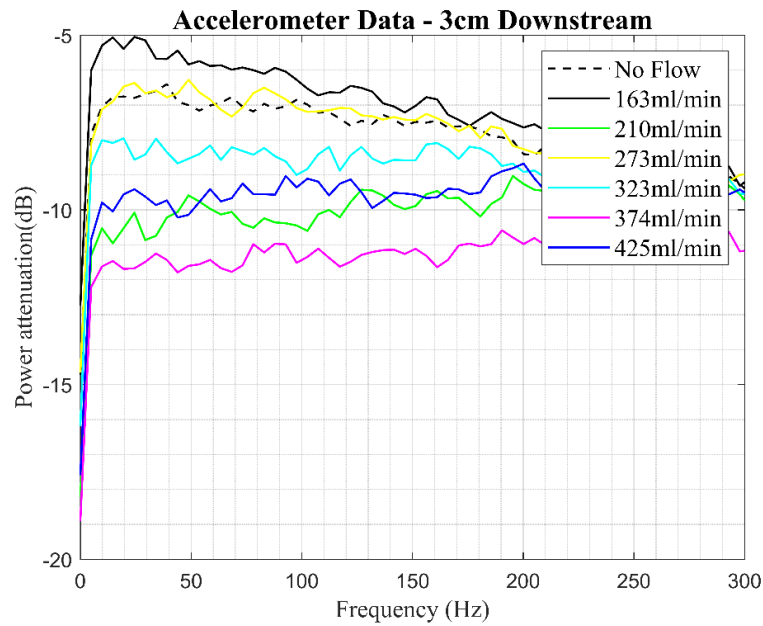


Figure 44: Power attenuation at the 3.0cm downstream location, recorded using an accelerometer

Hence, due to the lack of reliability of the accelerometers in this case, compared to the LDV, and the fact that the LDV offered a more robust non-contact method, the LDV was chosen to measure displacements on the skin surface. Further repeatability of the LDV was shown using error bars in the later chapters of the study, and in the Appendix C (section 8.3.3 for the 90% stenosis severity where strong effect of flow rate was present).

### 2.9.3. Pressure Transducer

Pressure transducers, as mentioned earlier, were explored to identify disturbances in the flow. This data could then potentially be used to seek a correlation with the disturbances at the skin surface. Alongside the identification of disturbances, the transducers would also allow monitoring the mean and pulse pressures during steady and pulsatile flow. The pressure transducers used in this study were catheter-tipped strain-gauge manometers (Gaeltec CTC-6F, Dunvegan, Scotland) with a diameter and sensitivity of 2mm and  $5\mu\text{V}/\text{V}/\text{mmHg}$ , respectively. Considering the ratio of the pressure transducer tip diameter to the tube diameter, a comparative study was conducted to evaluate the effects of introducing the pressure transducers inside the tube. The results of this study are discussed later in this section.

The pressure transducers were calibrated by passing them into the Penrose latex tube from each end, and priming the system with fluid as it would be during the final experiments (as detailed in chapters 3, 4 and 5). Subsequently, similar to the method used for inflation of the Penrose latex tube to measure its stiffness, the system was pressurised externally, and the pressure was recorded on an external mechanical manometer with a precision of 1mmHg. The system was inflated to pressures ranging from 0-200mmHg (at 20mmHg intervals) to ensure the physiological range was covered. These mechanical pressure readings were then used to calibrate the voltage readings obtained from the catheter tipped manometers. The calibration curves of both pressure transducers are shown in Figure 45. The difference between the transducers' calibration can be attributed to their different ages (several years).

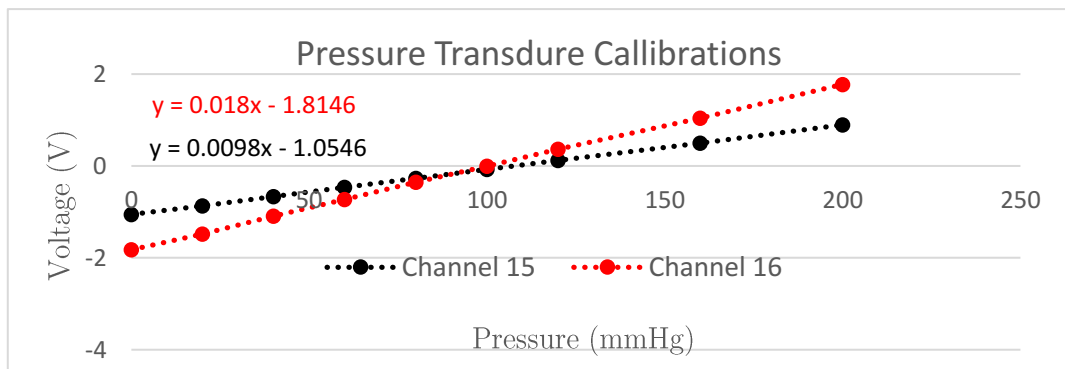


Figure 45: Pressure Transducer Calibrations (Channel 15 and Channel 16 correspond to two transducers)

### Effect of introducing pressure transducer inside the Penrose tube

A study was carried out in which fluid was passed through a stenosed tube (embedded within a phantom). LDV data were collected firstly at the P2 position (vertically above the stenosis) with no pressure transducer present. A pressure transducer was then positioned inside the tube (immediately after the throat of the stenosis) and the LDV signal was recorded again at the same position (P2). The experiment was repeated for three more positions, i.e., P3 (1.5cm downstream of the stenosis), P4 (3cm downstream of the stenosis) and P5 (6cm downstream of the stenosis). The results are presented in Figure 46 to Figure 49.

It can be seen from the figures that the set-up with the pressure transducer produced a stronger LDV signal when compared to that recorded with the pressure transducer absent. The effect was evident (at the stenosis and immediately downstream of the stenosis) throughout the frequency domain. Further away from the stenosis (i.e., at the P4 and P5 positions), the effect was less apparent but not absent. The ratio (obtained by the area under the power attenuation curves in 50Hz bands) of the LDV signal with and without the pressure transducer shown in Figure 50 further confirmed the effects of the presence of the pressure transducer in the tube.

The presence of the pressure transducer within the tube reduces the tube's overall lumen area, especially near the stenosis where the tube is already constricted. This reduction showed the introduction of further disturbances in the flow, which are challenging to isolate. Though not suitable for detecting disturbances, pressure transducers were still used to measure mean and pulse pressures for which they were located approximately 50D (50 x tube diameter length) further away from the stenosis to isolate the near-stenosis region from any effects of their presence.

The LDV was therefore chosen as a measuring device for identifying disturbances on the skin surface. In addition to being non-invasive (hence not interfering with the flow), it was also non-contact (except the retroreflective patch), quicker and more reliable to set up compared to the accelerometers. This would further aid in the clinical environment where patients are being screened.

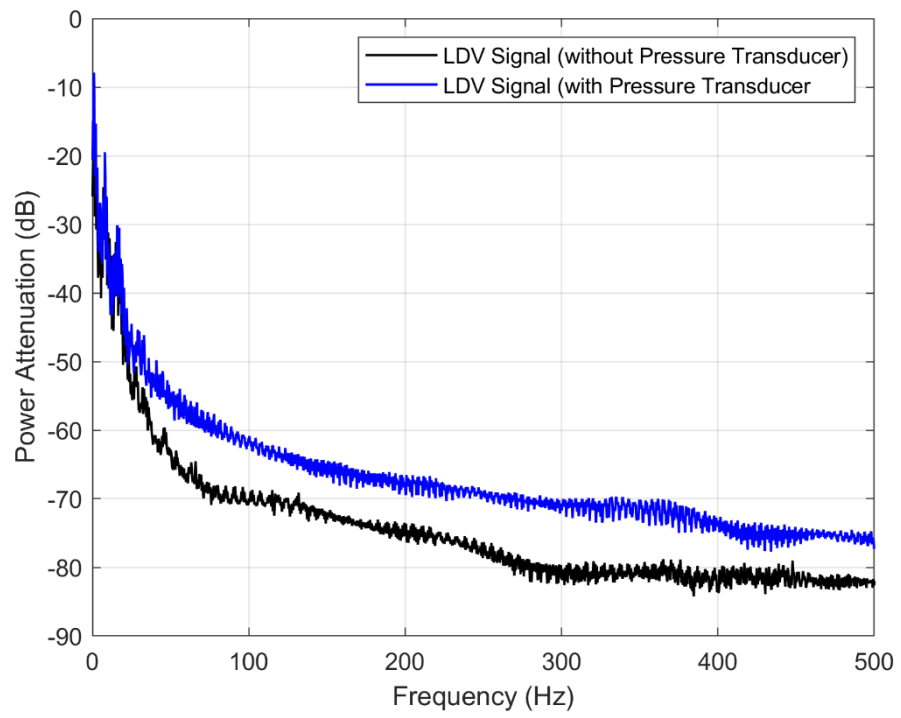


Figure 46: Comparison between LDV data obtained at stenosis with (blue) and without (black) pressure transducer

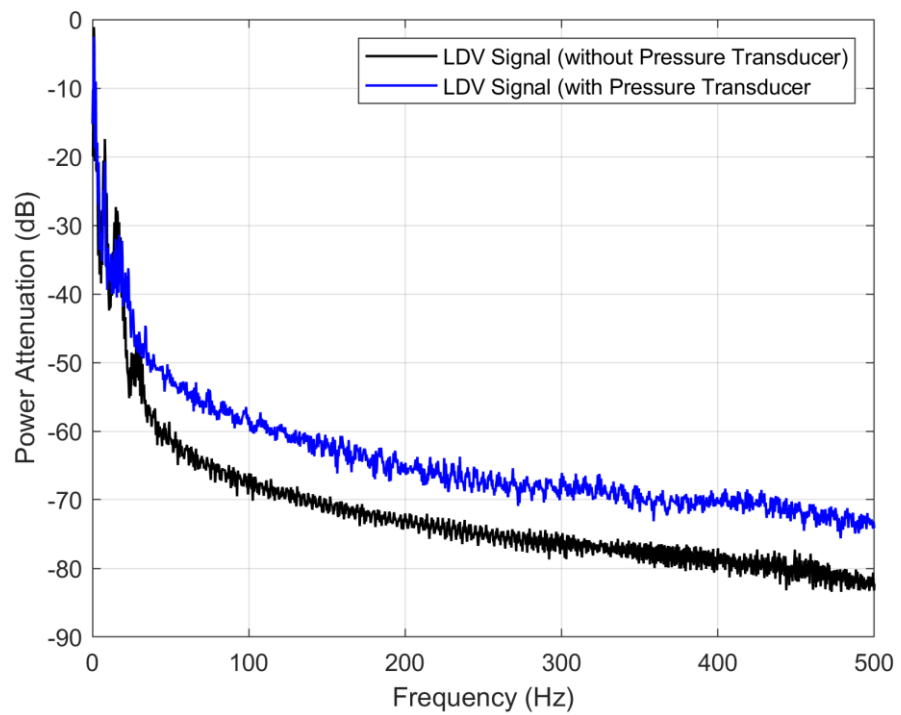


Figure 47: Comparison between LDV data obtained at 1.5cm downstream of the stenosis - with (blue) and without (black) pressure transducer

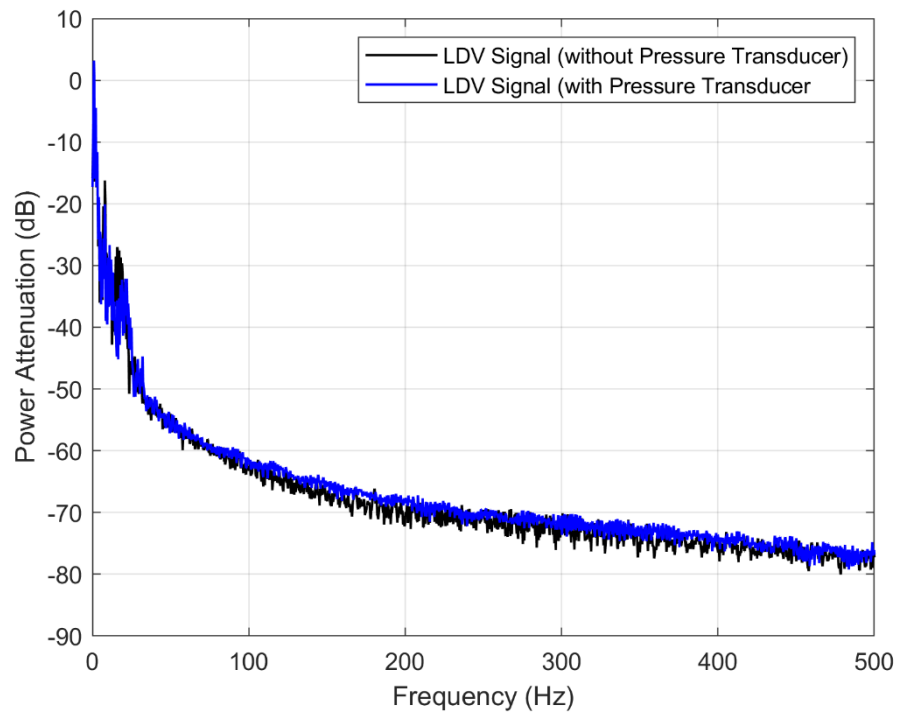


Figure 48: Comparison between LDV data obtained at 3.0cm downstream of the stenosis - with (blue) and without (black) pressure transducer

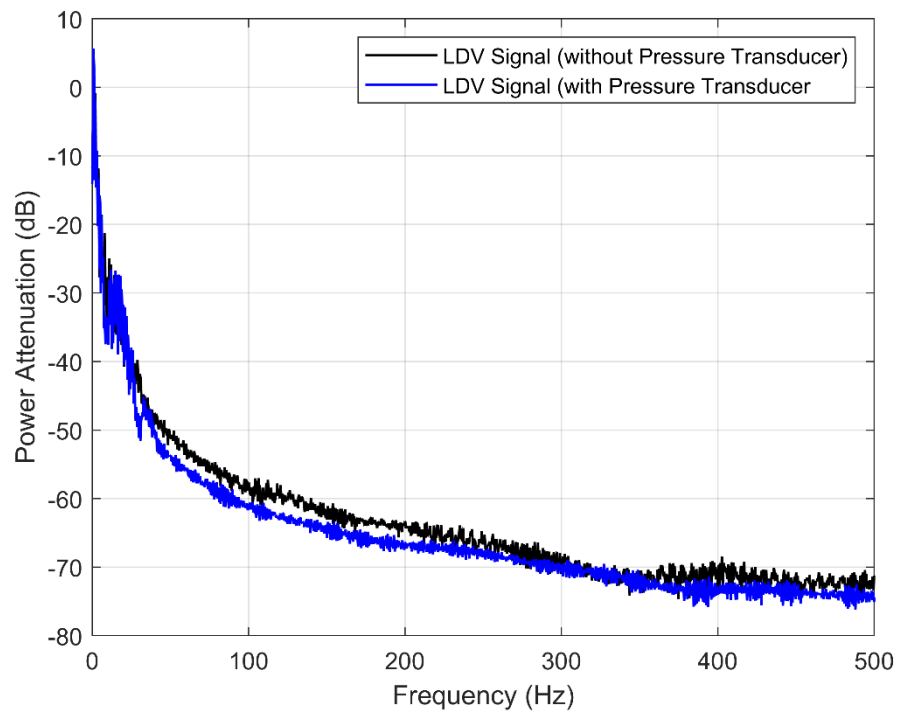


Figure 49: Comparison between LDV data obtained at 6.0cm downstream of the stenosis - with (blue) and without (black) pressure transducer

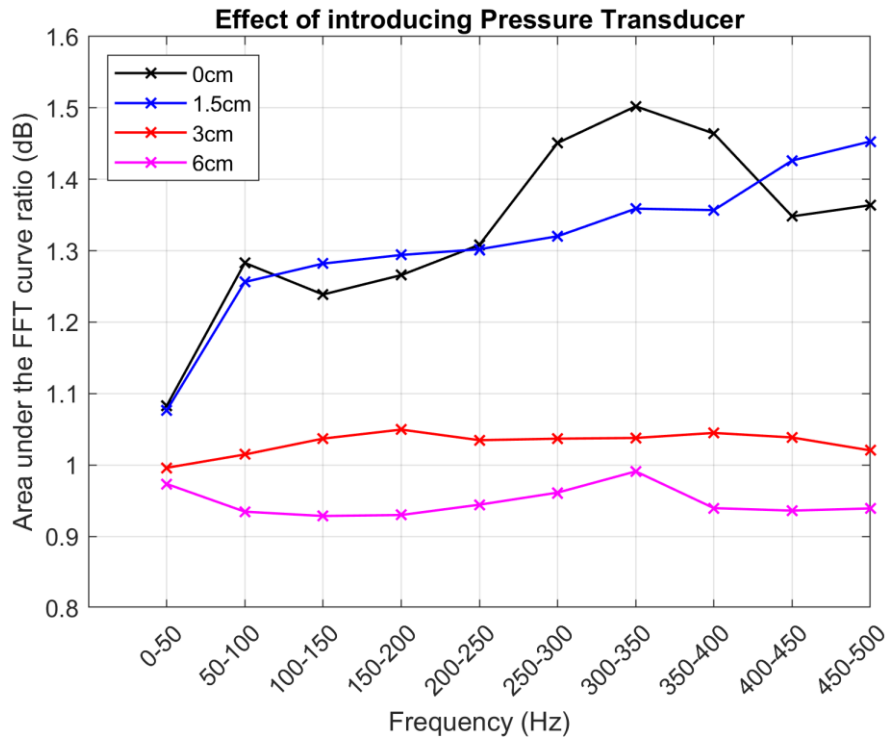


Figure 50: Effect of introducing pressure transducer in the 75% stenosed tube



### 3. Steady flow - Flow inside a bare tube

Following the design and evaluation of the experimental set-up, materials and measurement techniques, a set of experiments was devised to measure the disturbances in the bare tube and the neck phantom (in chapter 4). This chapter highlights the initial detection of disturbance (using the accelerometers) at the tube surface, followed by verification of the presence of local disturbances (using Duplex Ultrasound) within the flow. Finally, the results from the LDV device are discussed to highlight the effects of the fluid viscosity and stenosis symmetry, along with the increasing flow rates.

#### 3.1. Detection of flow disturbances at tube surface (using accelerometers)

##### Methods

For the bare tube experiments, water was initially used as specified in section 2.1. The fluid was perfused through the Penrose latex tube selected in section 2.2, with the stenoses type (axisymmetric) and severity discussed in section 2.3. A continuous flow circuit was set up as described in section 2.7 (with the programmable piston pump switched off to achieve a physiological steady mean flow ranging from 0-421ml/min.

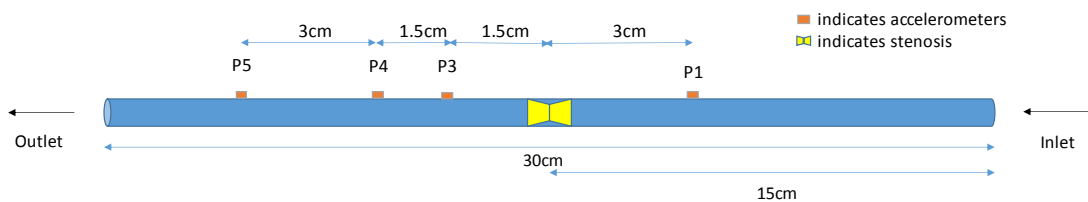


Figure 51: Stenosed bare tube, with accelerometers placed at four positions P1, P3, P4 and P5 to facilitate detection of the disturbances at the tube surface

Accelerometers (section 2.9.1) were the primary means of detecting tube wall movement from the bare tube experiments, and data (with single measurement/repeat) was collected at four positions; one upstream of the stenosis (-3cm) and three positions downstream, (1.5cm 3cm and 6cm), referred to as P1, P3, P4 and P5, respectively, in Figure 51. The notation 'P2' is reserved for the 0cm (at stenosis) location and will be used in later parts of the study.

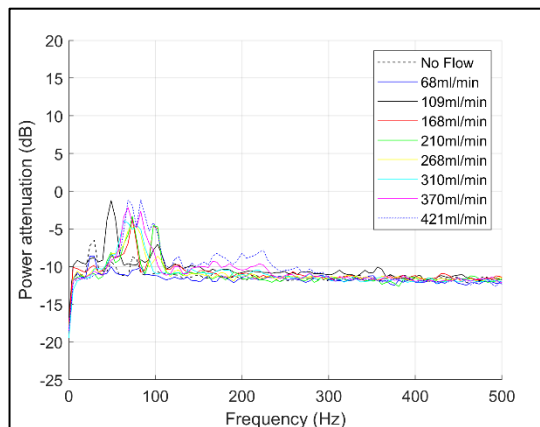
## Results & Discussion

The increasing flow rate and the presence of a stenosis inside the tube produced disturbances within the flow. Those disturbances caused vibrations of the tube surface, which were determined by the fluctuations in the data captured by the accelerometers. This study aimed mainly to identify the presence of disturbances and identify the flow rates and/or stenosis severity at which those disturbances can be detected.

Fourier spectra from the time-varying accelerometer signals were obtained (as detailed in section 2.8). Figure 52, firstly, confirms the presence of surface-level disturbances; furthermore, it provides a broad comparison of three different stenosis severities at four different locations (P1, P3, P4 and P5). Some noteworthy features here are the effects of increasing stenosis severity, increasing flow rate and finally, the behaviour at different positions.

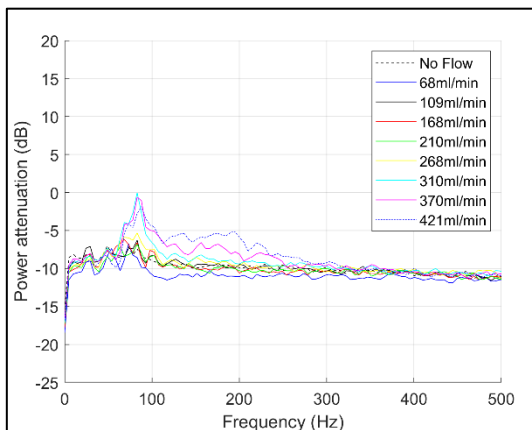
Figure 52 demonstrates the effect of stenosis severity. As the severity increases, the flow becomes more disturbed, which is evident from the increased amplitude of the power attenuation signal. Furthermore, as the severity increases, the spread of the peaks for all the positions also increases at all four positions, indicating the generation of higher frequency disturbances at higher severities. This is also true for increasing flow rates within a single severity stenosis, where higher frequency disturbances are detected at higher flow rates. The difference in power attenuation between the 60% and 75% stenosed tubes is small, upstream of the stenosis at P1. However, these differences are more apparent in the post-stenosed flow at the three downstream locations (P3, P4 and P5), especially for flow rates above 210ml/min. The effect is more pronounced in the 90% stenosed tube, where the differences are apparent at flow rates as low as 168ml/min. These effects are further verified in section 3.2, analysed and quantified in length with the LDV data in section 3.3.

60 % Stenosis

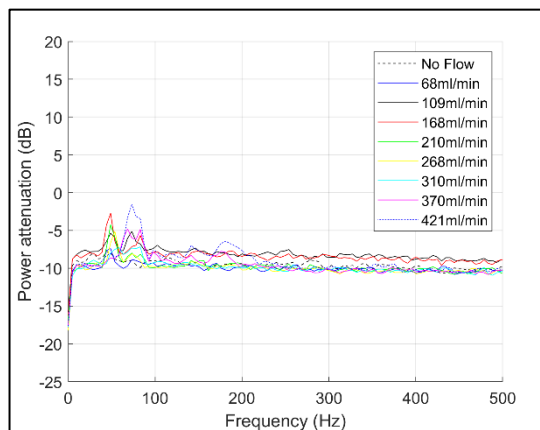
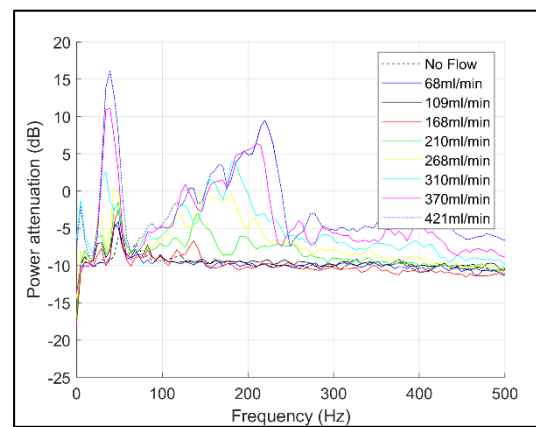


P1

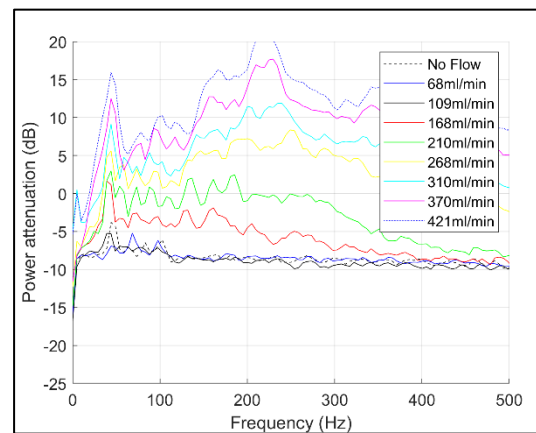
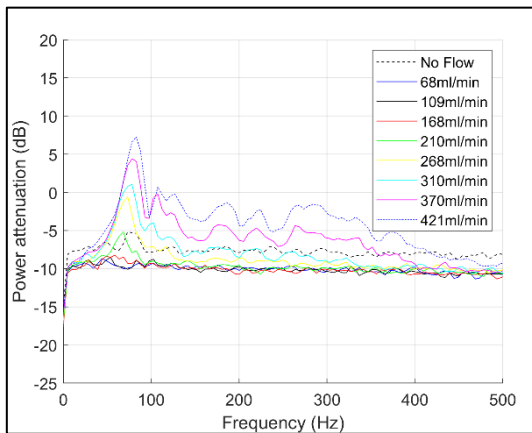
75 % Stenosis



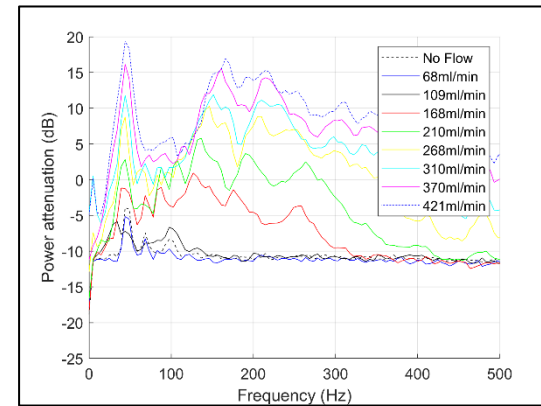
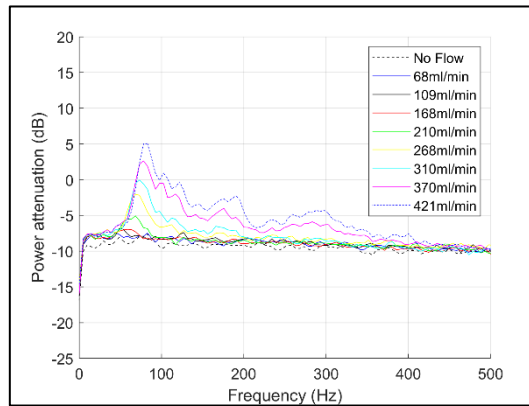
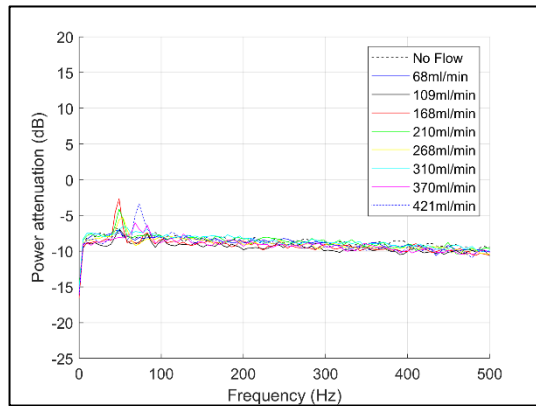
90 % Stenosis



P3



P4



P5

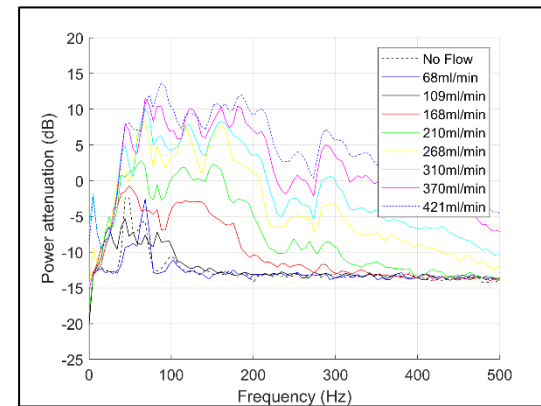
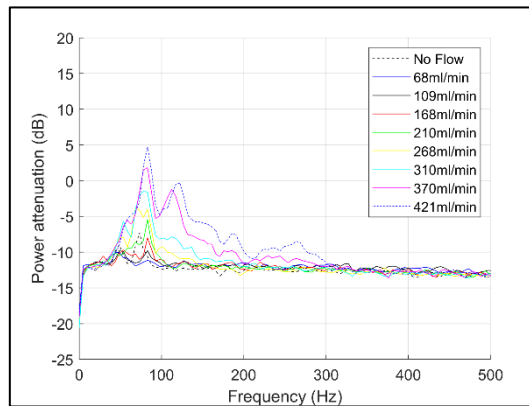
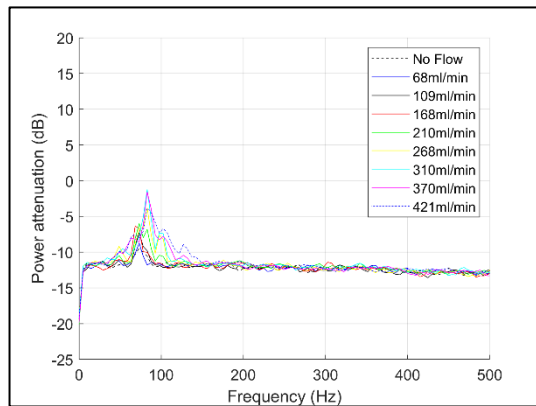


Figure 52: Fourier spectra showing the effect of stenosis severity, flow rate and measurement position on a bare latex tube at four different positions: P1 (-3cm upstream), P3 (+1.5cm downstream), P4 (+3cm downstream) and P5 (+6cm downstream)

### 3.2. Detection of flow disturbances inside the tube (using Duplex Ultrasound)

#### Methods

A supplementary technique to monitor the flow and stenosis-induced disturbances within the stenosed tube was duplex ultrasound. This technique was used to visualise the flow patterns in the pre- & post-stenosed regions of the tube and to confirm the presence of disturbed flow.

A bare stenosed Penrose latex tube (section 2.2) was placed within the Perspex casing of a phantom (as shown in Figure 53, dimensions of the phantom detailed in 2.6) and the phantom casing was filled with de-ionized water to act as a coupling agent. The scan head was placed vertically above the tube and moved to the 4 measurement positions as before, i.e., P1 (-3cm upstream), P3 (+1.5cm downstream), P4 (+3cm downstream) and P5 (+6cm downstream). An additional set of data was collected at P2 (vertically above the stenosis) to visualise the transition of flow inside the stenosis.

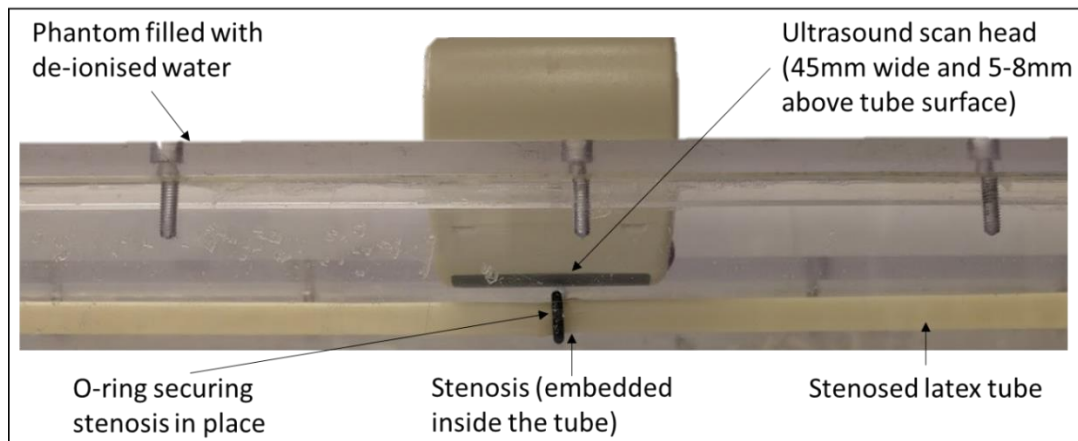


Figure 53: Duplex ultrasound set-up of a 90% stenosed tube

Two investigations were carried out: one focused on visualising the effects of the stenosis severity, and the other on increasing flow rates. In both cases, the fluid was perfused through the symmetrically stenosed tube, within a continuous flow circuit, set-up as described in section 2.7 (with the programmable piston pump switched off to achieve a

physiological steady mean flow). For the first case, fluid was perfused through the tube at two different steady mean flow rates of 200ml/min and 345ml/min while keeping a constant stenosis severity of 90%. For the second case, three different stenosis severities of 60%, 75% and 90% (as detailed in section 2.3) were investigated for a steady physiological mean flow rate of 345ml/min.

It is worth noting here that these investigations were conducted using a Perspex casing phantom and de-ionized water instead of the ultrasound gel, and that the Platilon skin was not used to cover the liquid. The main reasons for this were:

- Simplicity of the set-up allowing a quicker turnaround time for the phantom preparation along with increased flexibility of positioning the ultrasound probe.
- Water provides better coupling (due to lack of presence of air bubbles, which can be an issue with the ultrasound gel) and has lesser signal attenuation than the gel.
- Isolation of the flow behaviour inside the tube, from additional external reflections presumably arising from the Platilon surface.

### **Results & Discussion**

The presence of a stenosis and the increasing flow rates influenced the disturbances produced at the tube's surface, as discussed in section 3.1. Therefore, ultrasound scans were performed to visualise the flow features within the tube. The first investigation was to determine the effect of flow rate, as mentioned, in a 90% symmetrically stenosed tube.

Before conducting a detailed flow analysis, the mean flow velocities (inside the tube) from the ultrasound scans were verified by comparing them with calculated mean flow velocities. The verification was achieved by measuring the inflow of around 200ml/min and 345ml/min (derived from the ultrasonic flowmeter) and calculating the corresponding mean velocities (by the continuity equation) over the entire tube diameter, giving values of 10.5cm/s and 18.2cm/s, respectively. These velocities were then compared with the velocity profiles obtained from the ultrasound scans at a position 3cm upstream of the stenosis (i.e., P1). On comparing, both the flow rates of 200ml/min (Figure 54a) and 345ml/min (Figure 54b) provided a satisfactory agreement between the calculated and

scanned velocities (i.e., 10.5cm/s vs 10cm/s and 18.2cm/s vs 20cm/s, respectively). The fluctuations seen in the traces can be attributed to the ultrasound noise and electrical noise in the system (gain dependent), since the noise was present even in the non-stenosed case.

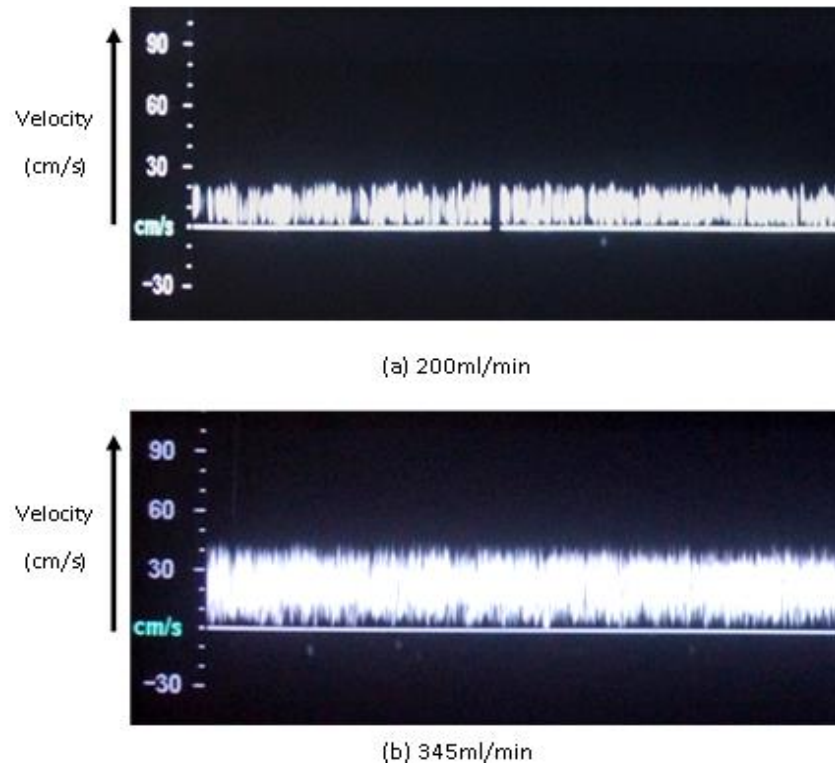


Figure 54: Flow velocity measurements (averaged across the tube diameter) obtained using Duplex ultrasound, at P1 (-3cm upstream) position in a water perfused 90% stenosed tube at (a) 200ml/min and (b) 345ml/min.

### 3.2.1. Effects of flow rate

Following the verification of the measured mean velocities measured at a single position, the analysis was extended to identify the trends in the flow at different positions. The results for the physiological flow rate of 345ml/min are presented first in this section, and a comparison is later made with the flow rate of 200ml/min.

At 345ml/min, a general trend can be seen from Table 10 such that, as the fluid approaches the centre of the stenosis (P2), it starts to accelerate, and a jet is formed in the post-stenotic region. It was difficult to obtain a good signal through the middle of the stenosis, as the distance between the two edges was close to the resolution limit of the ultrasound. (At the frequency used (6MHz) the wavelength was approximately 250 $\mu$ m).

However, on increasing the Doppler gain, higher velocity values were recorded, and even some distinctive peaks were seen at the 0cm position (within the stenosis), as shown in the Table 10 (b). The mean flow velocity here was still positive, as expected, since there are no adverse pressure losses until the fluid exits the stenosis, where the recirculation zones started to appear.

The jet mentioned above is seen at the P3 (1.5cm downstream) position in Table 10 (c). However, the jet is not symmetrically positioned with respect to the long axis of the tube. This can be explained by imperfections in the 3D-printed stenosis itself or the slightest misplacement of the stenosis within the tube. Looking at the colour map in Table 10 (c-i&ii), as the jet is formed, it gives rise to a low-pressure region just below it, thus encouraging the recirculation of the flow (blue). This is also evident from the velocity traces in Table 10 (c-i&ii) where the flow is predominantly positive near the upper surface of the tube and negative near the middle and bottom surface of the tube. The flow fluctuations were also evident along the central axis over the length of the tube, the velocity trace for which is provided in Appendix C (8.3.2).

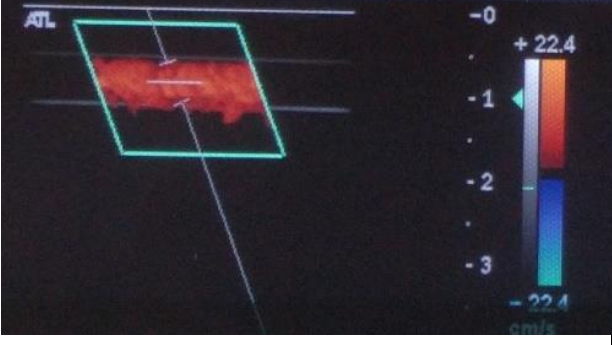
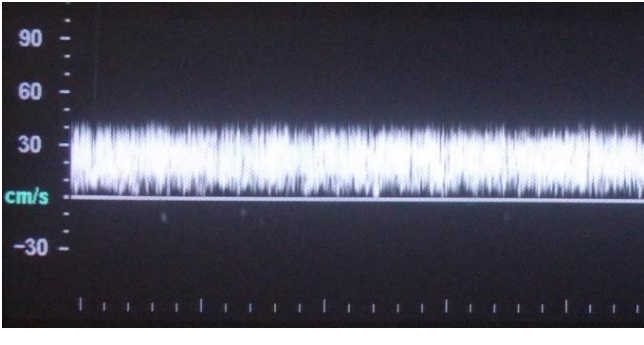
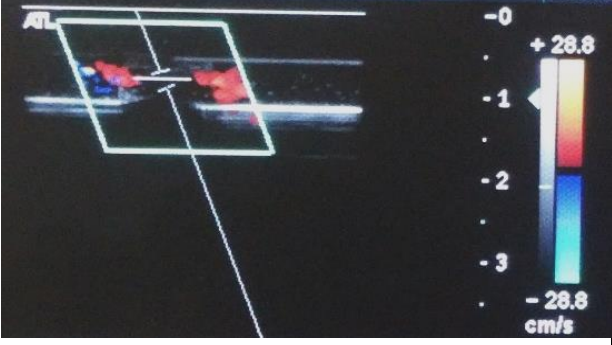
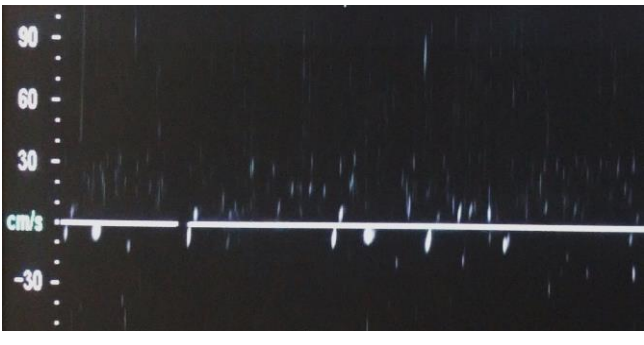
Similar behaviour is seen at the P4 (3cm downstream) position, where the positive flow is mostly attached to the upper surface of the tube and a recirculation zone is present beneath it where negative velocities are seen (Table 10 (d-i&ii)). However, the amplitude of the velocity is lower near the upper surface of the tube at P4 compared to the P3 position. Finally, at the P5 (6cm downstream) position, the velocity map shows that the positive flow is dominant across the diameter of the tube, with very few traces of negative flow. The velocity traces extracted from different locations across the diameter of the tube (Table 10 (e-i&ii)) also show a positive mean flow at this position.

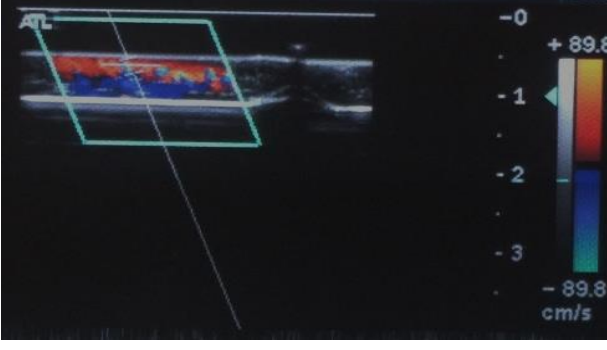
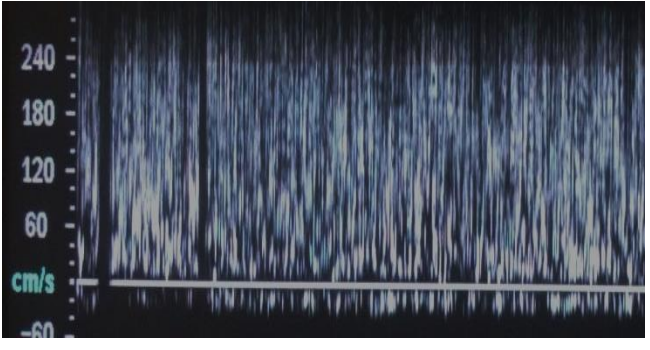
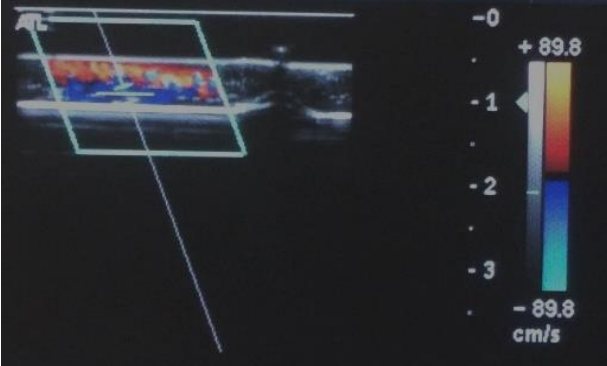

Taken together, these results indicate that the flow disturbances are maximal near the stenosis for this geometry and flow rate and that they are approaching a stable state as they travel away from the stenosis. The flow instabilities have almost entirely disappeared at a distance of approximately ten tube diameters downstream of the stenosis.

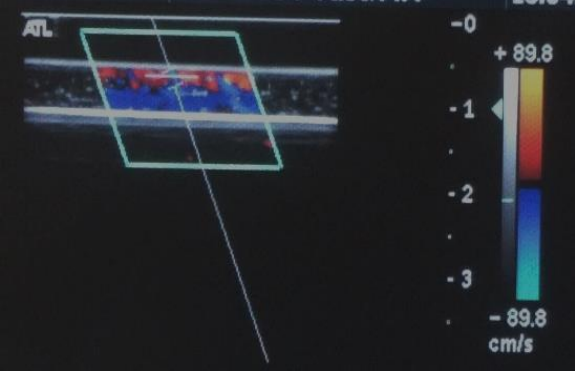

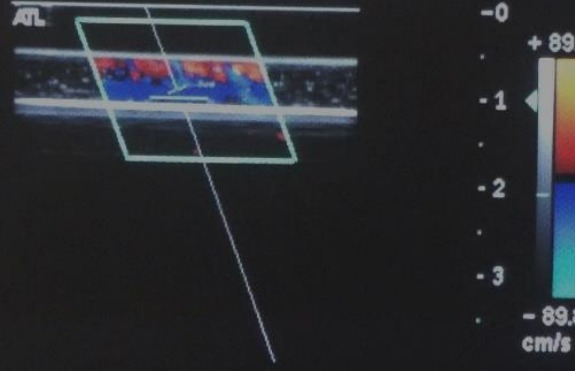

Following investigation at 345ml/min, the scans were repeated at a lower flow rate of 200ml/min. The general trends seen, in terms of the positional effect, were similar. At the



Table 10: Flow mapping, using Duplex ultrasound, of a 90% stenosed tube at different positions along the circumferential and longitudinal direction (at flowrate of 345ml/min)

Position	Location	Colour Map	Velocity (cm/s)
-3cm (a)	Average across central 5mm window	 <p>Colour Doppler map showing flow velocity distribution across a 5mm window. The scale ranges from -22.4 cm/s (blue) to +22.4 cm/s (red).</p>	 <p>Spectral Doppler waveform showing flow velocity over time. The y-axis is labeled 'cm/s' with markers at -30, 30, 60, and 90. The flow is concentrated between approximately 15 and 30 cm/s.</p>
0cm (b)	Average across central 2mm window	 <p>Colour Doppler map showing flow velocity distribution across a 2mm window. The scale ranges from -26.8 cm/s (blue) to +26.8 cm/s (red).</p>	 <p>Spectral Doppler waveform showing flow velocity over time. The y-axis is labeled 'cm/s' with markers at -30, 30, 60, and 90. The flow is concentrated between approximately 10 and 20 cm/s.</p>

Position	Location	Colour Map	Velocity (cm/s)
1.5cm (c-i)	Average across 2mm window near top surface		
1.5cm (c-ii)	Average across 2mm window near bottom surface		

Position	Location	Colour Map	Velocity (cm/s)
3cm (d-i)	Average across 2mm window near top surface		
3cm (d-ii)	Average across 2mm window near bottom surface		

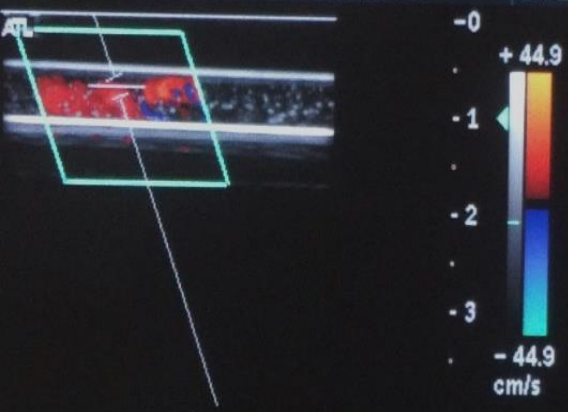

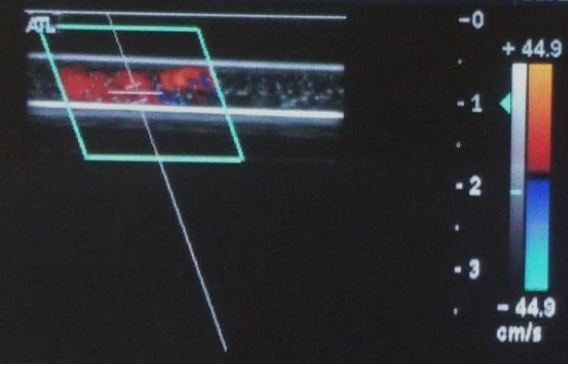

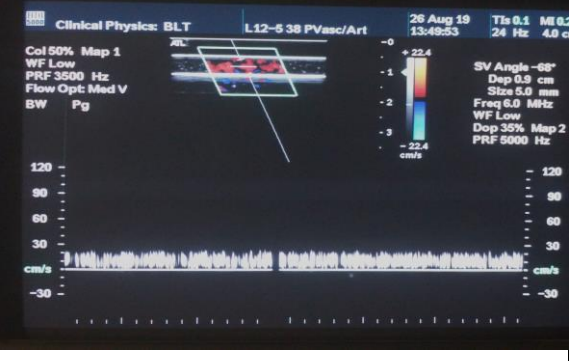
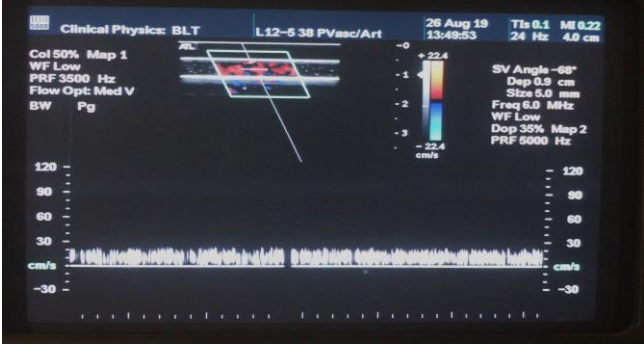
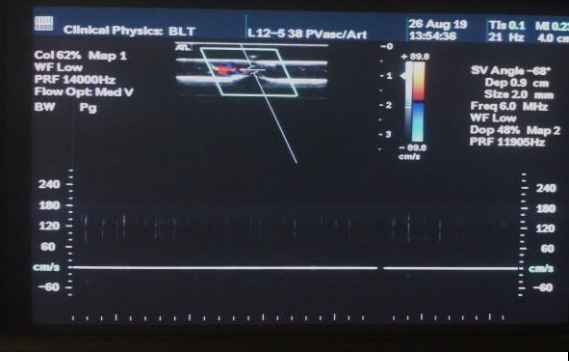
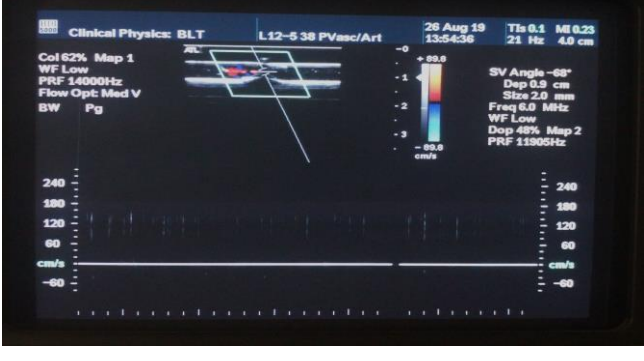
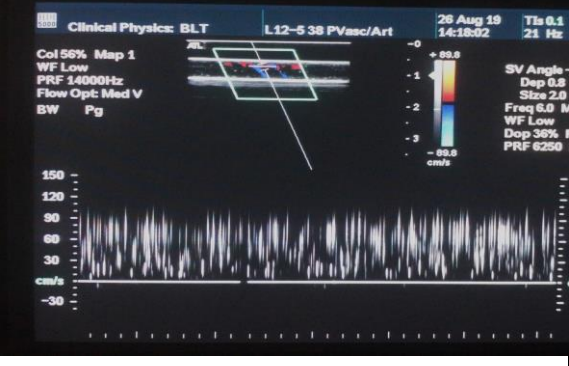
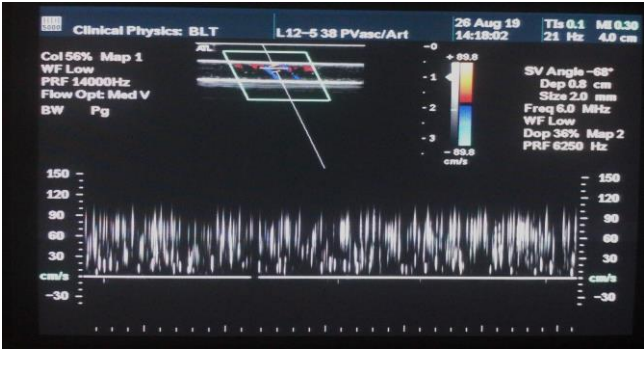
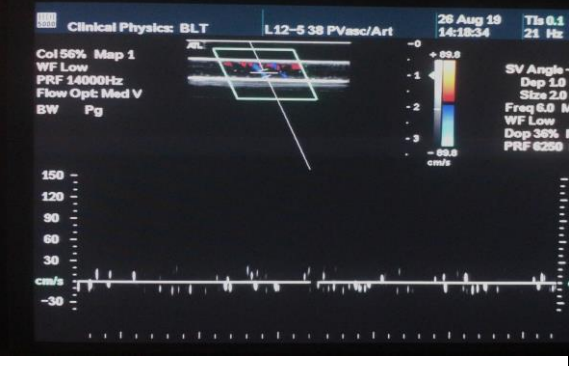
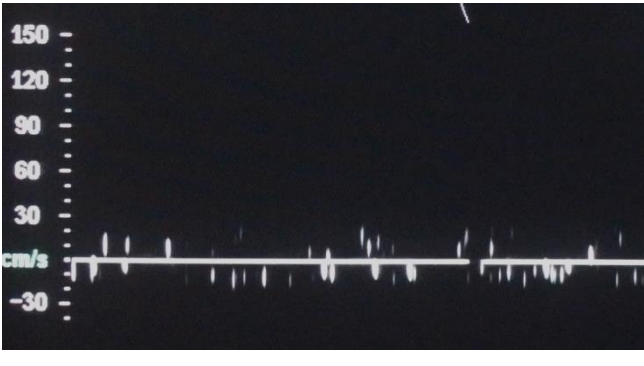
Position	Location	Colour Map	Velocity (cm/s)
6cm (e-i)	Average across 2mm window near top surface		
6cm (e-ii)	Average across 2mm window near bottom surface		

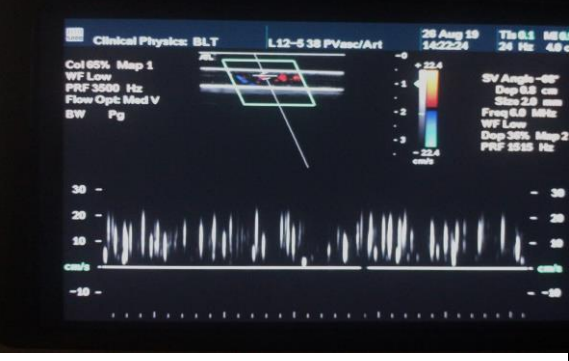
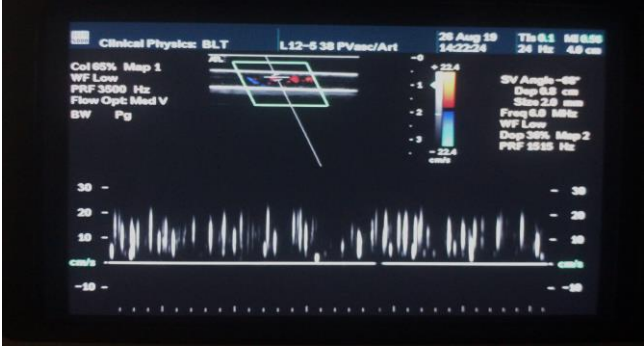
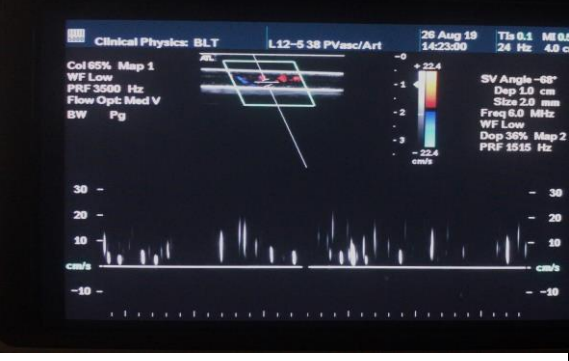
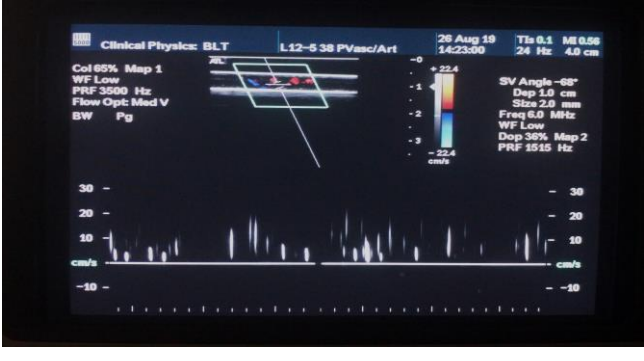
Table 11: Flow mapping, using Duplex ultrasound, of a 90% stenosed tube at different positions along the circumferential and longitudinal direction (at flowrate of 200ml/min)

Position	Location	Colour Map	Velocity
<p>-3cm (a)</p>	<p>Average across central 5mm window</p>	 <p>Clinical Physics: BLT L12-5 38 P/Vasc/Art 26 Aug 19 TIs 0.1 MI 0.1 13:48:53 24 Hz 4.0 cm Col 50% Map 1 SV Angle -68° WF Low Dep 0.9 cm PRF 3500 Hz Size 5.0 mm Flow Opt: Med V Freq 6.0 MHz BW Pg WF Low Dop 35% Map 2 PRF 5000 Hz</p>	 <p>Clinical Physics: BLT L12-5 38 P/Vasc/Art 26 Aug 19 TIs 0.1 MI 0.22 13:48:53 24 Hz 4.0 cm Col 50% Map 1 SV Angle -68° WF Low Dep 0.9 cm PRF 3500 Hz Size 5.0 mm Flow Opt: Med V Freq 6.0 MHz BW Pg WF Low Dop 35% Map 2 PRF 5000 Hz</p>
<p>0cm (b)</p>	<p>Average across central 2mm window</p>	 <p>Clinical Physics: BLT L12-5 38 P/Vasc/Art 26 Aug 19 TIs 0.1 MI 0.2 13:54:36 21 Hz 4.0 cm Col 62% Map 1 SV Angle -68° WF Low Dep 0.9 cm PRF 14000Hz Size 2.0 mm Flow Opt: Med V Freq 6.0 MHz BW Pg WF Low Dop 48% Map 2 PRF 11905Hz</p>	 <p>Clinical Physics: BLT L12-5 38 P/Vasc/Art 26 Aug 19 TIs 0.1 MI 0.23 13:54:36 21 Hz 4.0 cm Col 62% Map 1 SV Angle -68° WF Low Dep 0.9 cm PRF 14000Hz Size 2.0 mm Flow Opt: Med V Freq 6.0 MHz BW Pg WF Low Dop 48% Map 2 PRF 11905Hz</p>



Position	Location	Colour Map	Velocity
1.5cm (c-i)	Average across 2mm window near top surface		
1.5cm (c-ii)	Average across 2mm window near bottom surface		

Position	Location	Colour Map	Velocity
3cm (d-i)	Average across 2mm window near top surface	 <p>Clinical Physics: BLT L12-5 38 PVasc/Art 26 Aug 19 14:18:02 TIs 0.1 21 Hz</p> <p>Col 56% Map 1 WF Low PRF 14000Hz Flow Opt: Med V BW Pg</p> <p>SV Angle Dep 0.8 Size 2.0 Freq 6.0 MHz WF Low Dop 36% Map 1 PRF 6250</p> <p>150 120 90 60 30 cm/s -30</p>	 <p>Clinical Physics: BLT L12-5 38 PVasc/Art 26 Aug 19 14:18:02 TIs 0.1 MI 0.39 21 Hz 4.0 cm</p> <p>Col 56% Map 1 WF Low PRF 14000Hz Flow Opt: Med V BW Pg</p> <p>SV Angle -68° Dep 0.8 cm Size 2.0 mm Freq 6.0 MHz WF Low Dop 36% Map 2 PRF 6250 Hz</p> <p>150 120 90 60 30 cm/s -30</p>
3cm (d-ii)	Average across 2mm window near bottom surface	 <p>Clinical Physics: BLT L12-5 38 PVasc/Art 26 Aug 19 14:18:34 TIs 0.1 21 Hz</p> <p>Col 56% Map 1 WF Low PRF 14000Hz Flow Opt: Med V BW Pg</p> <p>SV Angle Dep 1.0 Size 2.0 Freq 6.0 MHz WF Low Dop 36% Map 1 PRF 6250</p> <p>150 120 90 60 30 cm/s -30</p>	 <p>150 120 90 60 30 cm/s -30</p>

Position	Location	Colour Map	Velocity
6cm (e-i)	Average across 2mm window near top surface		
6cm (e-ii)	Average across 2mm window near bottom surface		



P1 position (Table 11(a)), a uniform positive mean flow was seen, as for the higher flow rate, but with a lower mean flow velocity (approximately 10cm/s), which increased as the flow approached the stenosis at P2 (Table 11(b)).

A jet was seen in the post stenotic region at the P3 position (Table 11(c)). The approximate mean velocity near the upper edge of the tube at the P3 position (Table 11(c-i)) was lower (70-80 cm/s) in comparison to the 345ml/min case (110-135 cm/s). It is noteworthy here that the change in these measured mean velocities was almost proportional to the change in the perfused flow rates due to the axisymmetric nature of the stenosis geometry. Furthermore, the recirculation zone length was smaller and localised near the tube's bottom surface (rather than along the centre as seen in the colour map at the higher flow rate).

The flow had already started to stabilise at the P4 (3cm downstream) position, as seen from the velocity plots in Table 11 (d-i&ii). The mean flow velocity was positive at this location, both at the top and the middle of the tube, with a minor negative flow region nearer the bottom edge. It is noteworthy that the presence of eddies in the flow means that at certain time instances, the flow velocity normal to the probe will be zero. The gaps in the velocity trace in some of the scans demonstrated this behaviour, at positions distal from the stenosis. Finally, looking at the P5 (6cm downstream) position, Table 11 (e-i&ii) shows that the entirety of the flow was positive with fluctuations in the velocity. The fluctuations could be caused by vortices shed near the stenosis now moving downstream as they detach themselves while approaching the region of uniform positive flow. The fluctuations in the velocity at this position seem periodic, which could indicate flow turning from chaotic to periodic before it becomes laminar further downstream. Comparing Table 8e (i&ii) and Table 11e (i&ii) shows that these fluctuations were present at both flow rates; however, the frequency of these fluctuations seems to be higher for the high flow rate case. The effects of the flow rate on the frequency of disturbances are quantified and discussed in further detail in section 3.3, using the LDV data.

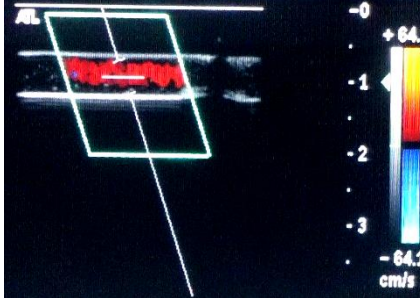

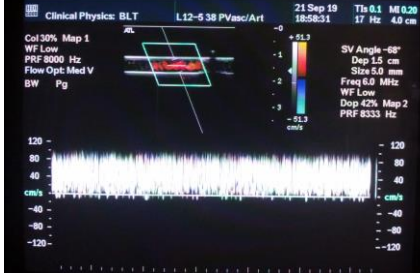
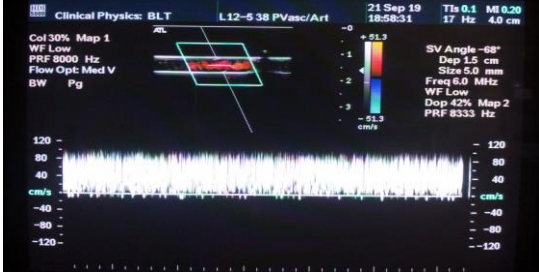


### 3.2.2. Effects of stenosis severity

To determine the effects of increasing vessel occlusion, three different stenosis severities (60%, 75% and 90% area reduction) were investigated as detailed above in the metho-

ds section, for a steady physiological mean flow rate of 345ml/min.

The results from the 90% stenosed case discussed earlier indicated that most of the flow disturbances resided at the P3 (1.5cm downstream) and P4 (3cm downstream) positions. Therefore, in the current investigation, the results from these two positions i.e., P3 and P4 are presented in Table 12 and Table 13, respectively.

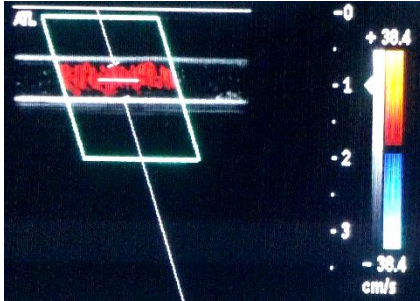

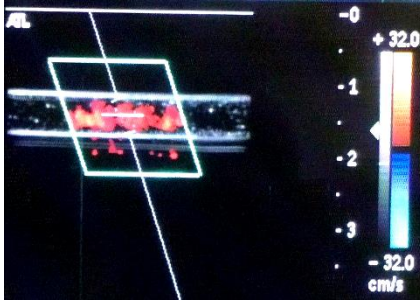
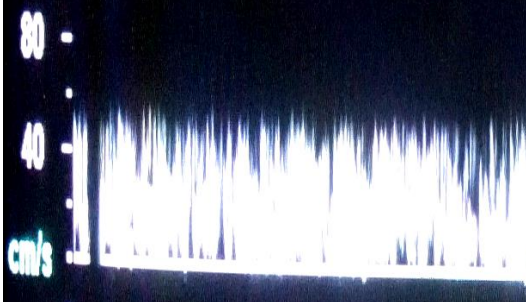
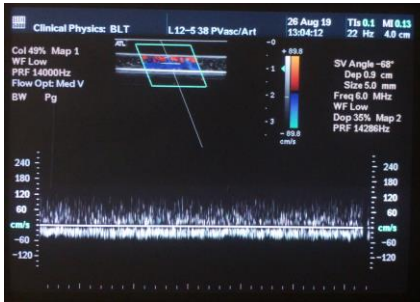
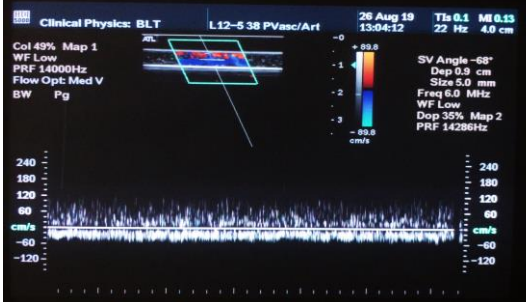
Table 12: Flow mapping, using Duplex ultrasound, of 60%, 75% and 90% stenosed tubes at 1.5cm downstream of the stenosis at a flow rate of 345ml/min

Steno- sis Sever- ity	Colour Map	Velocity (cm/s)
60%		
75%		
90%		

Raw velocity data could not be extracted due to limitations of the hardware, however, looking at the velocity traces from Table 12 and Table 13, both positions show an increased mean velocity with increasing stenosis severity. Furthermore, focussing only on

the peak velocity values at the P3 position from Table 12, the stenosis severities of 60%, 75% and 90% give rise to approximate velocities of 60, 90 and 260 cm/s, respectively. Similarly, from Table 13, the corresponding peak velocity values observed at the P4 position were 40 cm/s, 55 cm/s, and 120cm/s. This also shows that the difference between 75% and 90% severity is more substantial than that between 60% and 75%.

Table 13: Flow mapping, using Duplex ultrasound, of 60%, 75% and 90% stenosed tubes at 3cm downstream of the stenosis at a flow rate of 345ml/min

Steno- sis Sever- ity	Colour Map	Velocity (cm/s)
60%		
75%		
90%		

On further observation of the colour maps and velocity traces in these tables, the flow instabilities start to appear as the stenosis severity is increased. The first evidence of this can be seen for the 75% stenosis at the P3 position, which shows negative velocities,

indicating the presence of a recirculation zone. This effect is further amplified in the 90% stenosed case where a strong jet is formed, directed towards the upper edge of the tube, and a recirculation zone is formed near the lower edge. Further downstream, at the P4 position, this recirculation is only evident in the highly stenosed (90% severity) case.

### 3.3. Detection of flow disturbances at the tube surface (using LDV)

Following the preliminary detection of tube surface movement associated with disturbances in the flow using accelerometers and ultrasound, Laser Doppler Vibrometry was established as the primary means for measuring surface movement of the bare tube and the phantom skin (as discussed in the chapter 2). The data acquired using this technique was used to identify the effects (individual and/or combined) of flow rate, stenosis severity, stenosis symmetry and fluid viscosity.

#### 3.3.1. Effects of fluid viscosity

##### Methods

As mentioned in chapter 2.1, two different fluids were used in the experiments. The initial measurements were carried out with de-ionised water (dynamic viscosity  $\mu = 0.9\text{cP}$ ) as a proof of concept, however, a 40:60 (by volume) glycerine-water solution ( $\mu \approx 3.83\text{cP} - 4.15\text{cP}$  interpolated between  $17^\circ\text{C}$  and  $19^\circ\text{C}$  respectively as illustrated in Figure 55, corresponding to the ambient conditions at which experiments were conducted) was later introduced to mimic the viscosity of the blood (Segur and Oderstar, 1951; Yousif, Holdsworth and Poepping, 2009).

Patches of retroreflective tape were placed at four positions along the tube length i.e., P1 (3cm upstream), P3 (1.5cm downstream), P4 (3.0cm downstream), and P5 (6cm downstream), as shown in Figure 56. The fluid was perfused through the Penrose latex tube selected in section 2.2, with the stenosis type (axisymmetric) and three different stenosis severities i.e., 60%, 75% and 90% (discussed in section 2.3), to mimic the carotid artery. A continuous flow circuit was set-up as described in section 2.7 (with the programmable

piston pump switched off to achieve a physiological mean steady flow ranging from 0-450ml/min.

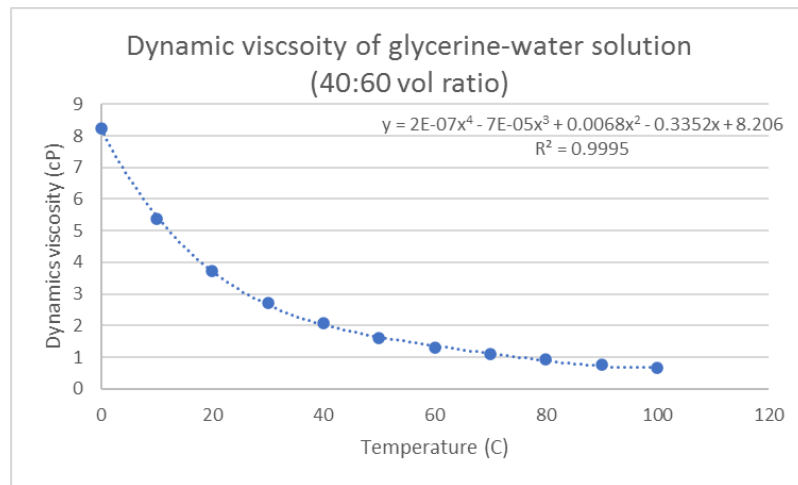


Figure 55: Variation of viscosity in 40:60 (volume ratio) of glycerine-water solution, with temperature [derived from (Segur and Oderstar, 1951; Trejo González, Longinotti and Corti, 2011)]

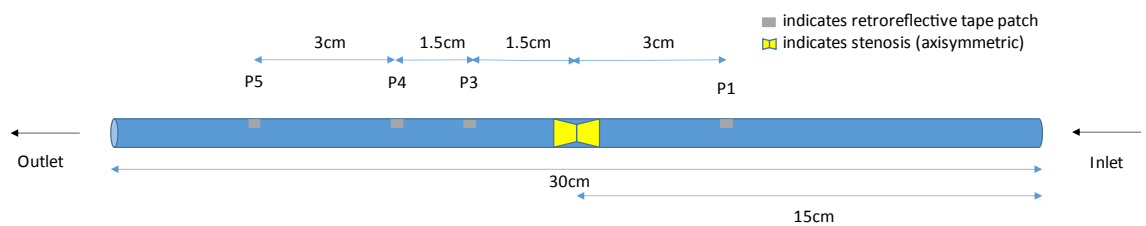


Figure 56: Stenosed bare tube, with patches of retroreflective tape at four positions P1, P3, P4 and P5 to facilitate data collection using LDV device from axisymmetrically stenosed tubes

Since the viscosity of blood is approximately four times higher than water, this would reduce the Reynolds number by the approximately the same factor. With the increased viscous forces within the glycerine-water solution, the flow disturbances would be expected to be damped, to appear at higher flow rates and/or at higher stenosis severities in comparison to the water only case. Therefore, bare tube experiments were carried out to study the effect of fluid viscosity, on the disturbances produced at the tube surface.

## Results & Discussion

The effects of fluid viscosity were investigated for the three different stenosis severities, 60%, 75% and 90%. For the effects to stand out, the initial investigation was conducted with the highest severity of 90% where the stenosed tube was perfused either with water or the glycerine-water solution. Power attenuation spectra (for all flow rates) at all four position P1, P3, P4 and P5 (Table 14 - Table 17) were firstly compared, and a further detailed analysis was conducted by comparing the respective ratios of the areas under the FFT spectra to reduce the data and to smooth out abrupt variations in the spectral power.

The areas under the FFT curves obtained for all flow rates were normalised to the no-flow condition as a control for background signal noise. The process was repeated for the other two stenosis severities, i.e., 75% and 60% and a comparison was then made between all three severities.

Firstly, on comparing each of the respective positions simply by looking at the power attenuation curves in Table 14 and Table 16, in the case of water perfused through a 90% stenosed tube, the effects of fluid viscosity become apparent at lower flow rates.

For instance, at the P1 (-3cm upstream) position in Table 14, differences in the FFT spectra start to appear at frequencies between 50-200 Hz at a flow rate of 200ml/min, however, the differences are more apparent for flow rates above 200ml/min where characteristic peaks start to appear. The signal gets stronger with the increasing flow rates and disturbances are spread over a wide range of frequencies. For the glycerine-water solution (Table 16), there is a subtle difference around 75 Hz, the peaks here show a reduction in the attenuation with increasing flow rate, from 200ml/min onwards. However, disturbances here are not spread over a wide range of frequencies as seen in the case of water.

Similar behaviour is seen at the P3 (+1.5cm) downstream position where disturbances become apparent at flow rates as low as 200ml/min in the case of water (Table 14) as opposed to 300ml/min for the glycerine-water solution (Table 16). A subtle difference at 200ml/min is seen again around 75 Hz in the glycerine-water solution (compared to the water only case). The difference is more apparent around 50Hz, 100Hz, and 140Hz. At

certain frequencies, the higher flow rates (e.g., 350ml/min, 400ml/min and 450ml/min) show an opposing trend i.e., a weaker signal is seen beyond a certain flow rate (at certain positions). An example of this behaviour is seen for P1 around 15 Hz and at 50Hz and for P3 position between 100-150 Hz.

Moving further downstream, 200ml/min remains the minimum flow rate for water (Table 15) at both the P4 (+3cm) and the P5 (+6cm) positions at which characteristic peaks are seen over a wide range of frequencies (starting from frequencies as low as around 1Hz). In the case of the glycerine-water solution (Table 17), this baseline value is increased to 300ml/min where the difference is apparent around 50Hz at P4 (+3cm) position. Here the signal strength increases until the flow rate reaches 400ml/min and then drops back down at 4450ml/min. A similar trend is seen at 100Hz between 300ml/min and 450ml/min. Furthermore, a clear distinction is seen between 50-100Hz where the effect strengthens with increasing flow rates above 300ml/min. Finally, at the P5 (+6cm) position, being further downstream from the stenoses, the energy in the flow dissipates further. The highest flow rate (450ml/min) is clearly differentiated, however, only hints of a viscosity effect are seen for flow rates above 300ml/min, these being in the vicinity of frequencies 15Hz, 28Hz, 75 Hz and between 100-150Hz.

As mentioned earlier, the FFT spectra were processed further to reduce the data and to smooth out abrupt variations in the spectral power. The areas under the FFT curves were obtained for all flow rates, which were then normalised to the no-flow condition as a control for background signal noise. The process was repeated for the three different stenoses severities.

From the spectra seen above, most of the notable differences between water and the glycerine-water mixture lie within the first 150Hz, therefore, comparisons were made with a focus on that frequency range. The areas under the FFT curve (normalised to no-flow) for all flow rates were, therefore, averaged between the 0-150Hz. In the case of 90% stenosed tube discussed above, a clear effect of increasing flow rates is demonstrated at all four positions.

Focusing on the water only case, indicated by the blue series in Figure 57 (a), the trend

Table 14: Bare tube run with water - FFT spectra obtained from LDV data at P1 and P3

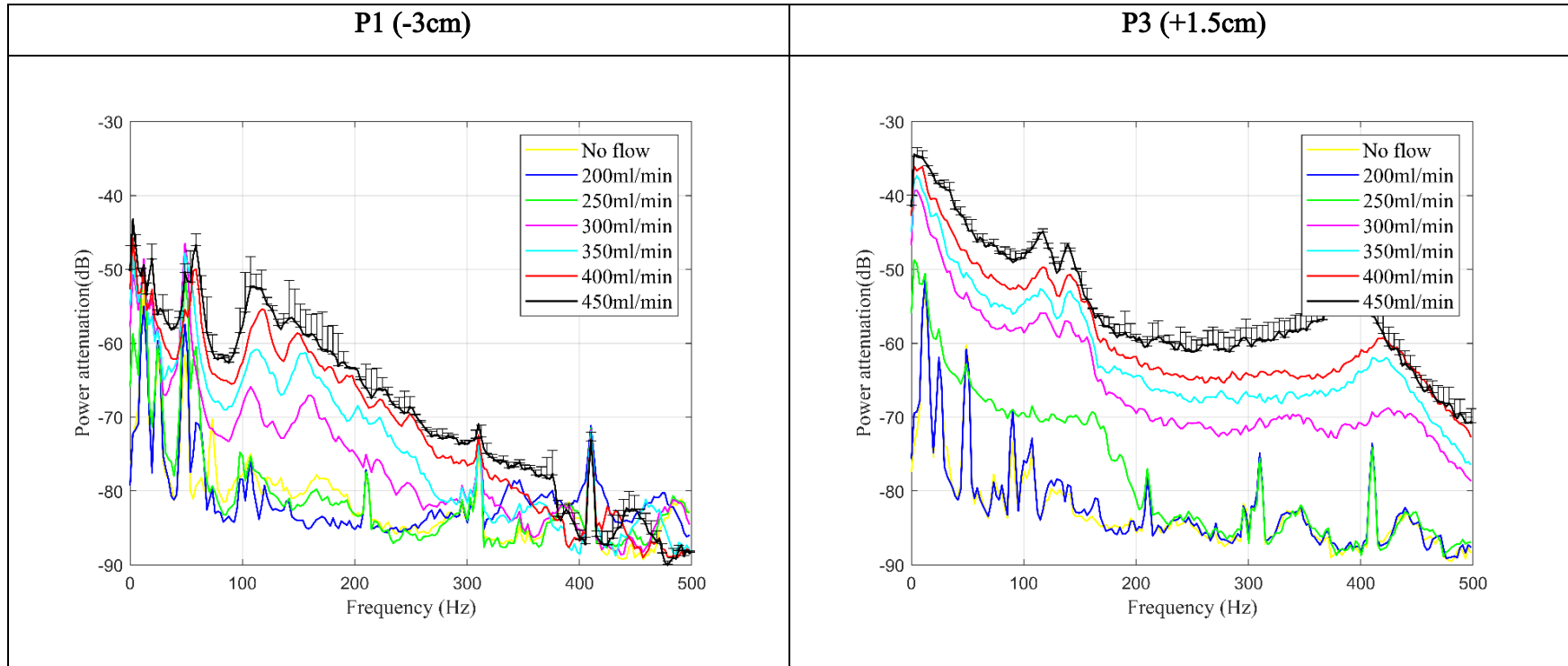




Table 15: Bare tube run with water - FFT spectra obtained from LDV data at P4 and P5

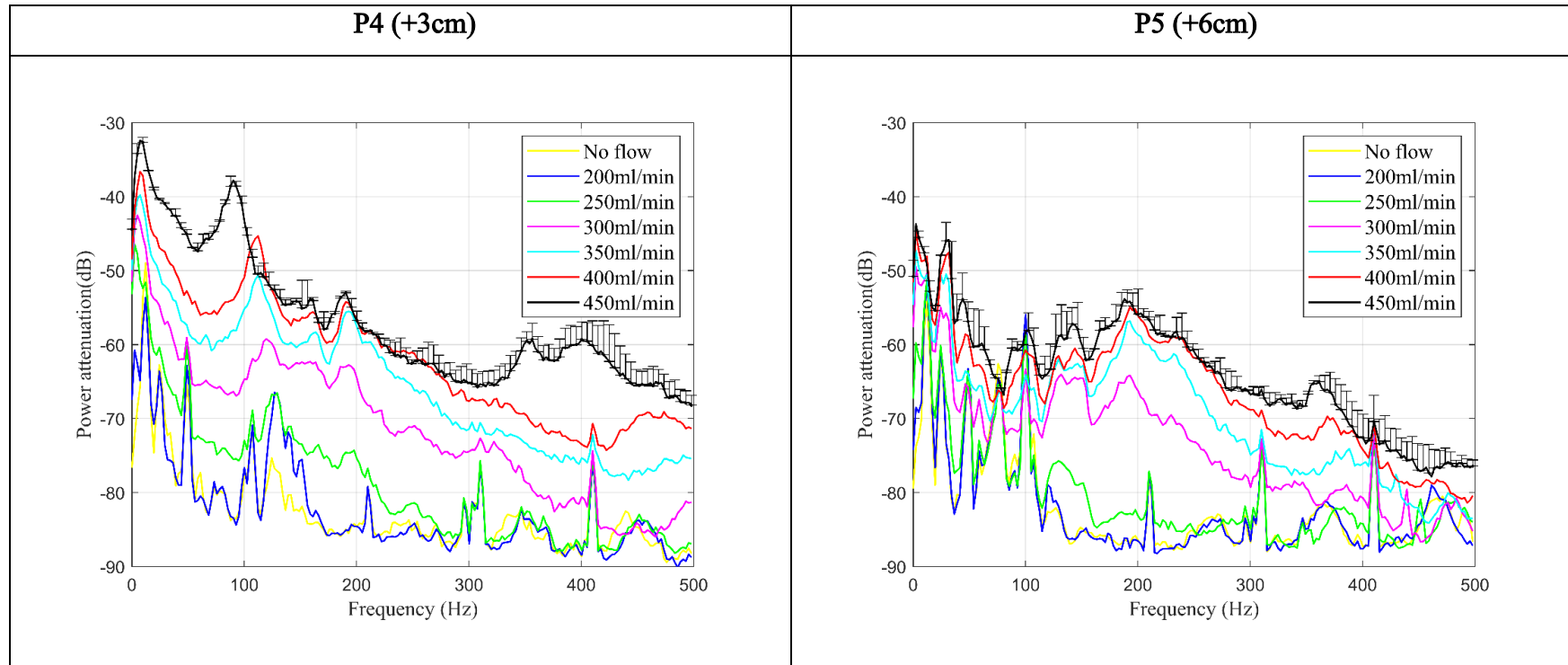


Table 16: Bare tube run with glycerine-water solution - FFT spectra obtained from LDV data at P1 and P3

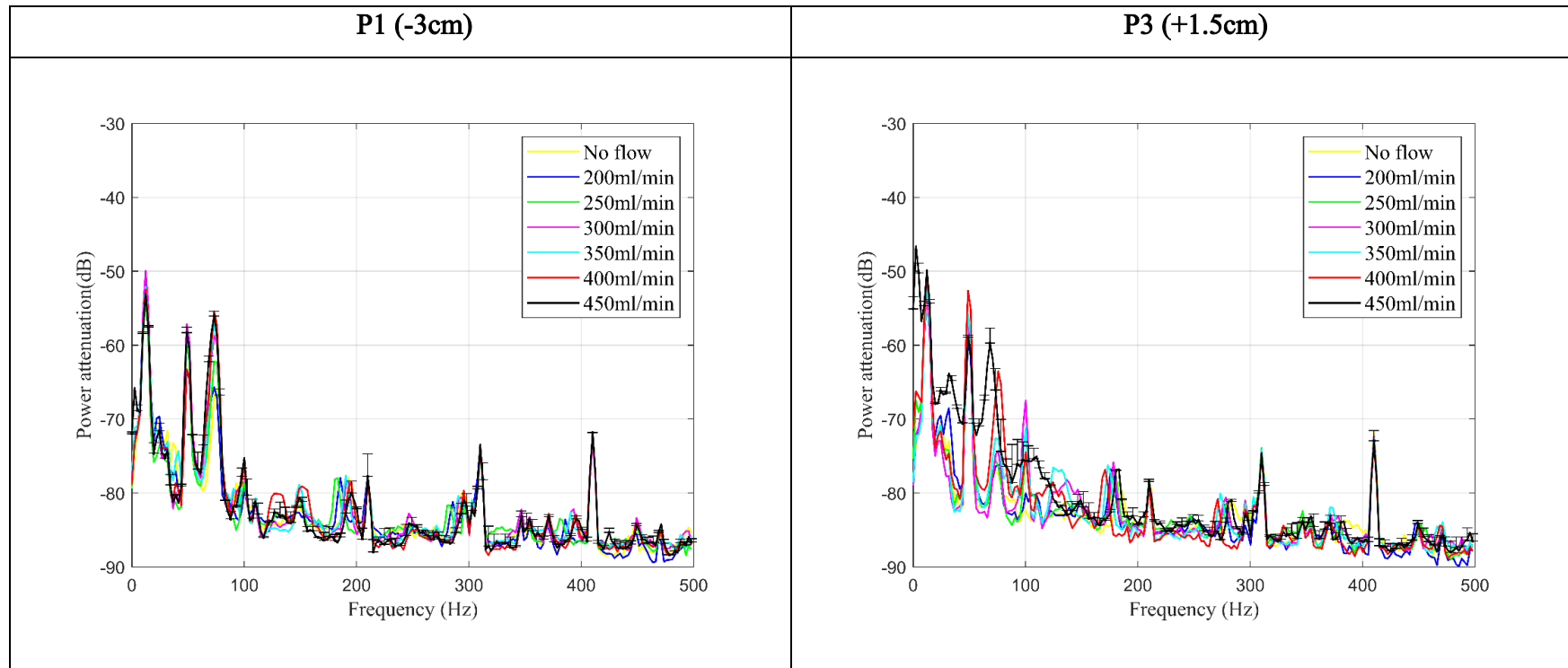
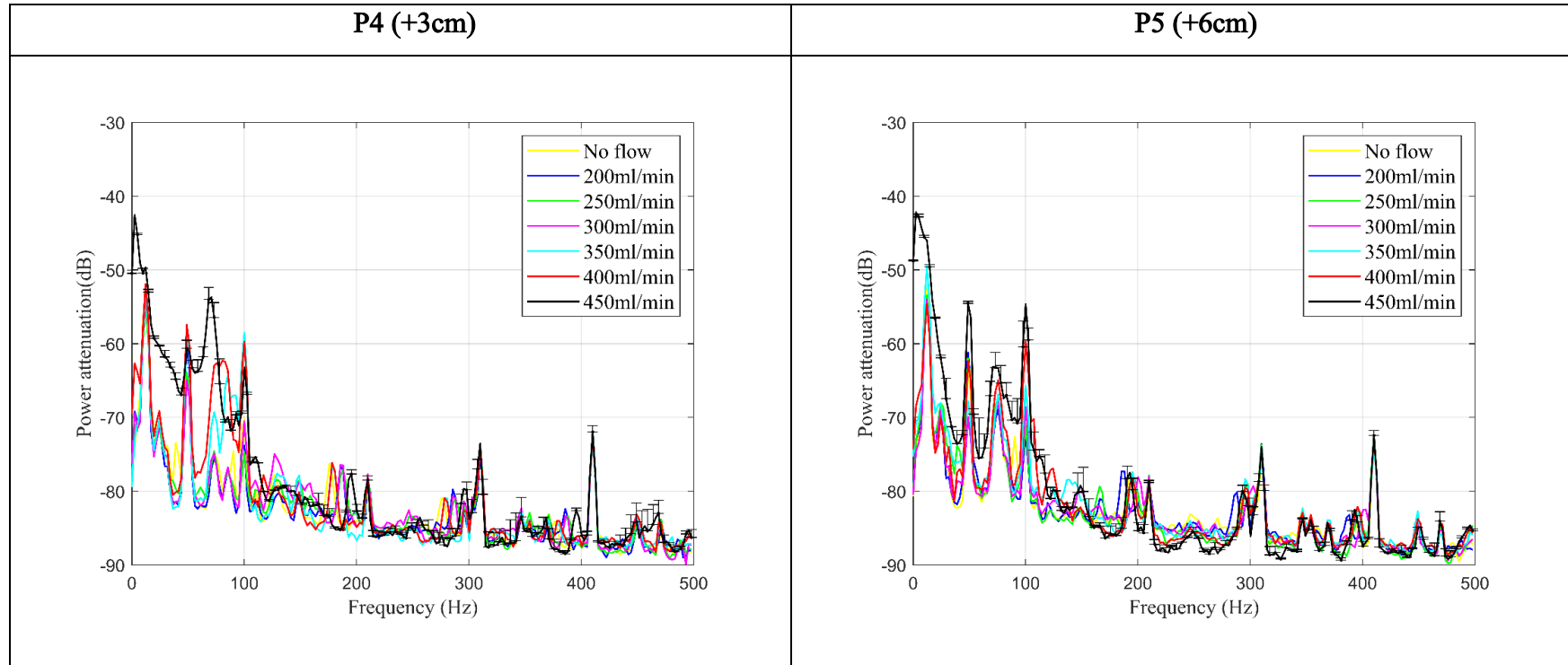


Table 17: Bare tube run with glycerine-water solution - FFT spectra obtained from LDV data at P4 and P5



resulting from increasing the flow rate starts to become apparent at the P1 position, where some of the disturbances measured might have been transmitted upstream, from the positions immediately downstream of the stenosis.

The smaller length of the recirculation zones, immediately downstream of the stenosis, results in a weaker signal for flow rates less than 200ml/min. However, as the flow rate was increased, the disturbances started to become apparent and higher averages of the area under FFT spectra were seen. At the P3 position (Figure 57 (b)), there was a sharp increase in the area ratio up till 300ml/min after which the rate of increase became shallower. As mentioned earlier while comparing the FFT spectra, this behaviour can be explained by the shifting of disturbances between different downstream positions for varying flow rates as can be seen by an almost constant increase at the P4 position (Figure 57 (c)) at flow rates above 100ml/min.

Finally, as the fluid travels further downstream towards the P5 position, the flow disturbances dampen out due to viscous losses, resulting in decreased average areas at the P5 position. It is worth noting here is that at flow rates less than 450 ml/min (the maximum set in these experiments), the disturbances were highest at the P3 position, i.e., close to the stenosis. However, at 450ml/min, where the jet length from the stenosis was increased, the averaged area at P4 approached the P3 value.

Focusing now on the glycerol-water solution results, similar trends of increasing FFT areas, with increasing flow rate were seen, but the effects were less pronounced, at the downstream positions only starting to become apparent at flow rates above 300ml/min. For the 90% stenosis, an independent samples t-test was conducted for the averaged FFT area ratios (normalised to no-flow), between 0-150Hz, where the data for all the flow rates and downstream positions was combined. The t-test was associated with a statistically significant effect,  $t(29)=3.09$ ,  $p=0.004$ . Thus, water perfused tubes yielded significantly higher means and thus larger flow disturbances than those perfused with glycerol-water solution. Further analysis, including 60% and 75% severities, is presented later in this section.

These differences can be explained by the relationship between flow and Reynolds

number. Given the differences between the density, and mainly the viscosity, of the two fluids, the Reynolds number for water is approximately four times higher than that of the glycerine-water solution. Obtaining a local Reynolds number (within the stenosis) was outside the scope of the study but based on the flow rates used, the maximum Reynolds numbers for the flow approaching the stenosis for water and glycerine-water solution were estimated to be approximately 1685 and 362, respectively (the ratio is slightly larger than 4 due to difference in densities). As the flow passes through the narrowing, it accelerates and increases the local Reynolds number, which means the flow rate nears the state at which turbulence is initiated ( $Re \approx 2000$ ) at lower velocities for water than the glycerine-water mixture. This behaviour is in agreement with a range of studies (on the effect of Reynolds number) cited earlier in the literature review. (Ahmed and Giddens, 1983; Liao, Lee and Low, 2004).

Finally, the effects of fluid viscosity were investigated for different stenosis severities. This is discussed in further detail in section 3.2.4, whereas the focus of this section is to compare trends for both the water-filled and the glycerine-water filled bare tubes. Figures 4 and 5 show the areas under FFT curves (normalised to no-flow), averaged over the frequency range 0 – 150Hz, for water-filled and glycerine-water filled bare tubes, respectively.

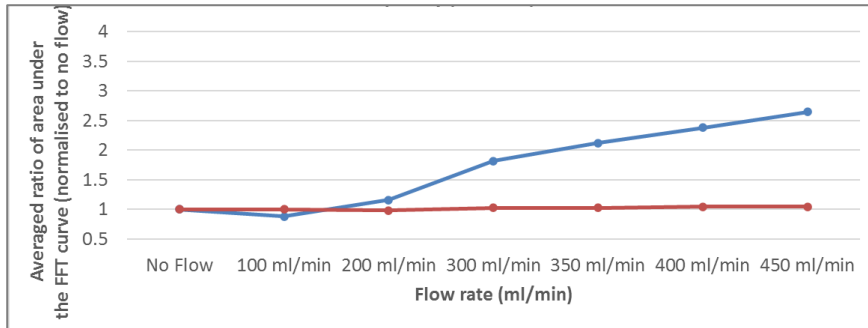
At first glance, Figure 58 shows increasing FFT area ratios with increasing the flow rates as expected, especially for the 75% and 90% stenosed tubes. Further observation shows the presence of an apparent trend of increasing FFT ratios, with the increasing flow rates, even for the 60% case. The effect is not visible upstream (P1) or far downstream of the stenosis (P5), but it can be observed closer to the stenosis at P3 and P4 positions for flow rates above 200ml/min.

These trends were validated by conducting a linear regression analysis for flow rates of 200ml/min and above. The gradients, coefficients of determination and  $f$  values from this analysis are summarised in Table 18, which confirms the dependence of FFT ratios on the flow rates for all positions and severities, apart from the moderate 60% stenosis at the two positions furthest from the stenosis (i.e., P1 and P5). Gradients also generally

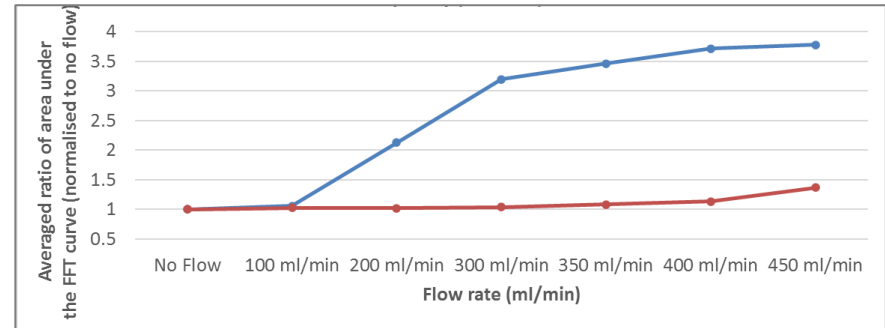
increased from P1 to P4 as the fluid passed through the stenosis and then there was a decreasing trend from P4 to P5 as the fluid travelled further away from the stenosis.

Considering similar trends in the glycerine-water filled tubes, Figure 59 shows that the effects of increasing flow rate or those of increasing stenosis severity were not as pronounced as those seen in figure 4 with the water-filled tubes. The upstream position (P1) showed no apparent trends with increasing flow rates or severities. Moving downstream, an increasing trend in the FFT ratios was seen in the severely (i.e., 90%) stenosed tube, for flow rates above 300ml/min, as the Reynolds number increased. Despite the smaller increase of FFT ratios, in comparison to Figure 58, their dependence on the increasing flow rate was validated with a linear regression analysis but, in this case, only for flow rates of 300ml/min and above. Table 19 reveals a trend for the 90% case at all downstream positions although it is only statistically significant at the 5% level for downstream position P4. The probability that the difference arose by chance for the P3 and P5 positions lies just outside the 5% range as the effect is not too strong until the flow rate reaches 450ml/min. For the 75% stenosis, there was a significant increase of the FFT area ratios at positions P3 and P5. No significant effect was seen for the 60% stenosis.

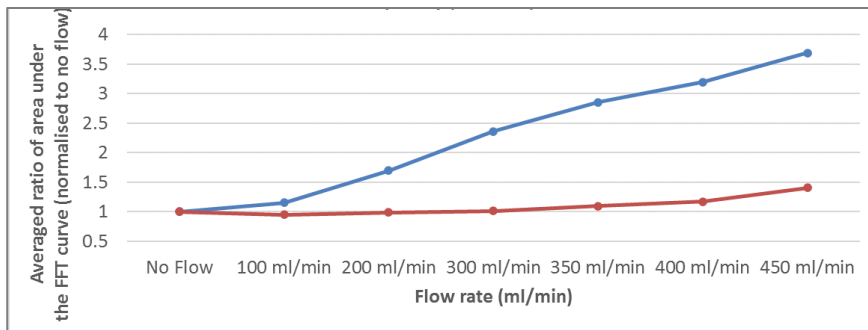
In summary, in the water filled tubes a significant positive relationship between the FFT area ratio and flow rate was seen in the 75 and 90% stenoses for flow rates higher than 200 ml/min, with a less consistent effect in the 60% case. Overall, a similar pattern was seen in the glycerol water experiments although the response was weaker, presumably because of the greater energy losses in this more viscous fluid. Thus, the fluctuations produced within the flow are too weak to generate detectable disturbances at the tube surface. The lack of detectable disturbances in the tube can be further attributed to the axisymmetric nature of the stenoses. The axial symmetry of the stenoses, combined with the low Reynolds number, would discourage the separation of flow and recirculation of flow in the post-stenotic region.



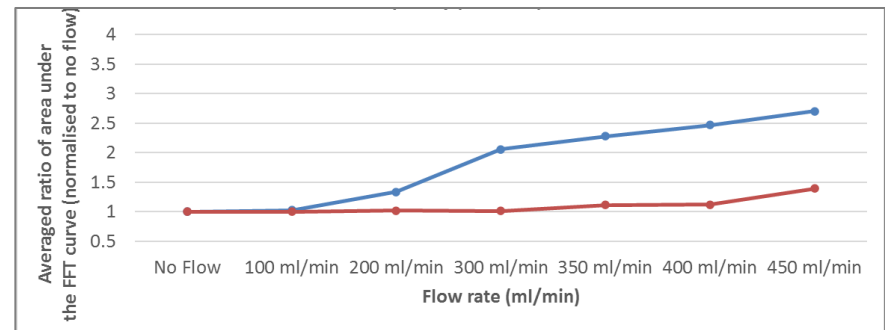
(a)



(b)

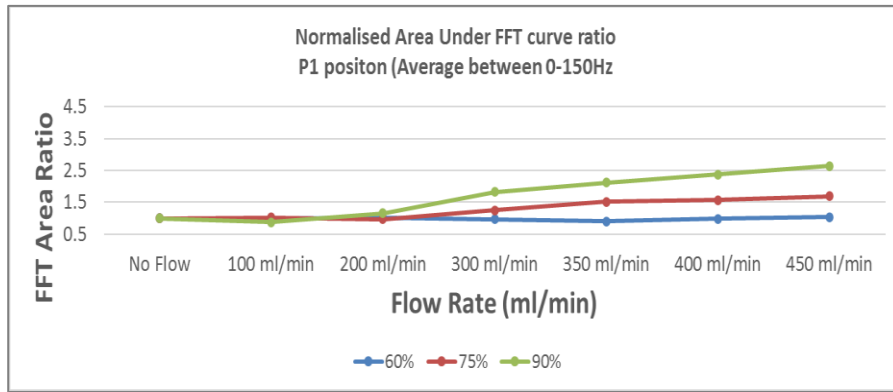


(c)

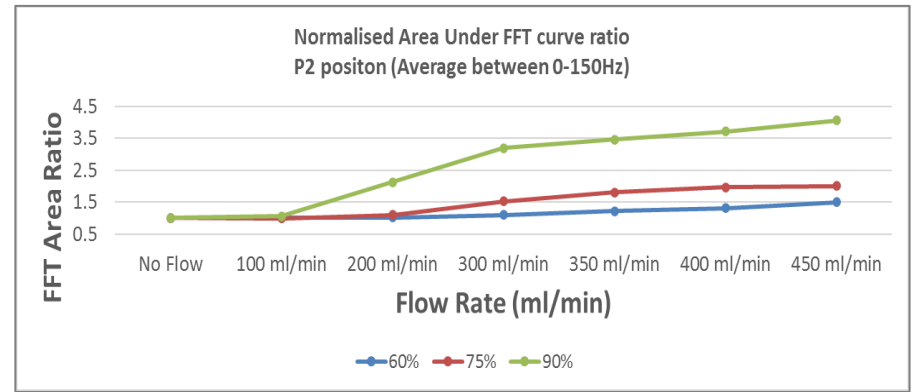


(d)

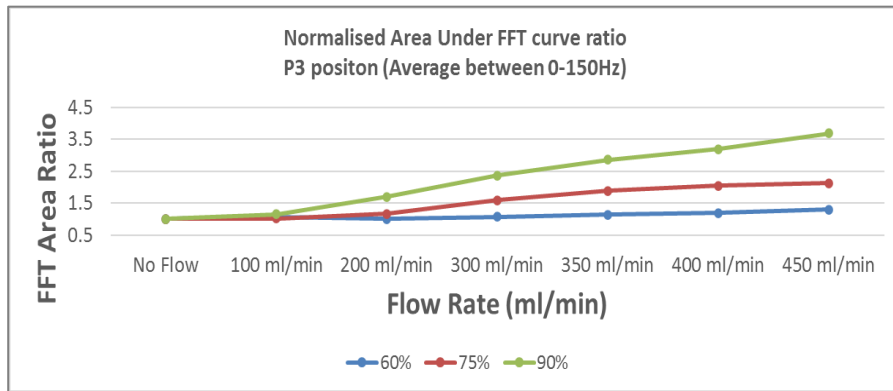
Figure 57: Ratios of area under the FFT curve (normalised to no flow) for a 90% stenosed tube, using water (blue) and glycerine-water solution (red) as the fluid medium, at P1 (b) P3 (c) P4 (d) P5 which are 3cm upstream, 1.5cm downstream, 3cm downstream, 6cm downstream of the stenosis, respectively



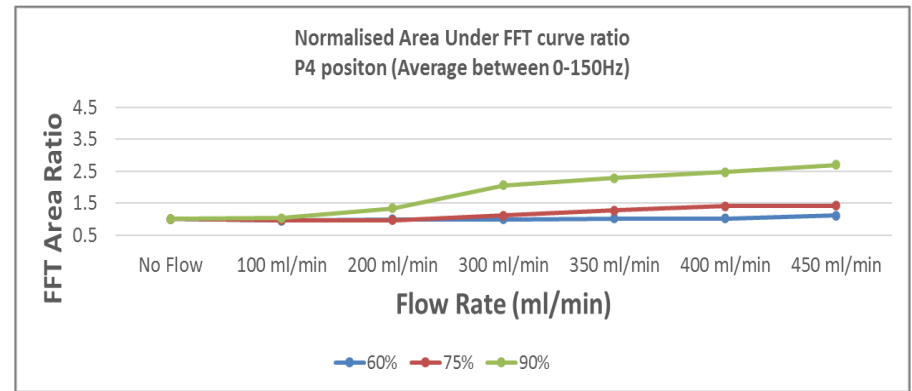
(a)



(b)



(c)



(d)

Figure 58: Area under the FFT curve (normalised to no flow) ratios with water, for 60% (blue), 75% (red) and 90% (green) bare stenosed tubes, at (a) P1 (b) P3 (c) P4 (d) P5, which are 3cm upstream, 1.5cm downstream, 3cm downstream and 6cm downstream, respectively



Table 18: Regression analysis of effect of flow rate in a bare stenosed tube, with water as perfusing liquid at P1 (-3cm upstream), P3 (+1.5cm downstream), P4 (+3cm downstream) and P5 (+6cm down-stream) positions – green (highly significant), and red (insignificant)

	<b>Severity</b>	P1	P3	P4	P5
Coefficient (Gradient)	60%	0.000	0.002	0.001	0.000
	75%	0.003	0.004	0.004	0.002
	90%	0.003	0.004	0.004	0.002
R-squared	60%	0.001	0.919	0.945	0.624
	75%	0.966	0.964	0.973	0.964
	90%	0.998	0.971	0.992	0.990
Significance p-value	60%	0.964	0.010	0.006	0.112
	75%	0.003	0.003	0.002	0.003
	90%	0.002	0.002	0.000	0.000

Table 19: Regression analysis of the effect of flow rate in a bare stenosed tube, with glycerine-water solution as perfusing liquid at the P1 (-3cm upstream), P3 (+1.5cm downstream), P4 (+3cm downstream) and P5 (+6cm down-stream) positions – green (highly significant), yellow ( $0.1 > p > 0.5$ ), and red (insignificant)

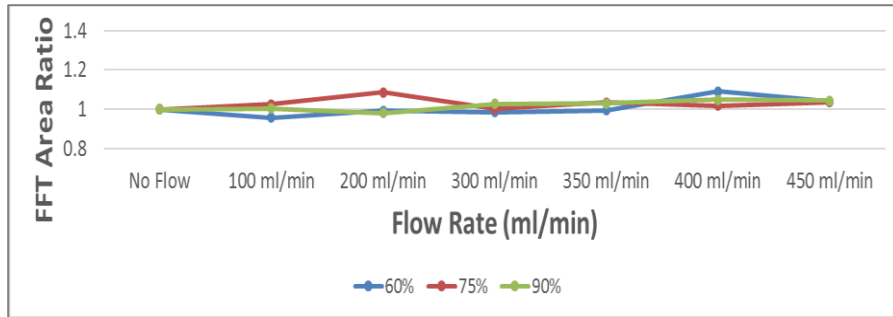
	<b>Severity</b>	P1	P3	P4	P5
Coefficient	60%	0.001	0.000	0.000	0.001
	75%	0.000	0.000	0.000	0.001
	90%	0.000	0.002	0.003	0.002
R -square	60%	0.475	0.290	0.191	0.466
	75%	0.466	0.946	0.035	0.937
	90%	0.676	0.889	0.919	0.828
Significance F	60%	0.311	0.462	0.563	0.318
	75%	0.318	0.027	0.813	0.032
	90%	0.178	0.057	0.041	0.090

To explore the combined effects of fluid type, stenosis severity and flow rate, a two-way between groups ANOVA was performed. The data were divided into three groups, based on flow rates, stenosis severity and the type of fluid used. The dependent variable in the analysis was the averaged (0-150Hz) area under the FFT curved (normalised to no-flow). The data from the three downstream positions (P3, P4 and P5) were combined to increase the number of degrees of freedom in the analysis. This in turn affected homogeneity of

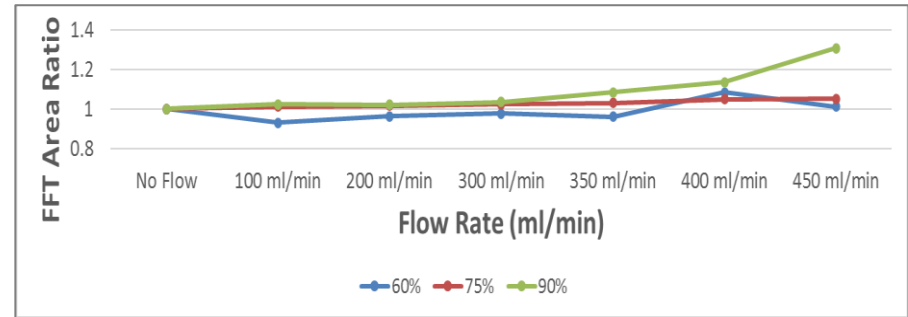
variance (as assessed by Levene's test  $F(84)=5.604$ ,  $p<0.05$ ), however, the variance can be the combination of data from the three downstream positions, which can be justified to study the effect of fluid type, severity or the flow rate as most of the disturbances were present in the downstream position as discussed previously.

The analysis showed that the effects of flow rate ( $F(6,84)=24.45$ ,  $p=0.000$ ), fluid type ( $F(1,84)=121.12$ ,  $p=0.000$ ) and stenosis severity ( $F(2,84)=37.03$ ,  $p=0.000$ ) were significant. The effect of flow rate was the largest, followed by the effect of fluid and the stenosis severity with the partial  $\eta^2$  (a measure of the effect size) values of 0.636, 0.590 and 0.469, respectively. In addition, the analysis also indicated the significance of interactions between fluid type & flow rate ( $F(6,84)=12.35$ ,  $p=0.000$ ), fluid type & stenosis severity ( $F(6,84)=16.13$ ,  $p=0.000$ ), and flow rate & stenosis severity ( $F(6,84)=3.45$ ,  $p=0.000$ ). Here, the effect of interaction was strongest between flow rate & fluid type, followed by that between severity & flow rate and finally severity & fluid type with partial  $\eta^2$  values of 0.469, 0.331 and 0.278, respectively. The combined interaction effect severity, flow rate and fluid type was not found to be significant ( $F(12,84)=1.632$ ,  $p=0.098$ ). The profiles comparing the means of these variables, for all the downstream positions combined, are illustrated in Figure 60. This clearly shows the trends of increasing means with increasing flow rates, increasing severities and decreasing fluid viscosity.

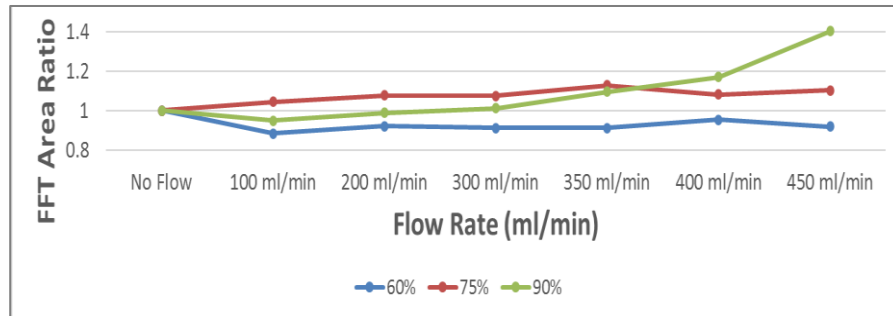
This investigation on the effects of fluid viscosity concludes that the fluid viscosity and flow rate have a significance effect on the flow features within moderate to severely stenosed tubes. The disturbances detected at the tube surface are generally in the higher frequency range, at higher flow rates and higher viscosity. In the glycerol-water solution, the reduced Reynolds number prevents the flow separation from the walls, hence, reducing the detectable perturbations in the flow, unless the tube is severely stenosed or the flow rates are high. The increased viscous damping results in greater energy dissipation as the fluid travels further away from the stenosis, hence inhibiting the detection of the disturbances. In a clinical environment it is critical to identify these disturbances under physiological flow rates and in the cases of highly stenosed arteries, high flow rates are not achievable either because the blood finds alternate paths with lower resistance, or the



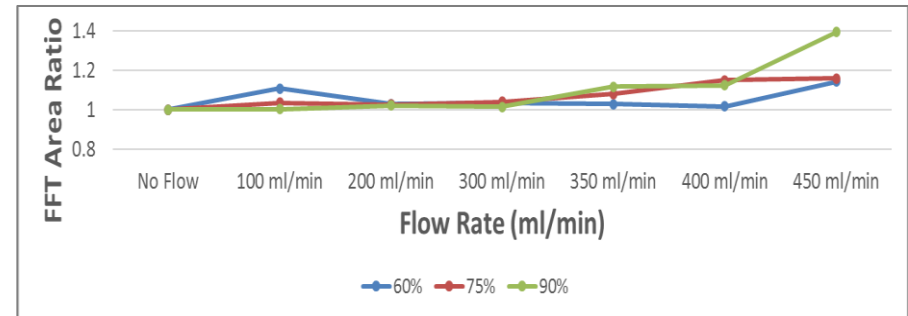
(a)



(b)

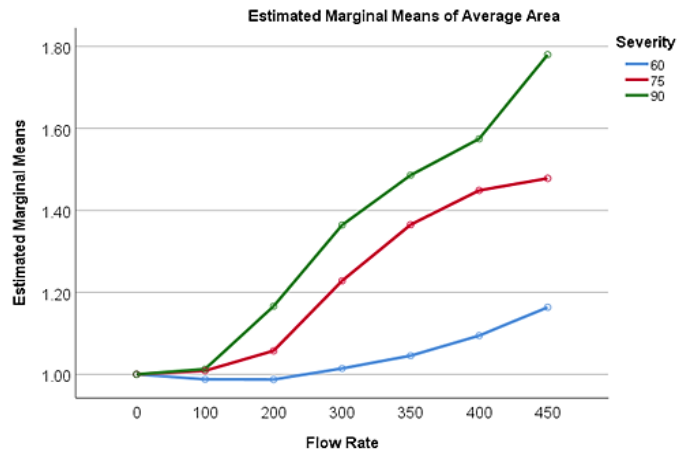


(c)

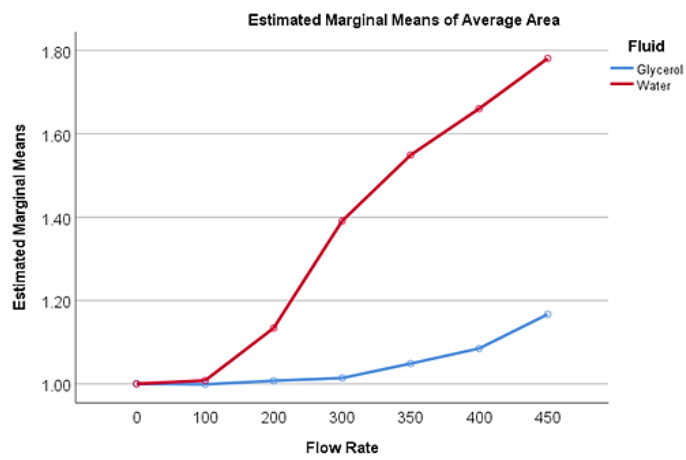


(d)

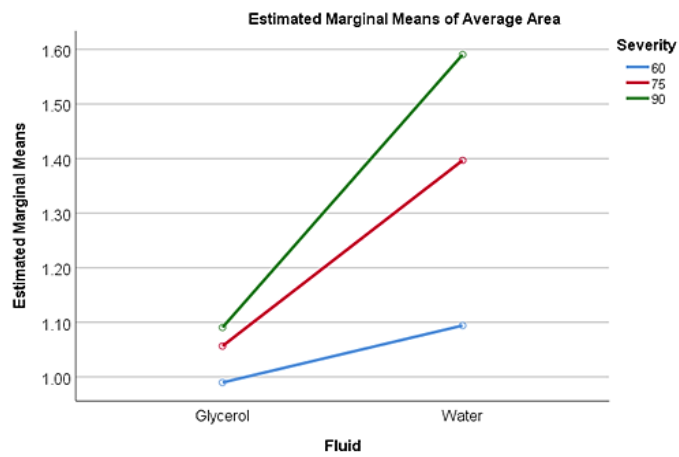
Figure 59: Area under the FFT curve (normalised to no flow) ratios with glycerine-water solution, for 60% (blue), 75% (red) and 90% (green) bare stenosed tube, at (a) P1 (b) P3 (c) P4 (d) P5, which are 3cm upstream, 1.5cm downstream, 3cm downstream and 6cm downstream, respectively



(a)



(b)



(c)

Figure 60: Means of averaged (0-150Hz) areas under the FFT curve (normalised to no flow), calculated from the combined downstream positions, showing the interactions between (a) flow rate (ml/min) & severity (b) flow rate (ml/min) & fluid type and (c) fluid type and severity

flow is limited by the failure of the heart as a constant flow pump . However, in real arteries it is also true that the stenoses are highly unlikely to be axisymmetric, and the presence of even a slight asymmetry in geometry can have a considerable effect on flow patterns in the post-stenotic region (Kaazempur-Mofrad *et al.*, 2005). Therefore, the effects of stenosis symmetry were further studied in isolation. Detailed results, presented in section 3.3.2, show significant improvement in the detection of disturbances in the downstream region, in the more realistic case of asymmetrically stenosed tube.

### 3.3.2. Effect of Stenosis Symmetry

As mentioned in chapter 2, two different approaches (cotton thread stenoses and 3D printed stenoses) were taken to produce the stenoses. The initial proof of concept study was carried out using a cotton thread tied around a silicone rubber tube, embedded within an agar gel phantom. Further details of this will be presented in the phantom experiments in Chapter 4. This section of the study focuses on the effects of stenosis symmetry studied in a bare-stenosed tube.

#### Methods

In this investigation, the effect of stenosis symmetry was studied in isolation, without considering the effect of viscosity. As the effect of stenosis severity for axisymmetric stenoses has been described earlier (section 3.2.1), this section focuses mainly on stenosis geometry (axisymmetric vs non-axisymmetric). To study the effects of the stenosis symmetry systematically, two stenoses (with 75% and 90% severity) were investigated where the constrictions were offset from the centre of the tube (Figure 61).

Figure 62 shows the experimental set-up where de-ionized water was perfused through a bare stenosed Penrose latex tube with flow rates ranging from 0 to 450ml/min, and data were captured at the same four positions as used in section 3.3.1 i.e., at P1 (3cm upstream), P3 (1.5cm downstream), P4 (3cm downstream) and P5 (6cm downstream). LDV was used to capture the disturbances on the tube surface and the data were recorded using the PowerLab set-up, described previously. The data obtained from both the 75% and the 90% stenosed tubes (axisymmetric and non-axisymmetric) were transformed to the frequency

domain using the fast Fourier transform and calculations of areas under the FFT curves (normalised to the no-flow conditions) were performed as detailed in section 2.8.

Severity	Axisymmetric	Non-axisymmetric
75%		
90%		

Figure 61: Cross section of axisymmetric and non-axisymmetric stenoses ( $x_1$  and  $x_2$ , both 1mm offset from geometric centre), with 75% and 90% reduction in area, respectively

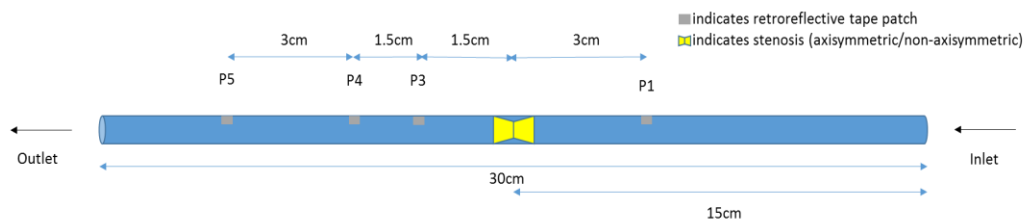
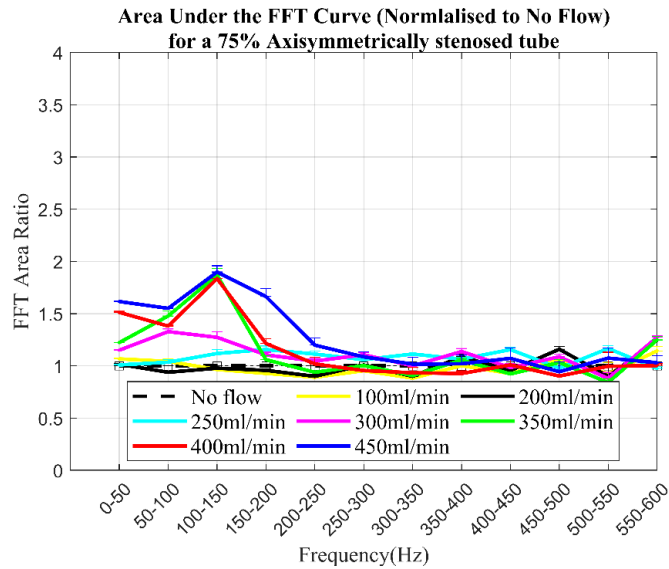


Figure 62: Stenosed bare tube, with patches of retroreflective tape at four positions P1, P3, P4 and P5 ensuring surface reflection of LDV beam from axisymmetrically and non-axisymmetrically stenosed tubes

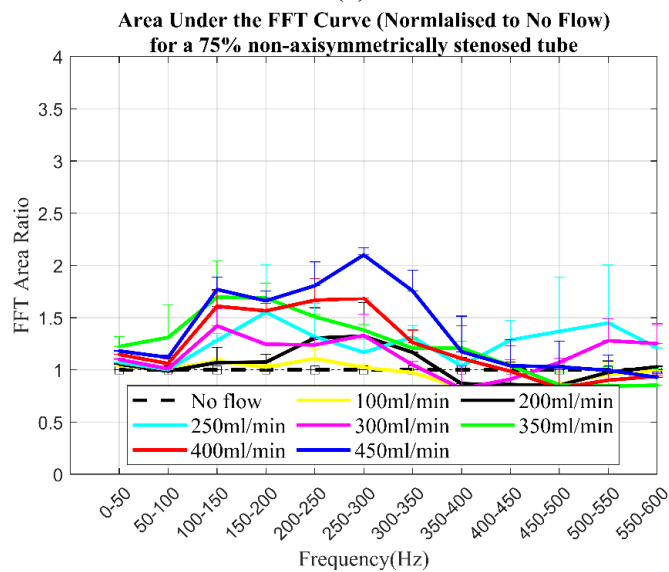
## Results & Discussion

For the 75% case, a comparison is shown in Figure 61 which highlights the differences in the areas under the FFT spectra for the 50Hz windows ranging from 0 to 600Hz. Looking at the upstream position (P1), it can be seen from Figure 63(b) that values above 1, indicating more disturbance, are spread over a wider range of frequencies for the non-axisymmetric stenosis, when compared to the axisymmetric stenosis of the same severity. Further observation highlights the appearance of a secondary characteristic peak between

250-350 Hz for the non-axisymmetric case, whereas the disturbances in the axisymmetrically stenosed tube are constrained within the first 250Hz, with maximum amplitudes around 150Hz.



(a)



(b)

Figure 63: FFT area ratios (normalised to no-flow) for 75% (a) axisymmetric and (b) non-axisymmetric cases tubes at P1 (-3cm upstream) position

It can also be seen that the effects of increasing flow rate start to become more apparent, with increasing stenosis severity in the non-axisymmetric case (especially above

300ml/min). These trends were confirmed by conducting a linear regression analysis for flow rates of 200ml/min and above, where the FFT area ratios were averaged in the range of 0-600Hz (since higher frequency disturbances were present here). The gradients, coefficients of determination and  $r$  values from this analysis, summarised in Table 20 confirm the dependence of FFT ratios on the flow rates, at all positions. Gradients also generally increased from P1 to P3 as the fluid passed through the stenosis and then there was a decreasing trend of gradients from P3 to P5 as the fluid travelled further downstream (with one inconsistency, the non-axisymmetric case at the P5 position).

Despite these noticeable differences in the relationship between area ratio and frequency, there is little difference between the two types of stenoses in the magnitude of the FFT area ratios at the P1 position. Since P1 is upstream from the stenosis, large differences were not expected here, before the flow entered the stenosis. The consistency in the trend (of the increasing flow rate) for the non-axisymmetrically stenosed tube can be explained, speculatively, by the shape of the stenoses (Figure 61). As the flow enters the non-axisymmetric constriction (vertically offset from the central horizontal axis of the tube), it bends upwards (Figure 64 (a)) asymmetrically on its approach to the middle of the stenosis where it impinges on the stenosis wall, causing vibrations on the tube's surface (as a result of vibrations in the stenosis as a whole) and thus transmitting the energy to the upstream position. This effect is amplified at the downstream positions, as discussed below. It can be speculated that some of the disturbances immediately downstream of the stenosis are detected at the upstream position as well, as the energy imparted to the latex tube is transmitted through its wall. The weaker effect in the axisymmetric case can be explained by the symmetrical post-stenotic velocity flow profile and smaller recirculation regions as shown in Figure 64 (b).

Moving downstream to the P3 position (Figure 65), similar trends were observed in terms of the distribution of disturbances across the frequency range. The non-axisymmetric stenosis caused large amplitude disturbances over a wider range of frequencies when compared to the axisymmetric case. A point worth noting here is that the amplitudes of the low frequency displacements (up to 100Hz) were larger for the axisymmetric case, after



which the non-axisymmetric stenosis takes over, with the appearance of new characteristic peaks at flow rates as low as 250ml/min. The amplitudes of these disturbances continue to increase at increasing frequencies up until 300-400 Hz, after which they start to decrease again, potentially due to viscous damping.

Table 20: Regression analysis of effect of the flow rate in a 75% bare stenosed (axisymmetric and non-axisymmetric) tube, with water as perfusing liquid, at P1 (-3cm upstream), P3 (+1.5cm downstream), P4 (+3cm downstream) and P5 (+6cm downstream) positions

	Gradient of the regression line		R-square		Significance (F)	
	Axisymmetric	Non-axisymmetric	Axisymmetric	Non-axisymmetric	Axisymmetric	Non-axisymmetric
<b>P1</b>	<b>0.00111</b>	<b>0.00093</b>	0.954	0.699	0.001	0.038
<b>P3</b>	<b>0.00256</b>	<b>0.00404</b>	0.972	0.988	0.000	0.000
<b>P4</b>	<b>0.00470</b>	<b>0.00204</b>	0.993	0.961	0.000	0.001
<b>P5</b>	<b>0.00152</b>	<b>0.00425</b>	0.977	0.999	0.000	0.000

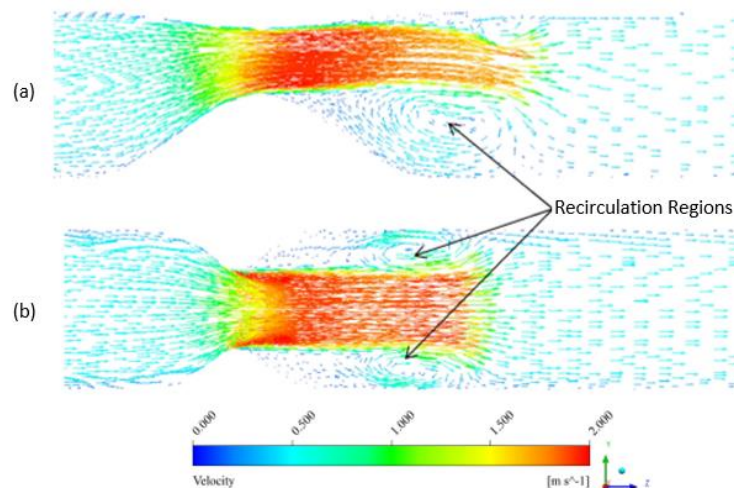
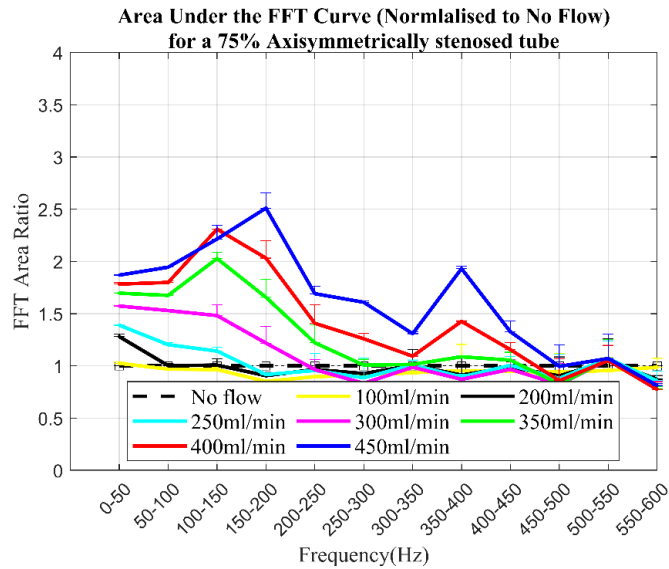


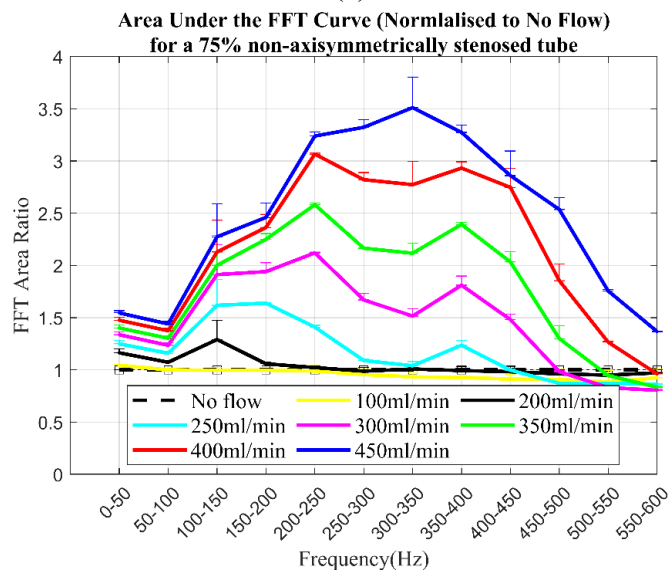
Figure 64: Vector field plots for flow through a 80% stenosed in the femoral artery (axisymmetric (a) and non-axisymmetric (b)) (Padukkage and Barber, 2014)

Similar trends are seen at the P4 (3cm downstream) and P5 (6cm downstream) positions (Figure 66), and it can further be seen (at P3, P4 and P5) that the differences in the area ratios, for the respective flow rates, start to decrease as the fluid travels further away from the stenoses, as expected. This can be further seen in Figure 67 which shows the means of the areas under the FFT curve for the entire 0-600 Hz frequency range, normalised to no flow. For the upstream position (P1), the averaged area appears to be slightly

lower for the non-axisymmetric case. , this can be explained as the FFT area ratios between 300-500Hz at the P1 position fell below 1 Figure 63 (b)), which affected the overall average in the 0-600Hz range.



(a)



(b)

Figure 65: FFT area ratios (normalised to no-flow) for 75% (a) axisymmetric and (b) non-axisymmetric cases at P3 (+1.5cm downstream) position

An independent samples t-test comparing the axisymmetric and non-axisymmetric cases showed that these differences were not statistically significant [ $t(14)=0.369$ ,  $p=0.718$ ] at

the P1 position. However, some differences were identified at specific frequencies as discussed above. Travelling further downstream, Figure 67 shows that the greatest effect of stenosis symmetry on the averaged area was at the P3 position (1.5cm downstream of the stenosis) and, as the flow travelled further downstream the effect was reduced at P4 and more so, at P5. This further emphasises that the stenosis-induced flow disturbances are detectable at lower flow rates for the non-axisymmetrically stenosed tube and that as the flow travels further downstream, the perturbations are reduced by viscous damping.

Considering the 90% stenosed tubes, the first thing that can be observed from Table 22 (at all positions) is that, at frequencies below 100Hz, the area ratios are higher for the axisymmetric stenosis when compared to the non-axisymmetric one, following the trend seen in the 75% stenosed case above. Furthermore, like the 75% case for the P3 and P4 positions, two plateaus seem to be forming (the first near 250Hz and the second near 500Hz). It can also be seen from Table 22 that the effect of increasing flow rates is amplified at the downstream positions for the non-axisymmetric case, especially at the P3 position, where larger disturbances are detected at higher frequencies (generally in the range 200-450 Hz). This can also be seen at the other downstream positions (i.e., P4 and P5) where these higher frequency disturbances appear to be amplified.

Comparing the 75% and the 90% cases, disturbances can be detected in the 90% stenosed tube at lower flow rates i.e., 200ml/min instead of 250ml/min. Furthermore, the non-axisymmetric stenoses allows for further verification of the trend, of increasing areas under the FFT spectra over the range of 150-600Hz. Figure 68 summarises the averages of these areas for the entire 0-600 Hz frequency range, normalised to their respective no flow conditions, for the 75% and 90% stenosed tubes (both axisymmetric and non-axisymmetric). It can be seen in Figure 68 that, as expected, the disturbances seen upstream of the stenoses are small in comparison to the downstream positions, although an exception to this was seen for the 90% axisymmetric case for flow rates above 250ml/min.

A linear regression analysis for flow rates of 200ml/min and above was conducted, where the FFT area ratios were averaged over the range 0-600Hz (where most of the disturbances were seen). The gradients, coefficients of determination ( $r^2$  values) and p va-

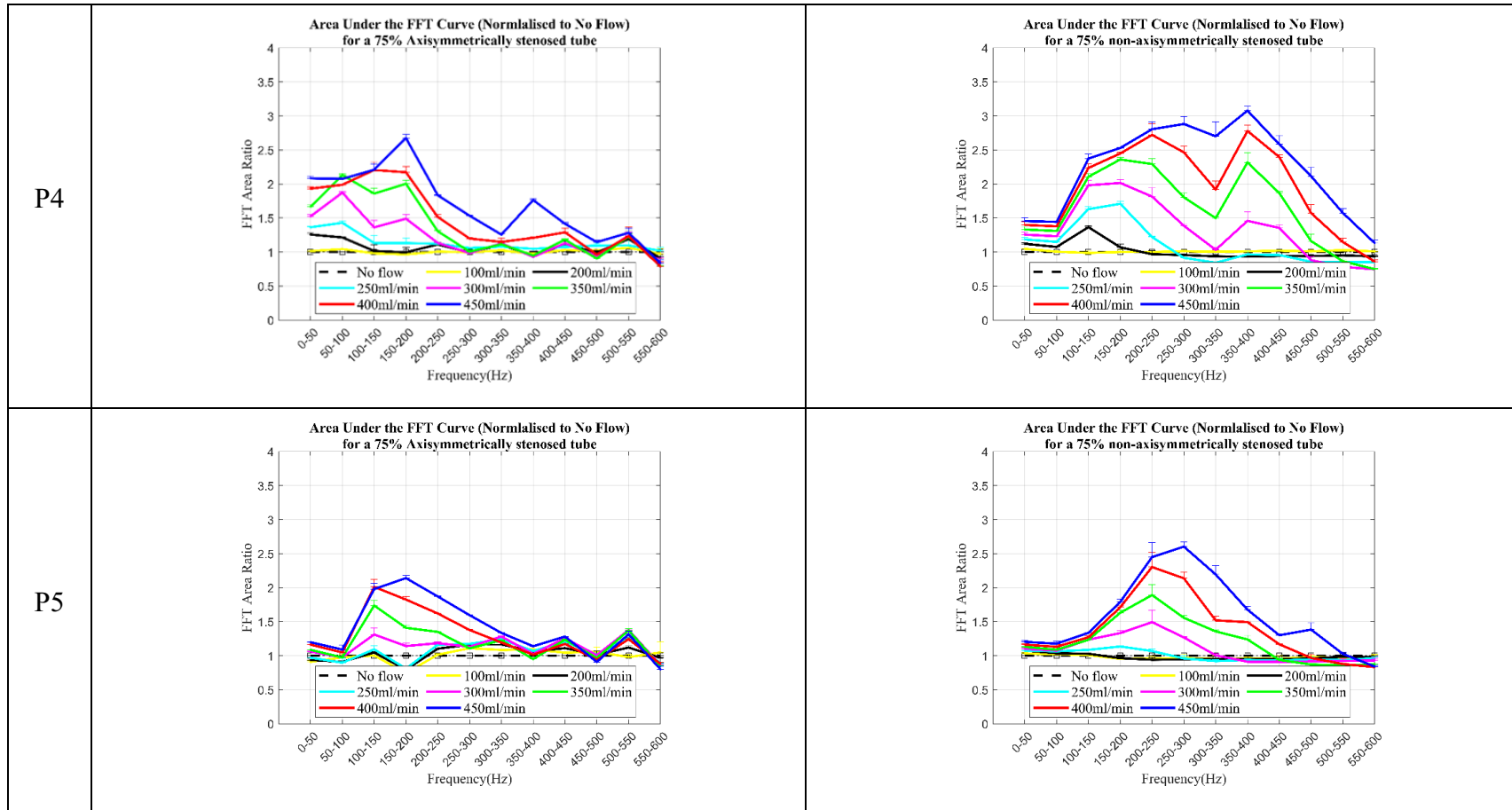
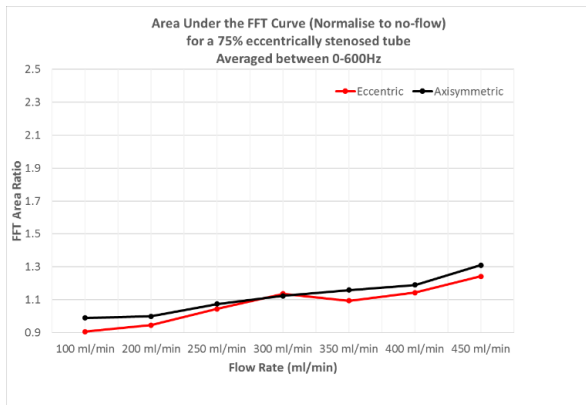
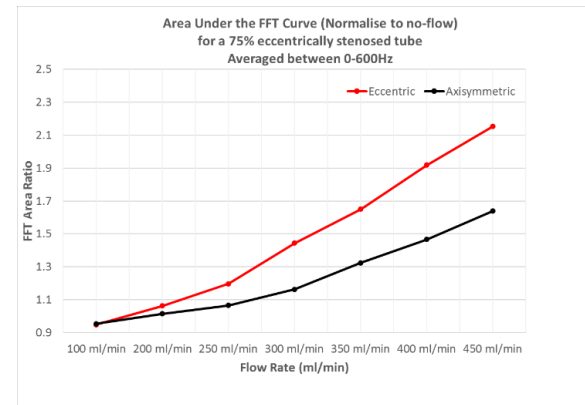


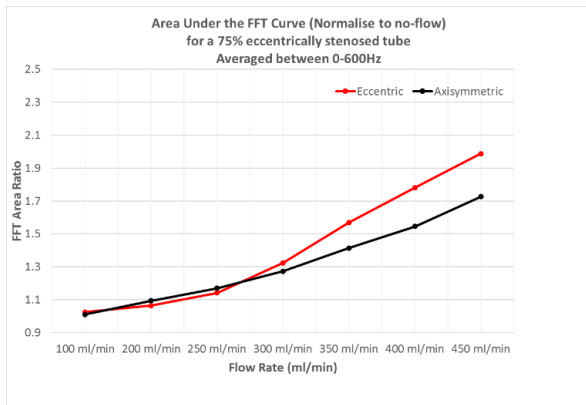
Figure 66: FFT area ratios (normalised to no-flow) for 75% axisymmetrically & non-axisymmetric stenosed bare tubes at P1 (-3cm), P3 (+1.5cm), P4(+3cm) and P5 (+6cm)



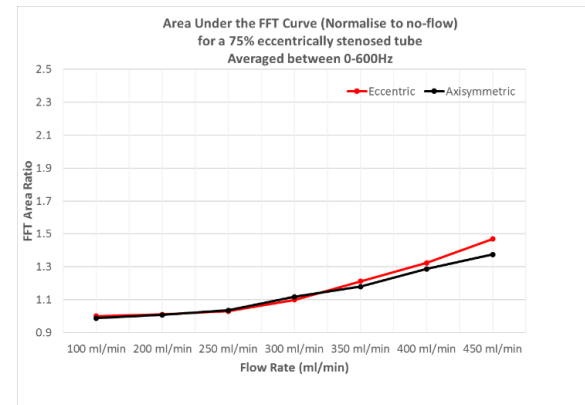
P1 (-3cm Downstream)



P3 (+1.5cm Downstream)



P4 (+3cm Downstream)



P5 (+6cm Downstream)

Figure 67: FFT area ratios (normalised to no flow) for 75% stenosed (axisymmetric (black) and non-axisymmetric (red). Data from bare tubes

lues from this analysis summarised in Table 21, firstly, confirm the dependence of FFT ratios on the flow rates, at all positions. Secondly the gradients at P3 were greater than at P1 as the fluid passed through the stenosis followed by a decrease from P3 to P5 as the fluid travelled further downstream. Finally, the gradients of the regression line at all the downstream positions were higher for the non-axisymmetric case, showing that the effect of increasing flow rate was greater for the eccentric stenosis than for its axisymmetric counterpart.

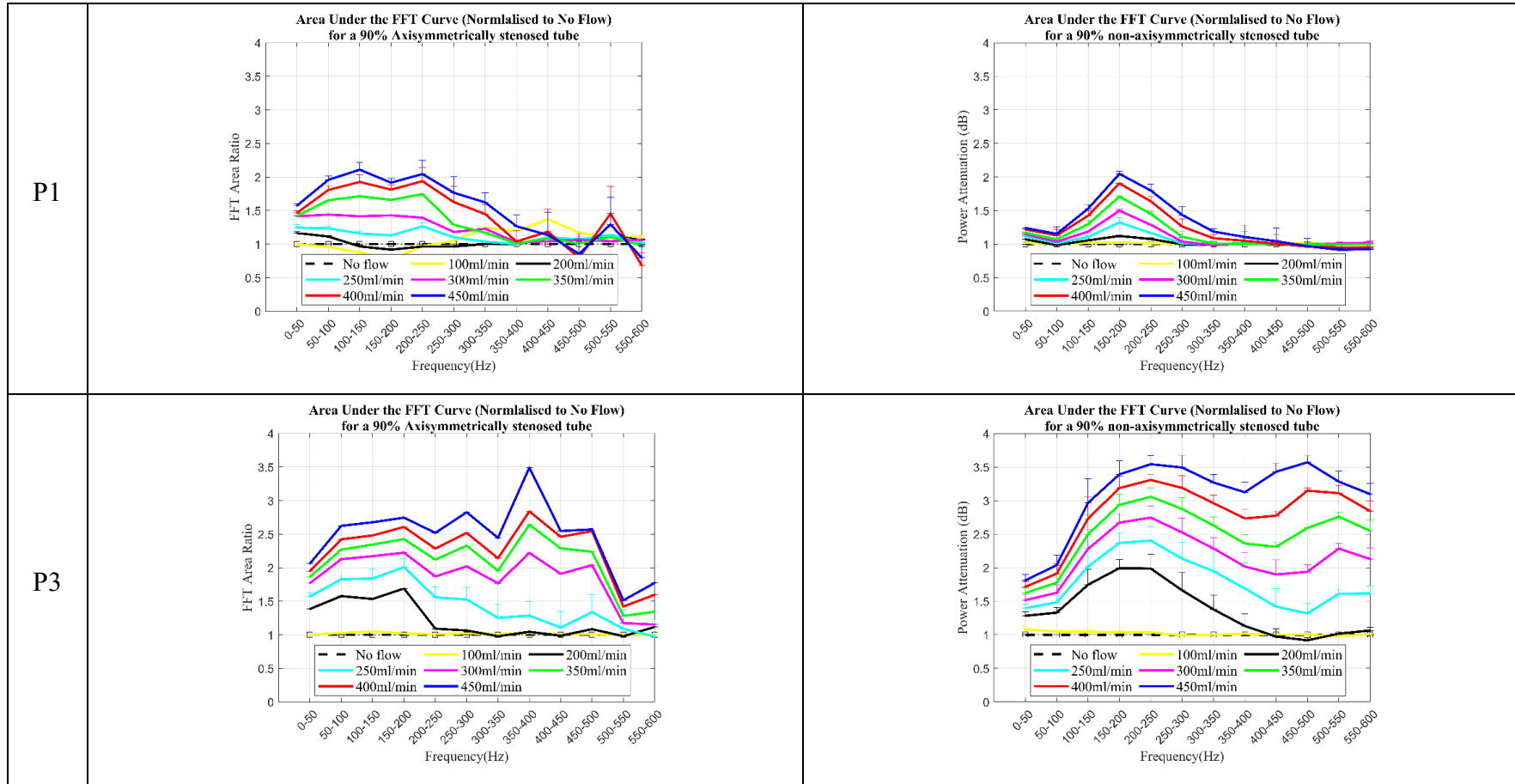
Table 21: Regression analysis of effect of flow rate in a 90% bare stenosed (axisymmetric and non-axisymmetric) tube, with water as perfusing liquid, at P1 (-3cm upstream), P3 (+1.5cm downstream), P4 (+3cm downstream) and P5 (+6cm downstream) positions

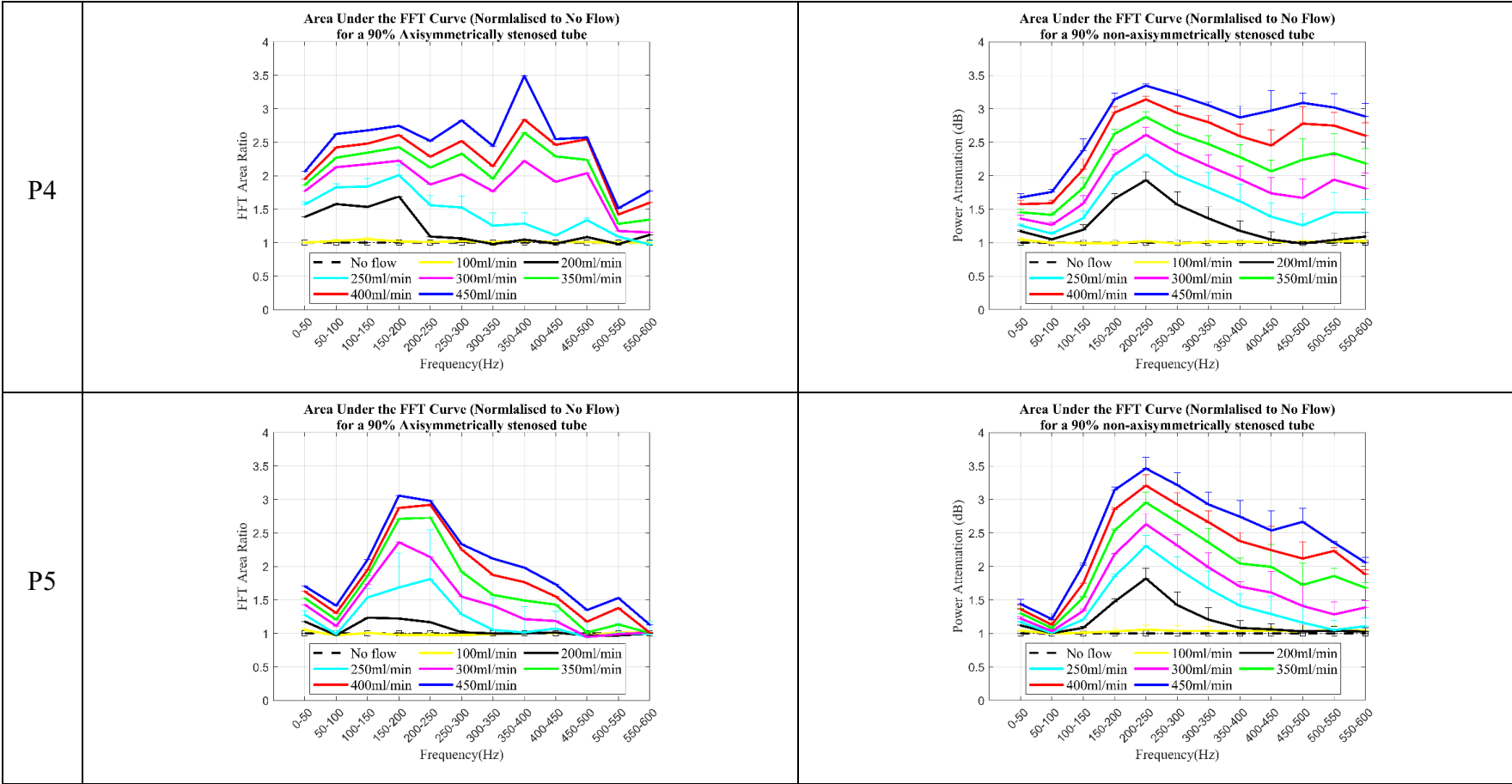
	Gradient of the regression line		R -squared		Significance (p)	
	Axisymmetric	Non-axisymmetric	Axisymmetric	Non-axisymmetric	Axisymmetric	Non-axisymmetric
<b>P1</b>	0.00213	0.00106	0.999	0.988	0.000	0.000
<b>P3</b>	0.00484	0.00573	0.980	0.996	0.000	0.000
<b>P4</b>	0.00470	0.00523	0.993	1.000	0.000	0.000
<b>P5</b>	0.00334	0.00425	0.998	0.999	0.000	0.000

Furthermore, from Figure 68, it can be observed that the difference between the axisymmetric and the non-axisymmetric stenosis is greatest at the P3 position for the 90% case and then the difference reduces at the P4 position before increasing again at the P5 position. However, for the 75% case, the difference is largest at the P3 position after which there is a continuing decrease both at P4 and P5 (where the difference is negligible). This behaviour can be explained as the disturbances introduced by the 90% stenosis were large (for both the axisymmetric and the non-axisymmetric cases) whereas for the 75% case disturbances were generally low for the axisymmetric tube and the introduction of the asymmetry in the stenoses introduced new characteristic peaks (Figure 63 to Figure 66).

As performed for the axisymmetric stenosis, to explore the combined effects of flow rate, stenosis severity and stenosis symmetry, a two-way, between groups ANOVA was performed. The data were divided into three groups, based on flow rates, stenosis severity and stenosis symmetry. The dependent variable in the analysis was the averaged (0-600Hz) area under the FFT curve (normalised to no-flow). The data from the three downstream

Table 22: FFT area ratios (normalised to no-flow) for 90% axisymmetrically & non-axisymmetrically stenosed bare tubes at P1 (-3cm), P3 (+1.5cm), P4(+3cm) and P5 (+6cm)







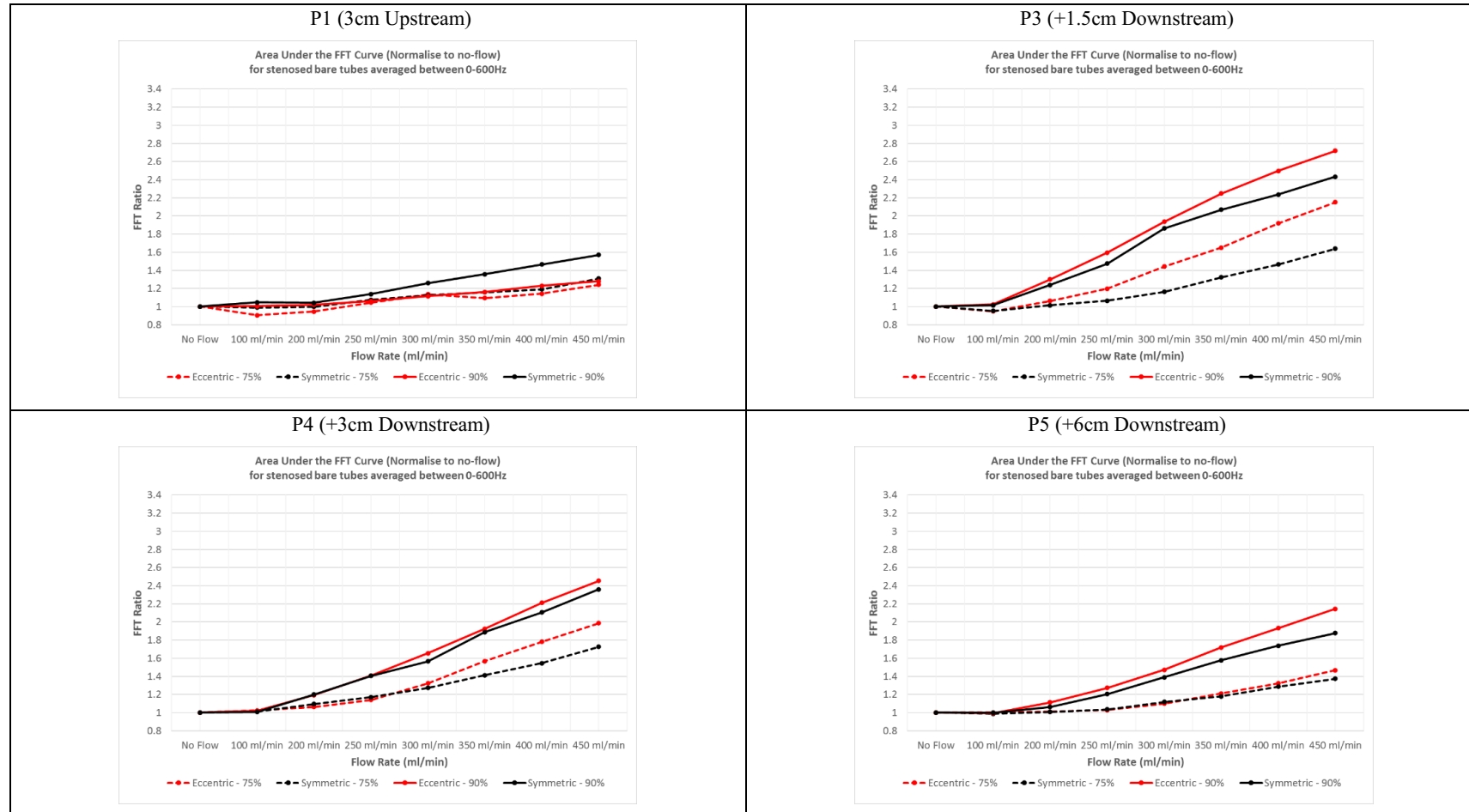


Figure 68: FFT area ratios (normalised to no flow) for 75% & 90% stenosed (axisymmetric and non-axisymmetric) tubes

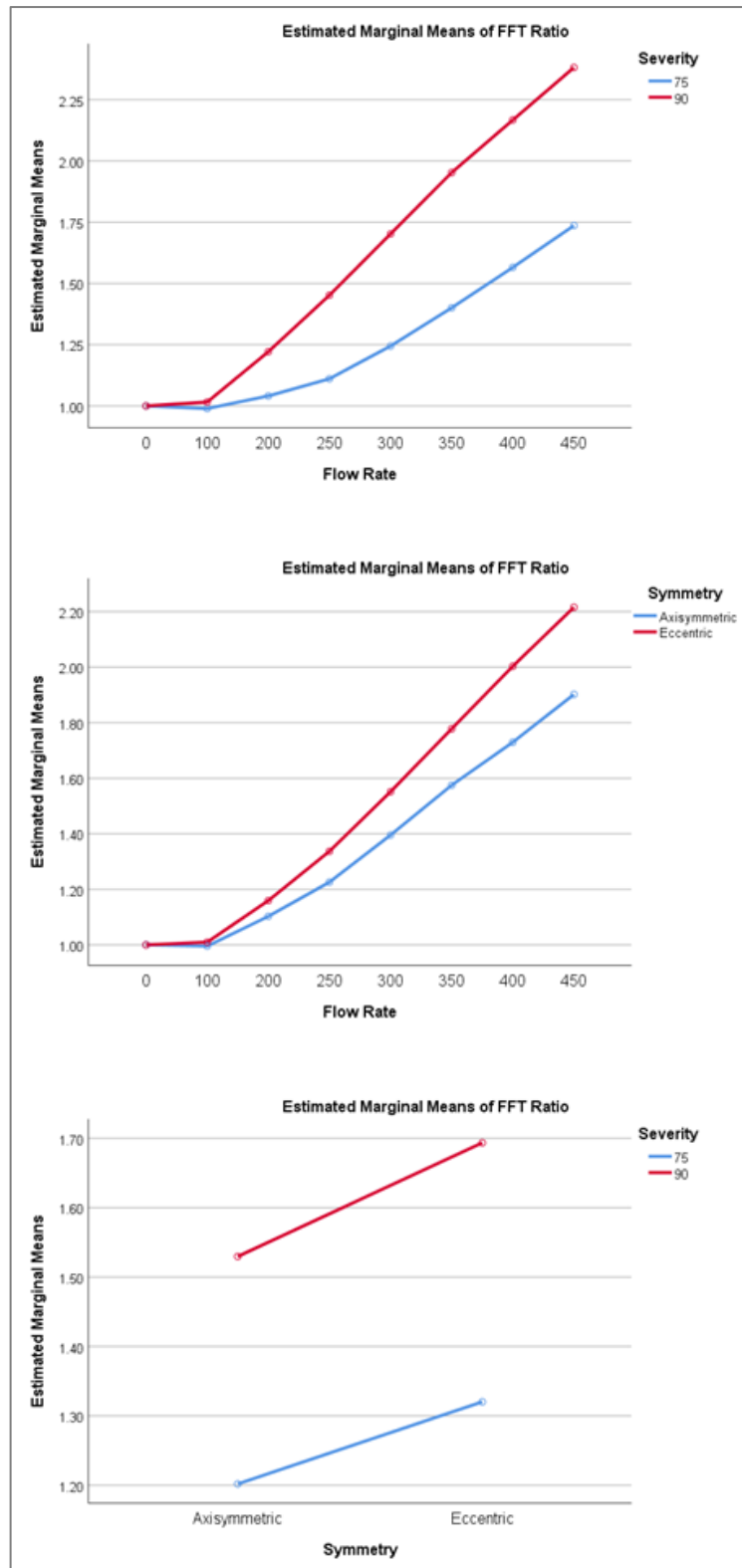


Figure 69: Means of averaged (0-600Hz) areas under the FFT curve (normalised to no flow), calculated from the combined downstream positions, showing the interactions between flow rate (ml/min) & severity, flow rate (ml/min) & symmetry, and symmetry & severity in bare stenosed tube

positions (P3, P4 and P5) were combined to increase the number of degrees of freedom in the analysis. This in turn affected homogeneity of variance (as assessed by Levene's test  $F(64)=2.97$ ,  $p=0.000$ ), however, the variance can be associated with different downstream positions and the combination of data from the three downstream positions and the exclusion of the upstream data can be justified when focussing on the effect of stenosis symmetry, severity and/or the flow rate, as the majority of the disturbances were present in the downstream positions as discussed previously in the axisymmetric case.

The analysis showed that the effects of flow rate ( $F(7,64)=58.81$ ,  $p=0.000$ ), severity ( $F(1,64)=89.8$ ,  $p=0.000$ ) and stenosis symmetry ( $F(1,64)=14.52$ ,  $p=0.000$ ) were significant. The effect of flow rate was the largest, followed by the effect of stenosis severity and symmetry with the partial  $\eta^2$  values of 0.865, 0.584 and 0.185, respectively. The analysis also indicated the significance of the interaction between flow rate & stenosis severity ( $F(7,84)=5.981$ ,  $p=0.000$ ). However, the combined interaction effects of flow rate & symmetry, and severity & symmetry were not significant here ( $p>0.05$ ). The profiles comparing the means of these variables, for all the downstream positions combined, are illustrated in Figure 69, which clearly shows the trends of increasing mean FFT areas with increasing flow rates and increasing severities. Furthermore, it is evident that presence of asymmetry in the stenosis increases the detectable disturbances on the tube surface.

### 3.4. Conclusion

The objectives of the investigation in this chapter were to detect the presence of stenosis induced disturbances at the tube surface using accelerometers, validate the presence of disturbances inside the tube using ultrasound and finally, using LDV, to quantify the effects on these disturbances at varying flow rates, stenosis severities, fluid viscosity, and symmetry. The results showed that the presence of stenosis did have a strong impact on the post-stenotic flow. With increasing flow rate and stenosis severity, the disturbances in the downstream region start to intensify and tend to move closer to the stenosis, over an increased range of frequencies. The pattern was seen using both the accelerometer measurements and the ultrasound scans and is consistent with the findings of others

(Young and Tsai, 1973a; Ahmed and Giddens, 1983; Sadeghi et al., 2011). The investigation with the LDV confirmed these trends. Furthermore, the introduction of asymmetry in the stenosis increased the detectable disturbances in the post-stenosed region, while introducing newer higher frequency flow perturbations.

The literature shows that clinically, stenoses are generally non-axisymmetric with more complex geometries than are modelled here, and the presence of a perfectly axisymmetric stenosis is unlikely (Massai *et al.*, 2012; Moerman *et al.*, 2019; Wang *et al.*, 2019; Strecker *et al.*, 2020). As discussed above, early detection of these stenoses is of great importance. The formation of a jet at the exit of the stenosis gives rise to a low-pressure zone immediately downstream, which causes further strengthening and growth of the flow disturbances (detailed in the introduction chapter). In spite of the simplified geometry of the stenoses investigated here, a comparison of the results (obtained using the LDV device) from axisymmetric and non-axisymmetric stenoses provide a promising basis for the detection of the stenoses in a clinical environment for a variety of flow rates, including those encompassing the physiological mean flow range. Further comparison of the effects of stenosis symmetry on a tube embedded within a phantom is discussed later in section 4.4.2 and the effect of pulsatile flow in chapter 5.

## **4. Steady flow - Flow inside a tube embedded within a neck phantom**

Following the investigation of disturbances generated within the fluid and at the tube surface, the study was extended to address the study's second aim. A simplified neck phantom model was developed to measure the vibrations generated at the skin surface, produced due to the post-stenotic flow-induced disturbances.

This chapter highlights the measurement (using LDV) of skin-surface level disturbances when a steady mean flow was perfused through the tube. Similar to the investigation of a bare tube in chapter 3, the effects (individual and/or combined) of flow rate, stenosis severity, stenosis symmetry and fluid viscosity were examined for the embedded tube.

### **4.1. Effect of stenosis severity and flow rate**

#### **Methods**

A 40:60 glycerine-water solution (section 2.1) was perfused through a Penrose latex tube (section 2.2). The tube was axisymmetrically stenosed for this investigation, with stenosis severities of 0, 60%, 75% and 90% (using 3-D printed stenoses detailed in section 2.3) to mimic a stenosed carotid artery. The tube was then embedded within the ultrasound gel (section 2.4.4), which was covered with skin mimicking material Platilon (section 2.5) to form a standardised neck phantom (section 2.6). A continuous flow circuit was set up as described in section 2.7 (with the programmable piston pump switched off to achieve a physiological steady mean flow ranging from 0-450ml/min). Patches of retroreflective tape (section 2.9.2) were placed (on the Platilon surface) at five positions along the tube length, i.e., P1 (3cm upstream), P2 (vertically above the stenosis), P3 (1.5cm downstream), P4 (3.0cm downstream), and P5 (6cm downstream), as shown in Figure 70. Two repeats of data were recorded at these five positions using the LDV (section 2.9.2) to measure disturbances at the skin surface.

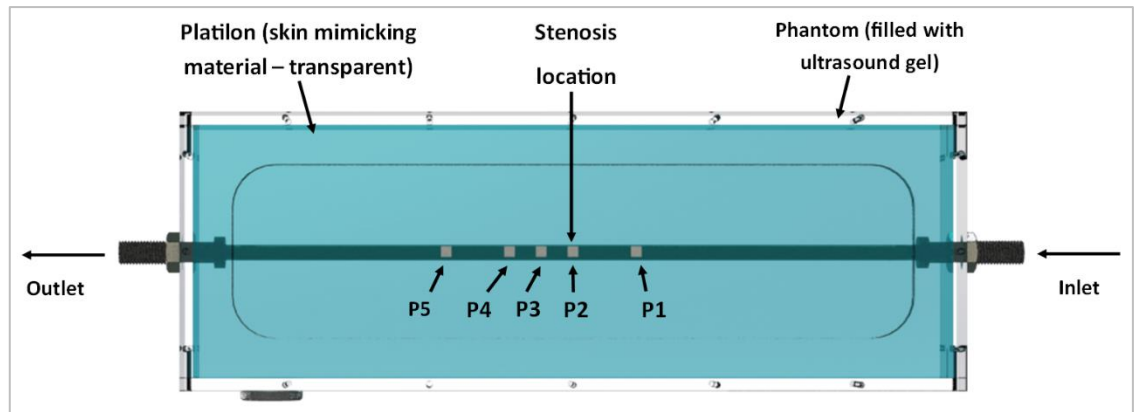


Figure 70: Stenosed embedded tube, with retroreflective patches placed at five positions, i.e., P1 (3cm upstream), P2 (vertically above the stenosis), P3 (1.5cm downstream), P4 (3.0cm downstream), and P5 (6cm downstream) to detect the surface level disturbances using LDV

## Results

The disturbances detected at the skin surface were expected to follow a similar trend to that seen in chapter 3. It was expected that the amplitude of the disturbances and/or their frequency would increase with increasing flow rates as the Reynold's number increases, and the effect would be further amplified as the severity of the stenosis increased.

The data obtained were transformed to the frequency domain using the fast Fourier transform, and calculations of areas under the FFT curves (normalised to the no-flow conditions) were performed as detailed in section 2.8.

Power attenuation spectra for all flow rates and stenoses severities, at each of the five positions, are presented in the Appendix C (section 8.3.3), along with the error bars for the 90% stenosed case (for which most of the stronger signals were seen). An initial comparison of these spectra showed that the effects of flow rate were not apparent at stenosis severities of 0, 60% and 75% at any of the positions and majority of the signal beyond 100Hz was apparently just electronic noise. However, the 90% stenosed case (Appendix C (section 8.3.3) showed a clear distinction, where differences were apparent within the 0-100Hz frequency range and beyond, as the flow rate increased. An extracted sample of this behaviour for a steady mean flow rate of 350ml/min (within the physiological range) is shown below in Figure 71 to Figure 74, which show no immediately apparent trends

for 60 and 75%, however, the 90% case showed an increase in the signal strength as the flow passed through the stenosis towards P3, P4 and P5 positions.

A further detailed analysis was conducted by comparing the respective ratios of the areas under the FFT spectra to reduce the data and smooth out abrupt variations in the spectral power. A common frequency range of 0-50Hz was selected to compare the areas under FFT spectra for the increasing flow rates, for consistency amongst all stenosis severities. The effect at higher frequencies was also investigated and, will be presented later in this section when comparing the effects of stenosis severity in detail in section 4.2.

Figure 75 to Figure 78 present the areas under the FFT spectra (normalised to no-flow conditions) at each of the five positions, for stenosis severities between 0-90%. Non-stenosed to moderately stenosed cases show no apparent trends with the increasing flow rates (Figure 75-Figure 77).

Generally, this well may not be the case when examining patients in clinical environment; however, the lack of any clear-cut trends in the embedded phantoms can be explained as follows. Firstly, for disturbances seen in-vivo, the stenoses are generally not axisymmetric, leading to the generation of highly disturbed flows at even low flow rates and moderate stenosis severities. Secondly, when disturbances are seen in axisymmetric stenoses of low to moderate severity, they are usually detected by looking at the velocity fluctuations inside the tube. However, the stenosed tube here is embedded within a phantom, and the disturbances generated by these stenoses lose energy by dissipation within the gel so that the amplitude of disturbances reaching the Platilon surface is reduced.

Finally, moving towards the highly stenosed tube, i.e., 90% reduction in lumen area, the effects of the increasing flow rates were much more apparent (Figure 78). The area ratios increased with increasing flow rate, and a clear distinction was seen at all downstream positions for flow rates above 300ml/min, which indicates that a certain flow rate is required before the effects of the presence of the stenosis can be identified. The second conclusion drawn from the figures was that the detected disturbances at P5 (6cm downstream) were stronger than those detected at P4 (3cm downstream) and P3 (1.5cm downstream) positions.

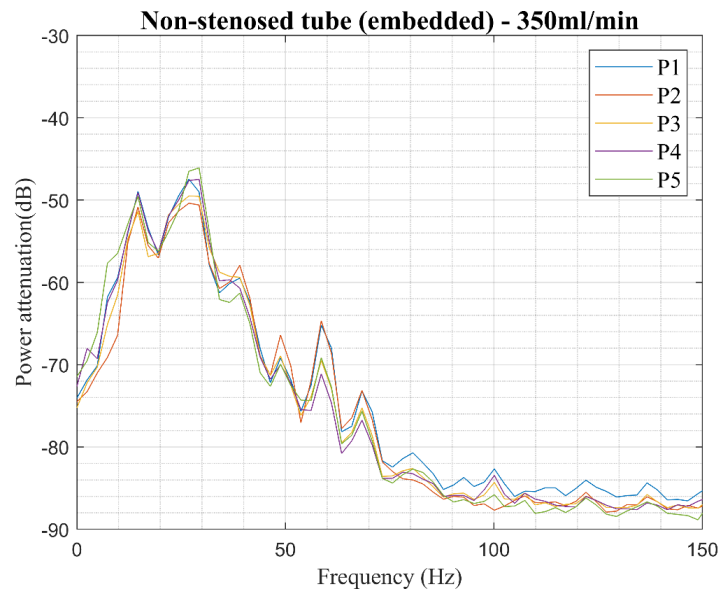


Figure 71: Power spectra for non-stenosed tube (embedded in the phantom) perfused with glycerine-water solution at flow rate of 350ml/min

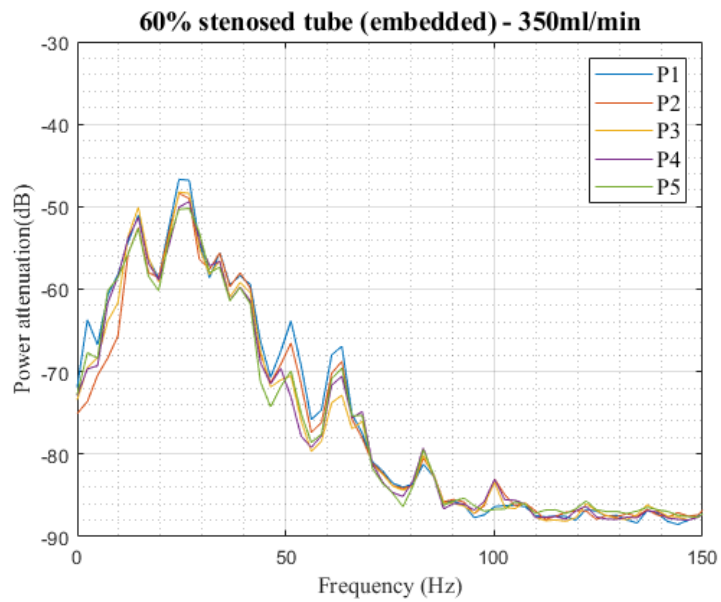


Figure 72: Power spectra for 60% axisymmetrically stenosed tube (embedded in the phantom) per-fused with glycerine-water solution at flow rate of 350ml/min



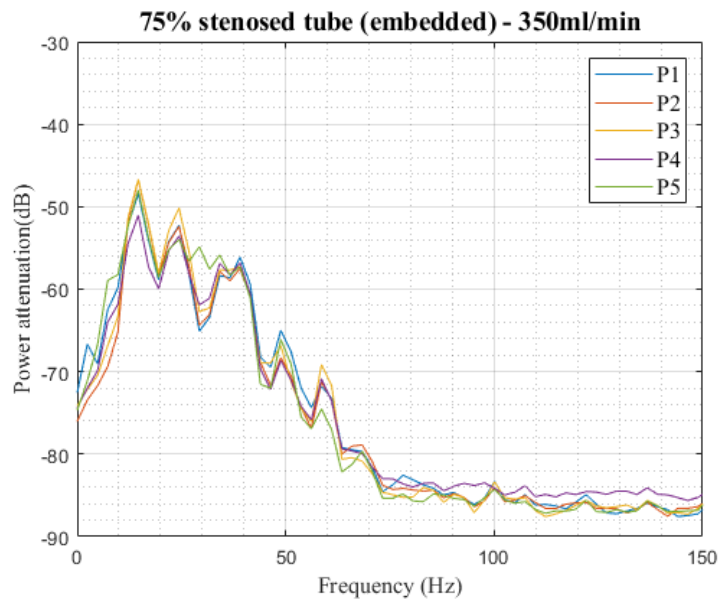


Figure 73: Power spectra for 75% axisymmetrically stenosed tube (embedded in the phantom) per-fused with glycerine-water solution at flow rate of 350ml/min

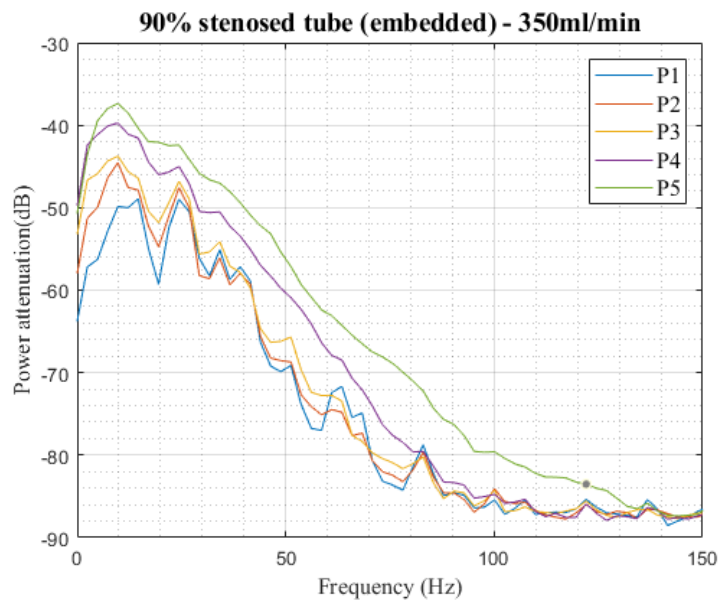


Figure 74: Power spectra for 90% axisymmetrically stenosed tube (embedded in the phantom) per-fused with glycerine-water solution at flow rate of 350ml/min – repeats shown in the Appendix C

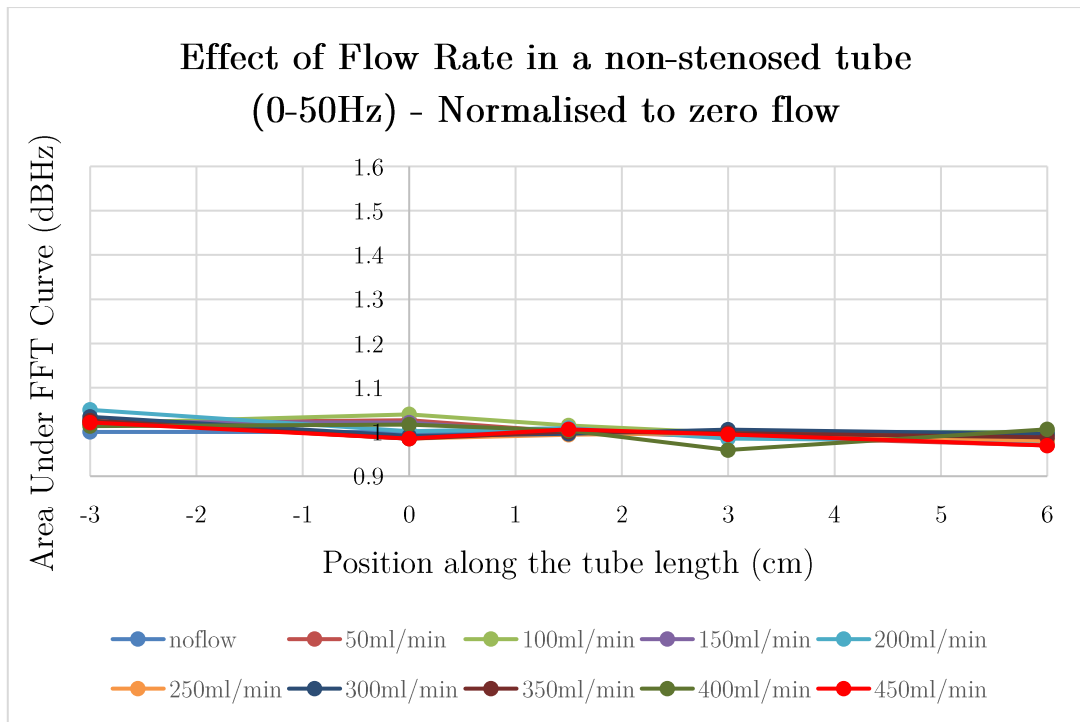


Figure 75: Effect of flow rate on skin movement from a non-stenosed tube embedded in the phantom 6-8mm below the Platilon skin surface. (In this and subsequent figures, the zero position corresponds to a location in the middle of the stenosis)

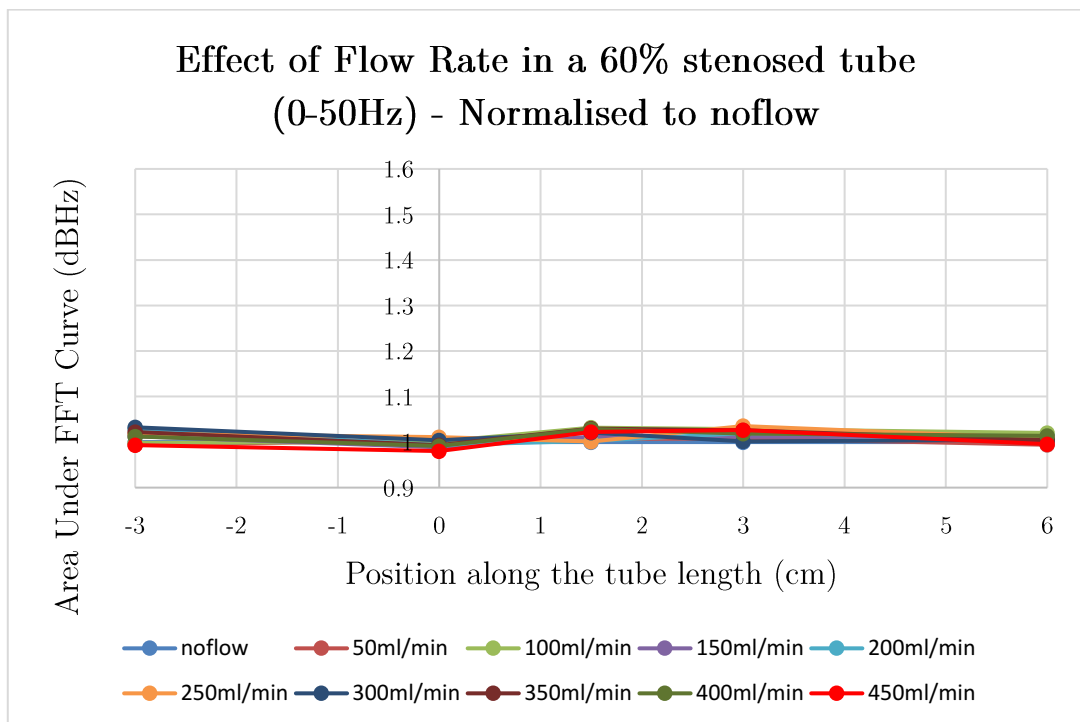


Figure 76: Effect of flow rate on a 60% stenosed tube embedded inside the phantom

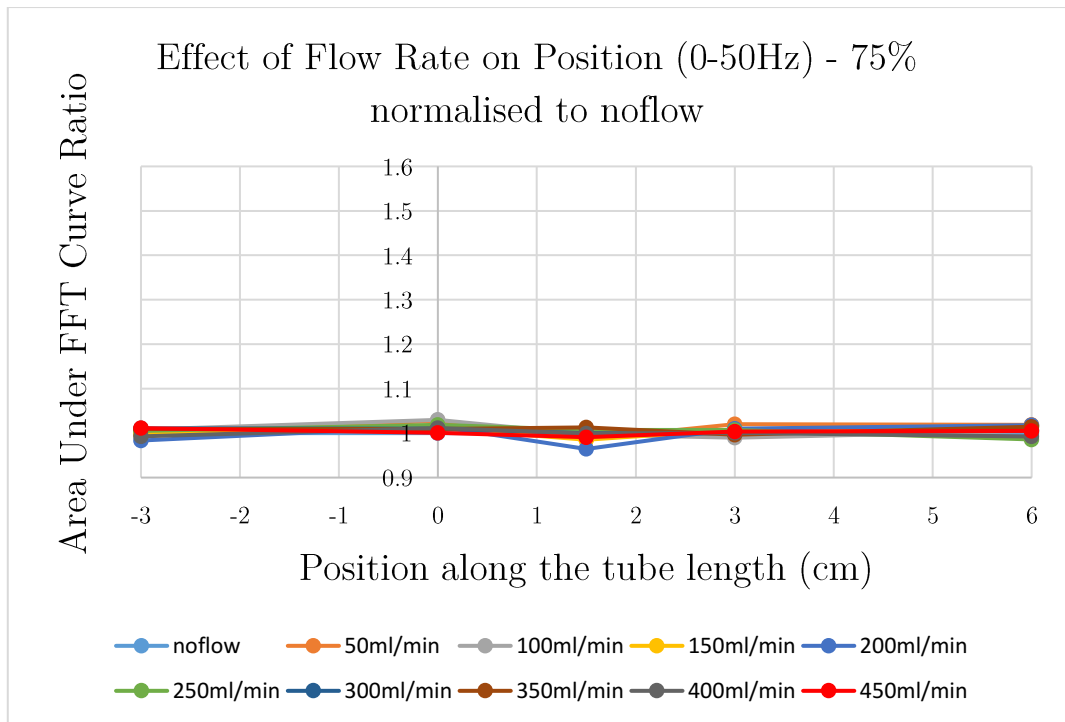


Figure 77: Effect of flow rate on a 75% stenosed tube embedded inside the phantom

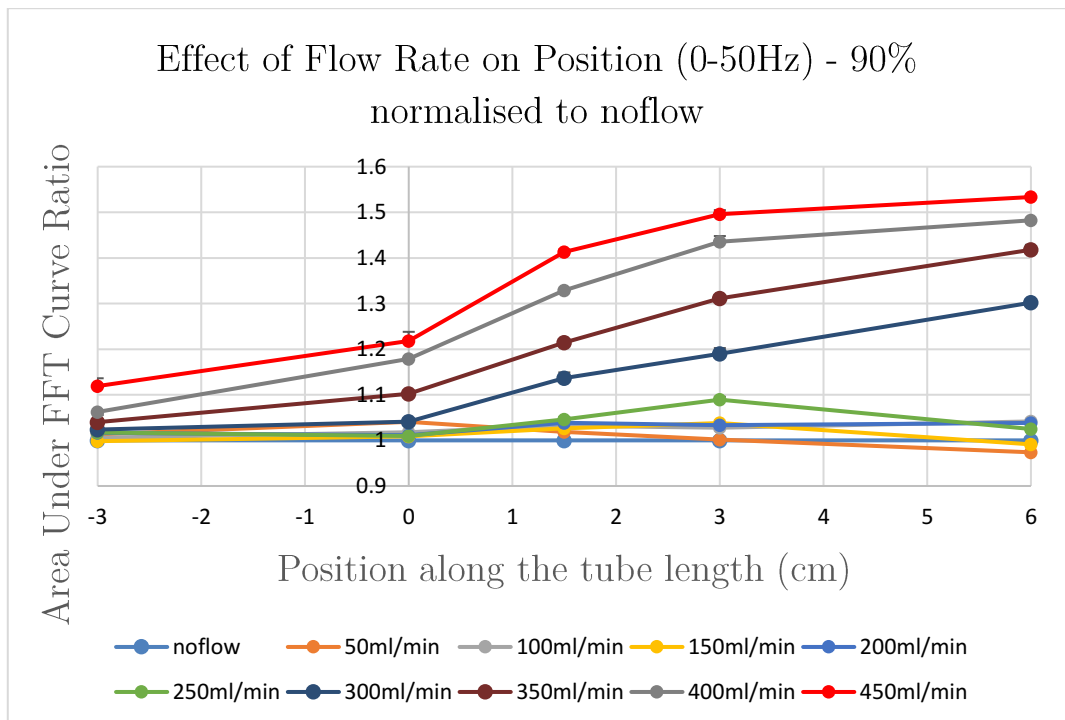


Figure 78: Effect of flow rate on a 90% stenosed tube embedded inside the phantom – small errors bars at -3cm, 0cm, and 1.5cm show small differences between the two repeats

Generally, the positions closest to the stenosis are expected to see the highest disturbances, but this does not seem to be the case here. A slight misorientation of the stenosis in the tube could have impacted the flow in the downstream position. With the axisymmetric stenosis (aligned horizontally), the disturbances detected at the tube wall in the downstream region are caused primarily by the vertical (transverse) component of the vortices in the fluid impinging on the tube's wall.

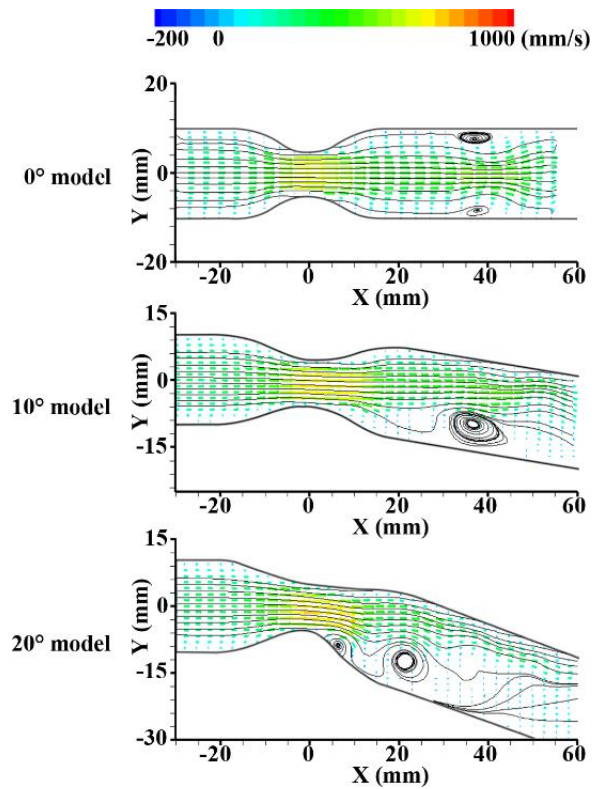


Figure 79: Instantaneous velocity vector fields at  $\phi = 0.5$  (peak inlet velocity) at  $Re = 160$  (Hong *et al.*, 2017)

When an upward tilt is introduced at the exit of the stenosis, the length of the recirculation zone immediately downstream of the stenosis (in the upper part of the tube) decreases with a corresponding increase in a transverse disturbance intensity. However, focusing slightly further downstream, the upwardly tilted jet that is now leaving the stenosis will impinge directly on the tube's upper wall, and it is speculated that the total disturbance here will be larger as it caused by both the transverse and streamwise components of the velocity of the fluid. In such a case, the location of maximum disturbance will depend on the degree of the tilt. A study conducted by (Hong *et al.*, 2017) has shown this impingement phenomenon of fluid on the wall (under pulsatile conditions), when the tube

curves downwards distal to the stenosis. Figure 79 shows that the length of the recirculation zone toward the upper surface of the tube is reduced as the degree of the bend increases. It also implies that a larger fraction of the fluid's momentum will be transferred to the upper wall of the tube as the tilt increases.

We speculate that a similar effect occurs in this study, with the main difference being that exit of the stenosis is bent upwards rather than the tube bending downwards. A brief insight into the effect of flow rate between 50-100Hz is provided in Appendix C (8.3.4).

Since the differences in the ratios of areas under the FFT curves were small for different stenoses severities, statistical analyses were carried out to determine the significance or otherwise of the differences. One-way ANOVA was used in which the variability between groups (due to the independent variable) is compared with the variability within each of the groups (commonly referred to as the error term).

Before conducting any one-way ANOVA, the data were checked against the following six assumptions (Pallant, 2016):

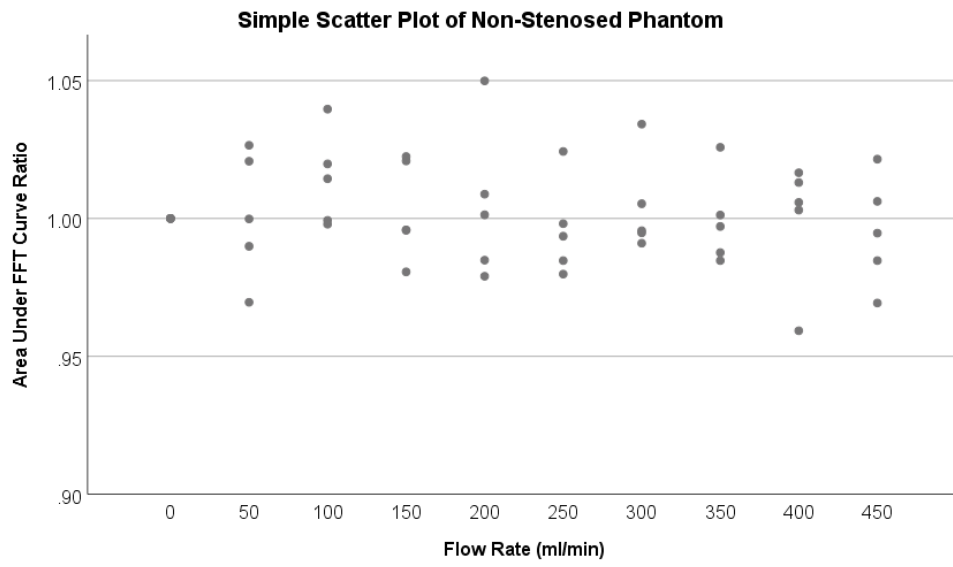
- The dependent variable should be continuous.
- The independent variable should consist of two or more categorical independent groups.
- Independence of observation, i.e., each measurement must not be influenced by another measurement.
- There should be no significant outliers, e.g., significant deviations from the mean value.
- Normal distribution – The dependent variable should be approximately normally distributed for each category of the independent variable. However, one-way ANOVA is quite robust to violations of normality.
- Homogeneity of variance – The variability of measurements for each group is similar; however, this assumption is also reasonably robust to violation provided the groups are of similar size.

For this study, the first three assumptions were met before the analyses as the Area under the FFT curve values are ratios and are continuous, the independent variables consist of two or more groups (e.g., stenosis severities, flow rates, steady vs pulsatile), and finally, the results from one group (e.g., flow rate) are not affected by the results from another flow rate group.

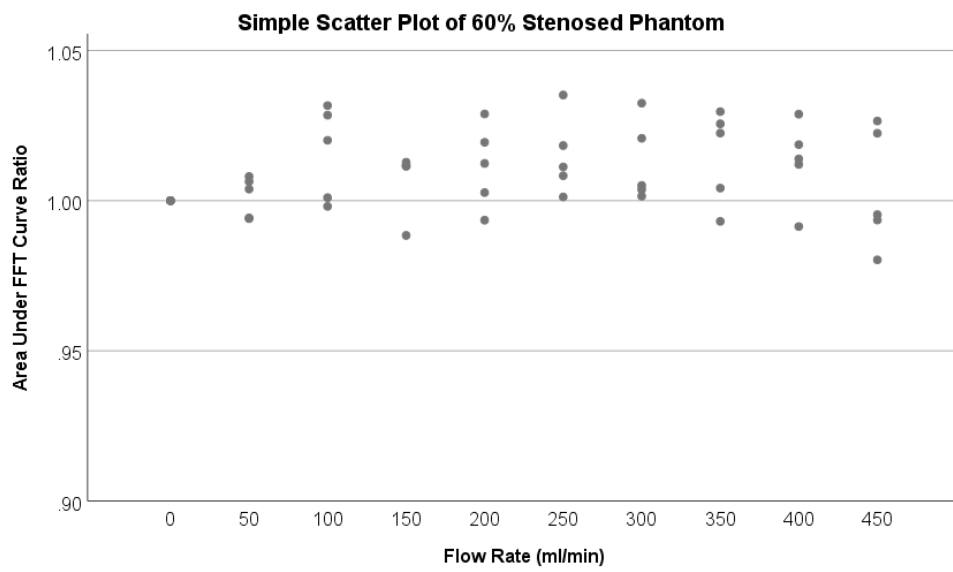
Special consideration was taken for the final three assumptions. Since the amount of data collected for each stenosis and flow rates was limited by the number of data sets collected, data from different (upstream and downstream) positions were combined to increase the number of degrees of freedom. This procedure was adopted when the differences between each position at certain flow rates were small, which was the case for all conditions.

A sample set of data for the flow rate analyses is shown in Figure 80. Each marker at every flow rate in Figure 80 (a, b, c & d) represents the area under the FFT curve ratio value at one of the five measurement positions, and it can be seen that the difference between each of these markers is minimal at all the flow rates and no significant outliers are present, except for the 90% stenosed tube for flow rates above 300ml/min. To confirm this, a box and whisker plot was made (Figure 81), which shows only one outlier for non-stenosed and 75% stenosed case, no outlier for 60% case and four outliers for 90% stenosed case. SPSS programme uses interquartile range (IQR) in such a way that if the values between  $1.5 \times \text{IQR}$  and  $3 \times \text{IQR}$  are treated as outliers and anything beyond  $3 \times \text{IQR}$  extremes (none of which are present in our data).

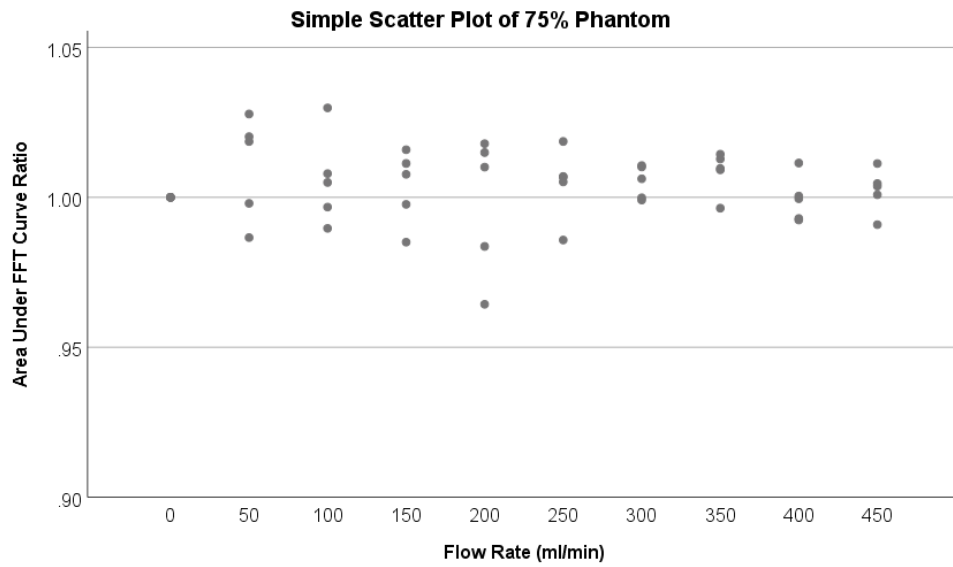
Similarly, a sample set of results from the normality test is shown in Table 23 indicating the normality of the data from different positions for each flow rate and stenosis severity. Skewness and kurtosis were present, but the z-values (defined here as the ratio of skewness [or kurtosis] to the standard error) were between -1.96 and +1.96, apart from a couple of exceptions where the values ranged from -2.1 to +2.4. Hence, it was concluded that the skewness and kurtosis in the data were acceptable (Pett, 2015).



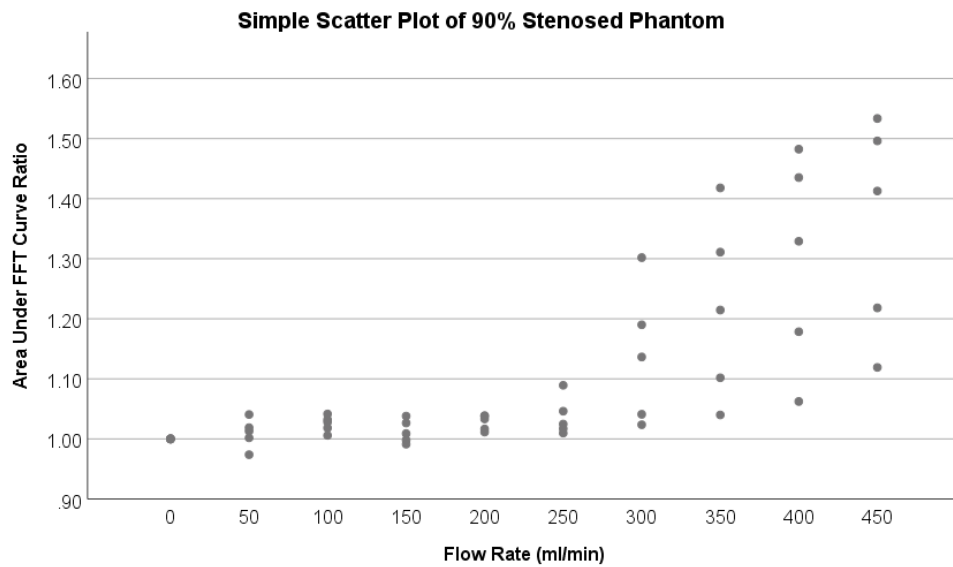
(a)



(b)



(c)



(d)

Figure 80: Comparison of FFT area ratios from all positions combined at (a) no stenosis, (b) 60% stenosis, (c) 75% stenosis and (d) 90% stenosis – Different scales on y-axis are shown to highlight the presence of small differences



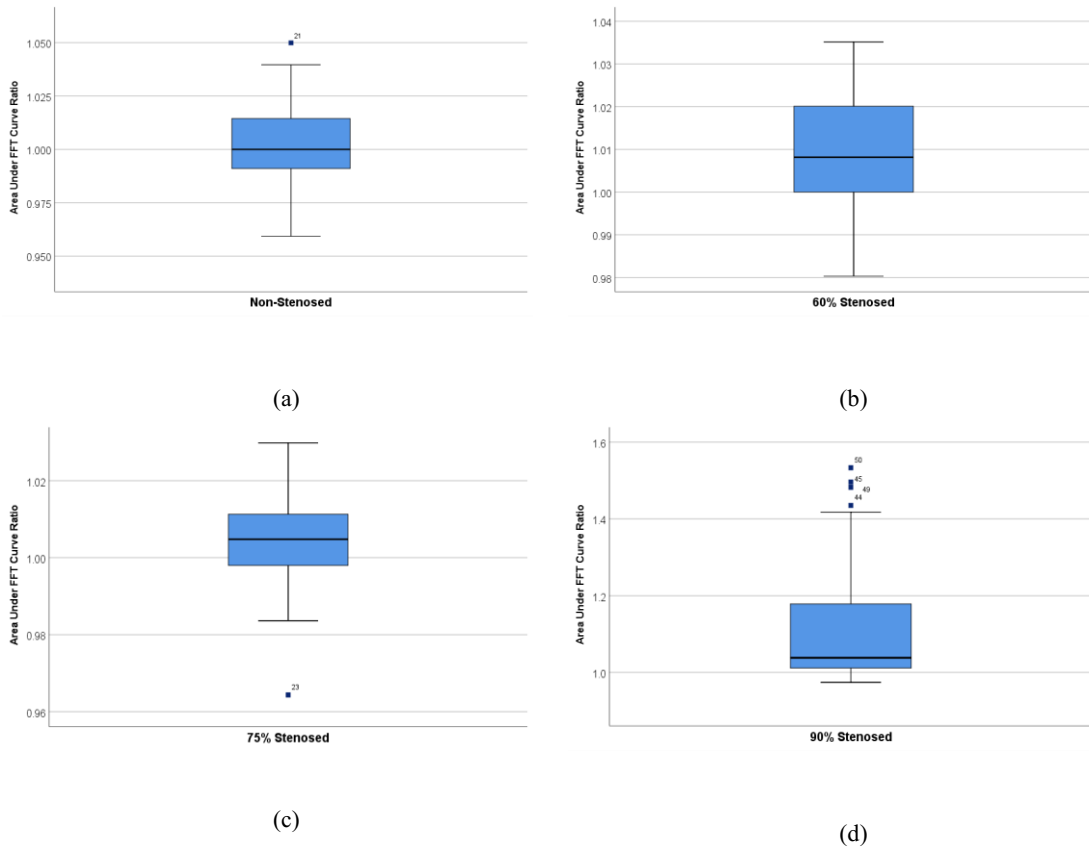


Figure 81: Box and whisker plot to determine the outliers in the data (blue rectangles indicate the two middle quartiles and the small dark blue squares indicate the outliers, with the adjacent number identifying the number of the observation) – Different scales on y-axis are shown to highlight the presence of small differences

Finally, the homogeneity of variance was investigated by determining the Levene’s statistic, which showed significance (p) values of 0.921, 0.681, 0.887 and 0.000004 for 0, 60%, 75% and 90% stenosed tubes, indicating all but 90% stenosed tube data passed this homogeneity assumption. Welch’s ANOVA results were used to determine the significance, where the above assumption failed. (Laerd, 2018).

For the non-stenosed tube, the ANOVA showed no statistically significant differences between the flow rates in the area under the FFT curve ( $F(9,40) = 0.386$ ,  $p = 0.935$ ). Similarly, for the 60% and 75% stenosis the ANOVA showed that no statistically significant differences were present between the flow rates ( $F(9,40) = 1.016$ ,  $p = 0.444$ ) and ( $F(9,40) = 0.493$ ,  $p = 0.871$ ) respectively. Finally, the above-mentioned flow rate effect for the 90% stenosis was supported by the statistical analysis, which showed there was a statistically significant difference ( $F(9,40) = 8.642$ ,  $p = .000$ ), and the post-hoc test show-

Table 23: Sample normality test for the effect of flow rate for all stenosis severities. Figures highlighted in orange indicate significant deviation of the data from the normal distribution

Tests of Normality			
Area Stenosis	Flow Rate (ml/min)	Shapiro-Wilk Statistic	Sig
0	0		
	50	0.952876102	0.757711
	100	0.916371089	0.506805
	150	0.88061731	0.312118
	200	0.895261986	0.384255
	250	0.895884454	0.387559
	300	0.788617235	0.065237
	350	0.883051237	0.323367
	400	0.764581766	0.040391
	450	0.986287323	0.937764
60%	0		
	50	0.831716	0.143293
	100	0.869562799	0.264658
	150	0.599653289	0.00062
	200	0.989450524	0.977734
	250	0.936015528	0.637923
	300	0.8473437	0.186267
	350	0.885832889	0.336583
	400	0.932974106	0.616788
	450	0.887764995	0.372861
75%	0		
	50	0.903497333	0.429516
	100	0.933985173	0.623787
	150	0.932950925	0.616627
	200	0.85895973	0.224537
	250	0.882659018	0.321535
	300	0.853869032	0.207061
	350	0.817735183	0.112148
	400	0.882684108	0.321652
	450	0.983631566	0.92297
90%	0		
	50	0.98015354	0.935439
	100	0.982870675	0.94937
	150	0.946645419	0.713215
	200	0.837697005	0.158656
	250	0.874468133	0.28499
	300	0.937366874	0.647387
	350	0.970150735	0.87622
	400	0.941550925	0.676923
	450	0.943355571	0.67489

Table 24: One-way ANOVA – (p-value analysis to assess the effect of flow rate) - Green shading indicates a significant difference

	Flow Rate (ml/min)	p-value			
		0	60%	75%	90%
Com- pared to no-flow (0)	50	1.000	1.000	0.949	1.000
	100	0.974	0.677	0.999	1.000
	150	1.000	0.997	1.000	1.000
	200	1.000	0.934	1.000	1.000
	250	1.000	0.750	1.000	1.000
	300	1.000	0.880	1.000	0.494
	350	1.000	0.740	0.985	0.044
	400	1.000	0.867	1.000	0.001
	450	1.000	1.000	1.000	0.000

ed the statistically significant differences were present for flow rates above 350ml/min as highlighted in green in Table 24. Similar to the flow rate analyses, data from different positions were combined to maximise the degree of freedom for the ANOVA.

#### 4.2. Effect of stenosis severity at high flow rates

The analysis conducted in section 4.1 indicated that the effects of stenosis severity were significant at the higher flow rates only. Therefore, to understand the effects of stenosis severity further, a physiological flow rate of 350ml/min was investigated. Furthermore, the effects were also explored at the highest flow rate used in this investigation (i.e., 450ml/min).

FFT spectra, for the physiological flow rate of 350ml/min, at the P3, P4 and the P5 positions are shown below (Figure 82-Figure 84). Firstly, an unusual peak at around 30Hz for the non-stenosed cases was observed at all positions. Secondly, it is evident from these figures that prominent effects of stenosis severity start to appear within the first 100Hz of the spectrum at the P3 position (Figure 82). Fluctuations were seen at multiple frequencies

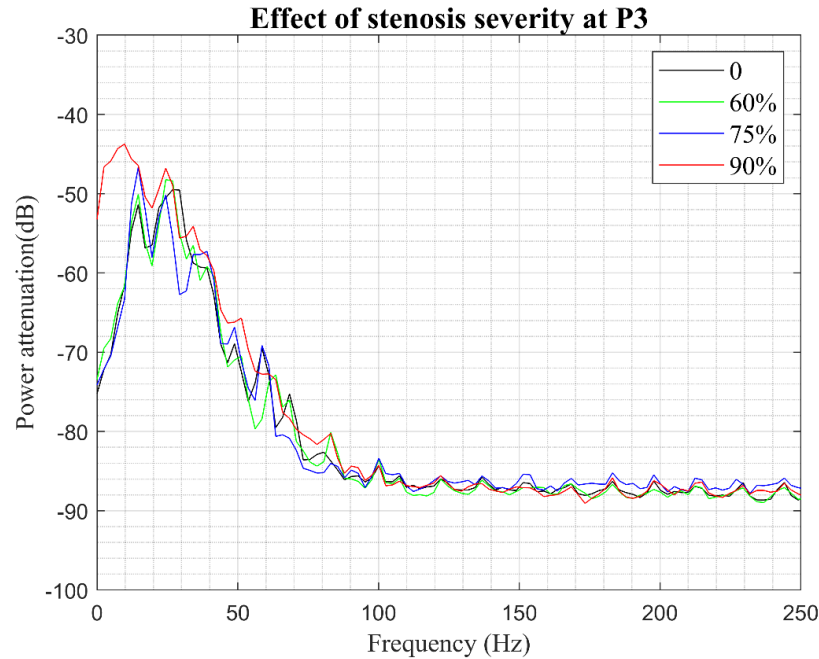


Figure 82: Power spectra, at the P3 position (1.5cm downstream of the stenosis) for axisymmetrically stenosed tube (embedded in the phantom) perfused with glycerine-water solution at flow rate of 350ml/min

at this position; however, the presence of the trend between 10-20Hz and 40-50Hz, where the signal's power increases with the increasing stenosis severity, is worth noting. The effect of stenosis severity was amplified further downstream at P4 (Figure 83) and P5 (Figure 84) positions, as the amplitude increased, and the disturbances spread over an increased range of frequencies. For an increased stenosis severity (i.e., 90%), the higher frequency disturbances were seen as expected, and the behaviour is in line with a recent study (Zhu, Seo and Mittal, 2019). The reason for stronger disturbances detected further downstream of the stenosis has been mentioned earlier in section 4.1, which was speculated to be a tilt in the orientation of the stenosis.

Further analysis of ratios of the areas under the FFT spectra was conducted. In this case, as the effects were apparent at frequencies beyond the first 50Hz, therefore, the areas under the FFT spectra were compared for two frequency bands, i.e., 0-50Hz and 50-100Hz, to encompass the major prominent features. The non-stenosed tube was set as the reference here to compare the effects of other stenosis severities. Therefore, the data used here was normalised to the non-stenosed condition rather than the no-flow condition.

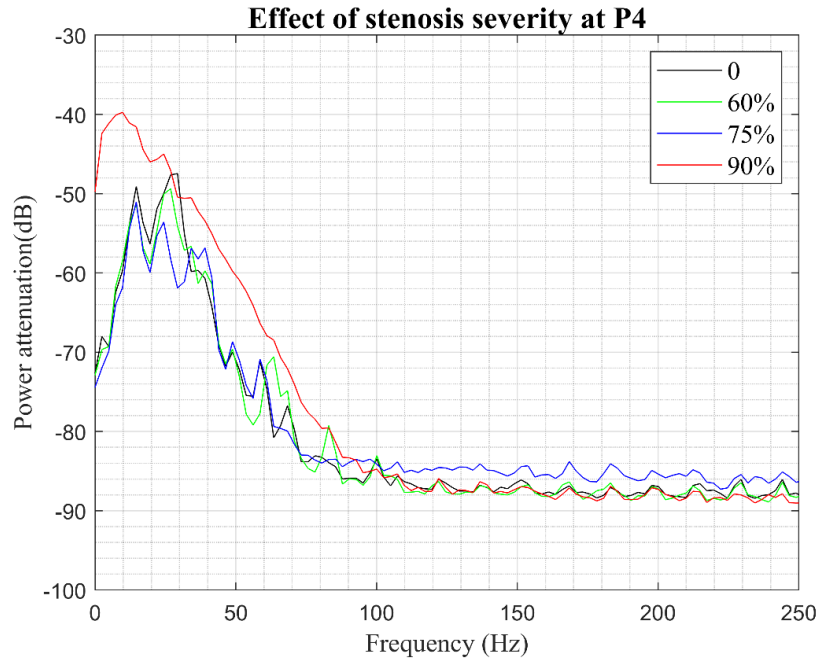


Figure 83: Power spectra, at the P4 position (3cm downstream of the stenosis) for axisymmetrically stenosed tube (embedded in the phantom) perfused with glycerine-water solution at flow rate of 350ml/min

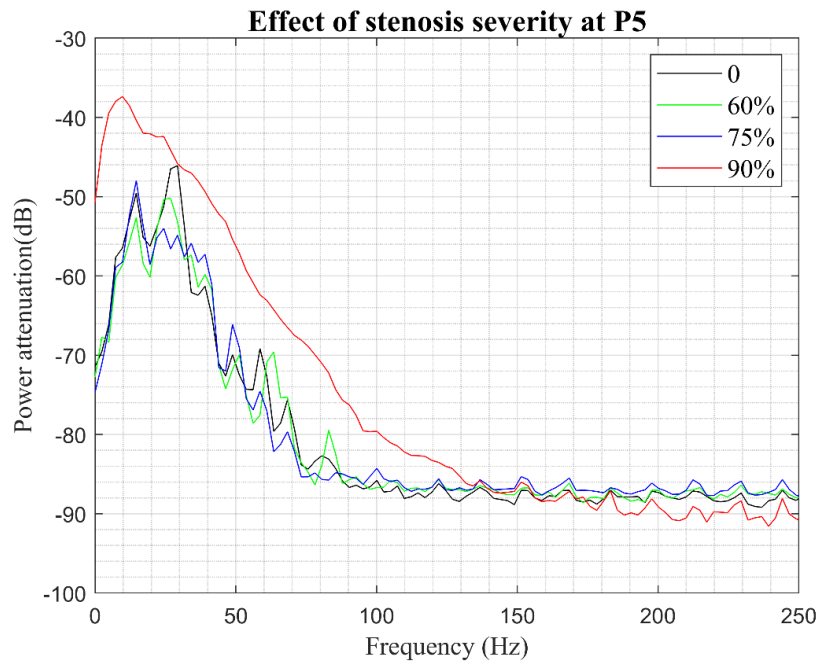


Figure 84: Power spectra, at the P5 position (6cm downstream of the stenosis) for axisymmetrically stenosed tube (embedded in the phantom) perfused with glycerine-water solution at flow rate of 350ml/min

The results from this procedure are summarised in Figure 85 to Figure 88. At the physiological mean flow rate of 350ml/min, it can be seen from Figure 85 and Figure 86 that for both frequency bands, the effect of introducing the 60% stenosis was minimal with fluctuations between +/-3% in comparison to the non-stenosed case.

Similarly, for the 75% stenosed tube, Figure 85 and Figure 86 show no appreciable disturbances, aside from that at the 3cm downstream location (with fluctuations within +/- 6%). Since the area ratios for both the 60% and 75% stenosed tube are small (and less than 1 in some cases), it is not obvious if these small differences are associated with stenosis severity. Hence ANOVA was carried out to determine the statistical significance of these results (see below).

Finally, for the 90% stenosed tube, in the 0-50 Hz frequency range (Figure 85), some disturbances were seen at P1 (3cm upstream) and P2 (vertically above the stenosis) positions. The presence of disturbances at these positions is speculated to be due to the energy of the downstream disturbances being transmitted to the upstream position through the tube wall, ultrasound gel and the Platilon skin material.

This severe stenosis had a clear effect at the other positions as well. An increase of 18% in relative area under the FFT curve was seen at the P3 (1.5cm downstream) position, which increased to 27% as it approached the P4 (3cm downstream) and P5 (6cm downstream) positions. A similar trend was seen in Figure 86 for the 50-100Hz frequency band. Compared to the 0-50Hz range, the main difference was that the area ratios were higher, indicating an even stronger effect at the P4 (3cm downstream) position, which continued to increase towards the P5 position.

As mentioned earlier, the effect of stenosis severity was investigated in more detail at two different flow rates. The FFT spectra comparing the two flow rates are shown in Appendix (8.3.3), where it is clear that the frequencies of the disturbances produced an increase, as discussed earlier in section 4.1. The findings from the 450ml/min flow rate are summarised in Figure 87 & Figure 88, which compares the results shown in Figure 85 and Figure 86 for the 350 ml/min flow rate.

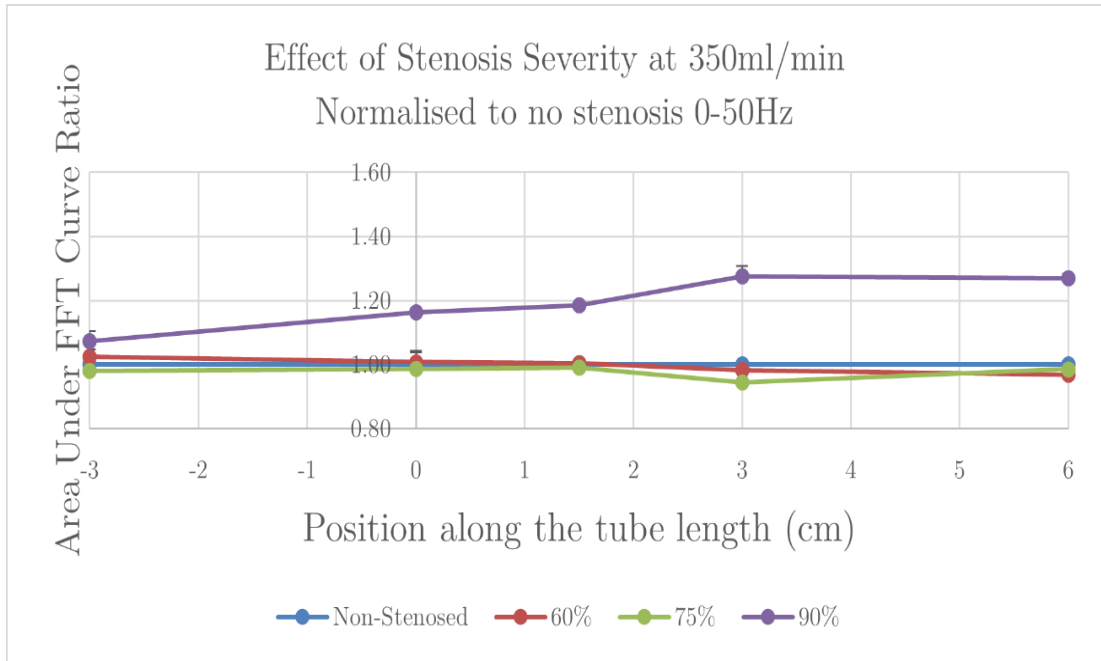


Figure 85: Effect of stenosis severity at 350ml/min mean flow rate (0-50Hz) for axisymmetrically stenosed tube (embedded in the phantom) perfused with glycerine-water solution

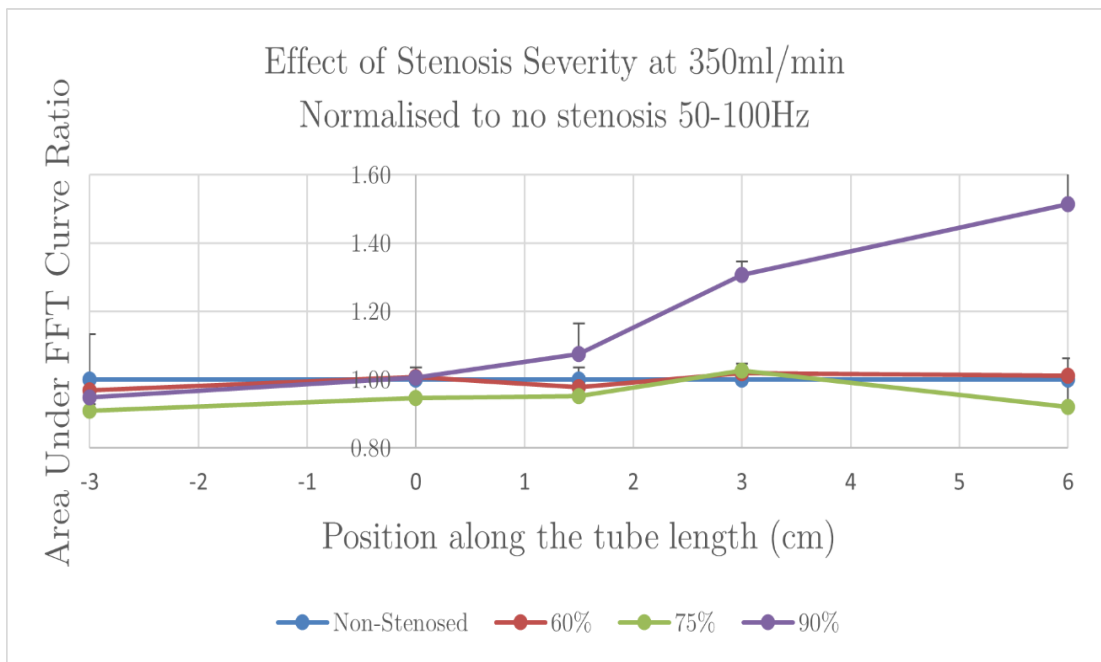


Figure 86: Effect of stenosis severity at 350ml/min mean flow rate (50-100Hz) for axisymmetrically stenosed tube (embedded in the phantom) perfused with glycerine-water solution

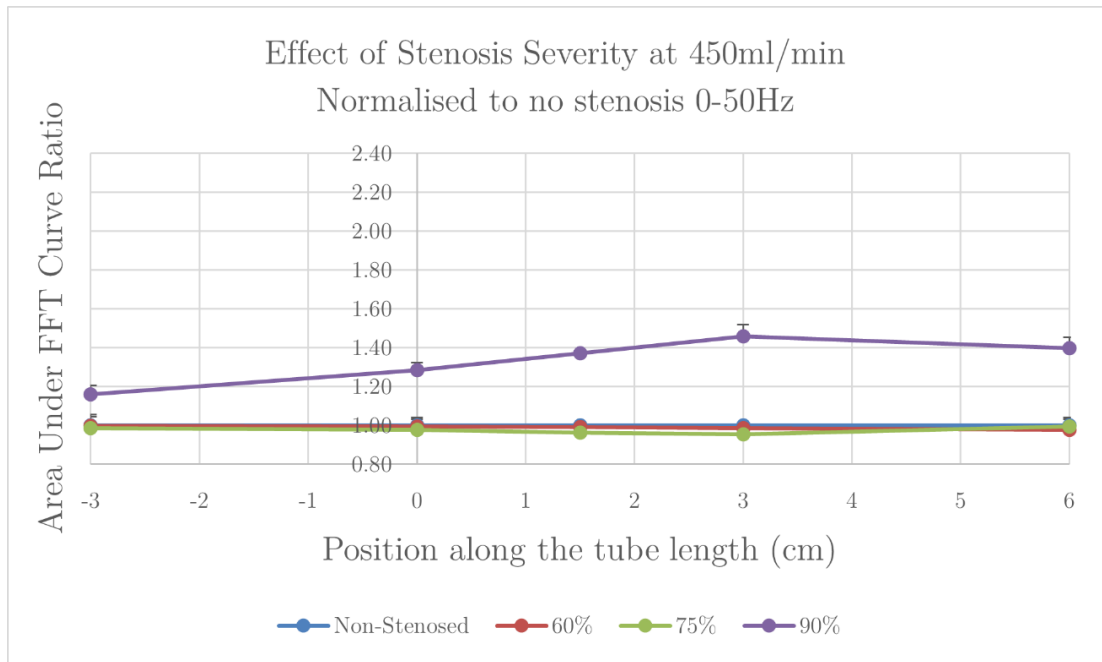


Figure 87: Effect of stenosis severity at 450ml/min mean flow rate (0-50Hz) for axisymmetrically stenosed tube (embedded in the phantom) perfused with glycerine-water solution

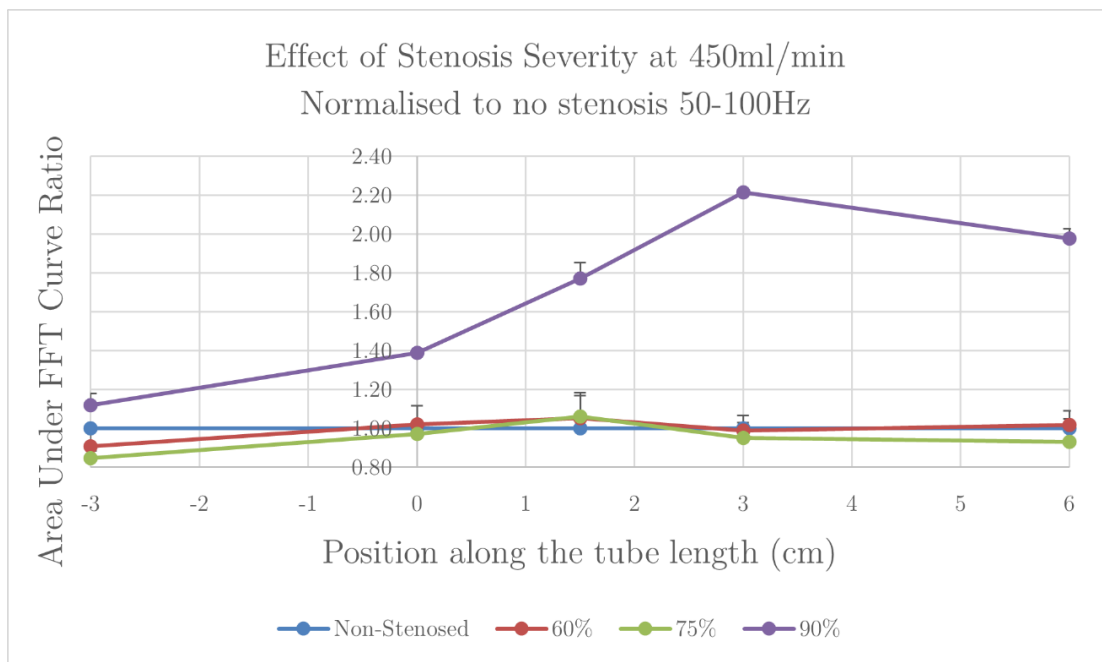


Figure 88: Effect of stenosis severity at 450ml/min mean flow rate (50-100Hz) for axisymmetrically stenosed tube (embedded in the phantom) perfused with glycerine-water solution



While comparing the results from the 0-50Hz frequency band (with the 50-100Hz frequency band) for the 90% stenosed tub (Figure 85 & Figure 87), the trend was similar for both 350ml/min and 450ml/min since in both cases, a gradual increase in the area ratio was seen up to the P4 (3cm downstream position), after which there was a small drop at the P5 (6cm downstream) position. It can further be seen that with the increase in flow rate, the effect of the stenosis severity was amplified at all the corresponding positions. This is in line with the ultrasound scans shown earlier in (section 3.2), which indicated that the disturbances started to appear closer to the stenosis for increasing flow rates and generally started to disappear as the fluid travelled further away from the stenosis.

Next, the results from the 50-100Hz frequency band were compared (with the 50-100Hz frequency band) in Figure 86 and Figure 88. A weak disturbance was seen at the P3 (1.5cm downstream) position for 60% and 75% stenoses, at 450ml/min, which was absent at 350ml/min. With the 75% stenosis, the area ratio at the P3 position increased by 11 %, whereas with the 90% stenosis, the area ratios at P3 and P4 increased by 65% and 70%, respectively.

As discussed above, the effect of flow rates starts to have a significant effect on the area ratio above 350ml/min; thus, it was important to establish when the effects of stenosis severity were significant. Since the difference in area ratio values for low to moderately stenosed tubes was small, it was important to determine whether these differences were statistically significant. Hence, a one-way ANOVA was carried out on a range of flow rates with stenosis severity as the independent variable. The results are summarised in Table 25, and highlighted in green where statistically significant.

Table 25: ANOVA (effects of stenosis severity within each flow rate)

Flow Rate (ml/min)	F value	p-value
150	0.943	0.443
250	1.923	0.167
350	26.502	0.000
450	43.930	0.000

The analysis showed statistically significant differences for flow rate rates above 350ml/min. A Tukey post-hoc test was then carried out to identify where the individual differences lay in terms of stenosis severities. The post-hoc results are summarised in Table 26 (a & b), which shows that all the significant differences (highlighted in green) were seen with the 90% stenosis at flows above 350ml/min.

Table 26: p- values from ANOVA showing statistical significance of effect of stenosis severity at two flow rates

Severities compared against

Fixed severities	<b>350 ml/min</b>	<b>0</b>	<b>60%</b>	<b>75%</b>	<b>90%</b>
	0	-	-	-	-
	60%	1	-	-	-
	75%	0.844	0.877	-	-
	90%	0.000	0.000	0.000	-

(a)

Severities compared against

Fixed severities	<b>450 ml/min</b>	<b>0</b>	<b>60%</b>	<b>75%</b>	<b>90%</b>
	0	-	-	-	-
	60%	0.993	-	-	-
	75%	0.906	0.978	-	-
	90%	0.000	0.000	0.000	-

(b)

### 4.3. Effect of Frequency and Position

From the investigation of the effects of different flow rates and stenosis severities, it was observed that the normalised FFT area ratios at different frequency bands and positions along the tube varied in a complex manner. To determine the statistical significance of these differences, an ANOVA was conducted.

For determining the effect of position, the data from only 90% stenosis were used for the ANOVA and that too for flow rates above 300ml/min, since they showed prominent differences in the earlier post-hoc analysis Table 25. The ANOVA revealed statistically

significant differences between the positions [ $F(4,15) = 9.236, p = 0.001$ ], highlighted in green in Table 27. It can be seen that the FFT area ratios are statistically significantly different at the 3cm and 6cm downstream position, when compared to 0cm position. This is in line with Figure 85 through to Figure 88 which showed maximum disturbance at those two positions.

Table 27: p-values related to the effect of position (Tukey post-hoc test)

		Position compared against				
		-3cm	0	1.5cm	3cm	6cm
Fixed position	-3cm	-	-	-	-	-
	0	0.839	-	-	-	-
	1.5cm	0.064	0.344	-	-	-
	3cm	0.007	0.048	0.760	-	-
	6cm	0.001	0.006	0.217	0.825	-

Although the results for the 1.5cm position do not differ significantly from those obtained at the other positions, it was seen from the ultrasound scans on the bare tube (section 3.1.1) that the disturbances near the 1.5cm positions are strong. The lack of statistical significance at this position can be explained by the speculated tilt in the stenosis as discussed earlier, and the dissipation of energy in the gel before it reaches the skin surface. Furthermore, the displacement detected at the gel surface could also be a result of waves generated by a combination of disturbances from different positions, and not only by the position vertically beneath it.

As with the positional study, ANOVA was carried out using the data only from the 90% stenosed tube at flow rates above 300ml/min, at the three downstream positions (1.5cm, 3cm and 6cm). The results (p-values) from the post-hoc Tukey tests for difference between frequency bands are summarised in Table 28, where the cells highlighted in green indicate statistically significant effects. The results show that statistically significant differences were present between the frequency bands [ $F(5,282) = 3.515, p = 0.004$ ], [ $F(5,282) = 3.564, p = 0.003$ ], [ $F(5,282) = 11.387, p = 0.000$ )] for the P3 (1.5cm downstream), P4 (3cm downstream) and P5 (6cm downstream) positions, respectively.

Table 28: p-values signifying the effect of frequency (post-hoc Tukey analysis) at three positions 1.5cm (top) 3.0cm (middle) and 6cm (bottom)

1.5cm		Frequency compared against (Hz)									
Fixed Frequency (Hz)		0-50	50-100	100-150	150-200	200-250	250-300	300-350	350-400	400-450	450-500
	0-50	-	-	-	-	-	-	-	-	-	-
	50-100	1.000	-	-	-	-	-	-	-	-	
	100-150	0.906	0.599	-	-	-	-	-	-	-	
	150-200	0.499	0.202	0.999	-	-	-	-	-	-	
	200-250	0.178	0.053	0.925	1.000	-	-	-	-	-	
	250-300	0.13	0.037	0.867	0.998	1	-	-	-	-	
	300-350	0.117	0.032	0.844	0.997	1	1.000	-	-	-	
	350-400	0.131	0.037	0.868	0.998	1	1.000	1.000	-	-	
	400-450	0.209	0.064	0.949	1	1	1.000	1.000	1.000	-	
	450-500	0.161	0.047	0.908	0.999	1	1.000	1.000	1.000	1.000	

3.0 cm		Frequency compared against (Hz)									
Fixed Frequency (Hz)		0-50	50-100	100-150	150-200	200-250	250-300	300-350	350-400	400-450	450-500
	0-50	-	-	-	-	-	-	-	-	-	-
	50-100	0.973	-	-	-	-	-	-	-	-	
	100-150	1.000	0.948	-	-	-	-	-	-	-	
	150-200	0.995	0.557	0.998	-	-	-	-	-	-	
	200-250	0.610	0.089	0.693	0.983	-	-	-	-	-	
	250-300	0.342	0.033	0.416	0.874	1.000	-	-	-	-	
	300-350	0.332	0.031	0.404	0.865	1.000	1.000	-	-	-	
	350-400	0.312	0.028	0.383	0.848	1.000	1.000	1.000	-	-	
	400-450	0.306	0.027	0.375	0.842	1.000	1.000	1.000	1.000	-	
	450-500	0.324	0.030	0.396	0.859	1.000	1.000	1.000	1.000	1.000	

6.0 cm		Frequency compared against (Hz)									
Fixed Frequency (Hz)		0-50	50-100	100-150	150-200	200-250	250-300	300-350	350-400	400-450	450-500
	0-50	-	-	-	-	-	-	-	-	-	-
	50-100	0.614	-	-	-	-	-	-	-	-	
	100-150	1.000	0.869	-	-	-	-	-	-	-	
	150-200	0.994	0.147	0.924	-	-	-	-	-	-	
	200-250	0.127	0.001	0.047	0.568	-	-	-	-	-	
	250-300	0.016	0.000	0.005	0.13	0.995	-	-	-	-	
	300-350	0.007	0.000	0.002	0.068	0.964	1.000	-	-	-	
	350-400	0.011	0.000	0.003	0.099	0.987	1.000	1.000	-	-	
	400-450	0.004	0.000	0.001	0.044	0.915	1.000	1.000	1.000	-	
	450-500	0.005	0.000	0.001	0.049	0.930	1.000	1.000	1.000	1.000	

A sample trace of the frequency spectra (for the 90% stenosis) at the P5 position was compared with the non-stenosed case (Figure 89). The spectrum shows the averaged response for flow rates between 350-450 ml/min, and it can be seen that the disturbances

between 0 and 150Hz were much larger than the ones above 250Hz. However, the difference in the FFT area ratios between the low-frequency regions themselves were not large enough to achieve statistical significance, as shown in Table 28.

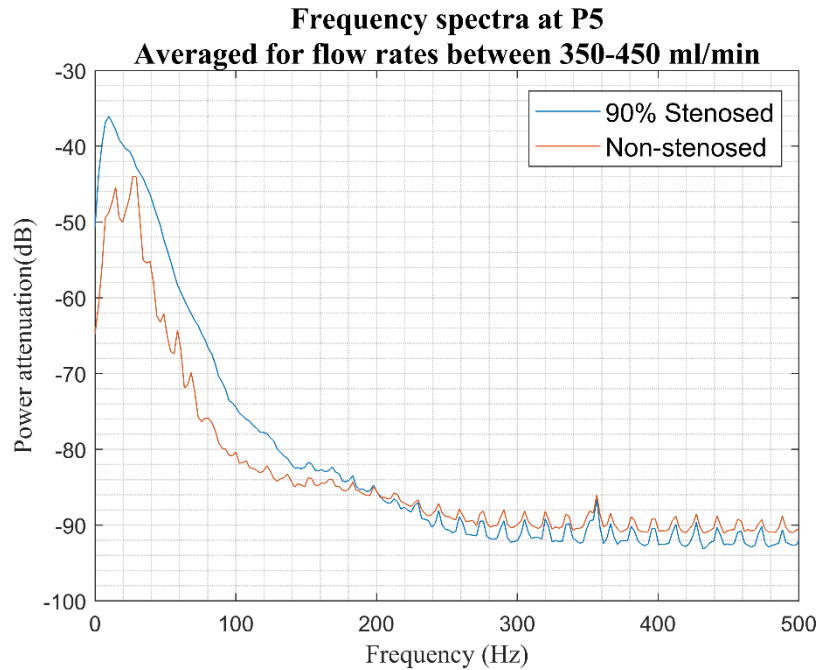


Figure 89: FFT comparison of a 90% stenosed-embedded tube (for FFTs averaged for flow rates between 350-450ml/min) at the P5 (6cm of the stenosis) position

Following the study of the effects flow rate, severity, frequency and measurement position, a two-way analysis of variance was conducted to identify the interaction effects of various combinations of two variables: flow rate & severity, flow rate & frequency, and severity & position.

The interaction effect between the flow rate and severity was investigated first. The data from all the positions and stenosis severities were combined (for flow rates above 300ml/min). The interaction effects were studied for frequencies within the 0-300Hz band (since most differences were within this range). It was determined that there was a statistically significant interaction between the effects of stenosis severity and flow rate for frequency bands up to 200Hz. The relation between flow rate and severity at different frequencies is shown in Table 29, where the frequencies with significant interactions are highlighted in green.

Table 29: Interaction effect of flow rate and stenosis severity (x=6, y=36)

Frequency (Hz)	F(x,y)	p - value
0-50	7.49	0.0000
50-100	7.14	0.0000
100-150	5.06	0.0007
150-200	2.49	0.0405
200-250	0.51	0.7962
250-300	1.30	0.2804

Table 30\* (a & b) shows that 90% stenosis severity was associated with the maximum values of the estimated marginal mean (EMMs) within the first 100Hz, which is consistent with the effect of stenosis severity alone, as previously discussed. Moving beyond 100Hz, it can be seen from Table 30 (c and d) that the values still showed an increasing trend for the 90% stenosis, but 75% started to dominate at the lower flow rates, and this is seen in Table 30 (e & f) where the 90% EMM values fall below those of the low and medium stenosed tubes. This also ties in with the frequency values in Table 29, which show significant differences between the low frequency and high-frequency bands.

Looking at the interactions between frequency and flow rate, two-way ANOVA did not show any significant differences between these groups for the 60% and 75% stenoses. However, for the 90% stenosis a strong interaction was observed between these two variables  $F(15,72) = 3.278, p = 0.0004$ ). Furthermore, a trend was observed which showed the FFT area ratios spreading over the higher frequency range with increasing flow rates and, generally, the highest area ratio was observed within the 50-100Hz bands, as seen in Figure 90.

Finally, for the position, neither the flow rate nor the severity had a strong interaction. A general difference in the area ratio values regarding position was seen earlier in Table 27, showing small differences in the area ratios at all the positions. Furthermore, statistically significant differences between positions were present while looking at the effect of positions only (as shown in Table 27 using one-way ANOVA).

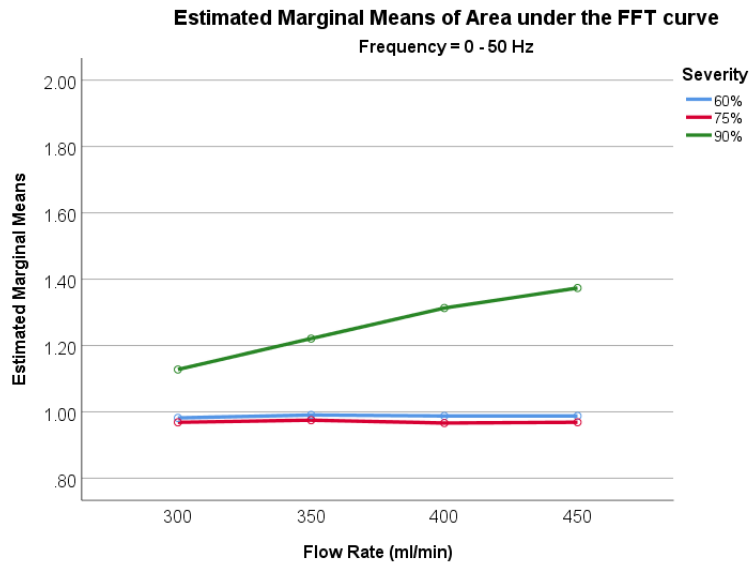
---

***\* Note for the reader before viewing Table 30***

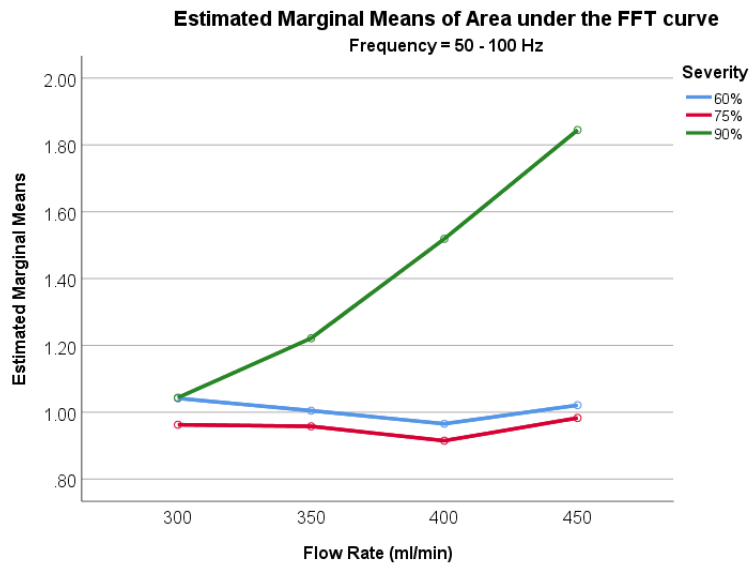
*The following pages showing estimated marginal means (EMMs) are the mean responses from descriptive statistics for each factor adjusted by any other variables in the model. In other words, one factor's marginal means are the means for the factors averaged for all levels of the other factors). In the SPSS software package, the EMMs adjust for the covariate (which is why it is usually used as a measure of interaction effect). However, since our model does not include any covariates, the EMMs obtained have the same values as the simple means from the descriptive statistics.*

---

Table 30: Interaction effects between stenosis severity and flow rate determined by two-way ANOVA

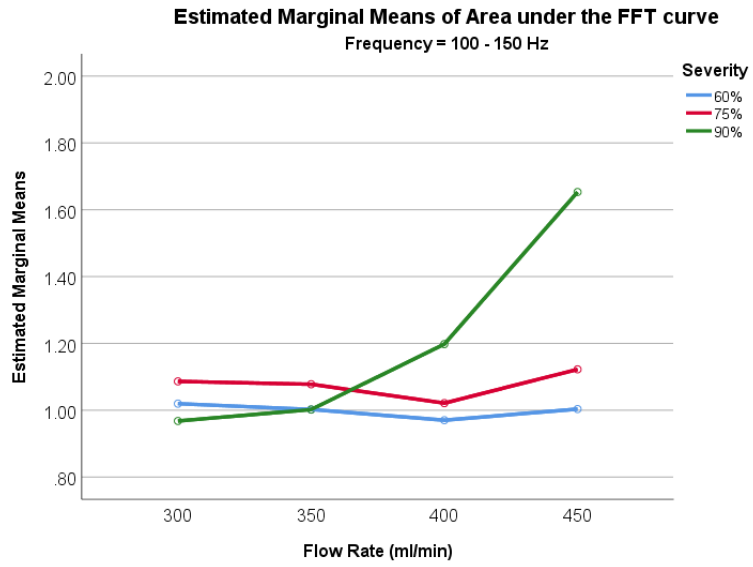


(a) 0-50Hz Frequency band

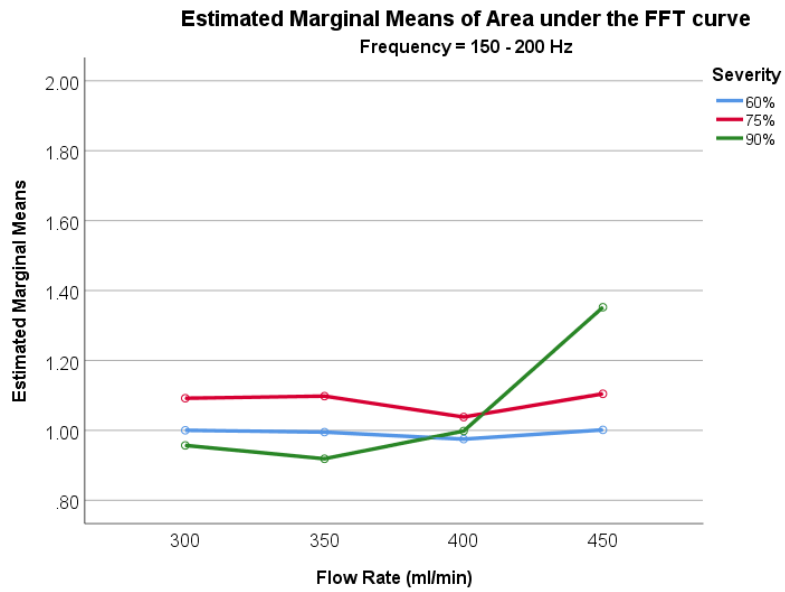


(b) 50-100Hz Frequency band

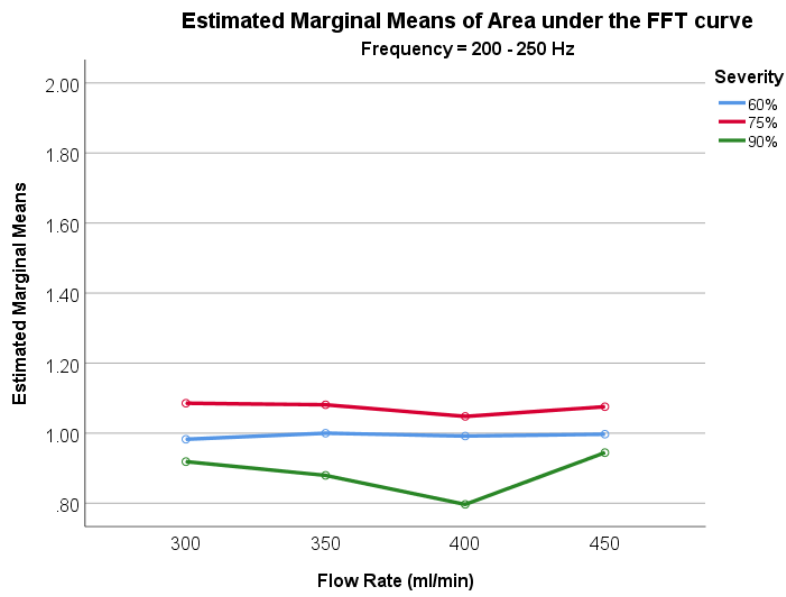




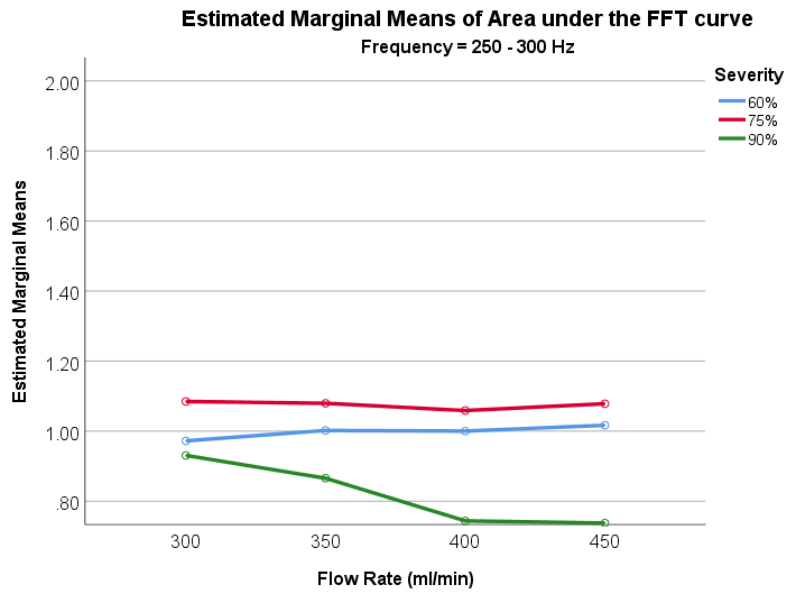
(c) 100-150Hz Frequency band



(d) 150-200Hz Frequency band



(e) 200-250Hz Frequency band



(f) 250-300Hz Frequency band

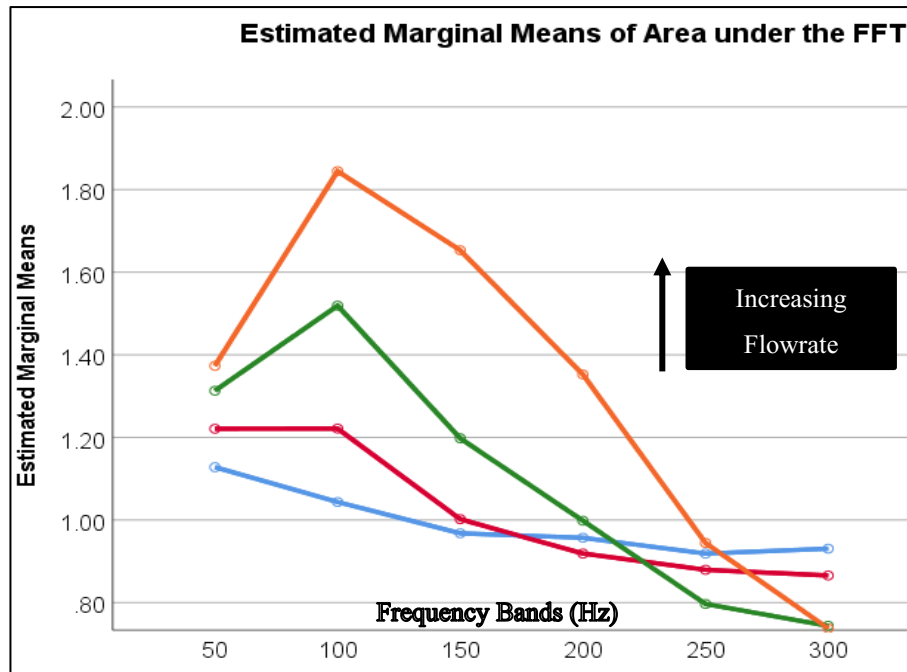


Figure 90: Combined effect of frequency (Hz) and flow rate (ml/min) for 90% area stenosis

Despite the lack of statistical significance from two way ANOVA in post-stenotic flow, the results may have some physical importance as the disturbance would be expected to vary depending on location, flow rate and stenosis severity, as discussed in the ultrasound scans in section 3.2 and in the literature (Ahmed and Giddens, 1983). Also, the presence of surrounding gel dissipates the energy (Liu, Zhang and Lu, 2018) before reaching the Platilon surface, as a result of which some of the distinct features relating flow rates and stenosis severities when combined with other variables can stay hidden.

#### 4.4. Effect of stenosis symmetry

##### 4.4.1. Early-stage proof of concept work

##### Methods

As mentioned in chapter 2, two approaches (cotton thread stenoses and 3D printed stenoses) were taken to produce the stenoses. The initial proof of concept study was carried out by tying a cotton thread around the centre of the silicone rubber tube (Figure 91) to form a 75% non-axisymmetric constriction. The 75% area constriction was ensured by placing a solid rod (with half the diameter of the tube's internal diameter) in the tube and

removing the rod once the cotton thread was securely tied around the tube. Figure 92 shows an agar gel phantom (section 2.4.1) from an early-stage experimental set-up, where de-ionized water was perfused through the tube (as described in section 4.1) with steady flow rates ranging from 0-360ml/min (though the maximum achieved in the stenosed tube was 299ml/min due to the added resistance). The data (at 0cm and +1.5cm downstream of the centre of the stenoses, i.e., P2 and P3 positions, respectively) in this set-up were captured using the accelerometers and the PowerLab set-up as discussed in section 2.9.

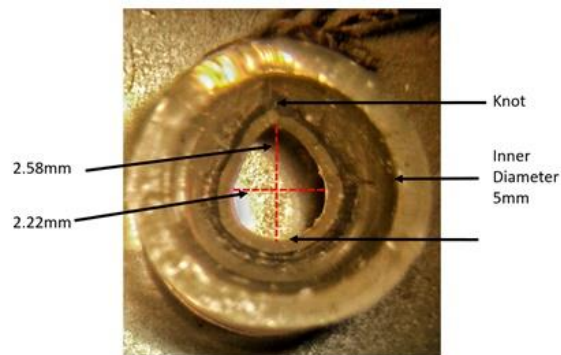


Figure 91: Cross-section of a 75% stenosed tube (with a 5mm original non-constricted inner diameter), using a cotton thread (black) tied around the outer surface

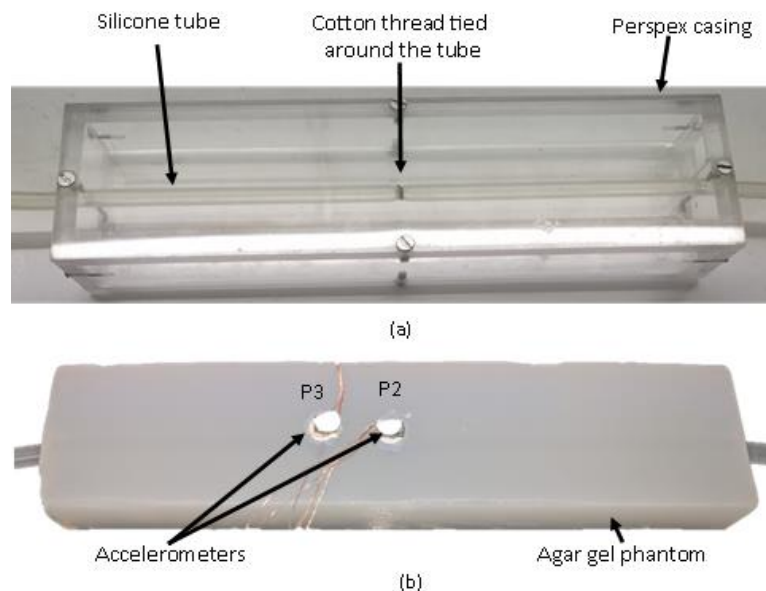


Figure 92: 75% asymmetrically stenosed tube (embedded in agar gel). Silver patches represent the accelerometers at P2 (0cm) and P3 (1.5cm) downstream of the stenosis

## Results

The time-domain signal was converted into the frequency domain using the FFT technique (section 2.8). On analysing the FFT data obtained from the accelerometers, disturbances were seen in the post stenotic region of the stenosed tube. Figure 93 and Figure 94 show the power attenuation signals at the P3 (1.5cm downstream) position of a non-stenosed and a 75% stenosed tube respectively, in which the asymmetry of the latter resulted from the knotted cotton. Firstly, looking at Figure 93, at flow rates above 151ml/min, some hints of an increasing flow rate effect are seen in the non-stenosed case between 250-350Hz.

Looking at the stenosed case (Figure 94), this effect was considerably stronger, and new peaks appeared from the stenosis induced flow perturbations. Some distinct areas of interest were around 154Hz, 210Hz, 245Hz and the band between 275-450Hz. To isolate this, averages of low (0 - 98ml/min), medium (149ml/min - 199ml/min) and high (250ml/min - 375ml/min) flow rates were taken at these frequencies. Figure 95 shows the clear association between increasing flow rate and increasing signal power.

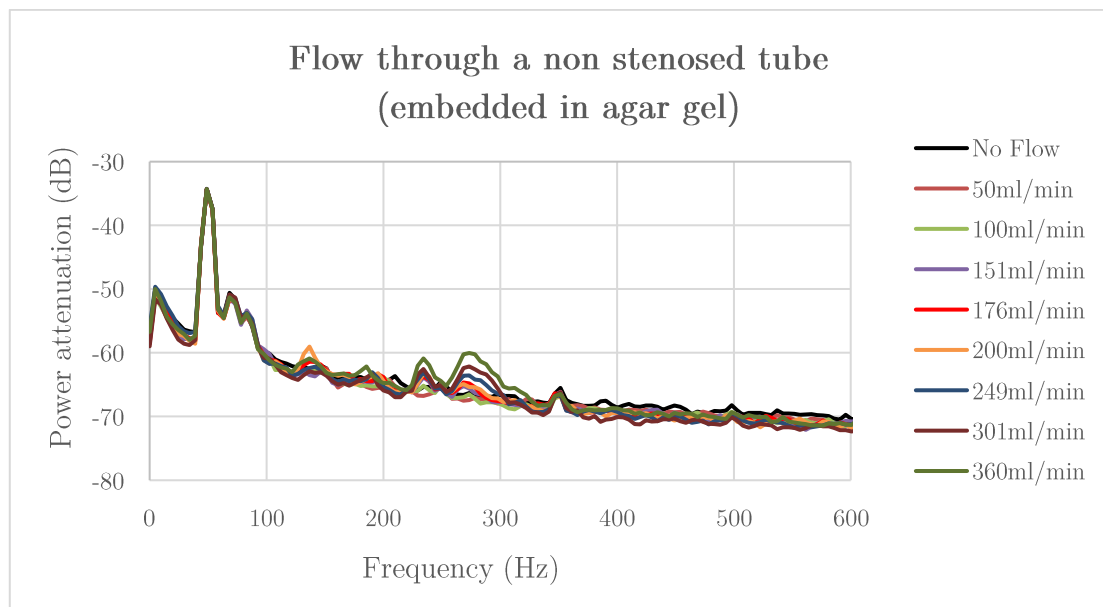


Figure 93: FFT of the accelerometer signal for flow measurements (at 1.5cm downstream position) from a non-symmetric & non-stenosed tube (embedded in agar gel)

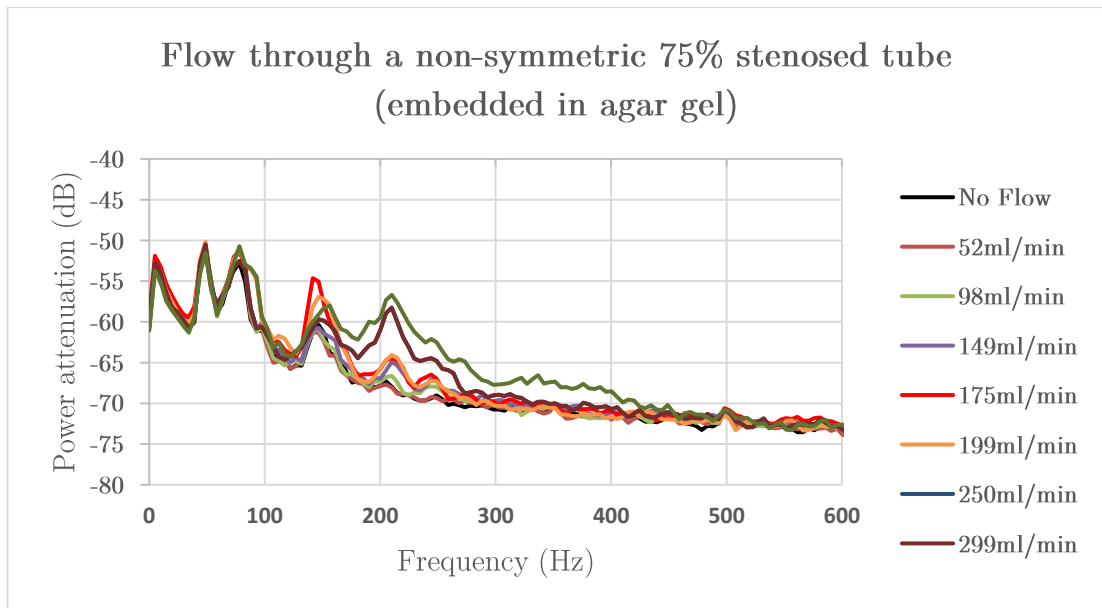


Figure 94: FFT of the accelerometer signal for flow measurements (at 1.5cm downstream position) from a non-symmetric 75% stenosed tube (embedded in agar gel)

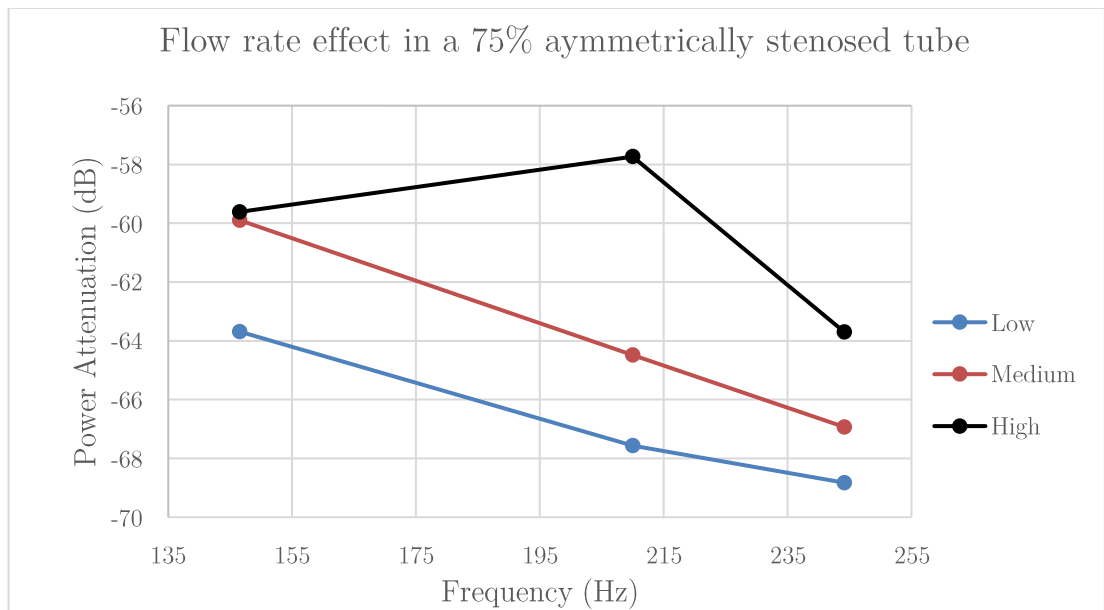


Figure 95: Effect of flow rate (in a 75% non-axisymmetrically stenosed tube) at low (0 - 98ml/min), medium (149ml/min - 199ml/min) and high (250ml/min - 375ml/min) flow rates

Despite the lack of flow disturbances detected in the earlier phantom experiments (sections 4.1 to 0), this experiment illustrated the effect of increasing flow rate and showed the presence of the disturbances in post-stenotic flow, due to asymmetry of the stenosis, which agrees with previous findings (Young and Tsai, 1973a; Tang *et al.*, 2003). The

previous lack of detectable disturbances in the 60% and 75% axisymmetrically stenosed embedded models can be attributed to the lack of asymmetry in the stenosis, where the perturbations produced within the flow are not strong enough to be transmitted to the phantom surface. Therefore, the phantom neck experiments were repeated with the introduction of asymmetry in the 3-D printed stenosis (discussed in the next section of this chapter).

#### 4.4.2. Tube embedded within the ultrasound gel neck phantom

##### Methods

Following the significance of the effects of stenosis symmetry in the bare-stenosed tube (section 3.3.2), the experiment was extended to determine its effects in the phantom (section 2.6), with the stenosed tube embedded inside the ultrasound gel. The same methodology was used as the one detailed in section 4.1, with the main difference being the stenosis type. Two different severities of 75% and 90% were investigated here, with the stenosis geometry detailed earlier (Figure 61) where the tube was axisymmetrically or non-axisymmetrically stenosed. Two repeats of data were collected at the same five positions, i.e., P1 (3cm upstream), P2 (vertically above the stenosis), P3 (1.5cm downstream), P4 (3cm downstream), and P5 (6cm downstream) of the stenosis.

##### Results

The effects of stenosis severity were initially investigated using the power attenuation spectra (for all flow rates) at all five positions. A further detailed analysis was then conducted by comparing the respective ratios of the areas under the FFT to reduce the data and smooth out abrupt variations in the spectral power. The areas under the FFT curves obtained for all flow rates were normalised to the no-flow condition as a control for background signal noise. The process was repeated for both stenosis severities, i.e., 75% and 90% and a comparison was then made between them.

##### 75% stenosed case

At the P1 position, in the axisymmetric case, an unexpected formation of peaks is seen

between 200ml/min – 450ml/min and the peaks seem to be increasing in amplitude and shifting towards the higher frequencies with the increasing flow rates (Figure 96a). The results from both repeats at this position were disregarded as they might have had an unknown interaction with the background, e.g., trapped particle/air bubble inside the tube. However, the non-axisymmetric case shows an increasing trend of FFT area ratio between the 100-150Hz band (Figure 96b), which is speculated to be a result of energy transmitted from the downstream disturbances. This could not have been the case with the axisymmetric result, as the disturbances downstream are barely detectable (as discussed below).

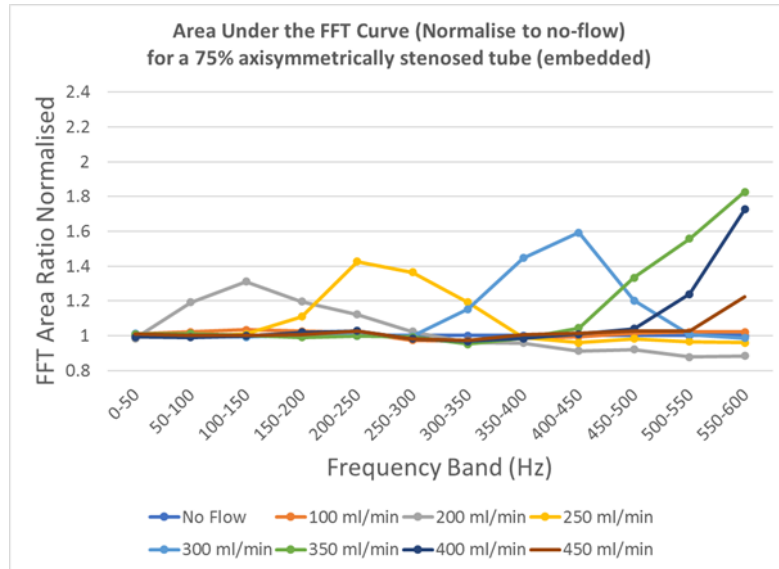
At the P2 (vertically above the stenosis) position, a large difference in amplitudes and frequencies was seen between the axisymmetric and the non-axisymmetric case. The non-axisymmetric case did not display any visible trends with the increasing flow rates (Figure 97a). On the contrary, a clear trend of increasing normalised FFT areas was seen with the increasing flow rates. The area ratios for the low flow rates (up to 250ml/min) were highest within the lowest frequency band of 0-50Hz, after which they continued to decrease (Figure 97b). However, for the flow rates above 250ml/min, the flow perturbations encompassed a much larger range of frequencies and the span increased with the increasing flow rates.

Moving downstream to the P3 position, the axisymmetric case showed disturbances only at the highest flow rate between the 50-200Hz region (Figure 98a). However, with the non-axisymmetrically stenosed tube, much larger disturbances were detected at the phantom surface for flow rates above 250ml/min. Figure 98b shows a clear increasing trend of the normalised FFT area ratios, with increasing flow rates. In addition to the values of the FFT area ratios than those seen at the P2 position as expected, the detected disturbances were spread over a wider range of frequencies, i.e., 0-550Hz.

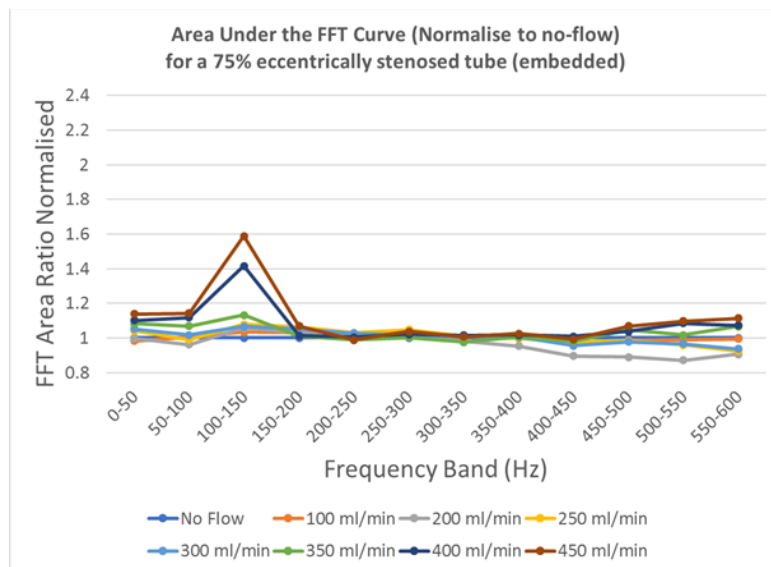
Moving further downstream to the P4 and P5 positions (Figure 99 & Figure 100 respectively), the axisymmetric cases show no visible trends with increasing flow rates as the fluid travels away from the stenosis. However, for the non-axisymmetric case, a clear distinction between the normalised FFT area ratios is still present for flow rates above 300ml/min and 350ml/min at P4 and P5, respectively. The trend of decreasing FFT area



ratios, with increasing distance from the stenosis is in keeping with the results discussed in the earlier sections of the bare-stenosed tube (3.3.2). This is also true for the increasing frequencies (and the corresponding FFT area ratios) of the disturbances, with the increasing flow rate.

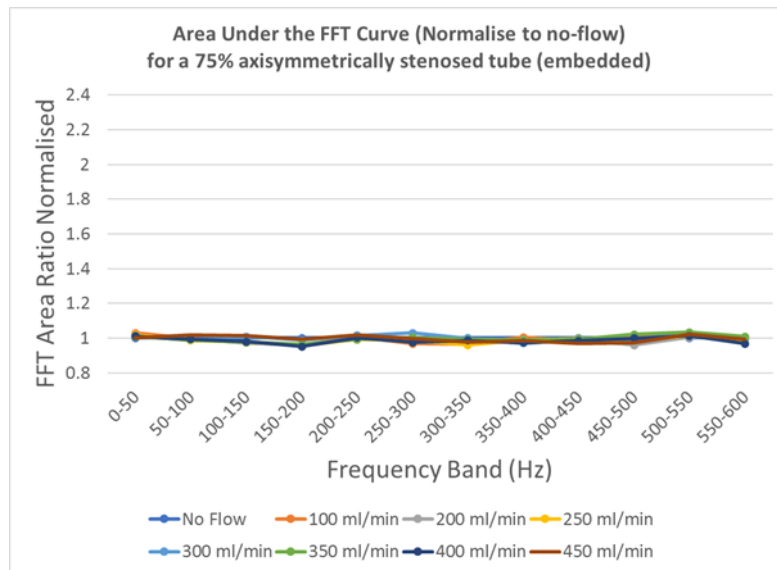


(a)

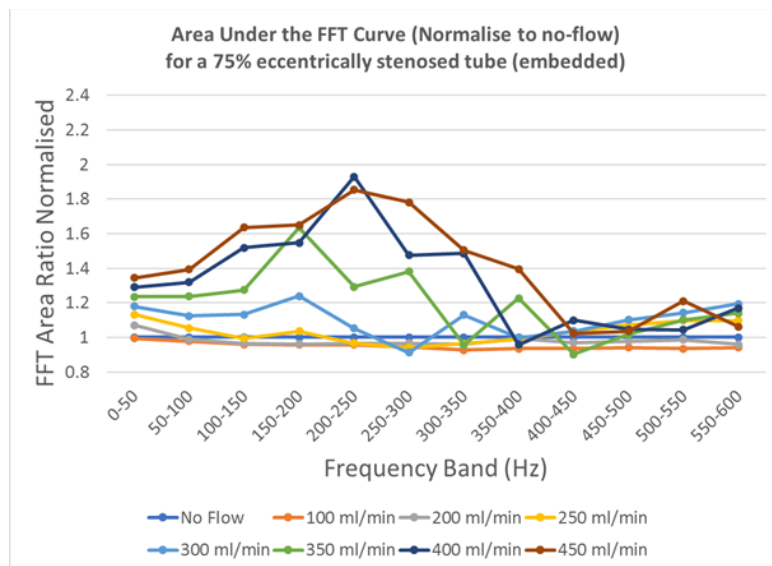


(b)

Figure 96: Area under the FFT curve, at P1 (-3cm upstream) for a 75% stenosed embedded tube (a) axisymmetric (b) non-axisymmetric

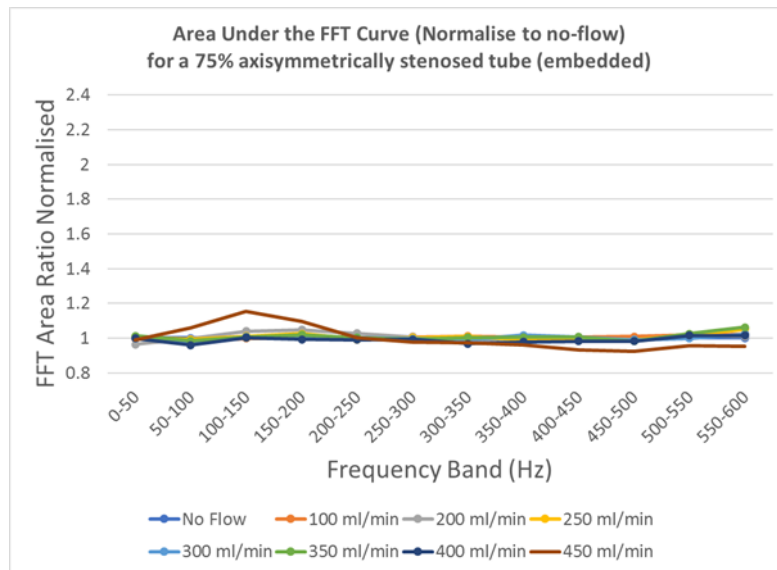


(a)

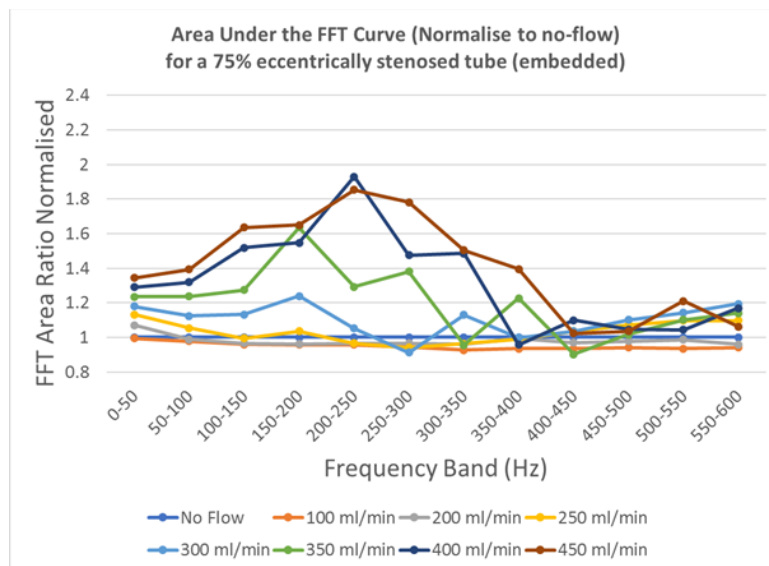


(b)

Figure 97: Area under the FFT curve, at P2 (0cm) for a 75% stenosed embedded tube (a) axisymmetric (b) non-axisymmetric

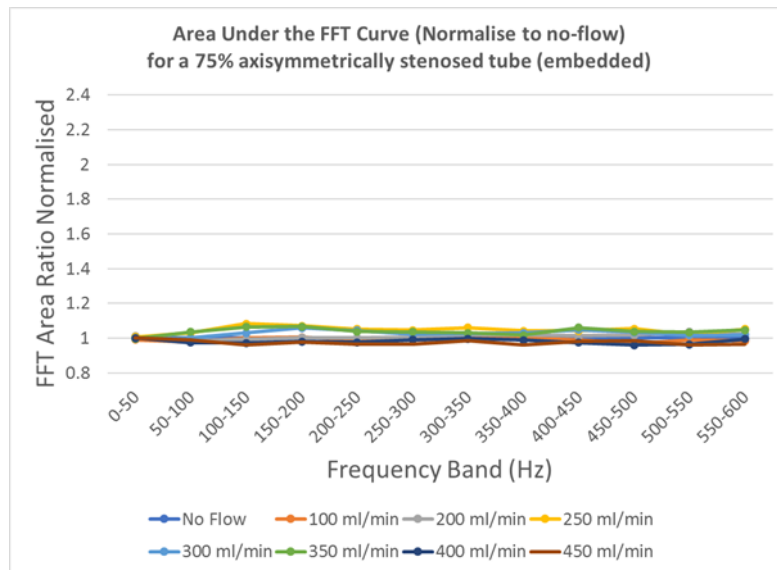


(a)

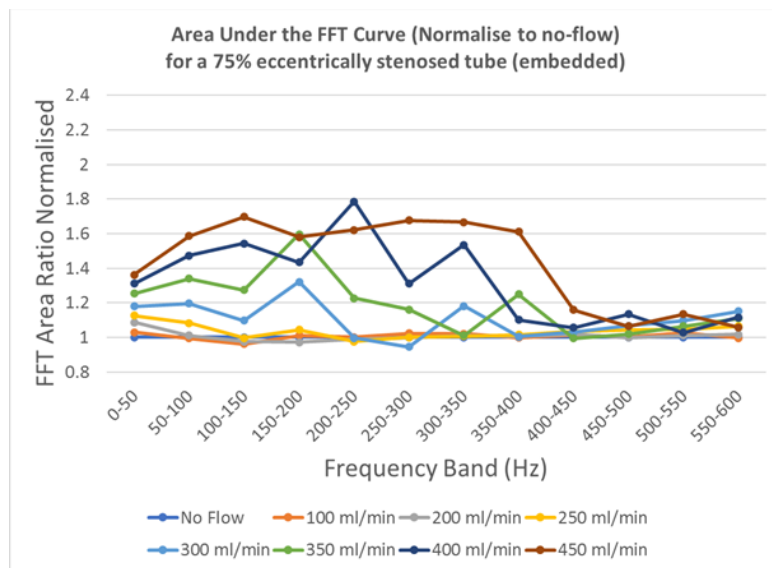


(b)

Figure 98: Area under the FFT curve, at P3 (+1.5cm) for a 75% stenosed embedded tube (a) axisymmetric (b) non-axisymmetric

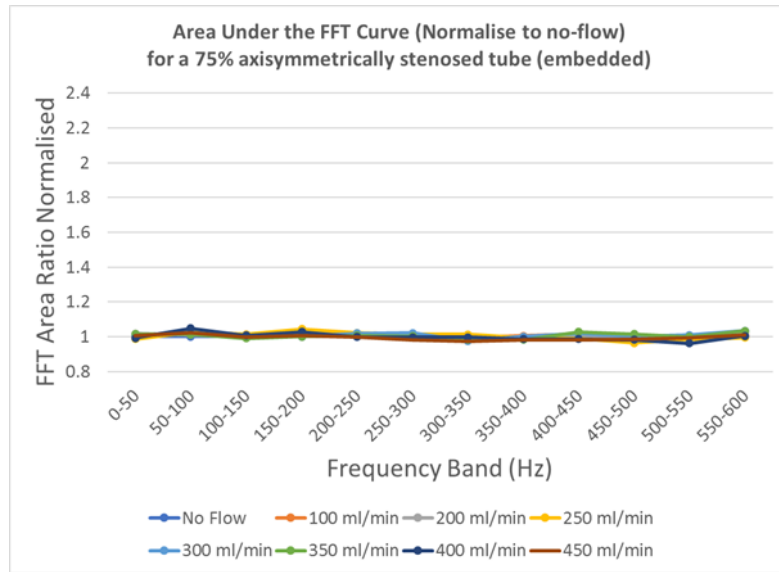


(a)

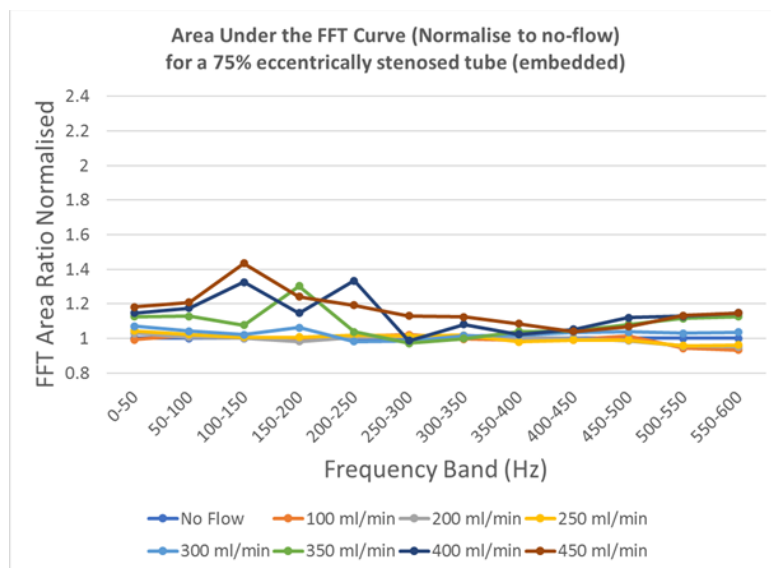


(b)

Figure 99: Area under the FFT curve, at P4 (+3cm upstream) for a 75% stenosed embedded tube (a) axisymmetric (b) non-axisymmetric



(a)



(b)

Figure 100: Area under the FFT curve, at P5 (+6cm upstream) for a 75% stenosed embedded tube (a) axisymmetric (b) non-axisymmetric

To confirm the effect of increasing flow rate on FFT ratios and to estimate the strength of the association, a regression analysis was conducted for flow rates above 200ml/min (with the normalised areas under the curve averaged between 0-600Hz). The results indicated a significant correlation ( $p < 0.05$ ) between the flow rate and the FFT area ratios for the non-axisymmetric case at all positions, however, no significant relation was seen for the axisymmetric case. Secondly, for the non-axisymmetric case, Table 31 shows that the gradient has the lowest values at P1 (upstream) and as the measurement site moves to the stenosis and beyond to the P3 position, the gradient increases, implying that increasing flow rate creates stronger disturbances. Peak value of gradient is reached at P3, after which the gradient decreases again. The confidence in this trend for the non-axisymmetric case is shown by the high  $R^2$  and low  $p$  values.

Table 31: Regression analysis of effect of flow rate in a 75% embedded stenosed (axisymmetric and eccentric) tube, with glycerol-water solution as perfusing liquid, at P1 (-3cm upstream), P2 (0cm), P3 (+1.5cm downstream), P4 (+3cm downstream) and P5 (+6cm downstream) positions – green (highly significant), yellow ( $0.1 > p > 0.5$ ), and red (insignificant)

	Gradient of the regression line		R-squared		Significance (p)	
	Axisymmetric	Non-axisymmetric	Axisymmetric	Non-axisymmetric	Axisymmetric	Non-axisymmetric
<b>P1</b>	0.0000	0.0005	0.000	0.949	0.976	0.001
<b>P2</b>	0.0000	0.0018	0.098	0.984	0.546	0.000
<b>P3</b>	0.0000	0.0030	0.370	0.964	0.200	0.001
<b>P4</b>	-0.0002	0.0018	0.418	0.960	0.165	0.001
<b>P5</b>	0.0000	0.0008	0.618	0.952	0.064	0.001

### 90% stenosed case

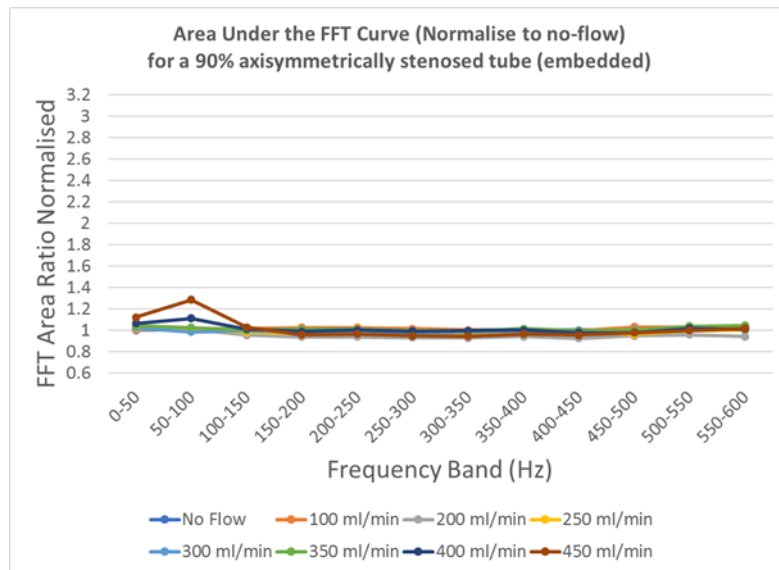
In the axisymmetric case, at P1 (Figure 101a), a very slight increase in the normalised FFT area ratios is seen. However, this occurs only at very high flow rates of 400ml/min and 450ml/min. On the other hand, the non-axisymmetric case highlights much clearer trends of increasing FFT ratios (Figure 101b), with increasing flow rates across a wider range of frequencies. The presence of these disturbances at the upstream position is speculated to be due to the energy of the downstream disturbances being transmitted to the upstream position through the tube wall, ultrasound gel and the Platilon skin material.

Moving down to the P2 position in the axisymmetric case, very small differences were seen in the FFT area ratios between 350-450 ml/min in the 0-50Hz band (Figure 102a), and a more noticeable difference started to appear at 450ml/min in the 50-100Hz band. For the non-axisymmetric case, noticeable differences were highlighted at flow rates above 200ml/min, with increasing frequency of the flow perturbations as the flow rate increased (Figure 102b).

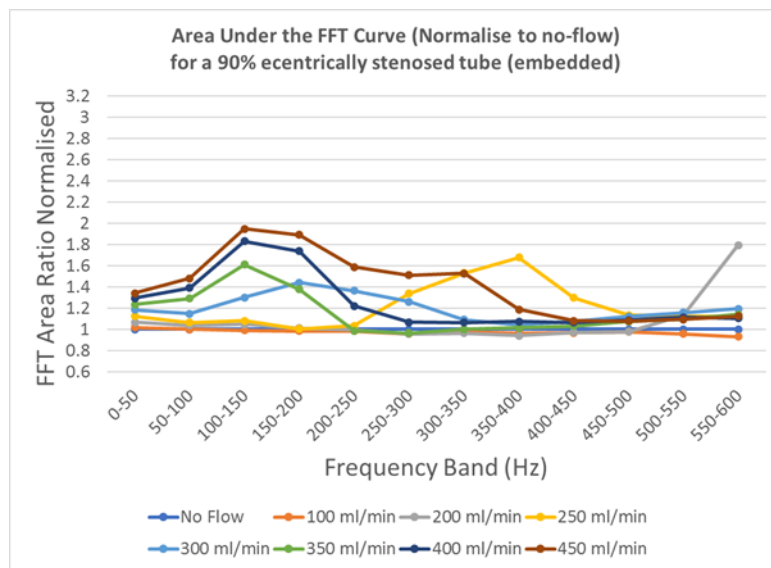
At the P3 position, for the axisymmetric case, the effects were amplified (Figure 103a). The differences in FFT ratios were more apparent between 0-50Hz, and the values at 400ml/min and 450ml/min are higher than those at the corresponding frequencies at the P2 position. Similarly, for the non-axisymmetric case, the amplitudes of the disturbances at 200ml/min had increased and these were now spread over a wider range of frequencies (Figure 103b). The peak FFT area ratios at the P3 position were generally higher than those at P2, e.g. the value of the FFT area ratio at the highest flow rate here was just under 3.2, whereas it was just under 2.6 at its respective P2 position.

Finally, moving down to the P4 and P5 positions (Figure 104 & Figure 105, respectively), a few things are worth noting. For the axisymmetric case, values of the normalised FFT area ratios were higher here when compared to the P3 position, and secondly, the trends of increasing FFT area ratios with increasing flow rates were more apparent here. However, for the non-axisymmetric case, the curves started to flatten as fluid travelled away from the stenosis, and disturbances started to dominate more in the lower frequency bands, with clear distinctions in FFT area ratios still present above 200ml/min.

As for the 75% stenoses, a regression analysis was conducted for the flow rates above 200ml/min (with the normalised areas under the curve averaged between 0-600Hz), to confirm the trends of the increasing FFT ratios with the flow rates. The results indicated a significant correlation ( $p < 0.05$ ) between the flow rate and the FFT area ratios for the non-axisymmetric case at all positions, however, apart from at P1, the upstream position, no significant relation was seen for the axisymmetric case, as was the case for the 75% stenoses.



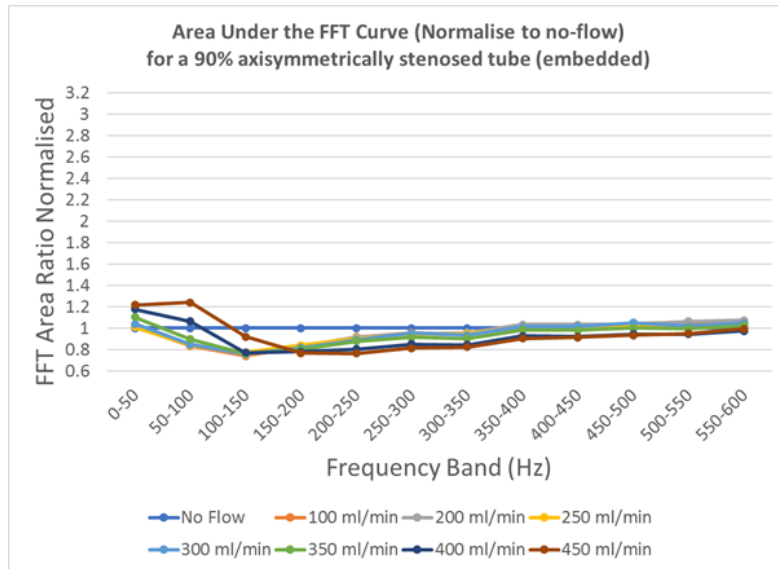
(a)



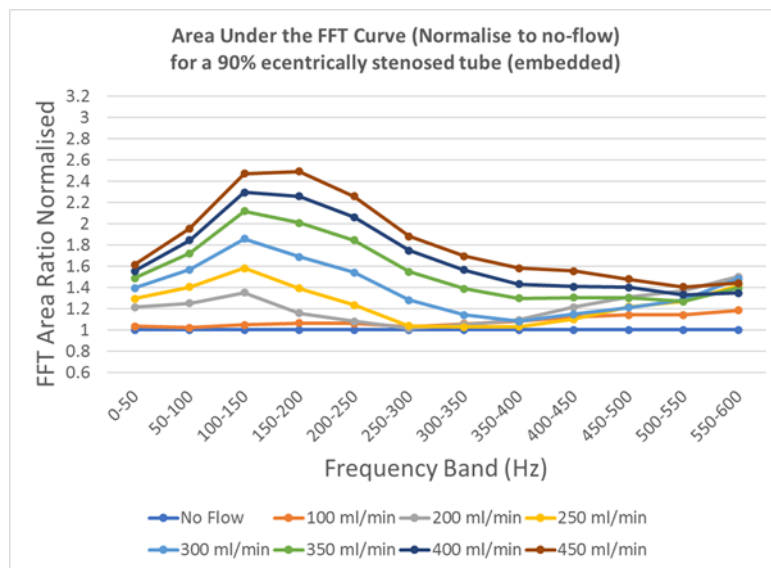
(b)

Figure 101: Area under the FFT curve, at P1 (-3cm) for a 90% stenosed embedded tube (a) axisymmetric (b) non-axisymmetric



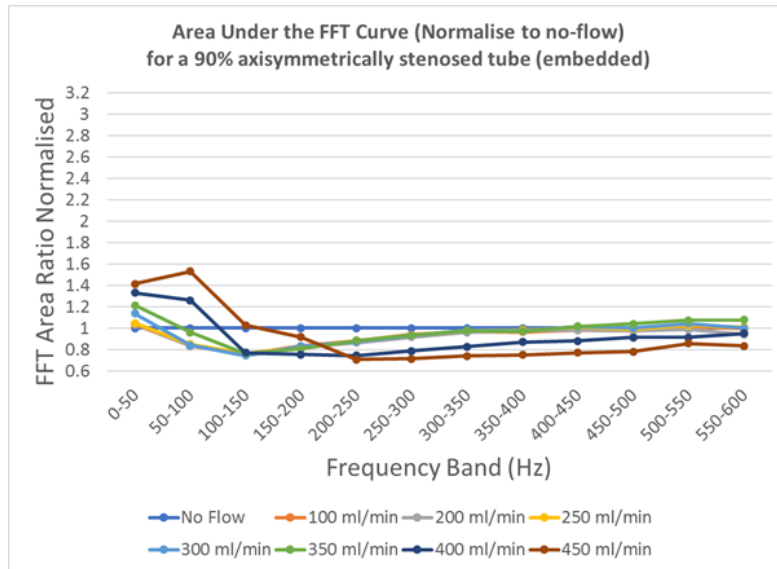


(a)

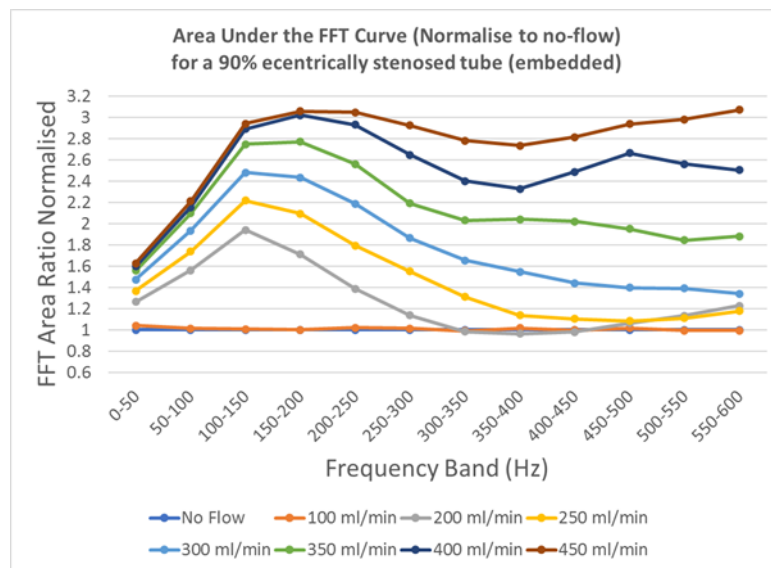


(b)

Figure 102: Area under the FFT curve, at P2 (0cm) for a 90% stenosed embedded tube (a) axisymmetric(b) non-axisymmetric

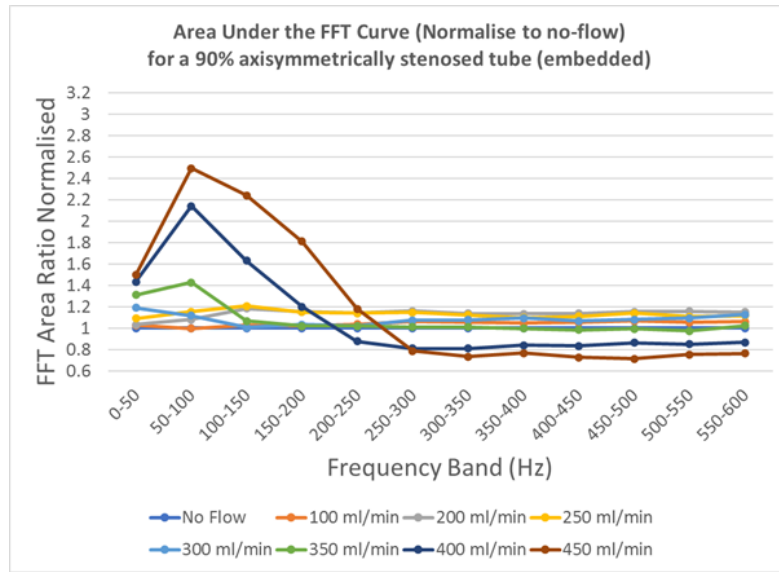


(a)

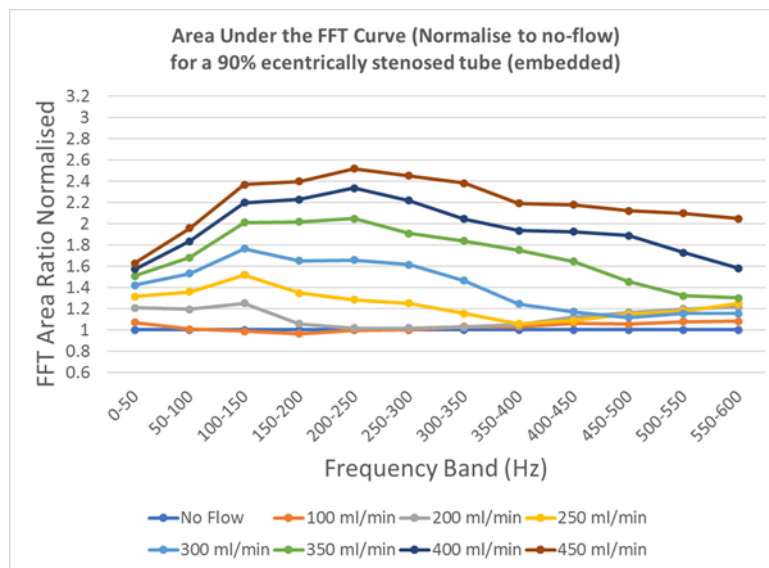


(b)

Figure 103: Area under the FFT curve, at P3 (+1.5cm) for a 90% stenosed embedded tube (a) axisymmetric (b) non-axisymmetric

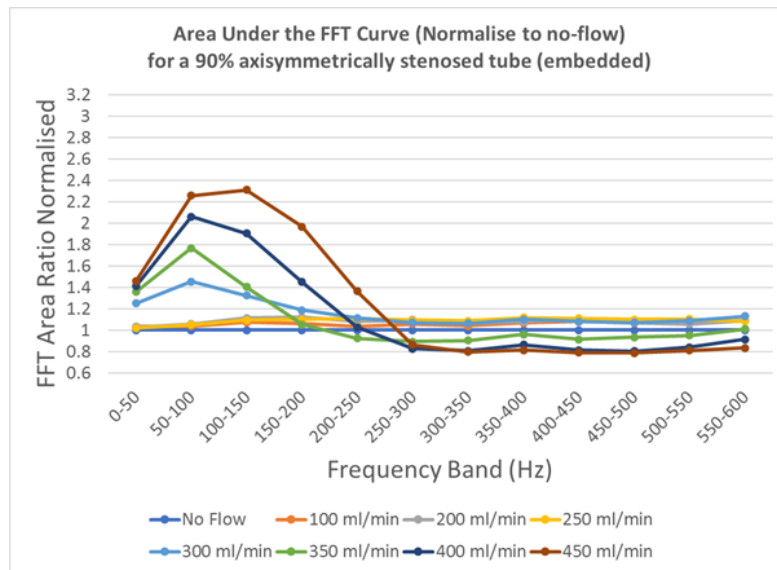


(a)

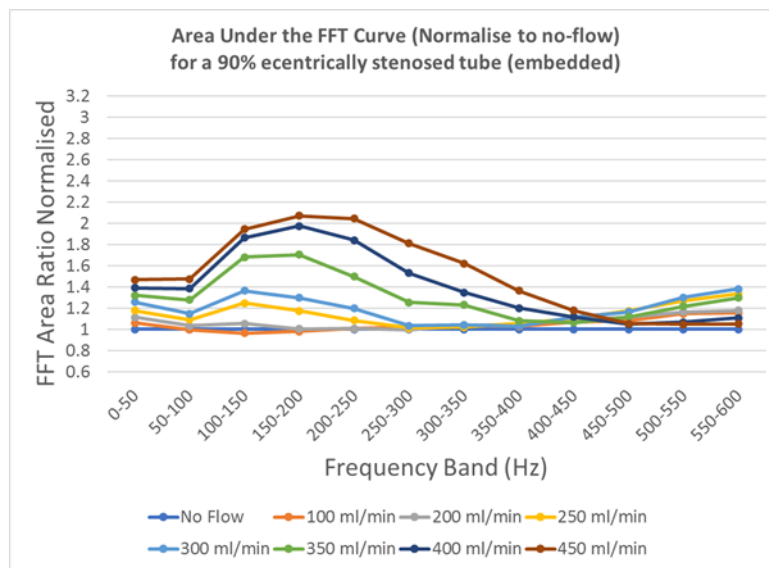


(b)

Figure 104: Area under the FFT curve, at P4 (+3cm) for a 90% stenosed embedded tube (a) axisymmetric (b) non-axisymmetric



(a)



(b)

Figure 105: Area under the FFT curve, at P5 (+6cm) for a 90% stenosed embedded tube (a) axisymmetric (b) non-axisymmetric

Further results are summarised in Table 32, which again shows that the gradients (in the non-axisymmetric case) have the lowest values at P1 (upstream) increasing at P2 and reaching a maximum at P3, after which the gradient decreases again. This trend is absent in the axisymmetric case as majority of the disturbances there were in the lower range of frequencies, a further statistical analysis of which was presented earlier (section 4.3). Finally, on comparing Table 31 and Table 32, it can be concluded that the effect of flow rate on the FFT area ratios is greater in the 90% embedded stenosed tube than the 75%, as indicated by higher gradients of the regression lines

Table 32: Regression analysis of effect of flow rate in a 90% embedded stenosed (axisymmetric and eccentric) tube, with glycerol-water solution as perfusing liquid, at P1 (-3cm upstream), P2 (0cm), P3 (+1.5cm downstream), P4 (+3cm downstream) and P5 (+6cm downstream) positions – green (highly significant), yellow ( $0.1 > p > 0.5$ ), and red (insignificant)

	Gradient of the regression line		R-squared		Significance (p)	
	Axisymmetric	Non-axisymmetric	Axisymmetric	Non-axisymmetric	Axisymmetric	Non-axisymmetric
<b>P1</b>	0.0002	0.0010	0.806	0.697	0.015	0.039
<b>P2</b>	-0.0001	0.0026	0.568	0.980	0.083	0.000
<b>P3</b>	0.0000	0.0062	0.015	0.991	0.816	0.000
<b>P4</b>	0.0001	0.0044	0.066	0.983	0.624	0.000
<b>P5</b>	0.0006	0.0018	0.597	0.987	0.072	0.000

Generally, the positions closest to the stenosis are expected to see the highest disturbances, but this does not seem to be the case here for the axisymmetric case, although at the downstream positions, the effect is not statistically significant. A slight misorientation of the stenosis in the tube could have impacted the flow in the downstream position. A slight upwards tilt on the exit side of the stenosis could force the flow to bend upwards along the length of the tube. If this were the case, the location of maximum disturbance would then depend on the degree of misorientation, as discussed earlier in section 4.1.

To explore the combined effects of flow rate, stenosis severity and stenosis symmetry, a two-way, between groups ANOVA was performed. The procedure used was the same as for the bare stenosed tube. The data were divided into three groups, based on flow rate, stenosis severity and stenosis symmetry. The dependent variable in the analysis was the averaged (0-600Hz) area under the FFT curve (normalised to no-flow). The data from the three downstream positions (P3, P4 and P5) were combined to increase the number of

degrees of freedom in the analysis. This in turn affected homogeneity of variance (as assessed by Levene's test  $F(64)=2.99$ ,  $p=0.000$ ), however, the variance can be associated with different downstream positions and the combination of data from the three downstream positions and the exclusion of the upstream data can be justified when focussing on the effect of stenosis symmetry, severity and/or the flow rate, as the majority of the disturbances associated with stenoses were present in the downstream positions as discussed previously.

The analysis showed that the effects of flow rate ( $F(7,64)=7.37$ ,  $p=0.000$ ), severity ( $F(1,64)=15.18$ ,  $p=0.000$ ) and stenosis symmetry ( $F(1,64)=46.61$ ,  $p=0.000$ ) were significant. The analysis also indicated a significant interaction between flow rate & stenosis symmetry ( $F(7,84)=5.83$ ,  $p=0.000$ ), and between stenosis severity and stenosis symmetry ( $F(7,84)=9.99$ ,  $p=0.002$ ). However, the combined interaction effects of flow rate & stenosis severity were not significant here ( $p>0.05$ ). The plots comparing the means of these variables, for all the downstream positions combined, are illustrated in Figure 106, which clearly shows the trends of increasing mean FFT area with increasing flow rates and increasing severities. Furthermore, it is evident that the presence of eccentricity in the stenosis increases the detectable disturbances on the skin surface. The large error bars are a result of the combined data sets from the downstream position, the reason for which has been detailed earlier.

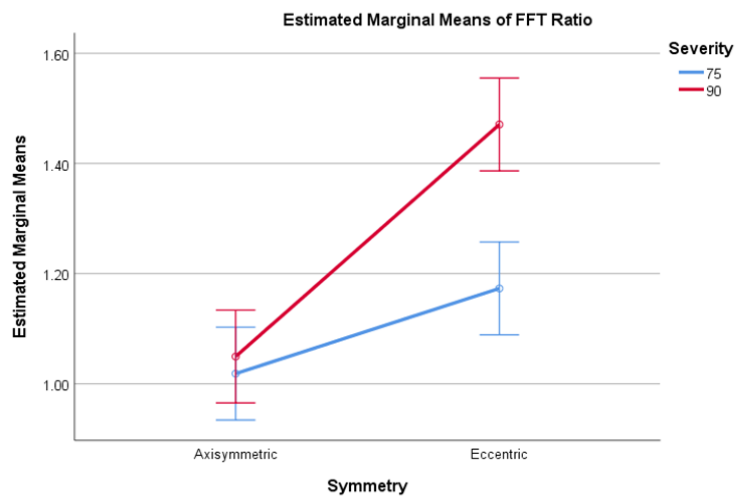
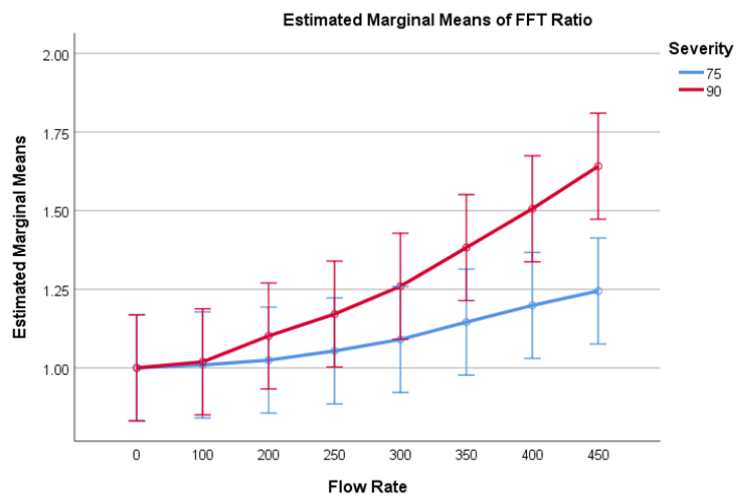
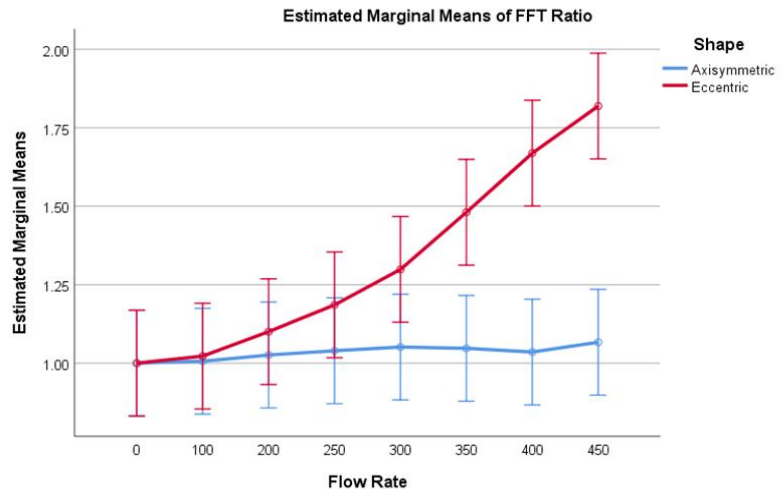


Figure 106: Means of averaged (0-600Hz) areas under the FFT curve (normalised to no flow), calculated from the combined downstream positions, showing the interactions between flow rate & severity, flow rate & symmetry, and symmetry & severity in embedded stenosed tube

## 4.5. Conclusion

The objectives of the investigation in this chapter were to determine the presence of stenosis induced disturbances (using the glycerol-water solution) at the skin surface using LDV and to quantify the effects on these disturbances of varying flow rates, stenosis severities, and symmetries.

The results from the steady flow investigation showed that the flow downstream of stenosis was disturbed, and that the disturbances increased with increasing stenosis severity. Furthermore, as the flow rate and severity are increased, the disturbances start to form nearer to the outlet of the stenosis. The increasing flow rates and stenosis severities also led to the formation of higher frequency disturbances. In the case of axisymmetric stenoses, noticeable disturbances were detected only in the severely stenosed tubes; however, larger disturbances were detected in moderate and severely stenosed tubes in the non-axisymmetric cases, suggesting that in-vivo, where stenoses are far from symmetric, they may be detectable when the degree of occlusion is not sufficient to cause symptoms.

Furthermore, the post-stenotic behaviour was location-dependent, and in general the disturbances start to disappear further downstream of the stenosis (as seen in the non-axisymmetric case). The opposite was seen for the axisymmetric stenoses, which was explained by their orientation. The trends for the increasing flow rates and stenoses severities are in agreement with the ultrasound scans (section 3.2), the preliminary flow simulations (Appendix A), and many previous studies (Young and Tsai, 1973a; Ahmed and Giddens, 1983; Long *et al.*, 2001; Lee and Xu, 2002; Mancini, Bergersen, *et al.*, 2019).

Based on the results discussed in this chapter, the LDV technique can be used to determine the presence of stenosis by measuring the disturbances at the skin surface under physiological mean flow rates. The effects of introducing pulsatile flow will be investigated in the next chapter.



## 5. Effect of superimposing pulsatile flow on the mean steady flow

Following the investigation of the disturbances generated at the phantom surface, under steady flow conditions (chapter 4), the study was extended to integrate pulsatility in the flow to mimic (more closely) the physiological conditions within the carotid artery. This chapter explores the measurement (using LDV) of skin-surface level disturbances when a pulsatile flow perfuses through the tube through stenoses of different severities.

### Methods

The same experimental set-up was used as that discussed for the steady flow experiments in chapter 4. A 40:60 glycerine-water solution (section 2.1) was passed through a Penrose latex tube (section 2.2). The tube was axisymmetrically stenosed for this investigation, with stenosis severities of 0, 60%, 75% and 90% (using the 3-D printed stenoses detailed in section 2.3). The tube was then embedded within the ultrasound gel (section 2.4.4), which was covered with skin mimicking material Platilon (section 2.5) to form a standardised neck phantom (section 2.6). A continuous flow circuit was set up as described in section 2.7. Self-adhesive patches of retroreflective tape approximately 4 x 4mm (section 2.9.2) were attached to the Platilon surface at five positions along the tube length, i.e., P1 (3cm upstream), P2 (vertically above the stenosis), P3 (1.5cm downstream), P4 (3.0cm downstream), and P5 (6cm downstream), as shown in Figure 70. Data were recorded for 30 seconds at each of these five positions, using the LDV device (section 2.9.2) to measure movement at the skin surface, normal to the surface.

The main differences in the set-up here were that the programmable piston pump was switched on (at 1Hz frequency and 7ml stroke volume) in this investigation, and a Windkessel chamber was added (as detailed in section 2.7.4). Another noteworthy difference in the setup here was the control of the flow rate. For the steady flow experiments discussed earlier in chapters 3 and 4, the resistance in the flow was controlled by using a valve far downstream of the tube. However, for the pulsatile flow, as the severity of stenosis increased, the flow rate with a given downstream valve resistance would fall due to

greater total resistance (due to valve and the increased stenosis severity) in the flow. Hence, it was important to devise a controllable variable to standardise the runs. The combined steady and pulsatile flow components provided a mean flow rate, which was maintained constant with all the stenoses severities, between 308-340 ml/min. The pump and the Windkessel were set up to ensure that the peak pressure remained below 110mmHg, and the minimum pressure remained above 60mmHg, to prevent collapsing of the tube. Finally, the pulse pressure was maintained between 30-40mmHg to replicate physiological conditions.

A typical pressure and velocity waveform from a phantom (with 90% stenosed embedded tube) is shown in Figure 107. The time delay between the two variables (determined by using foot of the wave as a reference) can be attributed to the physical gap between the flowmeter (placed upstream) and the pressure transducer (placed far downstream) to ensure that it does not affect the flow near the stenosis region.

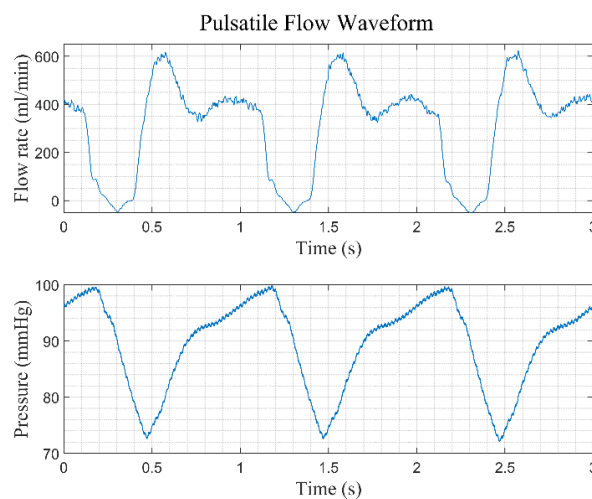


Figure 107: Pressure and Flow rate profile of a pulsatile waveform

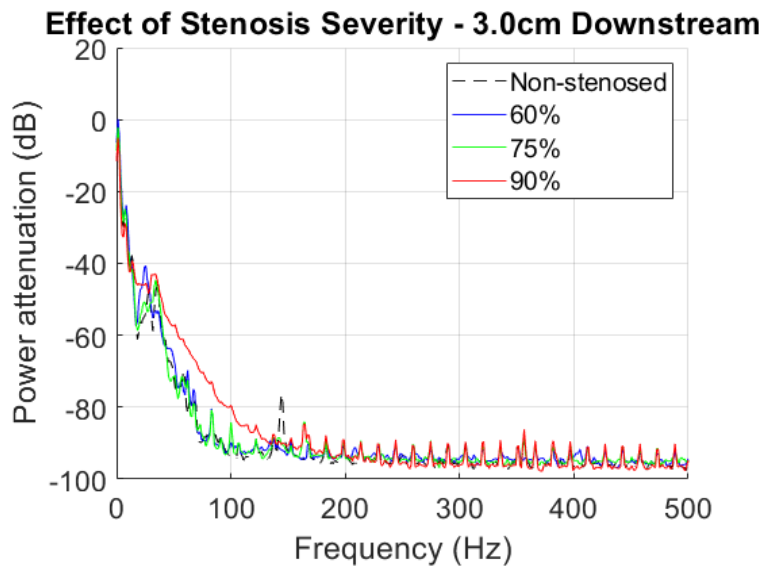
The mean pressure and the mean flow rate from the above traces were 90mmHg (with a pulse pressure of 30mmHg), and 308ml/min, respectively, which is within the physiological range (Keller *et al.*, 1976; Chemaly *et al.*, 2002; Correia *et al.*, 2016), a slightly low mean pressure was maintained to prevent ballooning of the latex tube due to elastic instability.

It can be seen from Figure 107 that the flow rate rises to 600ml/min within approximately the first quarter of each cycle, after which it decreases gradually. The secondary peak during each cycle can be attributed to wave reflections in the perfusion system. With this configuration, the mean flow rate was maintained between 308-340ml/min. There were minor departures from these conditions (depending on which stenosis severity was being investigated), but the pulse pressure range was maintained, i.e., between 30-40mmHg. This range of flow rates was chosen to replicate physiological conditions and also because the effect of increasing FFT area with the changing the stenosis severity was prominent over this range of mean flow rates, as seen in chapter 4.

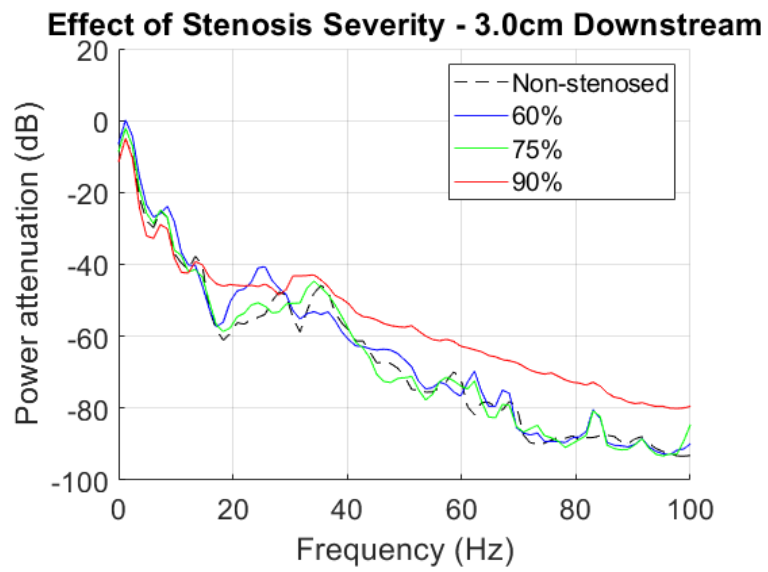
## Results

The time-domain signal was converted into the frequency domain using the FFT technique (section 2.8). On analysing the data obtained from the LDV, disturbances were detected in the post-stenotic region of the tube. Figure 108 (a & b) shows an example FFT spectrum obtained at the P4 position (3cm downstream of the stenosis). It can be seen that, despite some severity effects above 100Hz, the majority of the differences between the stenoses of different severities were seen at frequencies below 120Hz. Comparing the pulsatile flow (Figure 108-b) and the steady flow (Figure 109), the main difference was that for all the stenoses severities in the pulsatile flow, there was a sharp peak in the FFT spectra at very low frequencies, which was absent in the steady flow cases. To highlight this further, a direct comparison of the steady and pulsatile flow is given in Figure 110, which shows the FFT signals at the P4 (3cm downstream) position for a 75% stenosed tube. The strong peak at 1Hz corresponds to the pump frequency.

Another thing to be noticed from Figure 108 is that for the peaks near 1Hz and 10Hz there was an inverse relationship between the stenosis severity and the signal strength (i.e., the 60% stenosis gave rise to the strongest signal). This was because, during each pulse, a smaller volume of fluid flows through the stenosis as the stenosis severity is increased. Hence the downstream position sees a lower effect at those particular frequencies.



(a)



(b)

Figure 108: Effect of stenosis severity with pulsatile flow amplitude of approximately 600ml/min and mean flow rate around 330ml/min

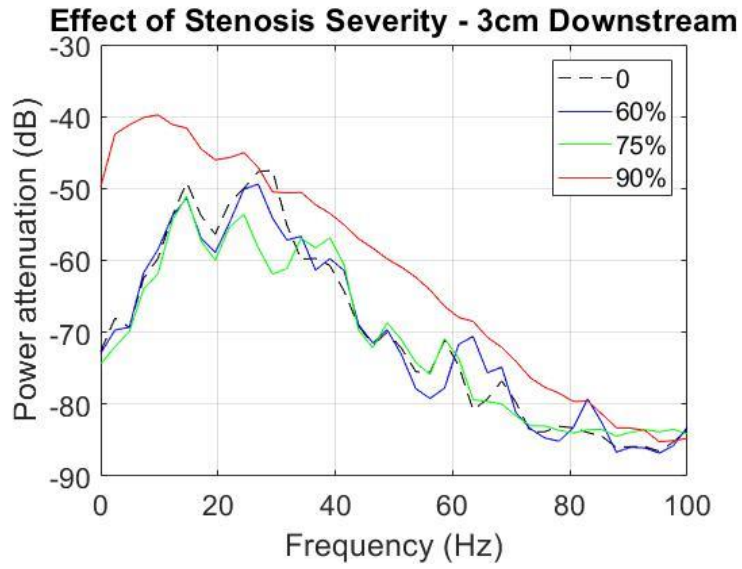


Figure 109: Effect of stenosis severity with a steady flow rate of 350ml/min

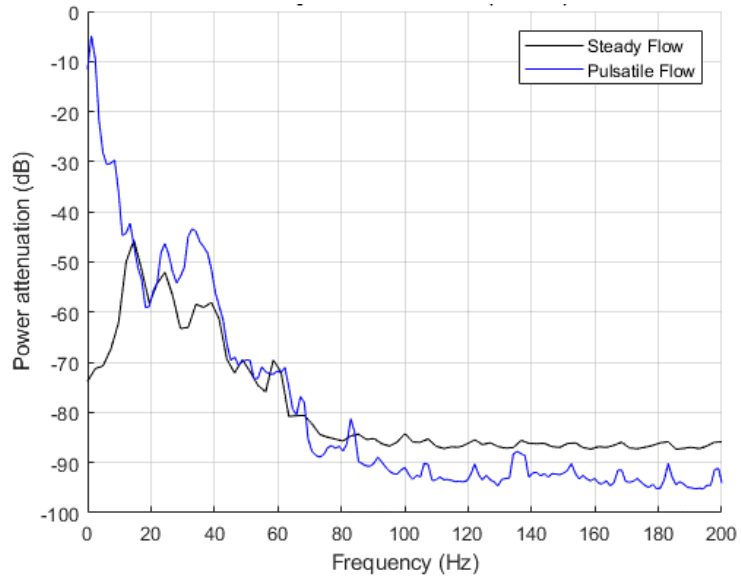


Figure 110: Comparison between steady (350ml/min) and pulsatile flow for a 75% stenosed tube at the P4 position, i.e. 3cm downstream of the stenosis

Another set of peaks was seen between 30-40Hz, where the 60% severity spectra were offset from the rest of the severities. At frequencies above 40Hz, a major difference was seen where the 90% stenosis dominated and had the strongest signal up to 150Hz (Figure 108-b). The strong signal for the 90% stenosis at higher frequencies is in keeping with the strong post-stenotic disturbances, as seen in the steady flow experiments in chapters 3 and 4.

Focusing on the effect of stenosis severities for pulsatile flow, the areas under the FFT spectra were calculated (as in chapters 3 and 4). The calculated areas were normalised to the non-stenosed case (i.e., 0% severity). On mapping these areas for each position (Figure 111), the first thing apparent is that the 75% and 90% stenoses are more dominant in terms of an increase in the normalised FFT area ratio than the 60% case. For the 60% stenosed tube, an increase in the FFT area ratio of 6% was seen at the P1 position. Then, the area ratio dropped down at the stenosis (P2). Beyond that, only some small differences were present for which statistical analysis was carried out (Table 33). For higher frequency disturbances, a dip was seen at the P3 (1.5cm downstream) position, as depicted in Figure 112, after which the flow disturbances did not seem to change substantially.

Table 33: Significance (p-values) of the effect of stenosis severity in Pulsatile Flow (between 0-600Hz), where statistically significant results are highlighted in green

		Compared against			
		0	60%	75%	90%
Fixed severities	0	-	-	-	-
	60%	0.998	-	-	-
	75%	0.729	0.621	-	-
	90%	0.002	0.004	0.000	-

Moving on to the 75% severity, some interesting features were seen. Figure 111 shows a small increase in normalised FFT area ratio at P2 (vertically above the stenosis), and the disturbance increased as the flow progressed towards the P3 (1.5cm downstream) and P4 (3cm downstream) positions. Finally, the disturbances start to disappear as the flow moves further away from the stenosis towards the P5 (6cm downstream) position. For the disturbances within the 50-100Hz frequency range, Figure 112 indicate high-frequency

disturbances upstream of the stenosis (at P1), which started to decrease as they entered the stenosis at P2. Very little or no disturbance was seen in the post-stenotic region within this higher frequency band as they are assumed to be dissipated in the ultrasound gel.

Although statistically not significant, the differences here still hinted at the presence of the disturbances in the post stenotic flow with a 75% stenosed tube. The small differences can be attributed to the signal damping through the ultrasound gel and the axisymmetric geometry of the stenosis. The non-symmetric stenosis generates more disturbed flow (with a much higher and abrupt pressure loss between the pre-stenotic and post-stenotic flow) than the axisymmetric cases (Young and Tsai, 1973a). This is further supported by the results shown in sections 3.3.2 and 4.4.2.

Finally, for 90%, there was detectable skin movement at P1 (Figure 111). These disturbances can be attributed to the reflections produced in the perfusion system due to the pulsatile nature of the flow and/or the speculated transmission of downstream disturbances to the upstream position (as discussed in chapter 4). The disturbance increased (by a small amount) in the 0-50Hz frequency band as the flow approached the stenosis at the P2 position. This trend followed the pattern seen earlier for the 70% stenosis.

As the fluid moved from P2 towards the P3 position, the disturbance developed further and kept on developing. The maximum disturbance seen at the P4 position (around a 9% increase in the area compared to the P3 position) persisted until the fluid reached the P5 position.

In contrast, over the 50–100Hz frequency band, Figure 112 shows an upstream effect (at the P1 position) wherein the area under the curve for the 90% stenosed case was 60% higher than the non-stenosed one. Following a drop at the P2 position, the normalised area ratio under the curve increased steadily. It is worth noting that the increase in the downstream signal in the 50-100 Hz band was stronger than the one seen in the 0-50 Hz band. The steep increase between the P3 and P4 positions indicates a highly disturbed flow in this region. The maximum disturbances were seen at the P5 position, and the gradient between the P4 and P5 positions was shallower than between the P3 and P4 positions. The statistical significance of these changes was investigated.

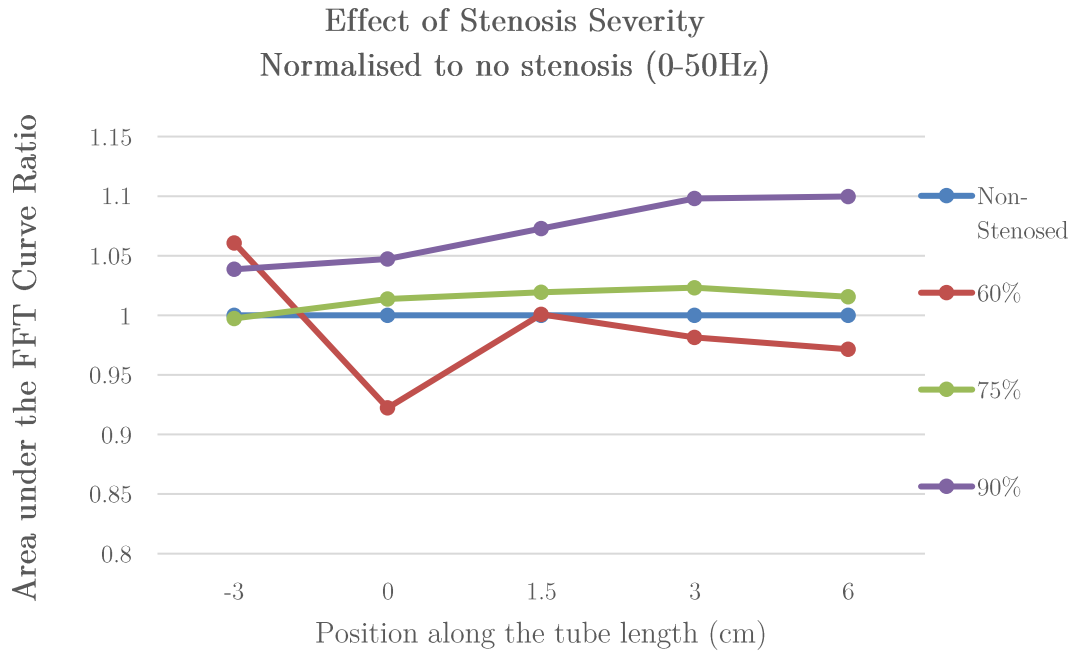


Figure 111: Effect of stenosis severity with the pulsatile flow within the 0-50Hz frequency band (mean flow rate between 310 and 340 ml/min and pulse-pressure between 30-40mmHg)

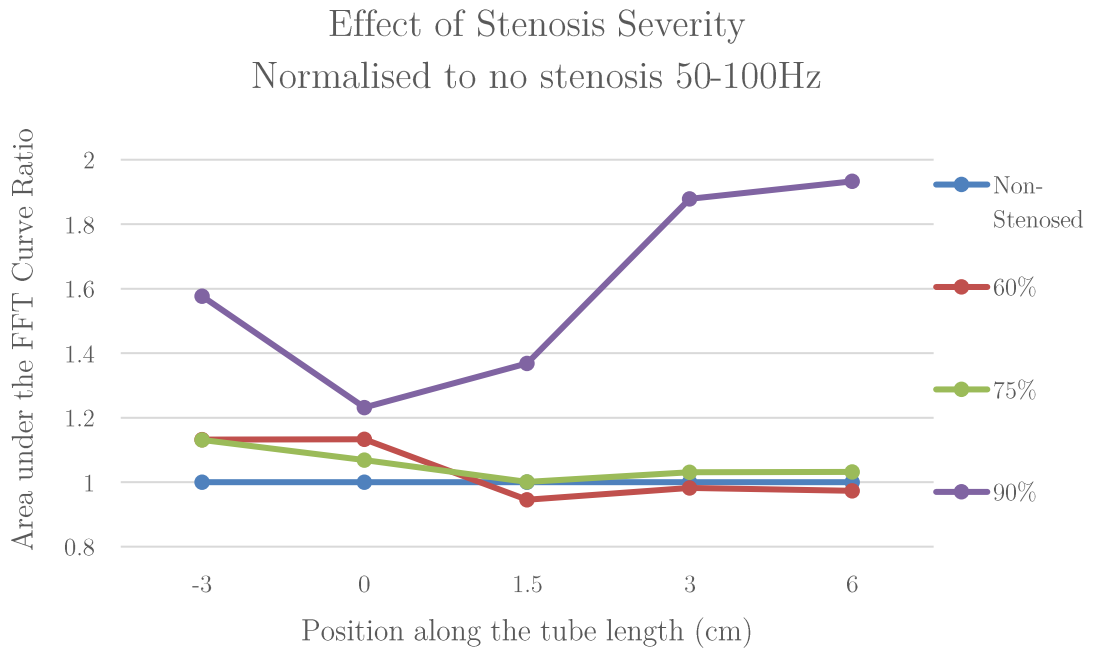


Figure 112: Effect of stenosis severity with the pulsatile flow within the 50-100Hz frequency band (mean flow rate between 310 and 340 ml/min and pulse-pressure between 30-40mmHg)



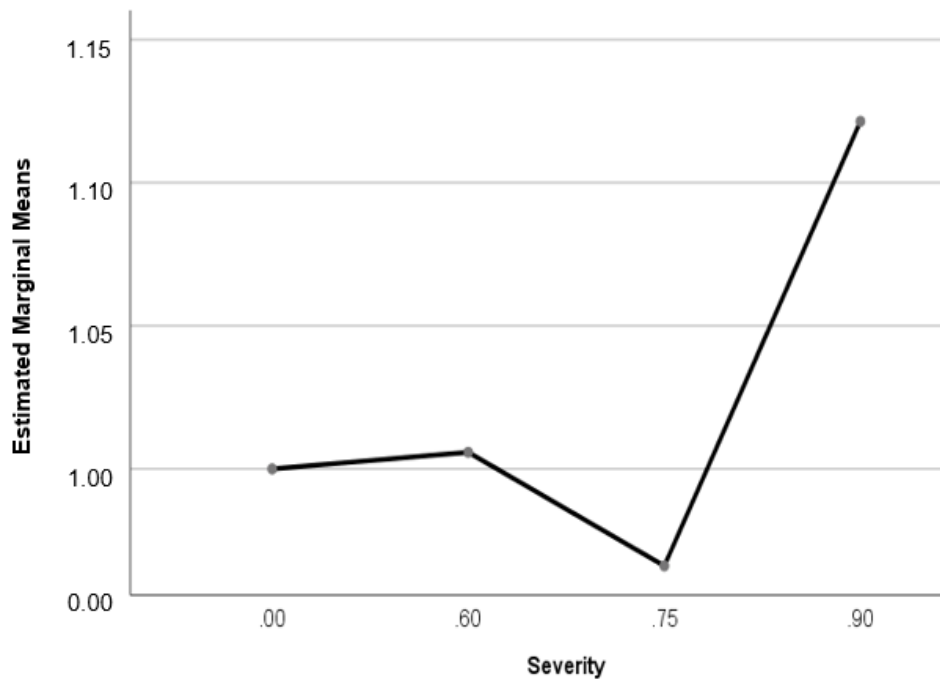


Figure 113: Averaged effect of stenosis severity across all positions shown by the estimated marginal means of the areas under the FFT spectra

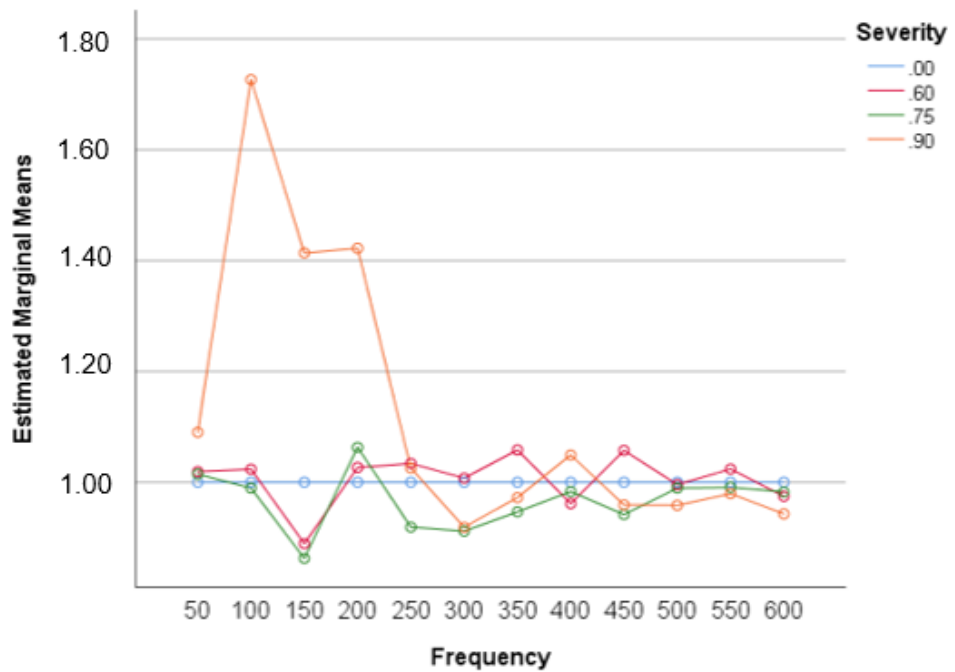


Figure 114: Averaged effect of frequency and stenosis severity across all positions shown by the estimated marginal means of the areas under the FFT spectra

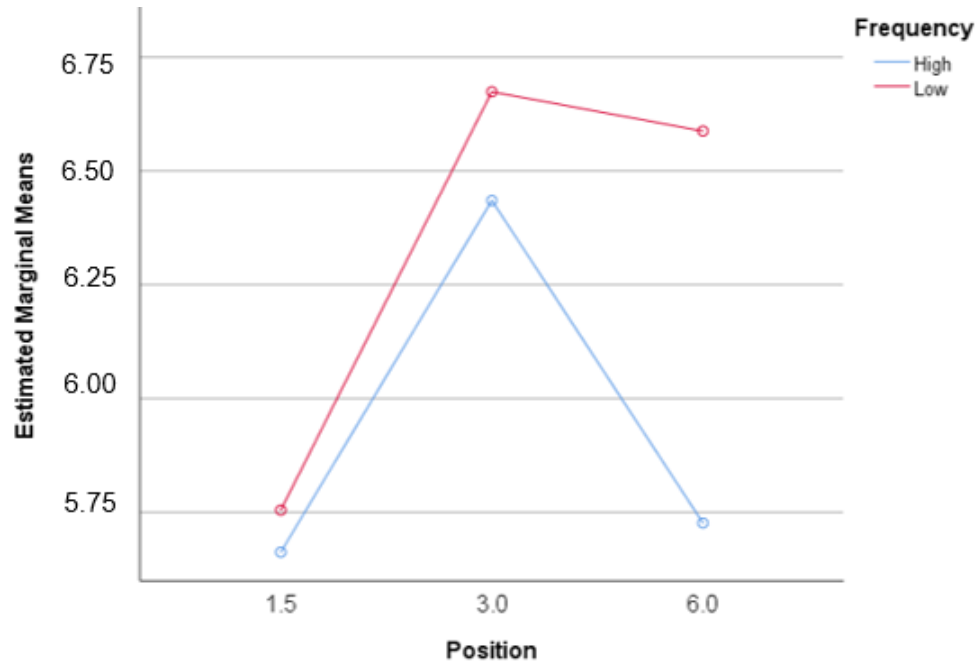


Figure 115: Averaged effect of frequency across all severities at downstream positions (Low Frequencies 0-300Hz, High frequencies 300-600Hz), shown by the estimated marginal means of the areas under the FFT spectra

A two-way ANOVA was conducted to identify the significance of the effect that severity and frequency have on the pulsatile flow individually and their combined interaction effect. To obtain more degrees of freedom (and therefore statistically more robust results), data were combined (as done for steady flow in chapter 4) to look at the averaged effect of stenosis severity and frequency across all positions.

Figure 113 shows no apparent effects of stenosis severity for the 60% and 75% stenoses, and the only dominant effect present was seen for the 90% case. In terms of frequency (Figure 114), high amplitude fluctuations for 90% stenosis were seen in the low-frequency region (up to around 300Hz). A further realisation of this is provided in Figure 115, showing that the disturbances at all downstream positions were greater in the lower frequency region (0-300Hz) compared to the higher frequencies (300-600Hz).

Ultimately, looking at the ANOVA results, the analysis showed statistically significant differences between stenosis severities and frequencies with ( $F(3,96) = 8.544, p = 0.000$ ) and ( $F(11,96) = 2.783, p = 0.004$ ), and the interaction of these two variables also had a

statistically significant effect ( $F(33, 96) = 2.747, p = 0.000$ ). To identify exactly where these differences were, a post-hoc test was carried out, the results of which are summarised in Table 33 and Table 34.

Table 34: Significance of the effect of frequency in Pulsatile Flow - Each number (x) represents a band of 50Hz from (x-50)Hz to xHz. The mean difference is significant at the 0.05 level.

Frequency (Fixed) (x) Hz	Compared against (x') Hz	p-value	Frequency (Fixed) (x) Hz	Compared against (x') Hz	p-value	
50	100	0.236	200	250	0.450	
	150	1.000		300	0.134	
	200	0.860		350	0.446	
	250	1.000		400	0.497	
	300	0.982		450	0.391	
	350	1.000		500	0.350	
	400	1.000		550	0.497	
	450	1.000		600	0.245	
	500	1.000		250	300	1.000
	550	1.000			350	1.000
600	0.998	400	1.000			
100	150	0.336	450		1.000	
	200	0.997	500		1.000	
	250	0.050	550		1.000	
	300	0.007	600		1.000	
	350	0.049	300		350	1.000
	400	0.060			400	1.000
	450	0.038			450	1.000
	500	0.032		500	1.000	
	550	0.060		550	1.000	
	600	0.018		600	1.000	

To conclude, disturbances were detected in moderate to highly stenosed tubes under the pulsatile flow conditions. However, most of the statistically significant effects were seen only in the highly stenosed tube (90% severity), where the disturbances were highest and between the 50-100Hz bands and were significantly different to other frequencies mentioned in Table 34. Furthermore, stronger disturbances were detected near the stenosis as the stenosis severity increased, agreeing with the ultrasound scans from section 3.2. An example of this was seen at the P3 position, where the area under the FFT curve for the 90% case was higher than the 75% case (Figure 111). It was also seen that as the flow changed from steady to pulsatile, small disturbances were seen in the 75% stenosed case, which were not previously seen under the steady flow conditions.

The results from this chapter suggest that there is the potential to identify disturbances at the skin surface (using LDV) for moderate to highly stenosed tubes and perhaps to localise it. Even though the disturbances detected here for the low-moderately stenosed tubes were weak in the axisymmetric cases (and effects of introducing pulsatile flow in the non-axisymmetric remain yet to be explored), it is evident from chapters 3 & 4 that the presence of a more realistic (non-axisymmetric) stenosis amplifies the disturbances and encourages their detection under physiological conditions.

## 6. Errors & Uncertainties, conclusion & future work

### 6.1. Errors & Uncertainties

There are a number of errors and uncertainties, including both systematic as well as random errors and uncertainties in the experimental work that need to be considered.

The flow rate in all the experiments was measured using cannulating electromagnetic flow probes in conjunction with a Transonic flow meter. This was calibrated by timing (thrice) the collection of a known volume of fluid (300ml) using a volumetric flask. The estimated error in the volume measurements was between 10-20ml, corresponding to an error of 3%-7% for a flow rate of 300ml/min.

With regards to the accelerometers, the manufacturer specified an alignment error of +/- 1 degree. However, a more important issue was the lack adhesion of the accelerometers onto the phantoms. Despite different approaches to stabilise the accelerometers on the surface (including double-sided tape, ultrasound gel and superglue), a satisfactory adhesion was not achieved. Hence, their use was discontinued in the main phantom experiments.

While using pressure transducers in the preliminary work, although the device had a sensitivity of  $5\mu\text{V}/\text{V}/\text{mmHg}$  and a low linearity & hysteresis error of  $< +/- 1\%$ , the flutter of the sensor (in the stream of the flow) has to be taken into account. This was a random error and it induced additional disturbances in the flow as was shown with a comparison done by the LDV readings with and without a pressure transducer inserted in the tube.

The LDV calibrations between the voltage and displacement, was done by using a 600 mm Vernier distance measuring device with a precision of 0.02mm. The Vernier scale was fitted with a magnifying glass to minimise the parallax error. However, there was a random instrumental error associated with the LDV equipment. There were instances when, after a prolonged continuous usage (over half a day), the signal would destabilise and completely drift off the scale. In some of these cases, the equipment was reset, and it continued to take readings as normal and when feasible, the equipment was allowed to

rest for a couple of minutes before resuming the experiments. Another potential error associated with the LDV measurements is the loading of the skin and gel by the retro-reflective patches. However, the weight of the patches was less than 5mg and hence this was considered to be negligible.

An environmental problem affecting both the LDV, and the accelerometer readings was the acoustic background noise in the lab. The set-up was sensitive to external vibrations (e.g., construction work around the lab, footsteps, vibrations from the return pump and the programmable piston pump). To minimise these problems, the pumps were placed on separate rigs. Secondly, a hard rubber damping material was placed under the tube/phantom to reduce vibrations transmitted through the lab benching. With that in place, the effect of small movements in the lab was negligible. However, runs recorded during which there were heavy footsteps and loud noise were discarded, and on occasions, the experiments had to be conducted late in the day when there was no audible external noise.

A final difficulty that is worth mentioning was the placement of the stenosis inside the tube. A small misalignment of the axisymmetric stenosis could cause disturbances in the post-stenotic region. Therefore, an effort was made to virtually align the stenosis co-axially with the long axis of the tube by using rods from either end to align it. However, on securing the stenosis with the O-rings, a slight misalignment may have occurred. A hint of this was seen in some of the ultrasound scans where the post-stenotic jet was projected in an upwards direction. Effects of this were also seen in the embedded phantom case as discussed in chapter 4. One of the possible solutions to this could be a 3D printed tube, with a stenoses integrated into the printed design, although achieving the appropriate elastic properties would be challenging.

## 6.2. Conclusion

Cardiovascular disease (CVD) is the leading cause of death in the developed world, with the incidence increasing elsewhere. The pathologies such as arteriosclerosis and atherosclerosis, the thickening and stiffening of arterial walls and/or the build-up of the

plaque inside the arteries can cause serious complications. Given the complex, chronic nature of these disorders, it has been agreed that screening of events during all stages of their pathogenesis could contribute to a better early diagnostic assessment, risk assessment and measurement of the treatment effects. With the current methods available for screening, there are added expense, technical complexities and potential risks and trauma to the patients. Therefore, there is a pressing need for a reliable and an easy to use early diagnostic technique for large populations.

This study was initiated with the identification of the materials to mimic the physiological conditions as detailed in chapter 2. A Penrose latex tube was chosen as a suitable material to model the carotid artery, through which a 40:60 (by volume) glycerine-water solution was perfused at physiological steady as well as pulsatile flows. Different stenoses were then introduced into the tube to mimic the atherosclerotic plaque, both axisymmetric and non-axisymmetric. The flow features in a bare tube were first studied and then to mimic a human neck, the stenosed tube was embedded within a standardised phantom, filled with the ultrasound gel (simulating the soft tissues). The phantom was then covered with a polyurethane film (Platilon), simulating the skin, and constraining the ultrasound gel in a well-defined shape. Once the flow perfused through the phantom, stenosis-induced disturbances were generated in the flow, and these disturbances were then detected at the Platilon surface using LDV. Other means, including the use of accelerometers and pressure transducers were also investigated, but the accelerometers did not provide meaningful results and the pressure transducers, due to their intrusive nature, affected the flow profile inside the tube. A collaboration was also initiated with the Drakakis group (at Imperial College) where microphones were mounted onto the Platilon surface, in an attempt to directly detect the sound caused by the post-stenotic disturbances (bruit). Some interesting features were seen there but no conclusions can yet be drawn at this early stage.

The effects of the flow rate, stenosis geometry, stenosis symmetry and the fluid viscosity were investigated in chapter 3, for a bare stenosed tube. An initial study with the accelerometers (on a bare tube) and ultrasound scans confirmed the presence of perturbations in the flow in an axisymmetrically stenosed tube (with area reduction  $\geq 75\%$ ). In this initial study, it was further seen that these disturbances in the tube varied along its

length. The disturbances moved closer to the stenosis with increasing flow rates and/or increasing stenosis severities, over an increased range of frequencies. The pattern was seen using both the accelerometer measurements and the ultrasound scans and is consistent with the findings of others (Young and Tsai, 1973a; Ahmed and Giddens, 1983; Sadeghi et al., 2011) and the measurements taken using the LDV device. Furthermore, the effects of the fluid viscosity were also studied in a bare stenosed tube, where it was established that disturbances originated at a lower stenosis severity and or a lower flow rate (and hence the Reynolds number) for fluids with a lower viscosity than that of blood (4cP). Also, as the viscosity was increased, some of these disturbances started to disappear, and re-appeared again at higher stenosis severity and/or higher flow rate. Finally, the introduction asymmetry in the stenosis enabled detection of the post-stenotic disturbances at lower flow rates and stenoses severities.

In chapter 4, the tube was embedded in the phantom, and it was seen that some of the disturbances seen earlier with the bare tube experiments were damped. It is acknowledged that the interaction between the tube wall and the gel has not been investigated in this study, hence the degree of damping and the effects of artefacts (such as air bubbles) is yet to be explored. This is a major undertaking and has formed a basis of a PhD thesis of another student in our group. The disturbances with a severely stenosed tube (90% reduction in area, axisymmetrically) were clearly visible at physiological mean flow rates.

There was no clear-cut trend seen for the 60% and the 75% axisymmetrically stenosed cases. Since physiologically, atherosclerotic plaques are invariably not symmetrical and the simplification of the model (of using axisymmetrically stenosed tubes) produced disturbances with insufficient energy to travel through the ultrasound gel and be detectable at the Platilon surface. However, when a highly stenosed tube was studied at flow rates above 300ml/min (well within the physiological range), the waves' amplitude was large enough to be detectable at the surface, in spite of the damping in the ultrasound gel. Also, with the increasing flow rates, it was seen that the disturbances covered a wider range of frequencies. Finally, the positional effect was also studied in the phantom, and it was seen that some of the highest disturbances that were earlier seen near the stenosis (in the bare tube experiments), were present at further downstream positions in the phantom. This



effect was explained by the speculated misorientation of the axisymmetric stenosis in the tube. The investigations in this chapter showed that disturbances generated due to a severe axisymmetric stenosis (i.e., 90% reduction in area) in the carotid are detectable in the post-stenotic region, provided that the flow rate is high enough (around 300ml/min as mentioned above). In vivo, a severe stenosis may or may not reduce the flow rate in the artery, depending on the organ's capacity to autoregulate its blood flow. In the case of autoregulation of the flow, it is acknowledged that that flow rate might not reach a high value to produce post-stenotic instabilities in the flow. However, if the flow rate is high enough, the results from this study provide a suitable method for detection of a stenosis and its approximate location. A recent in-vitro study showed that at very flow rates resulting from a severe stenosis, the downstream signal could be differentiated from that of a non-stenotic artery by low amplitude oscillations at frequencies below 50Hz (Mancini *et al.*, 2020). This phenomenon warrants further investigation and may also make it possible to detect severe stenoses by means of a specific acoustic signature.

Further in chapter 4, the investigation of the non-axisymmetric stenosis showed a high dependence of the downstream disturbances, on the symmetry of the stenosis geometry. It was shown that the disturbances were detectable at the skin surface for a moderately stenosed tube (non-axisymmetric), with a 75% severity. This agrees with a recent computational study, which showed the presence of flow instabilities in a patient specific (non-axisymmetrically) stenosed tube between 56-75% stenoses severities (Mancini *et al.*, 2020).

Following this, in chapter 5, the effect of introducing pulsatile flow was investigated and it was found that the effects at the 75% stenosis severity started becoming more apparent, although still weak. The positional variation in the post-stenotic flow was still present, making that another important variable in identification of the location of stenosis. An important feature that was seen in the studies with the pulsatile flow was that the 1Hz disturbances attributed to the piston pump frequency, were highest for the 60% stenosed tubes and lowest for the 90% one. This was due to the increased resistance in the flow path, due to the increased severity, which would increase the pressure inside the tube. In a physiological scenario, if flow through an artery is severely impeded, the cardiovascular

system would redistribute the flow through additional parallel paths thus reducing the flow rate in the stenosed vessel while still maintaining the required cardiac output and regulating the pressure.

Finally, preliminary computational (Appendix A) simulations were carried out, results of which yet remain to be validated. With the fluids' simulations, it was shown in (Appendix) that the trends of the effects of the stenosis severities and the flow rates were in-line with the experimental work. An attempt was made to develop a fluid-structure interaction model to validate the phantom experiments as well, however, the limitations of the available computational resources (discussed earlier, together with the magnitude of the difficulties as mentioned above) prevented the study from progressing in that direction.

In conclusion, the results from this study show that the presence of a stenosis induces disturbances in the post-stenotic flow. These disturbances are dependent on the flow rates, stenosis severities, stenosis symmetry and the viscosity of the fluid. Furthermore, the disturbances generated by changing these parameters influence the frequency and the location of these disturbances. In this work, a novel method was established for detecting the stenosis-induced disturbances in the arterial flow. The results from this suggest the feasibility of using LDV to infer the presence of a stenosis at an early stage before symptoms are evident.

### 6.3. Current limitations and Future Goals

To advance the work described in this thesis, there are a number of suggestions that can be made to enhance our understanding of the flow behaviour inside the carotid artery and its interaction with the surrounding tissues.

Firstly, more complex and patient specific stenoses can be investigated. The asymmetry in the geometry can give rise to the flow disturbance at low flow rates for even low to moderately stenosed tubes. These flow disturbances can then be directly detected at the skin surface without direct physical contact using LDV. Secondly, a further extension of these visualisations could be done by using particle flow velocimetry which would allow instantaneous measurements of the velocity over the cross section of the stenosed tube,

although sourcing a tube with the required transparency and elastic properties would be challenging. This would allow a non-invasive investigation of the flow patterns, in form of 3D velocity vectors, for the whole area throughout the length and cross section of the tube in the pre- and post-stenotic flow, which can then be directly validated against the CFD model.

A full model of the carotid artery (including the internal and the external branch) can be investigated. In a scenario where one of the branches is highly stenosed, this would allow for the relieving of the pressure in that branch, hence modelling a physiologically more realistic case. In addition to this, a more realistic cylindrical neck phantom can be made with composite materials to simulate muscle, tendon, ligaments and hard tissue.

Finally, a fluid-structure interaction model needs to be developed and tested. It must be noted that extensive computational power would be required to resolve the flow features at such small scales, as this would require turbulent models such as Large Eddy Simulation (LES) or Detached Eddy Simulation (DES). Hence, running a highly tuned CFD model and then strongly coupling it with the structural part will pose a serious challenge. Therefore, a good starting point, to visualise the flow features as well as the displacements in the structure, would be to start with a flow rate of 325-375ml/min passing through a horizontal tube with a moderate (approximately 75%) asymmetric stenosis. This could allow the model to run in a stable manner and allow us to study the energy transfer mechanisms from the disturbed post-stenotic flow to the arterial wall and thence through the soft tissue to the skin surface.

## 7. References

A. Scroggs, R. (2001) 'Validation of Computational Fluid-Structure Interaction Models By Comparison with Collapsible Tube Experiments'. University of Sheffield.

Abdul Khader, S. M. *et al.* (2010) 'A comparative fluid-structure interaction study of stenosed and normal common carotid artery', *World Journal of Modelling and Simulation*.

Abedin, M., Tintut, Y. and Demer, L. L. (2004) 'Vascular calcification: Mechanisms and clinical ramifications', *Arteriosclerosis, Thrombosis, and Vascular Biology*, 24(7), pp. 1161–1170. doi: 10.1161/01.ATV.0000133194.94939.42.

ADInstruments (2014) 'PowerLab /35 series - Owner's Guide - U-PL35XX/OG-35E'. ADInstruments Pty Ltd.

ADInstruments (2015) *Using Spectrum in LabChart 7. 1 These notes apply to LabChart v7. 1 or later versions*. Available at: <http://cdn.adinstruments.com/adi-web/software-tips/Spectrum.pdf> (Accessed: 3 February 2021).

ADInstruments (2019) 'ADXL337 Small, low power, 3-axis accelerometer'. Analog Devices. Available at: <https://www.analog.com/media/en/technical-documentation/data-sheets/ADXL337.pdf>.

Adla, T. and Adlova, R. (2014) 'Multimodality imaging of carotid stenosis', *International Journal of Angiology*, 24(3), pp. 179–184. doi: 10.1055/s-0035-1556056.

Aggoun, Y. *et al.* (2000) 'Mechanical properties of the common carotid artery in Williams syndrome', *Heart*, 84(3), pp. 290–293. doi: 10.1136/heart.84.3.290.

Ahmed, S. A. and Giddens, D. P. (1983) 'Flow disturbance measurements through a constricted tube at moderate Reynolds numbers', *Journal of Biomechanics*, 16(12), pp. 955–963. doi: 10.1016/0021-9290(83)90096-9.

Ahmed, S. A. and Giddens, D. P. (1984) 'Pulsatile poststenotic flow studies with laser Doppler anemometry', *Journal of Biomechanics*, 17(9), pp. 695–705. doi: 10.1016/0021-9290(84)90123-4.

Akhtar, R. *et al.* (2011) 'Characterizing the elastic properties of tissues', *Materials Today*, 14(3), pp. 96–105. doi: 10.1016/S1369-7021(11)70059-1.

Amen, R. (2014) *Summary of safety and effectiveness*. Available at: [https://www.accessdata.fda.gov/cdrh\\_docs/pdf13/K130581.pdf](https://www.accessdata.fda.gov/cdrh_docs/pdf13/K130581.pdf).

Anderson, M. E. and Trahey, G. E. (1998) 'The direct estimation of sound speed using pulse–echo ultrasound', *The Journal of the Acoustical Society of America*. doi: 10.1121/1.423889.

- Andreucci, M., Solomon, R. and Tasanarong, A. (2014) 'Side effects of radiographic contrast media: Pathogenesis, risk factors, and prevention', *BioMed Research International*, 2014. doi: 10.1155/2014/741018.
- ANSYS FLUENT 13 User's Guide (2013) *Ansys Fluent Theory Guide*, ANSYS Inc., USA.
- Bai, Y. and Bai, Q. (2018) *Subsea engineering handbook, Subsea Engineering Handbook*. doi: 10.1016/C2016-0-03767-1.
- Banks, H. T. *et al.* (2013) 'Material parameter estimation and hypothesis testing on a 1D viscoelastic stenosis model: Methodology', *Journal of Inverse and Ill-Posed Problems*, 21(1), pp. 25–57. doi: 10.1515/jip-2012-0081.
- Benjamin, E. *et al.* (2019) *Heart Disease and Stroke Statistics-2019 At-a-Glance Heart Disease, Stroke and other Cardiovascular Diseases*.
- Bentzon, J. F. *et al.* (2014) 'Mechanisms of plaque formation and rupture', *Circulation Research*. doi: 10.1161/CIRCRESAHA.114.302721.
- Binns, R. L. and Ku, D. N. (1989) 'Effect of stenosis on wall motion. A possible mechanism of stroke and transient ischemic attack', *Arteriosclerosis*, 9(6), pp. 842–847. doi: 10.1161/01.atv.9.6.842.
- Biyue, L. and Tang, D. (2000) 'Numerical simulation of viscous flows in collapsible tubes with stenoses', *Applied Numerical Mathematics*, 32(1), pp. 87–101. doi: 10.1016/S0168-9274(99)00015-X.
- Bressloff, N. W. (2007) 'Parametric geometry exploration of the human carotid artery bifurcation', *Journal of Biomechanics*, 40(11), pp. 2483–2491. doi: 10.1016/j.jbiomech.2006.11.002.
- Brewin, M. P. (2010) *Carotid atherosclerotic plaque characterisation by measurement of ultrasound sound speed in vitro at high frequency, 20 MHz*. Queen Mary University of London.
- Brewin, M. P. *et al.* (2015) 'Characterisation of Elastic and Acoustic Properties of an Agar-Based Tissue Mimicking Material', *Annals of Biomedical Engineering*, 43(10), pp. 2587–2596. doi: 10.1007/s10439-015-1294-7.
- Calderon-Arnulphi, M. *et al.* (2011) 'In vivo evaluation of quantitative MR angiography in a canine carotid artery stenosis model', *American Journal of Neuroradiology*, 32(8), pp. 1552–1559. doi: 10.3174/ajnr.A2546.
- Cebral, J. R. *et al.* (2008) 'Flow-area relationship in internal carotid and vertebral arteries', *Physiological Measurement*, 29(5), pp. 585–594. doi: 10.1088/0967-3334/29/5/005.

- Chan, W. Y., Ding, Y. and Tu, J. Y. (2007) 'Modeling of non-Newtonian blood flow through a stenosed artery incorporating fluid-structure interaction', *ANZIAM Journal*, 47, p. 507. doi: 10.21914/anziamj.v47i0.1059.
- Chemaly, E. *et al.* (2002) 'Comparison of the central pulse pressure estimated from the pulse wave propagation velocity and the carotid pulse pressure measured by applanation tonometry', *Archives des Maladies du Coeur et des Vaisseaux*, 95(7–8), pp. 637–640.
- Cho, Y. I. and Kensey, K. R. (1991) 'Effects of the non-Newtonian viscosity of blood on flows in a diseased arterial vessel. Part 1: Steady flows.', *Biorheology*, 28(3–4), pp. 241–62. Available at: <http://www.ncbi.nlm.nih.gov/pubmed/1932716> (Accessed: 15 November 2019).
- Cole, S. (2016) 'Reflective vs. Retroreflective tape'. Available at: <https://reflectivetape.info/reflective-versus-retro-reflective-tape-what-is-the-difference/>.
- Correia, M. *et al.* (2016) '4D ultrafast ultrasound flow imaging: In vivo quantification of arterial volumetric flow rate in a single heartbeat', *Physics in Medicine and Biology*. doi: 10.1088/0031-9155/61/23/L48.
- Covestro (2017) 'Product Information Plaiton ® U Highly Elastic Polyurethane Films'.
- Dabrowska, A. K. *et al.* (2016) 'Materials used to simulate physical properties of human skin', *Skin Research and Technology*, 22(1), pp. 3–14. doi: 10.1111/srt.12235.
- Dan Russell (2013) *Longitudinal and Transverse Wave Motion*, *The Pennsylvania State University*. Available at: <http://www.acs.psu.edu/drussell/demos/waves/wavemotion.html> (Accessed: 23 April 2017).
- Deplano, V. and Siouffi, M. (1999) 'Experimental and numerical study of pulsatile flows through stenosis: Wall shear stress analysis', *Journal of Biomechanics*, 32(10), pp. 1081–1090. doi: 10.1016/S0021-9290(99)00098-6.
- Fromageau, J. *et al.* (2007) 'Estimation of polyvinyl alcohol cryogel mechanical properties with four ultrasound elastography methods and comparison with gold standard testings', *IEEE Transactions on Ultrasonics, Ferroelectrics, and Frequency Control*. doi: 10.1109/TUFFC.2007.273.
- Gere, J. M. and Goodno, B. J. (2009) *Mechanics of materials*. Cengage Learning.
- Ghalichi, F. *et al.* (1998) 'Low Reynolds number turbulence modeling of blood flow in arterial stenoses', *Biorheology*, 35(4–5), pp. 281–294. doi: 10.1016/S0006-355X(99)80011-0.

Hasan, a B. M. T. and Das, D. K. (2008) 'Numerical Simulation of Sinusoidal Fluctuated Pulsatile Laminar Flow Through Stenotic Artery', *Journal of Applied FluidMechanics*, 1(2), pp. 25–35.

Herzig, R. *et al.* (2004) 'Comparison of ultrasonography, CT angiography, and digital subtraction angiography in severe carotid stenoses', *European Journal of Neurology*, 11(11), pp. 774–781. doi: 10.1111/j.1468-1331.2004.00878.x.

Hong, H. *et al.* (2017) 'Characteristics of pulsatile flows in curved stenosed channels', *PLoS ONE*. doi: 10.1371/journal.pone.0186300.

Hopkins, J. (2017) *Aortic Disease*. Available at: [https://www.hopkinsmedicine.org/heart\\_vascular\\_institute/conditions\\_treatments/conditions/aorta.html](https://www.hopkinsmedicine.org/heart_vascular_institute/conditions_treatments/conditions/aorta.html) (Accessed: 22 December 2017).

Hu, Y. *et al.* (2014) *Optimizing cardiac resynchronization therapy to minimize ATP consumption heterogeneity throughout the left ventricle: A simulation analysis using a canine heart failure model*, *Heart Rhythm*. Elsevier Inc. doi: 10.1016/j.hrthm.2014.03.021.

Hyun, S., Kleinstreuer, C. and Archie, J. P. (2000) 'Hemodynamics analyses of arterial expansions with implications to thrombosis and restenosis', *Medical Engineering and Physics*, 22(1), pp. 13–27. doi: 10.1016/S1350-4533(00)00006-0.

Iida, N. (1978) 'Influence of Plasma Layer on Steady Blood Flow in Microvessels', *Japanese Journal of Applied Physics, Part 1: Regular Papers and Short Notes and Review Papers*, 17(1), pp. 203–214. doi: 10.1143/JJAP.17.203.

Ismail, Z. *et al.* (2008) 'A power-law model of blood flow through a tapered overlapping stenosed artery', *Applied Mathematics and Computation*, 195(2), pp. 669–680. doi: 10.1016/j.amc.2007.05.014.

Johnston, B. M. *et al.* (2004) 'Non-Newtonian blood flow in human right coronary arteries: Steady state simulations', *Journal of Biomechanics*, 37(5), pp. 709–720. doi: 10.1016/j.jbiomech.2003.09.016.

Kaazempur-Mofrad, M. R. *et al.* (2005) 'Mass transport and fluid flow in stenotic arteries: Axisymmetric and asymmetric models', *International Journal of Heat and Mass Transfer*. doi: 10.1016/j.ijheatmasstransfer.2005.05.004.

Kalra and Lowe (2016) 'Mechanical Behaviour of Skin: A Review', *Journal of Material Science & Engineering*. doi: 10.4172/2169-0022.1000254.

Kanyanta, V., Ivankovic, A. and Karac, A. (2009) 'Validation of a fluid-structure interaction numerical model for predicting flow transients in arteries', *Journal of Biomechanics*, 42(11), pp. 1705–1712. doi: 10.1016/j.jbiomech.2009.04.023.

- Kapur, J. (1985) 'Mathematical models in biology and medicine'.
- Kaufmann, B. A. (2009) 'Ultrasound molecular imaging of atherosclerosis', *Cardiovascular Research*, 83(4), pp. 617–625. doi: 10.1093/cvr/cvp179.
- Keller, H. M. *et al.* (1976) 'Noninvasive measurement of velocity profiles and blood flow in the common carotid artery by pulsed doppler ultrasound', *Stroke*, 7(4), pp. 370–377. doi: 10.1161/01.STR.7.4.370.
- Khader, S. M. A. *et al.* (2014) 'FSI Simulation of Increased Severity in Patient Specific Common Carotid Artery Stenosis', in *3rd International Conference on Mechanical, Electronics and Mechatronics Engineering (ICMEME'2014) March 19-20, 2014 Abu Dhabi (UAE)*. Abu Dhabi, pp. 16–21.
- Khalafvand, S. S. and Han, H. C. (2015) 'Stability of Carotid Artery Under Steady-State and Pulsatile Blood Flow: A Fluid-Structure Interaction Study', *Journal of Biomechanical Engineering*, 137(6). doi: 10.1115/1.4030011.
- Khamdaeng, T. *et al.* (2012a) 'Arterial stiffness identification of the human carotid artery using the stress-strain relationship in vivo', *Ultrasonics*, 52(3), pp. 402–411. doi: 10.1016/j.ultras.2011.09.006.
- Khamdaeng, T. *et al.* (2012b) 'Arterial stiffness identification of the human carotid artery using the stress-strain relationship in vivo', *Ultrasonics*, pp. 402–411. doi: 10.1016/j.ultras.2011.09.006.
- Khanafer, K. and Berguer, R. (2009) 'Fluid-structure interaction analysis of turbulent pulsatile flow within a layered aortic wall as related to aortic dissection', *Journal of Biomechanics*, 42(16), pp. 2642–2648. doi: 10.1016/j.jbiomech.2009.08.010.
- Klabunde, R. E. (2007) *CV Physiology / Angina*. Available at: <https://www.cvphysiology.com/CAD/CAD007> (Accessed: 15 November 2017).
- Knowles (2013) 'Zero-Height SiSonic Microphone With Extended Low Frequency Performance', pp. 1–11. Available at: [https://media.digikey.com/pdf/Data Sheets/Knowles Acoustics PDFs/SPU1410LR5H-QB.pdf](https://media.digikey.com/pdf/Data%20Sheets/Knowles%20Acoustics%20PDFs/SPU1410LR5H-QB.pdf).
- Koeppen, B. M. and Stanton, B. A. (2017) *Berne & Levy Physiology, Berne & Levy Physiology*. Elsevier. doi: 10.1016/B978-0-323-07362-2.50044-9.
- Krejza, J. *et al.* (2006) 'Carotid artery diameter in men and women and the relation to body and neck size', *Stroke*. doi: 10.1161/01.STR.0000206440.48756.f7.
- Kundu, P. K., Cohen, I. M. and Dowling, D. R. (2011) *Fluid Mechanics with Multimedia DVD*. Academic Press. Available at: <http://www.google.com/patents?hl=en&lr=&vid=USPAT7962295&id=2gfnAQAAEBAJ&oi=fnd&dq=fluid+mechanisms+kundu&printsec=abstract> (Accessed: 15 November 2019).



Laerd (2018) *One-way ANOVA in SPSS Statistics, Laerd Statistics*. Available at: <https://statistics.laerd.com/spss-tutorials/one-way-anova-using-spss-statistics.php> (Accessed: 22 November 2019).

LaMorte, W. (2016) *Pathogenesis of Atherosclerosis, Boston University School of Public Health*. Available at: [http://sphweb.bumc.bu.edu/otlt/mph-modules/ph/ph709\\_heart/PH709\\_Heart3.html](http://sphweb.bumc.bu.edu/otlt/mph-modules/ph/ph709_heart/PH709_Heart3.html) (Accessed: 15 December 2017).

Lee, J. *et al.* (2019) ‘A computationally efficient mean sound speed estimation method based on an evaluation of focusing quality for medical ultrasound imaging’, *Electronics (Switzerland)*. doi: 10.3390/electronics8111368.

Lee, K. W. and Xu, X. Y. (2002) ‘Modelling of flow and wall behaviour in a mildly stenosed tube’, *Medical Engineering and Physics*, 24(9), pp. 575–586. doi: 10.1016/S1350-4533(02)00048-6.

Leondes, C. T. (2001) *Biomechanical systems: techniques and applications*. CRC Press.

Li, M. X. *et al.* (2007) ‘Numerical analysis of pulsatile blood flow and vessel wall mechanics in different degrees of stenoses’, *Journal of Biomechanics*, 40(16), pp. 3715–3724. doi: 10.1016/j.jbiomech.2007.06.023.

Liao, W., Lee, T. S. and Low, H. T. (2004) ‘Numerical studies of physiological pulsatile flow through constricted tube’, *International Journal of Numerical Methods for Heat and Fluid Flow*, 14(5), pp. 689–713. doi: 10.1108/09615530410539991.

Lip, G. Y. H. (2007) *Comprehensive hypertension, Comprehensive Hypertension*. Mosby. doi: 10.1016/B978-0-323-03961-1.X5001-6.

Liu, H., Zhang, J. and Lu, Y. (2018) ‘Yielding characterization of waxy gels by energy dissipation’, *Rheologica Acta*. Springer Verlag, 57(6–7), pp. 473–480. doi: 10.1007/s00397-018-1094-8.

Łoboz-Rudnicka, M. *et al.* (2018) ‘Gender-related differences in the progression of carotid stiffness with age and in the influence of risk factors on carotid stiffness’, *Clinical Interventions in Aging*, 13, pp. 1183–1191. doi: 10.2147/CIA.S161711.

Long, Q. *et al.* (2001) ‘Numerical investigation of physiologically realistic pulsatile flow through arterial stenosis’, *Journal of Biomechanics*, 34(10), pp. 1229–1242. doi: 10.1016/S0021-9290(01)00100-2.

Mancini, V., Tommasin, D., *et al.* (2019) ‘Detecting carotid stenosis from skin vibrations using Laser Doppler Vibrometry – An in vitro proof-of-concept’, *PLoS ONE*. doi: 10.1371/journal.pone.0218317.

Mancini, V., Bergersen, A. W., *et al.* (2019) ‘High-Frequency Fluctuations in Post-stenotic Patient Specific Carotid Stenosis Fluid Dynamics: A Computational Fluid Dynamics Strategy Study’, *Cardiovascular Engineering and Technology*. Springer New York LLC. doi: 10.1007/s13239-019-00410-9.

Mancini, V. *et al.* (2020) ‘Computed poststenotic flow instabilities correlate phenotypically with vibrations measured using laser doppler vibrometry: Perspectives for a promising in vivo device for early detection of moderate and severe carotid stenosis’, *Journal of Biomechanical Engineering*. doi: 10.1115/1.4046586.

Massai, D. *et al.* (2012) ‘Shear-induced platelet activation and its relationship with blood flow topology in a numerical model of stenosed carotid bifurcation’, *European Journal of Mechanics, B/Fluids*. doi: 10.1016/j.euromechflu.2012.03.011.

Mast, T. D. (2000) ‘Empirical relationships between acoustic parameters in human soft tissues’, *Acoustic Research Letters Online*. doi: 10.1121/1.1336896.

Mekheimer, K. S. and Kot, M. A. E. (2008) ‘The micropolar fluid model for blood flow through a tapered artery with a stenosis’, *Acta Mechanica Sinica/Lixue Xuebao*, 24(6), pp. 637–644. doi: 10.1007/s10409-008-0185-7.

Mittal, R., Simmons, S. P. and Najjar, F. (2003) ‘Numerical study of pulsatile flow in a constricted channel’, *Journal of Fluid Mechanics*, 485(485), pp. 337–378. doi: 10.1017/S002211200300449X.

Miura, K. (2020) ‘Tunica intima compensation for reduced stiffness of the tunica media in aging renal arteries as measured with scanning acoustic microscopy’, *PLoS ONE*, 15(11 November). doi: 10.1371/journal.pone.0234759.

Moerman, A. M. *et al.* (2019) ‘An MRI-based method to register patient-specific wall shear stress data to histology’, *PLoS ONE*. doi: 10.1371/journal.pone.0217271.

Mortazavinia, Z., Zare, A. and Mehdizadeh, A. (2012) ‘Effects of renal artery stenosis on realistic model of abdominal aorta and renal arteries incorporating fluid-structure interaction and pulsatile non-Newtonian blood flow’, *Applied Mathematics and Mechanics (English Edition)*, 33(2), pp. 165–176. doi: 10.1007/s10483-012-1541-6.

Muir, W. and Hubbell, J. (2009) *Equine Anesthesia, Equine Anesthesia*. Elsevier. doi: 10.1016/B978-1-4160-2326-5.X0001-6.

Müller, J. D. (2015) *Essentials of computational fluid dynamics, Essentials of Computational Fluid Dynamics*. doi: 10.5860/choice.196614.

Nguyen, K. T. *et al.* (2008) ‘Carotid geometry effects on blood flow and on risk for vascular disease’, *Journal of Biomechanics*, 41(1), pp. 11–19. doi: 10.1016/j.jbiomech.2007.08.012.

NHLBI (2015) *Carotid Artery Disease / National Heart, Lung, and Blood Institute (NHLBI)*. Available at: <https://www.nhlbi.nih.gov/health-topics/carotid-artery-disease> (Accessed: 6 June 2016).

NHS (2017) 'Stroke'. Available at: <https://www.nhs.uk/conditions/stroke/symptoms/>.

NI Instruments (2019) 'Understanding FFTs and Windowing Overview'. National Instruments. Available at: [http://download.ni.com/evaluation/pxi/Understanding FFTs and Windowing.pdf](http://download.ni.com/evaluation/pxi/Understanding%20FFTs%20and%20Windowing.pdf).

Ojha, M. *et al.* (1989) 'Pulsatile Flow Through Constricted Tubes: An Experimental Investigation Using Photochromic Tracer Methods', *Journal of Fluid Mechanics*. doi: 10.1017/S0022112089001424.

Olympus (2019) *Wave Propagation*. Available at: <https://www.olympus-ims.com/en/ndt-tutorials/flaw-detection/wave-propagation/> (Accessed: 25 November 2019).

Padukkage, R. and Barber, T. (2014) 'Effect of Non-Axisymmetry in Arterial Stenoses', (December).

Pallant, J. (2016) *SPSS Survival Manual: Julie Pallant: 9781760291952*. Allen & Unwin. Available at: <https://www.bookdepository.com/SPSS-Survival-Manual-Julie-Pallant/9781760291952> (Accessed: 22 November 2019).

Parker Laboratories (2011) 'Aquasonic 100 Ultrasound Transmission Gel Technical Data Sheet'. Parker Laboratories, Inc. Available at: <https://www.parkerlabs.com/pdf/AQUASONIC-100-ULTRASOUND-TRANSMISSION-GEL-SDS.pdf>.

Pawlaczyk, M., Lelonkiewicz, M. and Wieczorowski, M. (2013) 'Age-dependent biomechanical properties of the skin', *Postepy Dermatologii i Alergologii*. doi: 10.5114/pdia.2013.38359.

Perktold, K. and Rappitsch, G. (1995) 'Computer simulation of local blood flow and vessel mechanics in a compliant carotid artery bifurcation model', *Journal of Biomechanics*, 28(7), pp. 845–856. doi: 10.1016/0021-9290(95)95273-8.

Pett, M. A. (2015) *Nonparametric statistics for health care research: statistics for small samples and unusual distributions*.

Polytech (2019) 'VIBRATION MEASUREMENT METHODS'. Polytec GmbH. Available at: <https://www.polytec.com/uk/vibrometry/technology/>.

Razavi, A., Shirani, E. and Sadeghi, M. R. (2011) 'Numerical simulation of blood pulsatile flow in a stenosed carotid artery using different rheological models', *Journal of Biomechanics*, 44(11), pp. 2021–2030. doi: 10.1016/j.jbiomech.2011.04.023.

- Reeves, J. and Greenwald, S. (no date) *Greenwald Lab - Unpublished*. London.
- Riley, W. A. *et al.* (1992) ‘Ultrasonic measurement of the elastic modulus of the common carotid artery: The atherosclerosis risk in communities (aric) study’, *Stroke*. doi: 10.1161/01.STR.23.7.952.
- Rosenberg, A. J. *et al.* (2018) ‘Healthy aging and carotid performance: strain measures and  $\beta$ -stiffness index’, *Hypertension Research*. doi: 10.1038/s41440-018-0065-x.
- Rossing, T. D. and Russell, D. A. (1990) ‘Laboratory observation of elastic waves in solids’, *American Journal of Physics*, 58(12), pp. 1153–1162. doi: 10.1119/1.16245.
- RS (2016) *RS Silicone Rubber Compound #692-542*. Available at: <https://docs.rs-online.com/37d5/0900766b81166296.pdf> (Accessed: 25 August 2019).
- Safar, M. E., O’Rourke, M. F. and Frohlich, E. D. (2015) *Blood pressure and arterial wall mechanics in cardiovascular diseases, Blood Pressure and Arterial Wall Mechanics in Cardiovascular Diseases*. London: Springer-Verlag. doi: 10.1007/978-1-4471-5198-2.
- Saha, S. P., Whayne, T. F. and Mukherjee, D. (2010) ‘Evidence-based management of carotid artery disease’, *International Journal of Angiology*, 19(1), pp. 21–24. doi: 10.1055/s-0031-1278367.
- Sankar, D. S. and Lee, U. (2009) ‘Mathematical modeling of pulsatile flow of non-Newtonian fluid in stenosed arteries’, *Communications in Nonlinear Science and Numerical Simulation*, 14(7), pp. 2971–2981. doi: 10.1016/j.cnsns.2008.10.015.
- Segur, J. B. and Oderstar, H. E. (1951) ‘Viscosity of Glycerol and Its Aqueous Solutions’, *Industrial and Engineering Chemistry*, 43(9), pp. 2117–2120. doi: 10.1021/ie50501a040.
- Shaw, S. *et al.* (2009) ‘Pulsatile casson fluid flow through a stenosed bifurcated artery’, *International Journal of Fluid Mechanics Research*, 36(1), pp. 43–63. doi: 10.1615/InterJFluidMechRes.v36.i1.30.
- Shimizu, R. and Nonomura, Y. (2018) ‘Preparation of artificial skin that mimics human skin surface and mechanical properties’, *Journal of Oleo Science*, 67(1), pp. 47–54. doi: 10.5650/jos.ess17152.
- Shirwani, N. A. and Zou, M. (2010) ‘Arterial stiffness: a brief review’, *Acta Pharmacol Sinica*, 31(10), pp. 1267–1276.
- SIOS (2015) *SP-DS Series Double-Beam Plane-Mirror Interferometer*. Available at: <http://www.sios.de> (Accessed: 25 November 2019).
- Sobieszczyk, P. and Beckman, J. (2006) ‘Carotid artery disease.’, *Circulation*, 114(7), pp. e244-7. doi: 10.1161/CIRCULATIONAHA.105.542860.

Srivastava, N. (2014) 'Analysis of flow characteristics of the blood flowing through an inclined tapered porous artery with mild stenosis under the influence of an inclined magnetic field', *Journal of Biophysics*. doi: 10.1155/2014/797142.

Sary, H. C. *et al.* (1995) 'A Definition of Advanced Types of Atherosclerotic Lesions and a Histological Classification of Atherosclerosis', *Circulation*, 92(5), pp. 1355–1374. doi: 10.1161/01.cir.92.5.1355.

Sary, H. C. (2000) 'Lipid and macrophage accumulations in arteries of children and the development of atherosclerosis', *American Journal of Clinical Nutrition*, 72(5 SUPPL.), pp. 1297S-1306S. doi: 10.1093/ajcn/72.5.1297s.

Steinl, D. C. and Kaufmann, B. A. (2015) 'Ultrasound imaging for risk assessment in atherosclerosis', *International Journal of Molecular Sciences*, 16(5), pp. 9749–9769. doi: 10.3390/ijms16059749.

Strecker, C. *et al.* (2020) 'Carotid geometry is an independent predictor of wall thickness - A 3D cardiovascular magnetic resonance study in patients with high cardiovascular risk', *Journal of Cardiovascular Magnetic Resonance*. doi: 10.1186/s12968-020-00657-5.

Szabo, T. L. and Wu, J. (2000) 'A model for longitudinal and shear wave propagation in viscoelastic media', *The Journal of the Acoustical Society of America*, 107(5), pp. 2437–2446. doi: 10.1121/1.428630.

Tang, D. *et al.* (1999) 'Wall stress and strain analysis using a three-dimensional thick-wall model with fluid-structure interactions for blood flow in carotid arteries with stenoses', *Computers and Structures*, 72(1), pp. 341–356. doi: 10.1016/S0045-7949(99)00009-7.

Tang, D. *et al.* (2001) 'Steady flow and wall compression in stenotic arteries: A three-dimensional thick-wall model with fluid-wall interactions', *Journal of Biomechanical Engineering*, 123(6), pp. 548–557. doi: 10.1115/1.1406036.

Tang, D. *et al.* (2003) 'Effect of stenosis asymmetry on blood flow and artery compression: A three-dimensional fluid-structure interaction model', *Annals of Biomedical Engineering*, 31(10), pp. 1182–1193. doi: 10.1114/1.1615577.

Trejo González, J. A., Longinotti, M. P. and Corti, H. R. (2011) 'The viscosity of glycerol-water mixtures including the supercooled region', *Journal of Chemical and Engineering Data*. doi: 10.1021/je101164q.

Tu, C. and Deville, M. (1996) 'Pulsatile flow of Non-Newtonian fluids through arterial stenoses', *Journal of Biomechanics*, 29(7), pp. 899–908. doi: 10.1016/0021-9290(95)00151-4.

Urman, M. K. and Caren, J. F. (2007) 'Coronary artery disease', *3D Echocardiography*, pp. 27–35. doi: 10.1016/B978-0-12-802509-3.00015-7.

Waltz, A. G., Sundt, T. M. and Michenfelder, J. D. (1972) 'Cerebral blood flow during carotid endarterectomy.', *Circulation*, 45(5), pp. 1091–1096. doi: 10.1161/01.CIR.45.5.1091.

Wang, J. *et al.* (2019) 'Carotid Bifurcation With Tandem Stenosis—A Patient-Specific Case Study Combined in vivo Imaging, in vitro Histology and in silico Simulation', *Frontiers in Bioengineering and Biotechnology*. doi: 10.3389/fbioe.2019.00349.

Wells, R. G. (2013) 'Tissue mechanics and fibrosis', *Biochimica et Biophysica Acta - Molecular Basis of Disease*, 1832(7), pp. 884–890. doi: 10.1016/j.bbadis.2013.02.007.

Yazicioglu, Y. *et al.* (2005) 'Coupled vibration and sound radiation from a fluid-filled and submerged or embedded vascular tube with internal turbulent flow due to a constriction', *The Journal of the Acoustical Society of America*, 117(4), pp. 2587–2588. doi: 10.1121/1.4777189.

Yongchareon, W. and Young, D. F. (1979) 'Initiation of turbulence in models of arterial stenoses', *Journal of Biomechanics*, 12(3), pp. 185–189. doi: 10.1016/0021-9290(79)90141-6.

Young, D. F. and Tsai, F. Y. (1973a) 'Flow characteristics in models of arterial stenoses - I. Steady flow', *Journal of Biomechanics*. doi: 10.1016/0021-9290(73)90099-7.

Young, D. F. and Tsai, F. Y. (1973b) 'Flow characteristics in models of arterial stenoses - II. Unsteady flow', *Journal of Biomechanics*, 6(5), pp. 547–559. doi: 10.1016/0021-9290(73)90012-2.

Yousif, M. Y., Holdsworth, D. W. and Poepping, T. L. (2009) 'Deriving a blood-mimicking fluid for particle image velocimetry in Sylgard-184 vascular models', in *Proceedings of the 31st Annual International Conference of the IEEE Engineering in Medicine and Biology Society: Engineering the Future of Biomedicine, EMBC 2009*. IEEE Computer Society, pp. 1412–1415. doi: 10.1109/IEMBS.2009.5334175.

Zhang, C. *et al.* (2012) 'Flow patterns and wall shear stress distribution in human internal carotid arteries: The geometric effect on the risk for stenoses', *Journal of Biomechanics*, 45(1), pp. 83–89. doi: 10.1016/j.jbiomech.2011.10.001.

Zhu, C., Seo, J. H. and Mittal, R. (2019) 'Computational modeling and analysis of murmurs generated by modeled aortic stenoses', *Journal of Biomechanical Engineering*. doi: 10.1115/1.4042765.

## 8. Appendices

### 8.1. Appendix A

#### 8.1.1. Computational fluid model

##### 8.1.1.1. Methods

The flow rate in the carotid artery can reach peak values of up to 430ml/min due to the pulsatile nature of blood flow and the mean flow rate in carotid artery can reach 243ml/min (Cebal *et al.*, 2008), and even higher as seen earlier in the experimental chapters. The initial focus of this chapter is on steady flow rates corresponding to physiological mean values (mentioned later in this chapter), following this, the model will be extended to include pulsatile flow. Water is used as the working fluid with density and dynamic viscosity of 998.2 kg/m<sup>3</sup> and 0.001 Pa s, respectively.

#### a) Geometry of tube

The geometry of the tube plays a vital role in setting up the simulations to compute flow features within the fluid domain. There are several parameters that define geometry of the tube, namely its overall length; stenosis length; upstream length of tube; downstream length of tube; shape of the stenosis; stenosis severity and hydraulic diameter (internal diameter) of the tube. These parameters not only control the flow profiles within the fluid domain but also have a significant effect on the computational resources required for the simulation.

For the purpose of this study, we will look at these parameters and determine how they affect the flow and computation time. Before considering the parameters relating to the stenosis itself, we will consider the impact of upstream and downstream lengths since they comprise the majority of the domain.

To test the effect of geometry, a cylindrical solid tube with diameter  $D$ , upstream length  $20D$ , stenosis length  $10D$  and downstream length  $20D$ , with a uniform circular stenosis

of 60% (by diameter) was modelled, as shown in Figure 116. A flow with constant velocity was introduced at the inlet and flow profiles at different locations across tube were computed and analysed.

Once the optimum upstream and downstream lengths were determined, the other geometric parameters were investigated. Two different stenosis shapes were studied; one with a nonlinear reduction in area (Figure 116 & Figure 118a) and another with linear change (Figure 117 & Figure 118b). Both these shapes were analysed for different severities of stenoses.

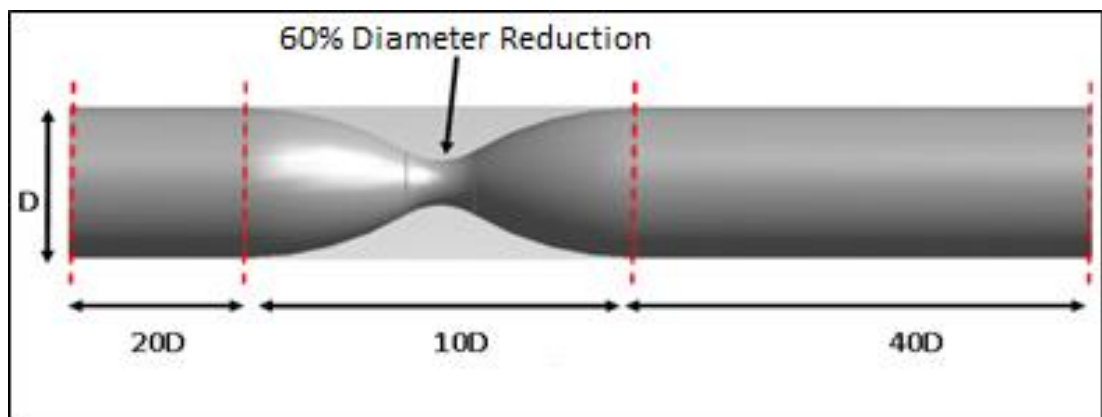


Figure 116: Smooth stenosis with 60% diameter reduction (i.e. 84% by area)

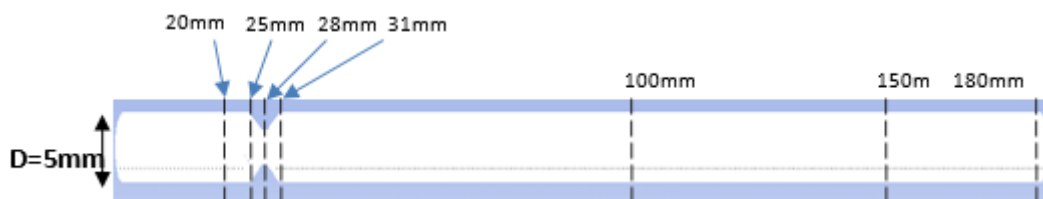


Figure 117: Linear trapezoidal stenosis with 50% diameter reduction (i.e. 75% by area)



## b) Discretisation of the domain

The area covered by the flow simulation, the domain, is sectioned into small cells which do not overlap, the finite volumes. This is called a mesh, and each cell contains a specific amount of momentum, mass and energy. According to Müller, 2015 “to compute entities in each cell:

- An initial solution has to be set, as the equations describe the evolution in time of the flow. Tracing this evolution requires a starting point.
- Fluxes of the conserved quantities are calculated between neighbouring cells. Fluxes also need to be computed at the boundaries of the domain to provide the required information for flow entering or leaving the domain. In the finite volume method the flux leaving one cell either enters the neighbouring cell or passes through a boundary. This is the key advantage of the finite volume method: by construction it is guaranteed to be conservative
- The next step is to compute for each finite volume or cell the sum of the fluxes entering or exiting over all its sides, as well as the integral of acting forces. This residual is equal to the average rate of change in the volume, e.g., if there is more mass entering than exiting, the net mass in the cell increases over time. If the sum of fluxes is zero, the cell is in balance and the state won't change: what enters the volume is equal to what exits.
- To advance the solution in time the average state in each finite volume needs to be updated frequently; this procedure is called time-stepping. Having computed the rate of change or residual in the volume, we can then extrapolate that rate for a small time “dt” to obtain the value for the state at the time  $t + dt$ .
- Time-stepping can be compared to observing an unsteady flow at frequent intervals. Most of the times, however, CFD is used to find the steady state solution. The simulation is started with some initial guess for the solution, e.g., uniform flow. Then the time-stepping process is performed until either the residual, that is the rate of change of the states in the cells, has become acceptably small or

until quantities of interest are no longer changing to a fixed number of digits.”  
(Müller, 2015)

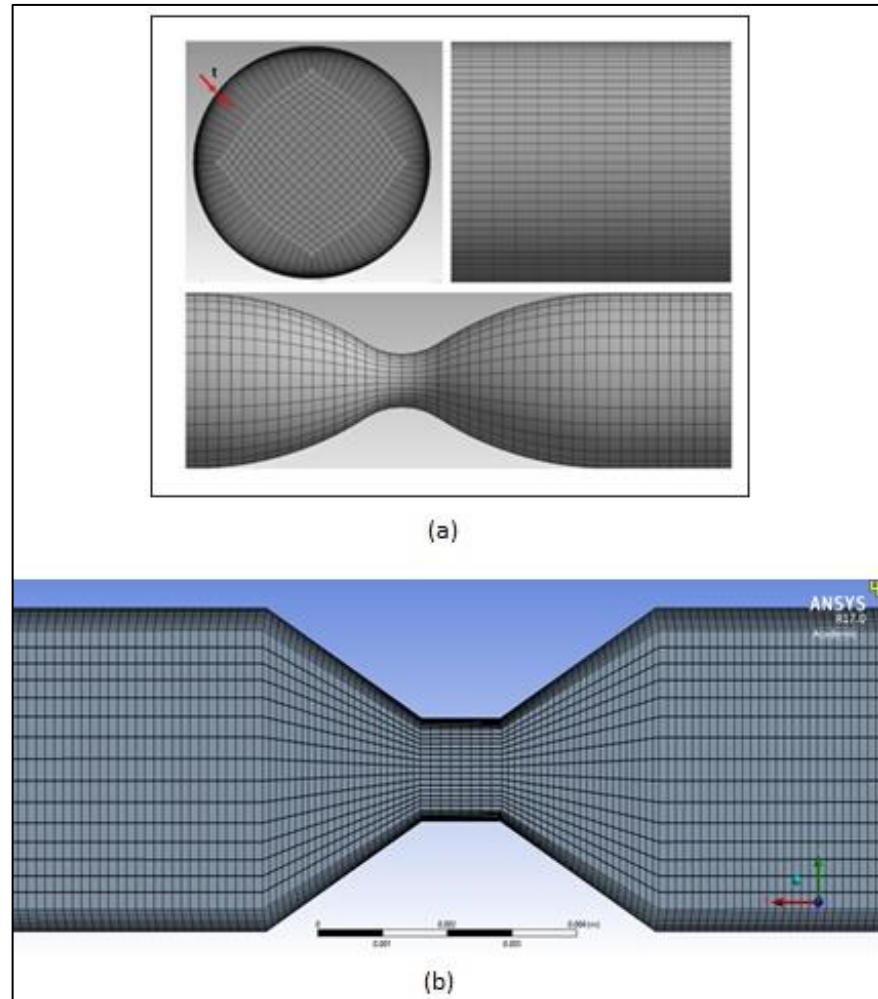


Figure 118: Discretisation of the fluid domain (a) smooth bell shaped stenosis (b) linear trapezoidal stenosis

### c) Governing equations

The fluid is considered as Newtonian and incompressible, and is governed by the incompressible Navier-Stokes equation:

$$\frac{\partial u}{\partial x} + \frac{\partial v}{\partial y} + \frac{\partial w}{\partial z} = \text{div } \vec{u} = \nabla \cdot \vec{u} = 0 \quad (4)$$

$$\frac{\partial \mathbf{u}}{\partial t} + \bar{u} \nabla \mathbf{u} + \frac{1}{\rho} \frac{\partial p}{\partial x} = \nu \nabla^2 \mathbf{u} \quad (5)$$

where  $u$ ,  $v$ , and  $w$  are velocities in  $x$ ,  $y$ , and  $z$  directions.

The above equations can be further simplified to the following form:

$$\rho \left( \frac{\delta \mathbf{u}}{\delta t} + \mathbf{u} * \nabla \mathbf{u} \right) = -\nabla p + \mu \nabla^2 \mathbf{u} \quad (6)$$

$$\nabla * \mathbf{u} = 0$$

Where  $\mathbf{u}$  is velocity vector,  $p$  is pressure and  $\mu$  is dynamic viscosity (Quartapelle, 1993)

“A Semi-Implicit Method for Pressure Linked Equations (SIMPLE) scheme, standard scheme for incompressible flow, is used to solve the Navier-Stokes equation. For each iteration or time-step, the following is calculated:

- Guess a pressure field  $p^*$  (or use  $p^n$  from the last iteration).
- Solve the momentum equations for the velocity field  $u^*$ , which will not be divergence-free

$$\frac{\partial u}{\partial t} = -u \nabla u - \frac{1}{\rho} \nabla p + \nu \nabla^2 u \quad (7)$$

- Solve the pressure correction equation for  $\Delta p$ ,

$$\begin{aligned} \nabla \cdot (\nabla(p^* + \Delta p)) &= \nabla^2 (p^* + \Delta p) \\ &= \rho \nabla \cdot (-u^* \nabla u^* + \nu \nabla^2 u^*) \end{aligned} \quad (8)$$

- If  $\Delta p$  is “small enough”, the time step is completed, equations solved, if not,
- Correct the pressure  $p^*$

$$\nabla p = \nabla(p^* + \Delta p) \quad (9)$$

- Correct the velocities  $u^*$  with the modified pressure gradient.
- Go to step 2.” (Müller, 2015)

The resulting systems are solved implicitly, The SIMPLE scheme avoids solving implicit systems of equations for the entire system of  $u, v, w, p$ . Instead, it only solves four much smaller systems for  $u$ , then  $v$ , then  $w$ , then  $p$ , hence, typically converging in a fast and efficient manner.

A second order transient formulation is used for a higher order of accuracy by minimising the numerical diffusion. The flow is assumed to be laminar and heat transfer aspects of the problem are neglected. To obtain an inlet boundary condition, mass flow rates ranging from 50 ml/min to 350 ml/min are simulated in a long tube to obtain fully developed velocity profiles, and validated with parabolic profiles for velocity ( $u$ ) obtained from the Hagen-Poiseuille's law:

$$u_z = -\frac{1}{4 \times \mu} \frac{\delta p}{\delta z} (R^2 - r^2) \quad (10)$$

Where pressure  $p$  is only a function of axial coordinate  $z$ , and  $\mu$  is dynamic viscosity (Schaschke, 2005).

#### d) Time-stepping

In Figure 119, the flux balance on the right hand side is called the residual. It is this imbalance that drives the flow since it is equivalent to the rate of change on the left hand side. The residual is a measure of the unsteadiness of a flow, it is not a measure of error in the solution. A zero residual can however not be achieved on a digital computer as there is only a finite precision of the numbers in storage. Fluent for example, uses single precision numbers, they are represented with around 7 significant digits. This will mean that a residual can converge to at most machine zero of  $10^{-7}$  for single precision numbers.

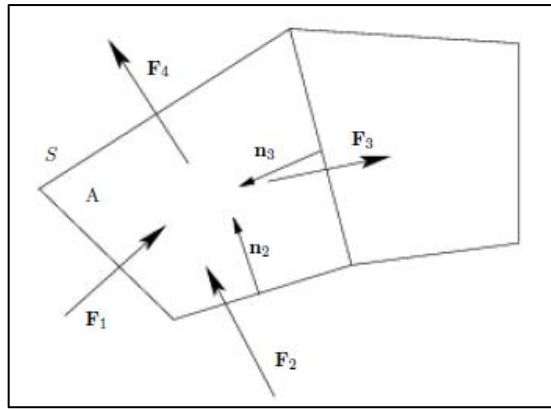


Figure 119: Fluxes around a finite volume (Müller, 2015)

With experience a user will know what levels of residual correspond to a sufficiently steady quantity of interest. In cases of periodic flows or disturbed flows, e.g. vortex shedding behind a cylinder, flow past a severely stenosed tube, the residuals will oscillate and not converge to low values.

*i. Steady flow*

Since the maximum Reynolds number we are working with is between 1200 and 1500, and the stenoses are symmetric, we start this study with the assumption that it is a steady state problem. Therefore, an initial case is run under steady state conditions.

The fully developed velocity profiles (shown in the previous section) are then used as inlet boundary conditions and flow is simulated with Reynolds numbers between 176.39 and 1234.17, corresponding to the physiological mean flow rates of 50ml/min and 350ml/min in the carotid artery (Khalafvand and Han, 2015). Gauge pressure of 0 is applied at the outlet and a non-slip boundary condition is used at the walls (i.e. when fluid meets solid at the boundary, there is no relative motion between solid and the fluid hence they both have the same velocities (ANSYS FLUENT 13 User's Guide, 2013). The equations together with prescribed flow conditions were solved using FLUENT solver (ANSYS, Inc.).

A 2D axisymmetric case was set up where water with density and viscosity of  $998\text{kg/m}^3$  and dynamic viscosity of  $0.001\text{cP}$  was passed through a rigid tube with a diameter of  $6\text{mm}$ . A stenosis  $91\%$  (by area) was introduced at  $10$  diameters length ( $1/3^{\text{rd}}$  of the tube length) from the inlet. A fine mesh was used with  $45925$  elements, though this number was changed later for varying upstream and downstream lengths. The flow was computed using the Navier Stokes approach detailed in the earlier section, with a second order up-wind scheme and  $2000$  iterations for the residuals to reduce below the order of  $10^{-6}$ .

*ii. Unsteady*

Following the results from steady analysis, it was observed that the problem was not steady, as discussed in results section later. Therefore, a transient three dimensional model was set up to investigate the disturbances in the flow field, and a combination of flow rates (Table 35) were used to identify the transition point where the flow starts to get unsteady.

In CFD, since the solution progresses in every time step in each cell, a number of combinations of mesh sizes and time steps were used to ensure that temporal and spatial convergence was achieved. Convergence criteria was set up such that the residuals for  $x$ ,  $y$  and  $z$  velocities fell below the order of  $10^{-6}$ .

Table 35: Flow rates and their corresponding Reynolds numbers

Mass Flow Rate at inlet (ml/min)	Flow Rate (kg/s)	Inlet Velocity (m/s)	Reynold's Number
<b>100</b>	1.667E-03	8.504E-02	4.231E+02
<b>150</b>	2.500E-03	1.276E-01	6.347E+02
<b>175</b>	2.917E-03	1.488E-01	7.405E+02
<b>200</b>	3.333E-03	1.701E-01	8.463E+02
<b>250</b>	4.167E-03	2.126E-01	1.058E+03
<b>300</b>	5.000E-03	2.551E-01	1.269E+03

**Steady State Analysis**

## a) Effect of upstream length on pre-stenotic flow

Preliminary two-dimensional studies of a symmetrical stenosed tube, with mean flow rates, of extreme cases; 50 ml/min and 350 ml/min, were carried out to ensure fully developed flow at the stenosis entrance. These particular flow rate values were chosen as they are reported in the literature to be representatives of flow conditions in a carotid artery (Waltz, Sundt and Michenfelder, 1972; Calderon-Arnulphi *et al.*, 2011). Results were plotted for the case of 50 ml/min and it was observed that the flow at the stenosis entrance was not fully developed. It can be seen in Figure 120(a) that the radial velocity of flow is varying as flow progresses from the inlet towards the stenosis; similar was the case with a flow rate of 350 ml/min.

Therefore, cases were set up (for flows ranging from 50 ml/min to 350 ml/min) with a long horizontal (non-stenosed) tube and the fluid was allowed to flow until it was fully developed. In the case of 50 ml/min, it can be observed from Figure 120(b) that the radial velocity profile became almost stable at 750 mm from inlet, which was taken as the point where flow became fully developed. The parabolic profile from this run was compared with the analytical solution given by the Hagen-Poiseuille's law (defined earlier) and the results were essentially in agreement, as can be seen in Figure 120(c). The velocity profile at the outlet from this simulation was then used as the inlet boundary condition for subsequent cases. The same approach was used for other flow rates. Simulations were run for sufficient number of iterations to ensure a steady solution was reached with the residuals minimised as shown in Figure 121.

While using the fully developed flow boundary condition, it was observed that the flow stream did not change until it entered the stenosis. This allowed reduction of the upstream length from the initial 20D to just 0.5D, thereby reducing the number of required mesh elements by 21.9%.

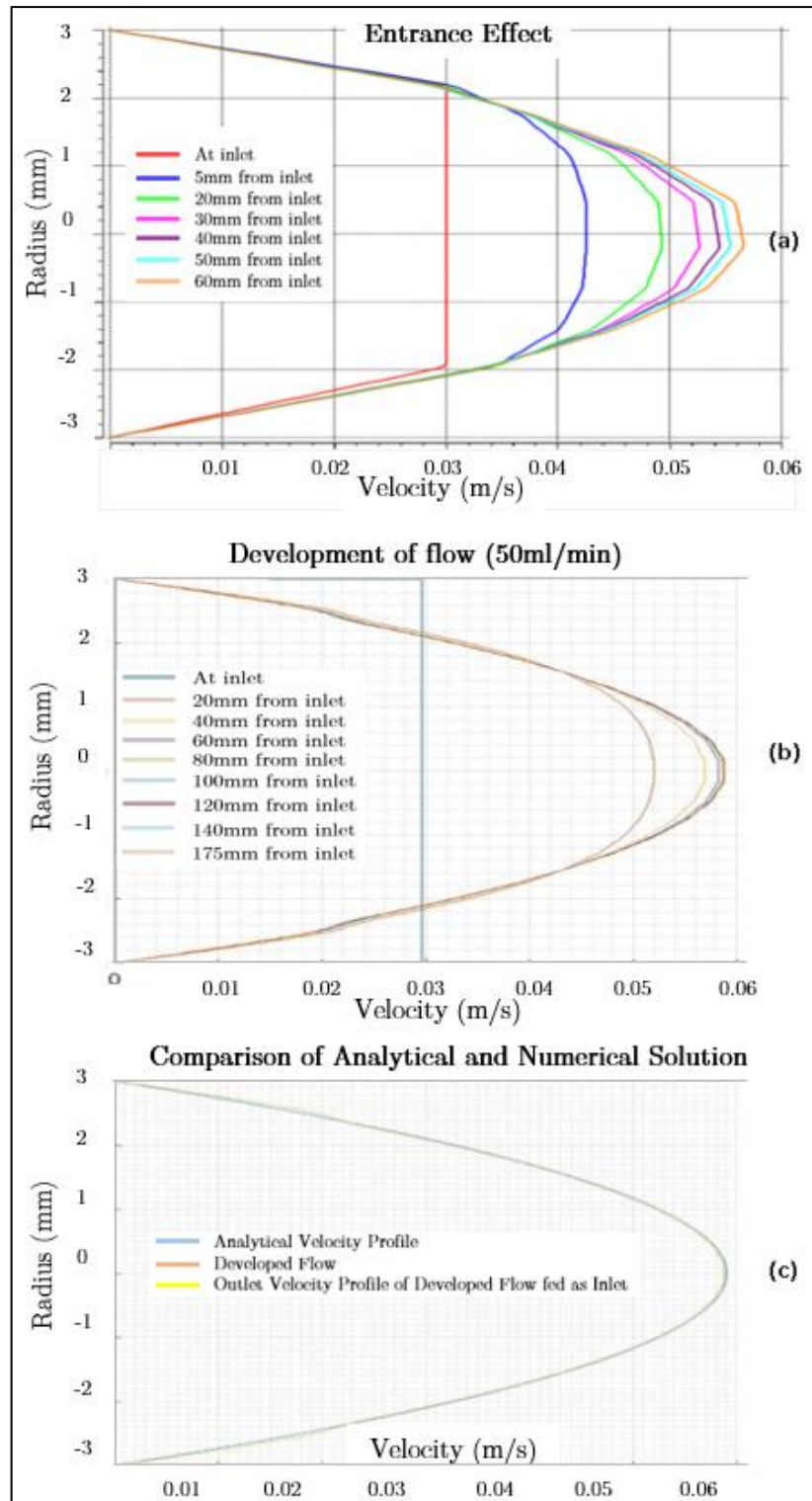


Figure 120: Velocity profiles showing development of flow (a) Entrance effect (b) Flow development (c) Comparison between analytical and numerical solution



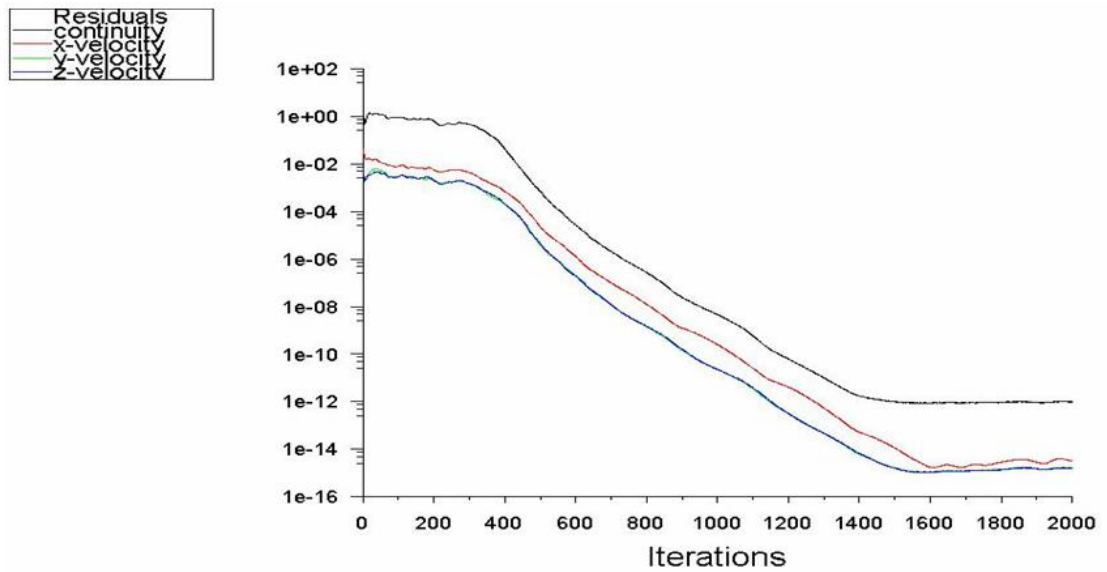


Figure 121: Residuals from the flow solver for the three velocity components

b) Effect of downstream length on pre-stenotic flow

Simulations were run with mass flow rates of 50 ml/min and 350 ml/min, for downstream lengths of 5D and 20D as shown in Figure 122(a). It was concluded from Figure 122(b) that pre-stenotic flow was independent of the downstream length and velocity profile at the stenosis entrance was not affected by the downstream length of the tube.

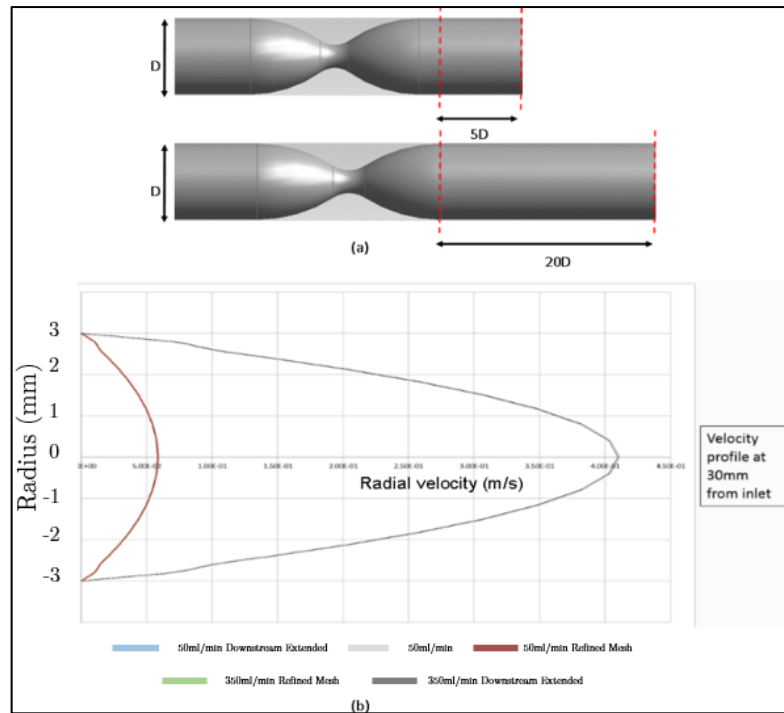


Figure 122: Effect of downstream length on pre-stenotic flow

### c) Effect of Reynolds number

With increasing Reynolds number, it was seen that unsteadiness started to develop in the post-stenotic flow. Although the Reynolds numbers in our model are below 2300 and in the expected domain of steady flow, the presence of the stenosis drives the unsteadiness. To study the effect of Reynolds number here, mean flow rates of 25ml/min, 50 ml/min, 100 ml/min and 150 ml/min were analysed to identify the transition point of the flow field through a severely stenosed (91% by area) tube. It can be seen from Figure 123 that, as the Reynolds number increases, there is not a noticeable difference between flow fields for 25ml/min and 50ml/min. However, as the flow rate increases towards 100ml/min, unsteadiness is observed in the post stenotic region. On further increasing the flow rate to 150ml/min, the region of unsteadiness is seen to move nearer to the throat of stenosis.

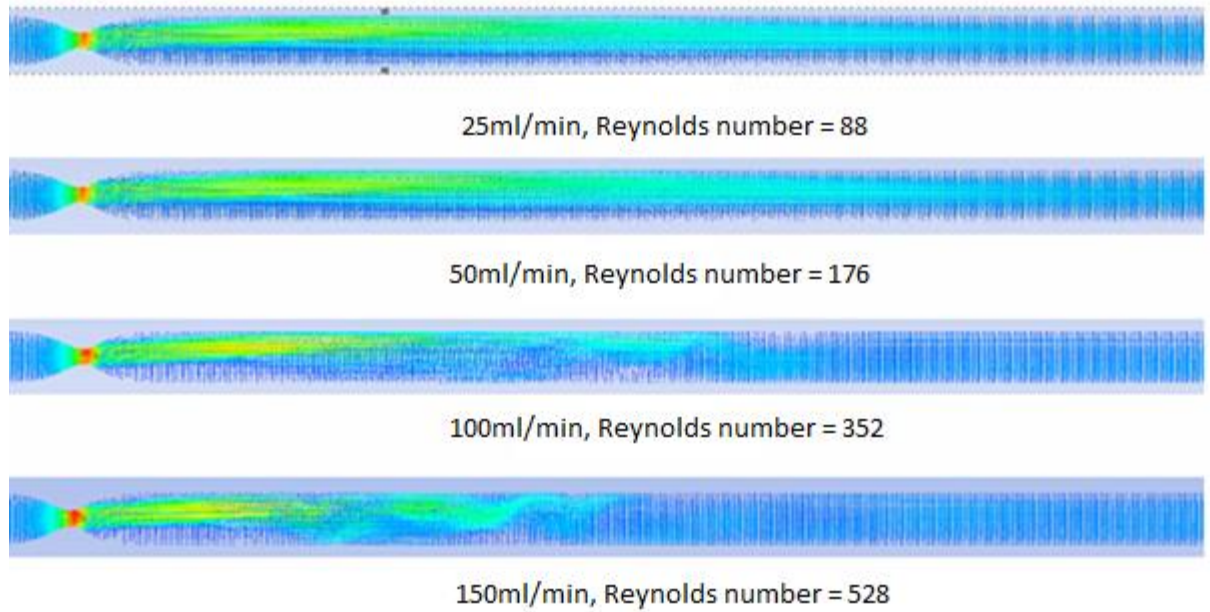


Figure 123: Effect of Reynolds number on the velocity field in the post-stenosed region (red shows regions of highest velocity and blue shows lowest)

Although the effect of Reynolds number is evident from the simulation, it can be seen that the flow field is disturbed for higher flow rates, which indicates that the steady state model will be not suitable to extend the study further and a transient model should be used.

### **Transient analysis**

#### ***Spatial and Temporal Resolution***

Before proceeding to a transient analysis, it is important to determine the spatial and temporal resolution required to identify the features of interest in the flow. Since the flow is most disturbed at high flow rates with a severe stenosis, an extreme case was tested. A mesh refinement study was carried out and a structured mesh, with 1.48 million elements and extra inflation layers, was ultimately chosen, as further refinement did not result in significant changes in the simulation. An example of a highly refined mesh used in a later part of this study is shown in Figure 125.

Once mesh convergence was achieved, the next step was to choose an appropriate time step through which the solution would evolve. A time stepping interval of 5ms was chosen as a starting point and the duration was decreased to 0.625ms in four stages. The results from each stage are shown in Figure 124.

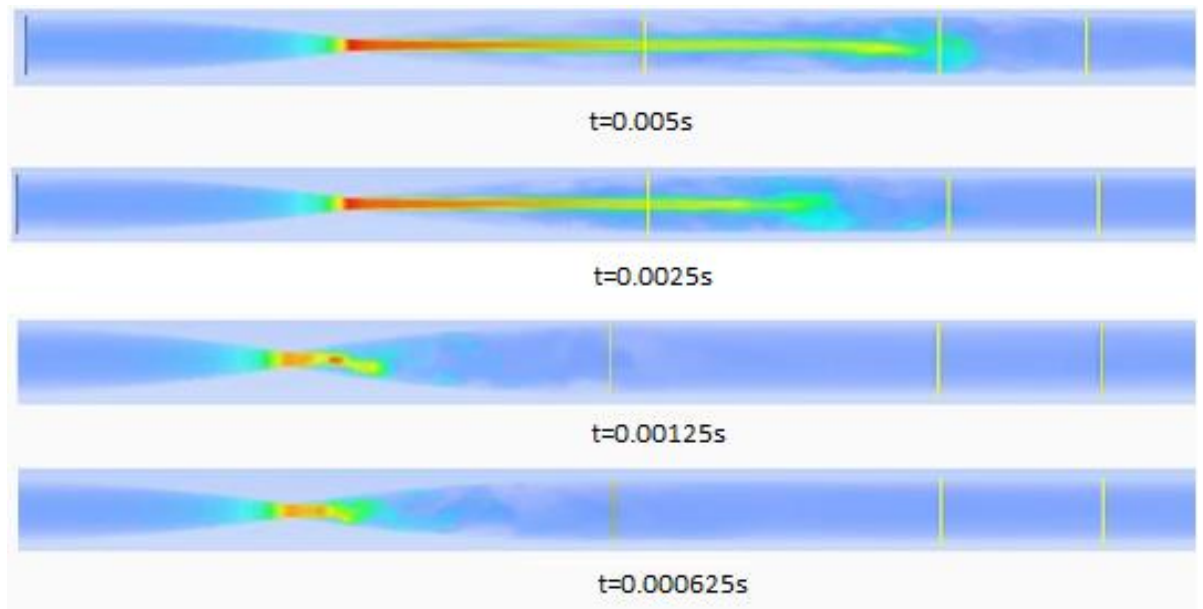


Figure 124: Effect of decreasing the time steps from 0.005s down to 0.000625s

It can be seen that there is a significant different in velocity field when the time stepping interval is reduced from 5ms to 1.25ms. The disturbances near the throat of the stenosis were not noticeable at higher intervals whereas by reducing the time-step, disturbance near the throat can be seen. However, with the decrease from 1.25ms to 0.625ms, there is no noticeable change in the velocity field. Therefore, a time step of 0.125ms is chosen as a standard for the following flow simulations.

A 3-D model with a 75% area stenosis (Figure 125) was constructed and mean flow rates ranging from 50ml/min to 350ml/min were simulated. The effect of increasing Reynolds number was similar to the 2-D analysis however the transient analysis allowed us to look at the time evolution of the flow. It can be seen from Figure 126 that, with an increase in Reynolds number, the transition point is found to be at  $Re=740$  for this particular stenosis geometry, and as the Reynolds number is increased, disturbances moved closer to throat of the stenosis. This can be further supported by the time evolution of the

velocity plots presented in Figure 127, which are taken at a point near the end of the tube. It can be seen how the disturbance starts sooner at the highest flow rate, starting progressively later as the flow rate is reduced.

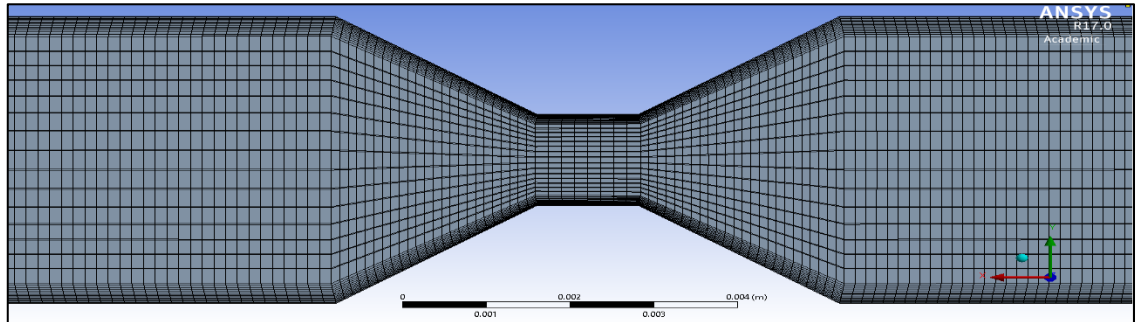


Figure 125: A 3-D model with a trapezoidal stenosis with 75% reduction in area

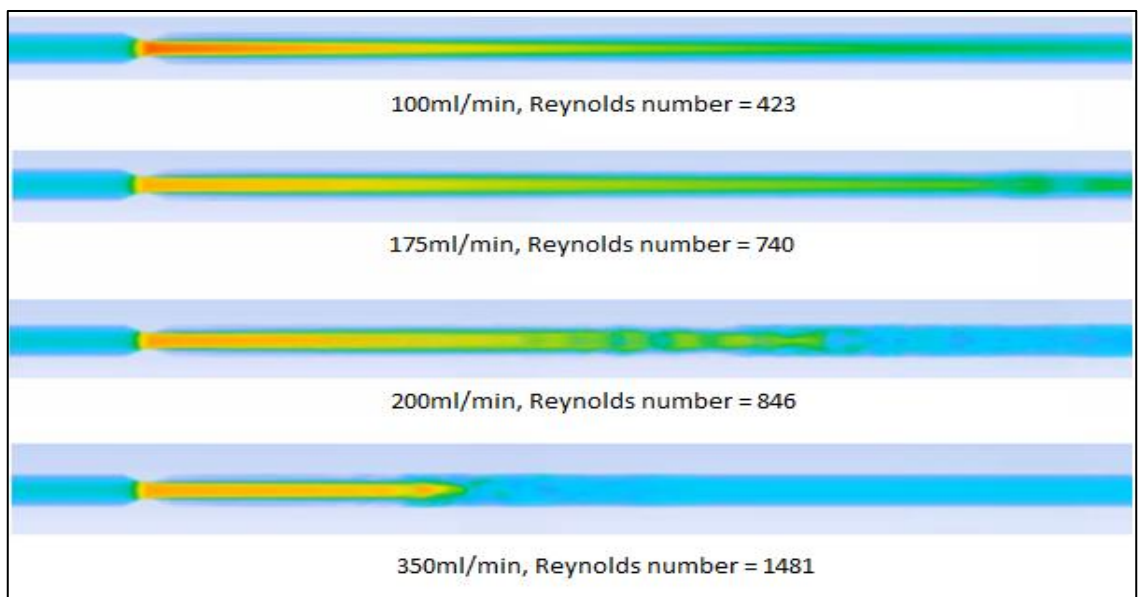


Figure 126: Effect of Reynolds number on post stenotic flow for Re values of 423, 740, 846 and 1481

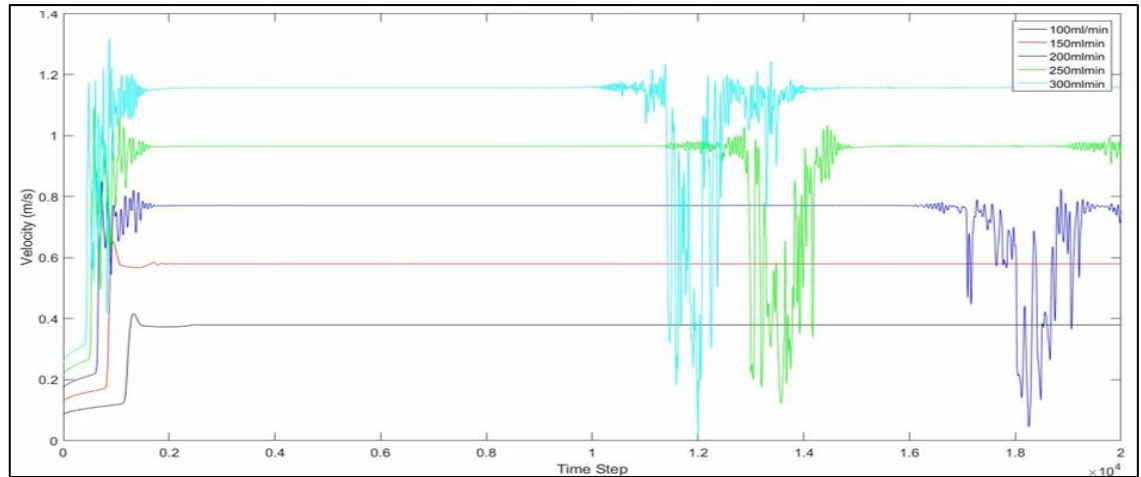


Figure 127: Time dependant velocity trace at a point 1mm before the exit of the tube (or 30D from centre of the stenosis)

#### d) Effect of stenosis shape and severity

It can be seen in the previous static case that the disturbance in the flow field started at a flow rate of 100ml/min as compared to 175ml/min in the current case. This is due to the difference in geometry, namely that the earlier more severe stenosis caused disturbances at a lower flow rate.

To investigate this further, two different stenosis severities (75% and 90% reduction in areas) were simulated and from Figure 128 it can be seen that for the more severe stenosis, the disturbance has moved closer to throat of the stenosis. From this it can be concluded that both, increasing the Reynolds number or increasing the stenosis severity have similar qualitative effect on the flow field i.e. disturbances tend to move upstream towards the stenosis.

This can further be supported by looking at the velocities at different points along the length of the tube for both the 75% and 90% cases, as can be seen in Figure 129 and Figure 130, which show that disturbances are more marked in the flow region with a higher degree of stenosis.

Firstly, looking at the 75% stenosed case in Figure 129, fluctuations in the velocities are seen for roughly for the first 0.65 seconds. These fluctuations are present as the flow

is still perfusing through the tube for the first time and still developing. Once a velocity profile throughout the domain is established, the flow becomes fully developed and these fluctuations start to disappear.

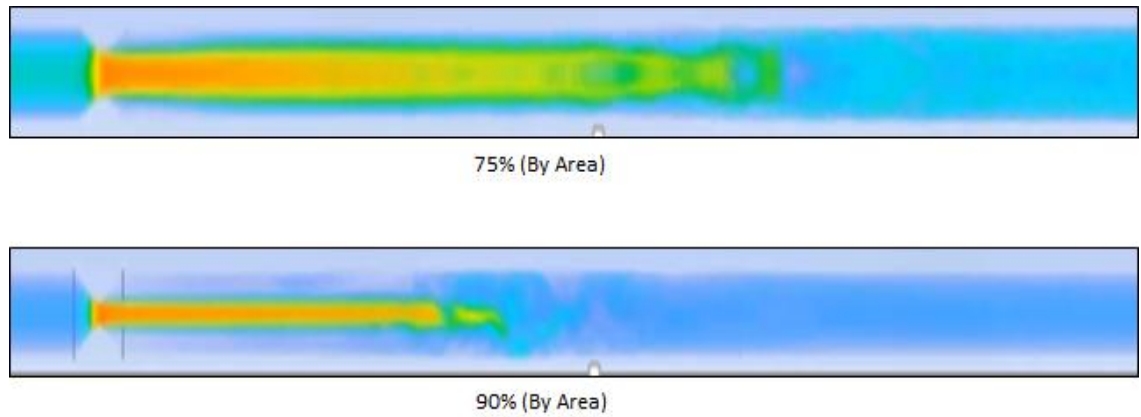


Figure 128: Effect of stenosis severity

In the case of 90% stenosed tube, it can be seen from Figure 130 that the disturbances are maintained. For instance, if we look at the velocity profiles immediately after stenosis, constant high velocities are seen showing the presence of a jet until 44mm position. At 44mm slight oscillations in the flow are seen which are amplified at 55mm position, after which the flow starts to develop again and oscillations start to disappear. This is in line with the experimental outcomes from the bare tube experiments conducted earlier in chapter 3.

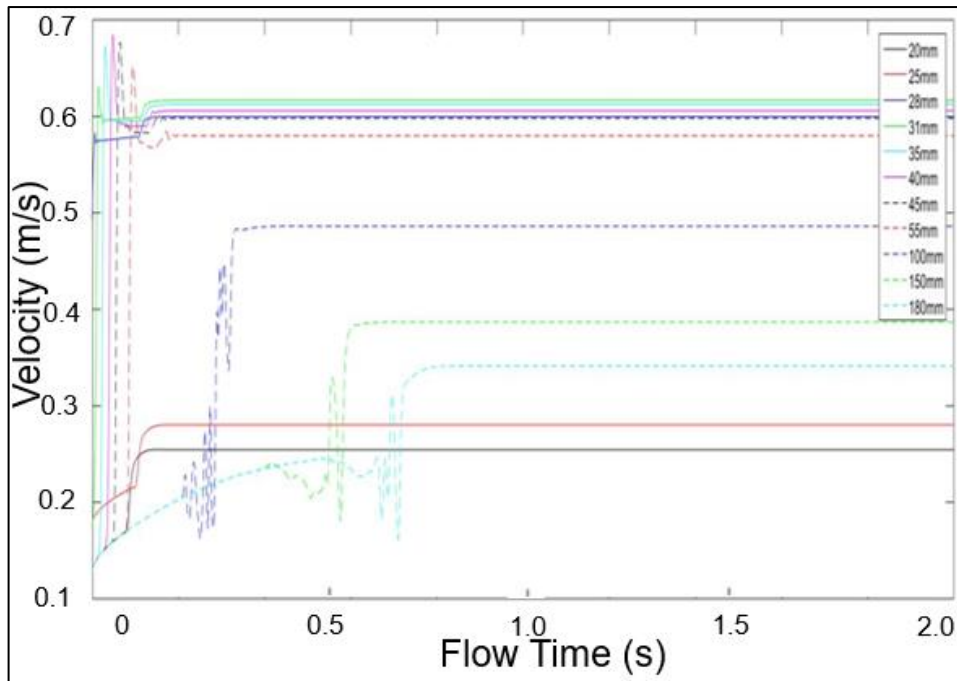


Figure 129: Velocity evolution at different positions for 50% Stenosis

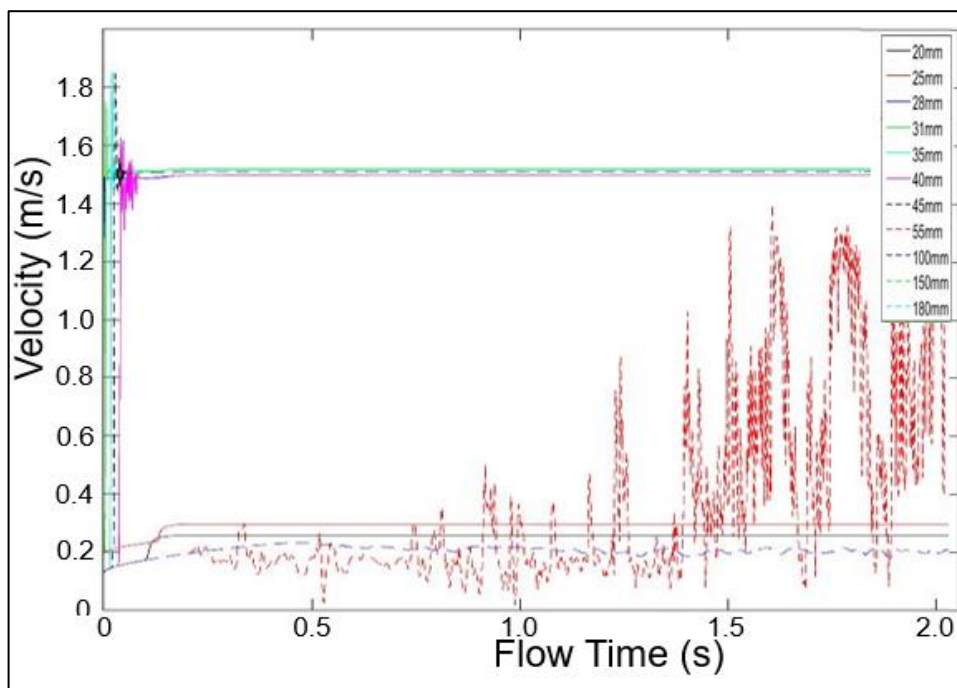


Figure 130: Velocity evolution at different positions for 90% stenosis



## 8.1.2. Computational structural model

### 8.1.2.1. Methods

#### a) Wave propagation in viscoelastic solids

As discussed above, disturbances are likely to occur in the post stenotic flow. These disturbances in turn, interact with the vascular endothelium, creating shear and pressure waves which travel through the various layers of soft tissue before reaching the surface of the neck.

Wave propagation in solids and liquids obeys the three fundamental conservation laws:

- Conservation of energy
- Conservation of mass
- Conservation of momentum

Within solids, the wave can propagate in four principle forms classified according to the manner in which the particles oscillate: shear, longitudinal, surface and also plate waves in thin materials. The shear, and to some extent the longitudinal waves are the ones that will be focused on here (Rossing and Russell, 1990; Szabo and Wu, 2000).

In longitudinal waves, the transfer of energy occurs in the same direction as the disturbance within the medium of propagation- i.e. oscillatory motions are in the very direction of wave propagation. Due to the presence of compression and dilation forces, they are often referred to as compressional waves (Dan Russell, 2013).

These waves consist of high and low density regions called condensations and rarefactions respectively, which refer to the movement of the particles that allow the energy to be transferred. The speed ( $v_p$ ) at which these longitudinal waves travel through a medium is given by:

$$v_p = \sqrt{E/\rho} \quad (11)$$

where E is the Young's modulus, and  $\rho$  is its density.

Young's modulus (E) can be calculated using the following expression:

$$E = \frac{\text{Stretching force per unit cross-sectional area}}{\text{Increase in length per unit length}} \quad (12)$$

Shear waves on the other hand involve particle oscillations that are at right angles (or transverse) to the direction of propagation. A good example is a vibrating string in which despite all the points within it being constrained to move only at right angles to the string axis, the wave peaks and troughs, and this perpendicular displacement will progress along the length of the string.

However, the wave is not limited to a single pulse and can in fact consist of several pulses, or a continuous series of pulses. This occurs in situation of the source forcing oscillations about a given equilibrium position over a period of time where the initial pulse is followed by the next, which causes opposite displacement. This phenomenon is sometimes referred to as the 'wave train'. (Rossing and Russell, 1990; Szabo and Wu, 2000)

Shear waves require a solid medium for efficient propagation and are therefore, not readily propagated through liquids or gasses. In a thin rod, shear wave velocity is determined by the shear modulus (one of the three moduli of elasticity used to describe the stiffness of materials) and can be calculated using the following expression:

$$v_s = \sqrt{G/\rho} \quad (13)$$

where G is the shear modulus of the rod, and  $\rho$  is its density.

And the shear modulus itself can be calculated directly as:

$$G = (\text{Tangential Force per unit Area}) / (\text{Angle of shear})$$

Considering the equation, wave velocity = frequency x wavelength, the longitudinal wave velocity is greater than that of a transverse wave (as they travel parallel to direction of propagation of wave) at any given frequency. Hence, the wavelength of a shear wave

will be less than that of a longitudinal wave (Olympus, 2019). Although shear waves undergo a greater degree of attenuation whilst propagating through a material such as the neck, their lower wavelength at a given frequency allows a greater spatial resolution and thus, more precise localisation of the stenotic lesion.

#### b) Model set-up

Along with rigid wall simulations, flow will also be simulated in a deformable tube that vibrates as a result of flow induced disturbances. Since the disturbances are a function of time, the loads on the wall will be time dependent. Therefore, a transient structural analysis is used, which is given as:

$$[M]\ddot{U} + [C]\dot{U} + [K]U = F(t) \quad (14)$$

Where  $M$  is the structural mass matrix,  $C$  is the structural damping matrix and  $K$  is the structural stiffness matrix.  $\ddot{U}$ ,  $\dot{U}$  and  $U$  are acceleration, velocity and displacement vectors.  $F(t)$  is the time dependent applied load (Abdul Khader *et al.*, 2010).

Preliminarily, ether-based polyurethane is selected as a suitable material used to mimic the arterial wall. Based on the small scale of displacements, as compared to the scale of the whole geometry, our atherosclerotic tube model will assume linear isotropic elastic behaviour with Young's modulus, density, and Poisson's ratio of 5 MPa, 1000 kg/m<sup>3</sup> and 0.4995, respectively (Kanyanta, Ivankovic and Karac, 2009). It is assumed that the material is linearly elastic for small scale displacements and thus, Hooke's law applies (Gere and Goodno, 2009). Compared to other literature values the Young's modulus value used by (Kanyanta, Ivankovic and Karac, 2009) is very high; therefore, lower values for a more compliant tube will also be considered. For instance (Abdul Khader *et al.*, 2010) assumed a Young's modulus of 0.9 MPa, which we have established (section 2.2) is a better approximation of the stiffness of the carotid artery.

#### c) FSI model

The ANSYS coupling service will be used to set up a strongly coupled 2-way FSI model where the fluid flow exerts hydrodynamic forces on the structure and deforms or

translates it. This deformed/translated structure then imparts velocity to the fluid domain, hence changing the shape of the structure and the fluid flow field. This is an iterative process which is set to run until convergence is achieved. A set of coupling conditions, kinematic coupling and traction coupling, are used at the coupling surface.

The kinematic coupling condition can be satisfied when the time derivative of solid structure displacement is equal to the flow field velocity at fluid-structure interface.

$$u = \frac{\delta a}{\delta t} = \dot{a} \quad (15)$$

Where  $u$  and  $a$  represent fluid velocity and displacement at the solid boundary respectively (Olsson & Kesti, 2014).

For the traction condition, stress or force balance between structure and fluid can be used. The traction vector  $t$  (stresses expressed as force per unit area with a normal  $n$ ) for the fluid-structure can be expressed as:

$$t^f = -p^f n + \tau n^f \quad (16)$$

Where  $p$  is the normal stress and  $\tau$  is the shear stress (Olsson & Kesti, 2014).

$$t^s = \sigma n^s \quad (17)$$

In stress balance, the traction vectors for solid and fluid will sum to zero as shown in equation (16).

$$t^s + t^f = 0 \quad (18)$$

Where f and s are fluid and solid respectively.

One of the FSI models was set up for flow through an unconstrained compliant tube, and in another model that tube was embedded within a soft tissue mimicking gel as shown in Figure 131.

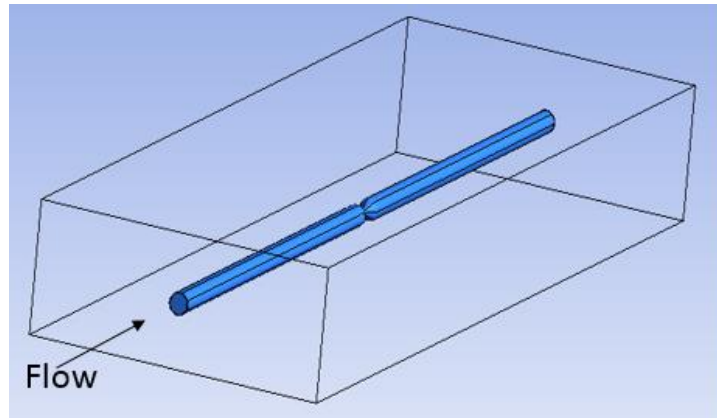


Figure 131: Schematic of a tube embedded inside a gel

#### 8.1.2.2. Results

##### a) Flow inside a compliant tube

A fully coupled 2-way FSI model (as described in section 3.3) was set-up and simulated, with a steady flow rate of 300ml/min. However, the run could not be completed due to an error generated by the solver, highlighting extensive deformation in the tube. The deformation obtained just before the error occurred is shown in Figure 132. The wall displacement instabilities can be seen both upstream and downstream of the stenosed region. As the fluid passes through the stenosis (towards the right), the flow field is disturbed and as the highly disturbed flow hits the tubular wall, large deformations are seen at the tube surface. Due to random fluctuations in the flow, the wall starts to react in an uncontrolled manner as a result of which the simulation is aborted.

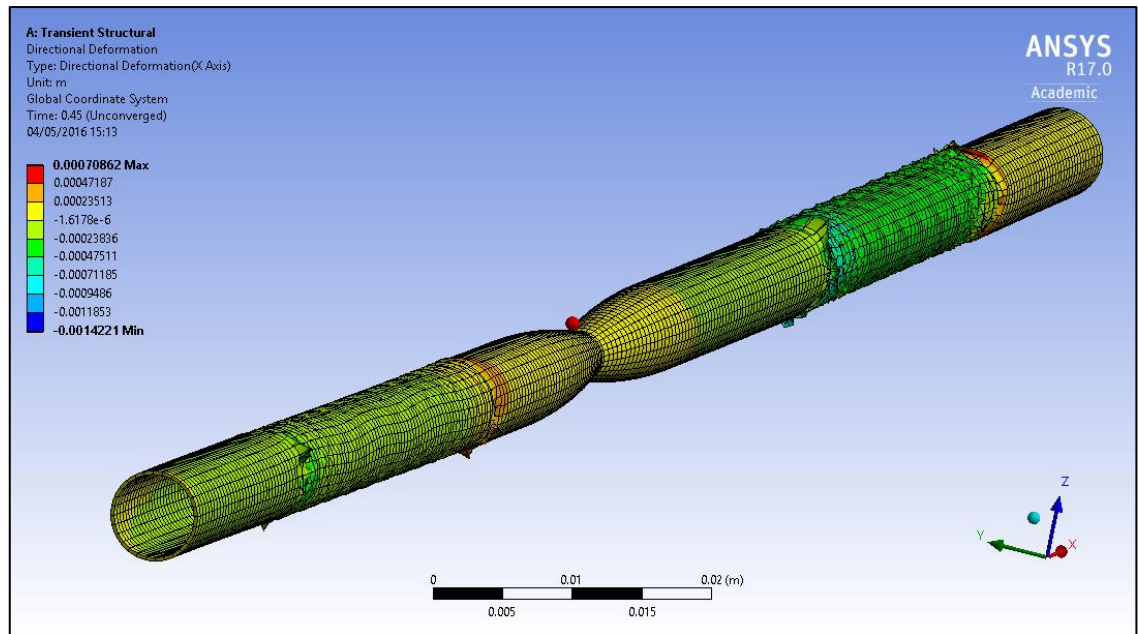


Figure 132: Distorted structure of a deformable tube

Simulations were run with tubes of decreasing Young's modulus from 5MPa down to 1.8 MPa, which is the critical value below which the simulation fails. The displacement values increased with the decreasing Young's modulus as expected, and this can be seen in Figure 133 and Figure 134. However, once the critical value for Young's modulus was achieved, large structural deformation was observed, which is when the simulation would fail. Similarly, large deformation was observed for the higher flow rates (150 ml/min – 350 ml/min).

A possible cause of this excessive deformation is the rapid change in the flow field. Therefore, the incorporation of gradual increases in flow rate was investigated as it could allow more stable increments in displacement of the tube wall.

Three possible solutions were proposed; one is to set up the same simulation in the rigid tube and then take the fully developed velocity profile of the whole domain and input that to the deformable tube. Second, set up a constant flow inlet and induce a ramping coupling step\* within the solver which would transfer the loads to the wall in small increments. Finally, increase the flow rate at the inlet gradually until it reaches a physiological flow rate of interest.

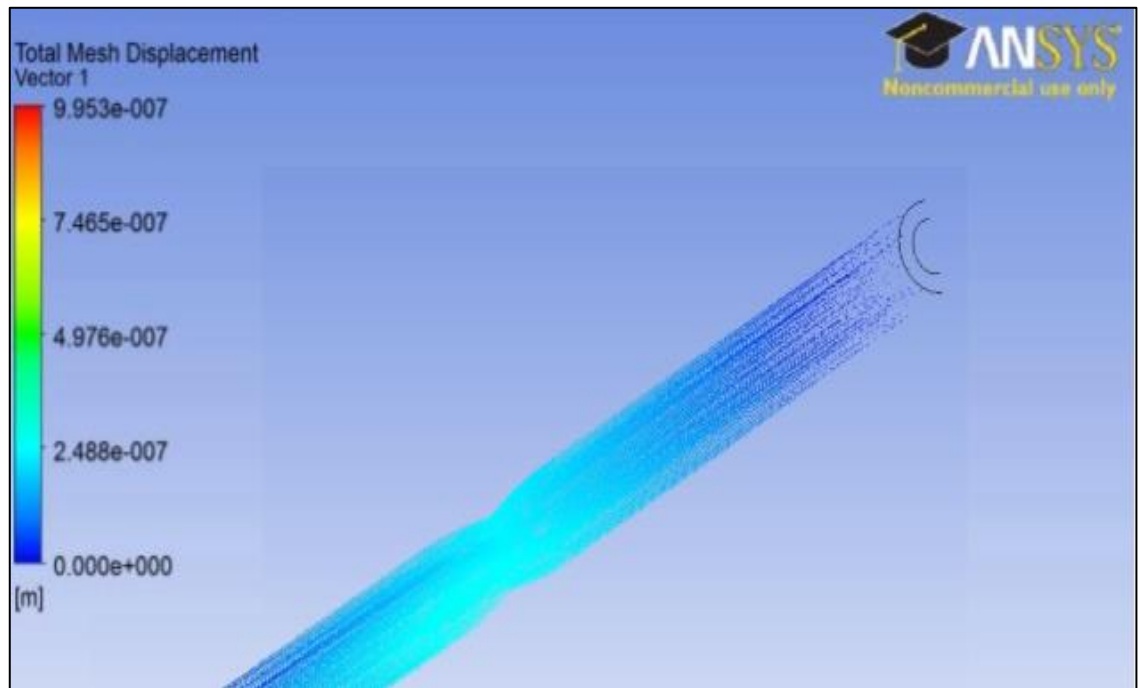


Figure 133: Solid mesh displacement for E=5MPa

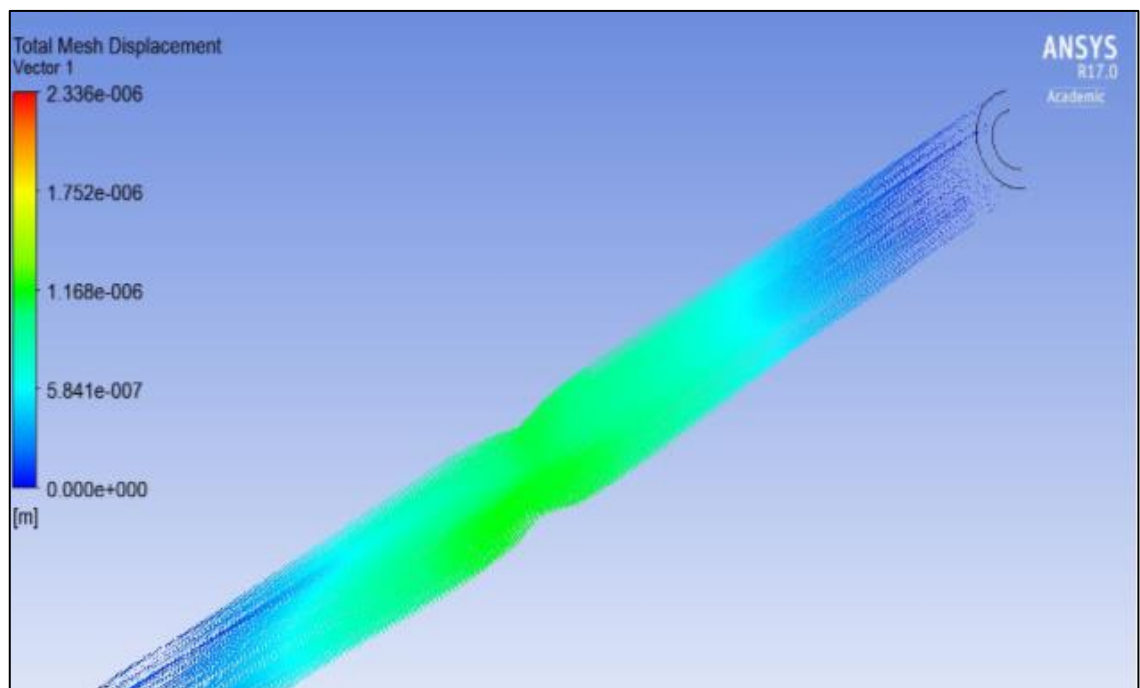


Figure 134: Solid mesh displacement for E=1.8MPa

\*In this scheme, there are several iterations within a single time step, and the loads from previous time steps are transferred gradually within those internal increments rather than abruptly in a single iteration, therefore allowing more time for the solution to stabilise. A generic step in this scheme is shown in Figure 135. During the  $i^{\text{th}}$  coupling iteration (for  $i/N_{\text{min}}$ ), the ramping factor equals  $i/N_{\text{min}}$ . The full data transfer value is applied for all coupling iterations that are equal to or greater than the minimum number of coupling iterations. As  $N_{\text{min}}$  is always reached, the full data transfer value is always applied by the end of each coupling step. (ANSYS, 2017)

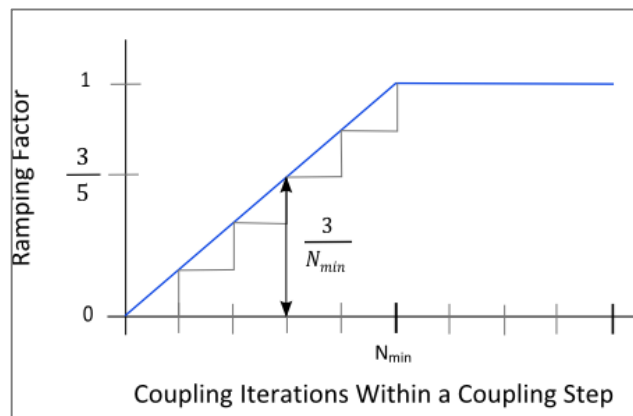


Figure 135: Ramping method to stabilise the solver (ANSYS, 2017)

The first proposal did not yield positive results as introduction of the developed profile from the rigid tube into the compliant tube caused sudden expansion of tubular wall. This is because the flow in the rigid tube was not just axial, but also radial due to the disturbances induced by stenosis.

Therefore, a second attempt was made by introducing the ramp function within the ANSYS software. The same boundary conditions were used; the only difference was that the loads between each time step were set to be transferred over smaller intervals rather than in one big step. The system was stable initially but with the passage of time, large deformations started to take place, and the tube started to oscillate, as can be seen Figure 136, which shows the wall velocities. Ultimately, a similar final solution was reached and the mesh deformed excessively (Figure 134) causing the solver to crash.





Figure 136: Displacement of the arterial wall (green shows high wall velocities and blue shows low wall velocities)

To test the third option, a sinusoidal wave (as shown in Figure 137 (a & b)) was introduced as the inlet velocity boundary condition. This would allow the flow to ramp up over a period of time (as in pulsatile flow) and the tube would deform gradually.

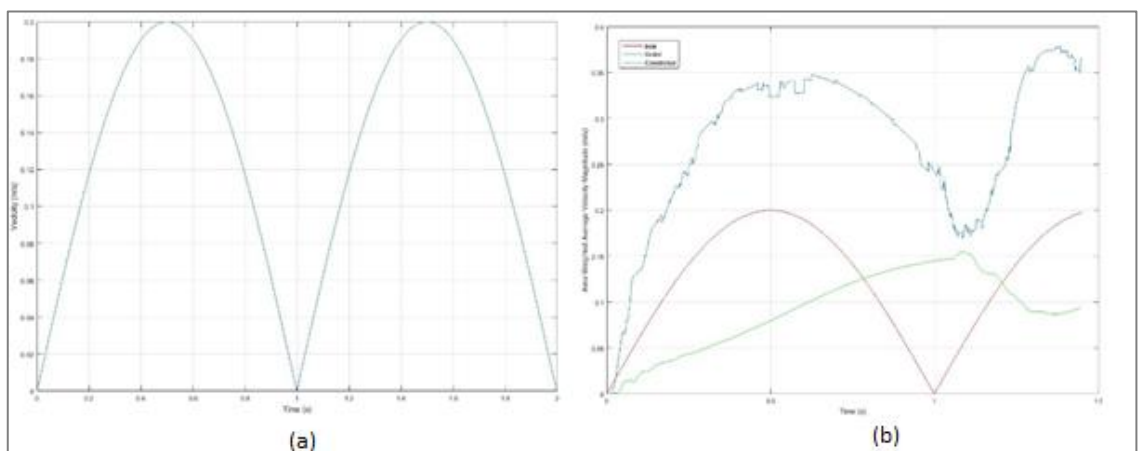


Figure 137: Introduction of a sinusoidal wave to allow gradual variations in velocities (a) inlet (b) inlet (red), outlet (green) and at the stenosis (blue) – y axis is velocity(m/s) and x axis is time(s). (Velocity=  $0.2|\sin(\pi t)|$ ), with a period of 2 seconds)

The results from this approach were more promising in comparison to the earlier attempts, as not only the large-scale oscillation of the tube disappeared, but the solver progressed past the first peak of the sinusoidal wave. However, as soon as the solver reached the second peak, it crashed unexpectedly. To confirm it was not a computer error, the simulation was performed again but the same outcome was achieved. The reason for this is not understood but it might be due to some sort of memory effect within the structure i.e. since the structure was deformed in the previous half cycle, there still might be some expansion in the tube and with the flow from the second half cycle superimposed on the existing flow, this caused the tube to expand further while making the solver unstable. Figure 138 shows the velocity of the tubular wall just before the solver crashed, it can be

seen that the highest velocity (in red) is in the region where flow is expected to be disturbed (recirculation zone) due to presence of the stenosis.

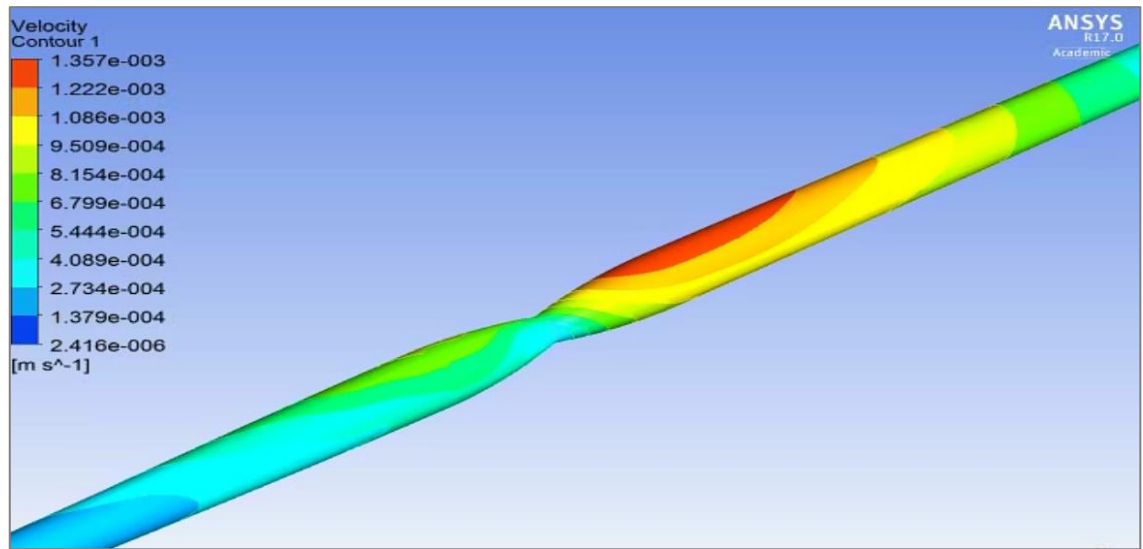


Figure 138: Velocity contour showing velocity at which the arterial wall is deforming

Another possible reason for this excessive deformation can be the limitations in the constraints around the tube. Despite it being constrained by atmospheric pressure, additional constraints could possibly resolve this issue, such as embedding the tube in a gel (section b)).

#### b) Preliminary model of tube embedded with the gel

Following the simulations on the compliant tube and the challenges faced with its implementation, an attempt was made to integrate the tube within a cuboid gel structure (287mm x 100mm x 37.5mm). This would not only be a somewhat more realistic approach to the anatomy of the neck but also was thought to aid in stabilising the artery due to the additional support provided by the gel structure.

The model is still in its preliminary stages to investigate its scope. As mentioned earlier, the model was simulated with a relatively stiffer gel (in comparison to real neck tissues) with a Young's modulus of 0.5MPa. Figure 139 (a) shows the magnitude of deformation of the gel at the tube-gel interface in metres. It can be seen that the maximum deformation occurs just upstream from the stenosis (left hand side in figure) as the flow accelerates

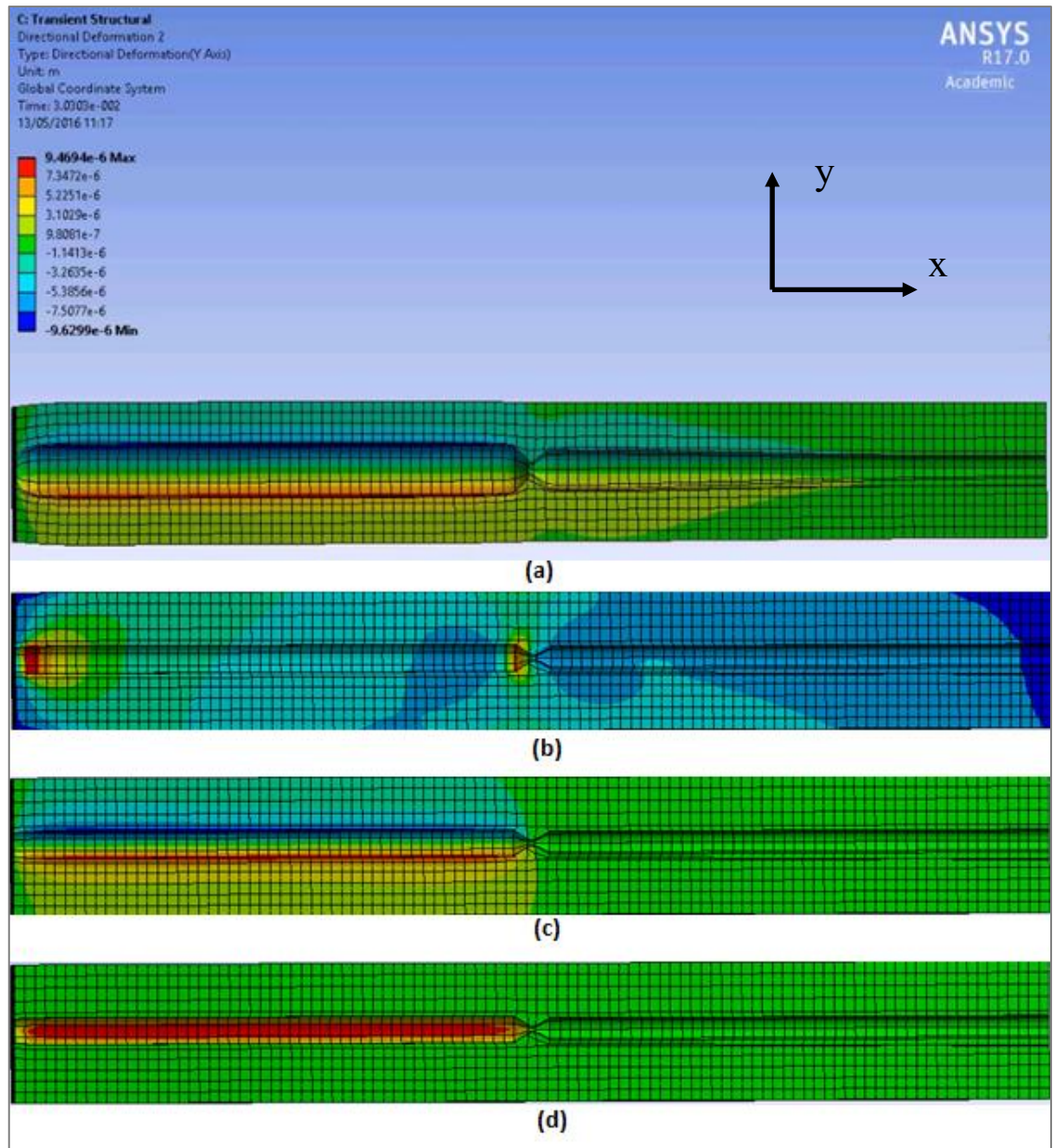


Figure 139: Directional displacement of gel structure with dimension 37.5mm (height) 100mm (depth) and 287mm (length) (a) RMS Magnitude (b) X-Plane (c) Y-Plane (d) Z Plane.

through the tube, but as the flow develops, a uniform displacement is observed in the gel. Figure 139(b) shows that maximum displacement in the x-direction is at the entrance where the flow enters the tube, and then just before the stenosis as the stenotic lesion is obstructing the flow. Figure 139(c) shows axisymmetric displacement in the y-direction, red and blue contours show displacement in opposite directions, though the magnitudes

are almost the same. Finally, in the z-direction, Figure 139(d) shows the maximum displacement occurs in the lateral direction as expected (similar to the displacement in y-direction), due to the hydrodynamic pressure associated with the flow.

The current model was only tested with Young's modulus greater than 0.5MPa. Several iterations of this model needs to be tested by varying parameters such as Young's modulus, Poisson's ratio, flow rate and viscosity of the fluid, geometry and severity of the stenosis, etc. To test all these parameters, a large number of simulations needed to be conducted. This required running multiple jobs in parallel, for which the use of a high-performance computing (HPC) equipment was necessary. However, due to technical issues (as specified in section 1.4) with the current build of HPC at Queen Mary University of London did not allow the FSI simulations to run.

### c) Computational Errors & Uncertainties, conclusion & future work

Computational modelling uses complex numerical schemes to compute and analyse the flows, and there are numerical errors associated with the modelling techniques. These errors can primarily source from spatial and temporal discretization along with the enhanced numerical diffusivity associated with discretisation non-linearity of Navier-Stokes equation.. These inherent errors cannot be eliminated entirely unless the flow is fully resolved; which requires high computational time and power, although they can be reduced using the modelling capabilities of Navier-Stokes within the limits of the available computational power.

Firstly, when setting up the model, the correct choice of boundary conditions must be imposed to ensure convergence. To minimise the problem, an attempt was made to match the boundary conditions of the flow simulations to the lab measurements. A large inlet length (approximately 15cm) was used in the lab to allow the flow to fully develop before entering the stenosed region, and this was modelled in the software by applying a fully developed flow boundary condition at the inlet. Regarding the outlet, the outflow from the stenosed tube, in the experiment, was into a reservoir which was maintained at atmospheric pressure, allowing us to use a pressure boundary condition at the outlet in the computational model.

Along with the application of realistic boundary conditions, the quality of the mesh was controlled to minimise any mesh-related convergence errors. To ensure a good mesh quality, cell regularity was maintained, skeweness was minimised, size variation control was applied near the stenosis to ensure the flow features in this area of interest were captured, and inflation layers were added to achieve a  $y^+$  (wall function) of less than 1, to accurately model the near-wall region.

Another source of error that can prove to be troublesome at points is the “artificial viscosity”. Addition of a non-physical artificial viscosity to the mathematical model is necessary in order to maintain stability and this viscosity scales with the mesh width ( $h$ ) for the first order discretisation and  $h^2$  for the second order. Hence, to minimise any the errors here, a combination of a fine mesh along with the second order discretisation was used.

Finally, another type of error that can significantly affect the results is the modelling error. A laminar model was used in the simulations conducted in this study, due to the axisymmetric nature of the problem. However, it was seen that local Reynolds number (for the highly stenosed tubes) just after the stenosis lied in the laminar to turbulent transitional region, and using the laminar model in such a scenario might lead to insufficiently precise results.

## 8.2. Appendix B

### 8.2.1. Visualisation of flow disturbances

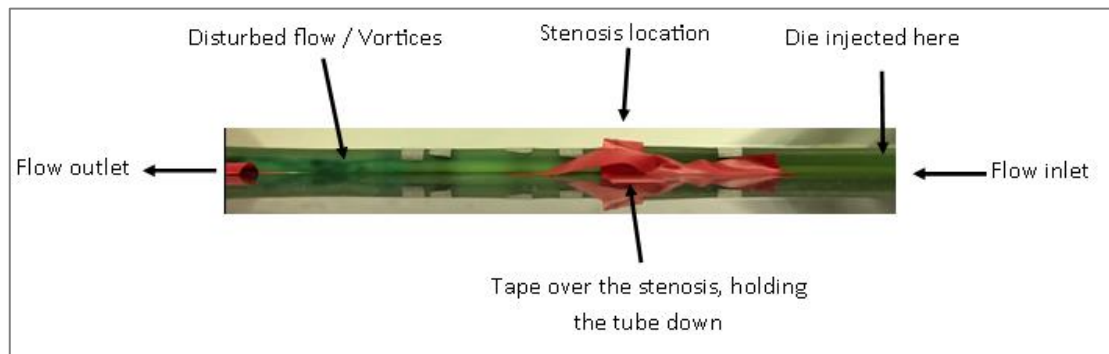


Figure 140: Flow visualisation of a post-stenotic disturbed flow

The above figure shows that as the flows goes past the stenosis, a jet is formed immediately downstream of the stenosis (shown by a thin black line in the middle of the tube) and vortices are seen in the further downstream position.

### 8.2.2. Homogeneous tissue models

This section reports on the development of and experiments on homogenous tissue samples, subjected to precise dynamic mechanical loading conditions. The described experiments date from 2015 and were conducted prior to the start of the project. As these experiments provide the experimental basis for the development of the computer model of wave propagation, the data are briefly summarised here. These experiments were conducted on agar gel phantoms. When deemed relevant, some of the experiments were repeated using PVA phantoms.

#### Agar gel dynamic measurements

These experiments were designed to investigate the propagation of shear waves, of known amplitude and frequency, originating from a known position in a material mimicking soft tissue in the neck and chest. The specimens were circular cylinders (diam. 52 mm, length 52 mm) cast around a spherical bead (diameter 9 mm) located at one of three vertical positions within the gel, through which passed a stainless-steel rod, connected

externally to an electromagnetic actuator (Figure 141). The beads were cast with their centres in one of three vertical positions: 13, 26 or 39 mm below the upper surface of the gel (referred to as top, middle and bottom, respectively).

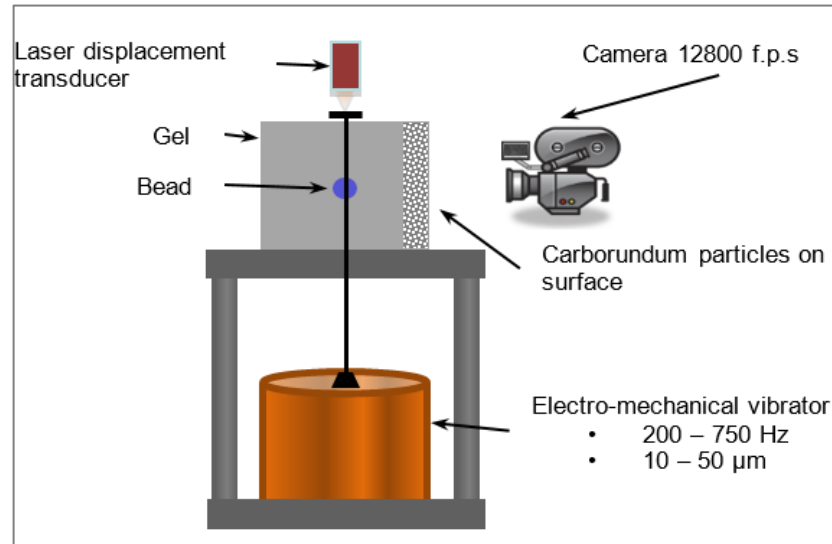


Figure 141: Vibrating bead set up. Vertical bead movement monitored by laser at top. Surface movement measured by video camera tracking movement of adherent reflective particles. Bead and camera position are adjustable (Reeves and Greenwald, unpublished)

Figure 141 shows the vertical bead movement and the corresponding in-plane movement at the gel surface, the latter being measured by a highspeed camera and in-house software tracking the motion of up to 8 reflective carborundum particles. The attenuation and wave propagation speed are estimated by measuring the relative amplitudes and phase shifts of the bead and surface movement. Figure 142 and Figure 143 summarises the results. Note that the wave speed corresponds to a Young's modulus of  $10^5$  Pa, in good agreement with tensile test values for agar gel mentioned earlier.

Viscoelastic creep was investigated in circular cylindrical specimens (diameter 52 mm length 52 mm) subjected either to a normal or shearing load of 48.0g. The measurements were performed under temperature-controlled conditions ( $24.9 \pm 0.2^\circ\text{C}$ ). Displacement of the upper surface of the gel was measured to the nearest  $0.5 \mu\text{m}$  using a laser sensor (AR700, Schmitt Industries, Oregon, USA). A typical result for a normal load is shown in Figure 144.

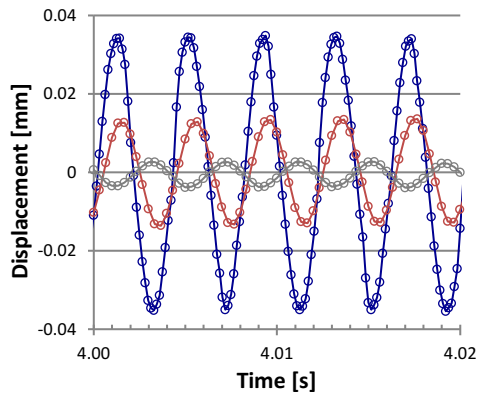


Figure 142: Bead movement (blue), vertical surface movement (red) and horizontal surface movement (grey). Wave velocity calculated from phase lag between vertical bead and surface movements and gel dimensions. Middle bead, Excitation frequency 250Hz (Reeves and G)

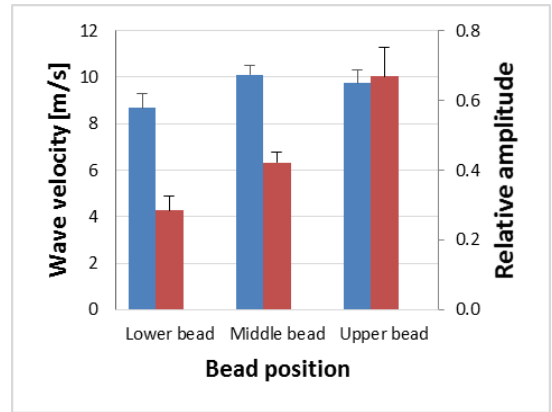


Figure 143: Wave velocity (blue bars, left hand scale) averaged for 5 gels. Surface/Bead displacement amplitude (red bars, right hand scale). Lower bead position 12.5 mm from gel base, middle at 25 and upper at 37.5. Note increased surface movement away from base.

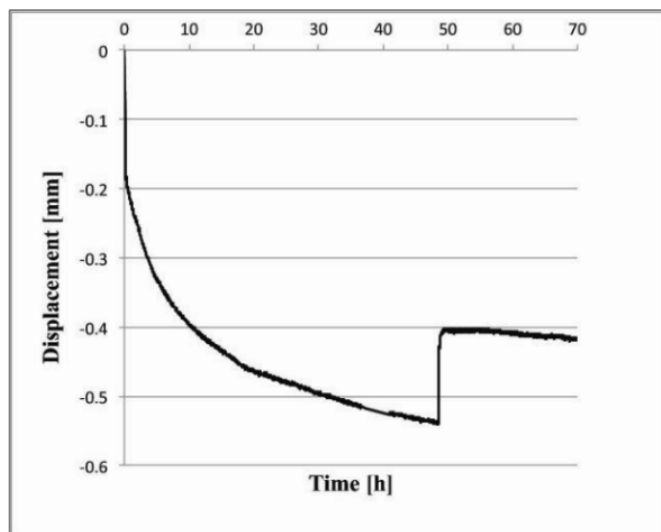


Figure 144: Time displacement relationship for agar gel subjected to a normal load showing creep from time zero to 45 hours, after which the load was removed. Note the permanent deformation revealing when the load was removed (Reeves and Greenwald, unpublished)



## Vegetarian Gelatine

### Shear wave generation by magnet embedded in vegetarian gelatine gel

The data derived from the flow through a stenosed tube experiments, while essential for validating the numerical models, do not provide information about the exact position of the vibration source or its amplitude and frequency. The limitation in the moving bead experiment was the push rod passing through the gel connecting the bead to the vibrator, it produced false vibrations in the system i.e., vibrations along the length of the rod due to its contact with the gel. A new approach to investigate the transfer of shear waves from within the gel to its surface was explored. A small cylindrical permanent neodymium magnet (with a diameter and length of 3mm and 4mm respectively) is embedded centrally (in all three axes). To introduce the magnet inside the gel, a thin wire is passed through the mould as shown in Figure 145, and magnet is carefully attached in the desired orientation. Following that, the mould is closed, and the gel solution is poured in the mould (Figure 145). The gel is then allowed to cool. Once the gel is set, the thin wire is swiftly pulled out leaving behind the magnet stays in its place. The gel with the embedded magnet is then taken out and placed on a horizontal platform as depicted in Figure 146.

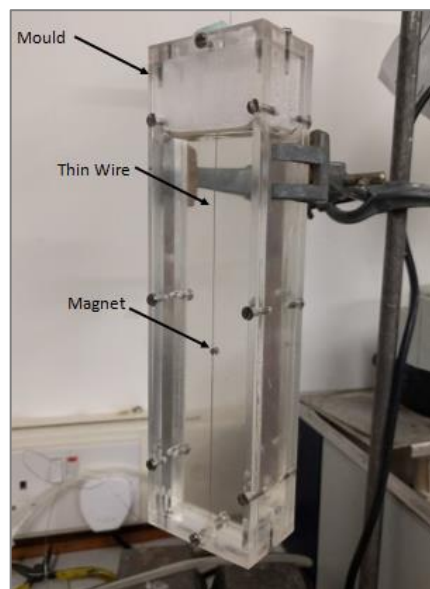


Figure 145: Embedding magnet within the gel

A separate jig is assembled with a magnet mounted onto an electric motor which is clamped and is placed directly under the gel as shown in Figure 146. To control the frequency, the magnet on the motor is rotated at different speeds by adjusting the supply voltage. This rotation of the external magnet causes the magnet inside the gel to oscillate and the energy from the oscillation is then transferred to the gel surface in the form of displacements. The amplitude of these displacements is determined by collecting the data from accelerometers which are placed on the surface of the gel directly above the magnet, 2 cm to the right and 2cm to the left of the magnet as can be seen in Figure 146. The experiments are repeated with the motor being moved closer to the gel i.e. the vertical distance between rotating magnet and magnet embedded within the gel is decreased thereby increasing the magnetic field strength and thus increasing the displacement amplitude of the embedded magnet. The experiments are repeated to collect data for four different vertical positions of the driving magnet.

Since the magnet connected to the motor can be rotated at a known frequency by carefully controlling the voltage thus determining the oscillation frequency of the embedded magnet, an attempt was made to track the movement of the magnet embedded within the gel, using a high-speed camera.

Before testing it inside the phantom, a separate test rig was created. A small cylindrical magnet ( $r=1.5\text{mm}$ ,  $h=4\text{mm}$ ) was placed inside a closed system as shown in Figure 147. The magnet was loosely constrained with a thread in order to allow for some rotation and translation in all directions. A rotating motor was then installed with a magnetic head and was placed in different positions; A, B and C and heights; C1, C2, and C3. The speed of the external rotating magnet was controlled by adjusting the voltage supplied to the motor and the whole system was placed under a camera to identify the patterns of movement of the embedded magnet for different orientations of the external magnet. One of the sides of the magnet was marked (and engraved) to allow the post processing of the images.

The results from this set-up were inconclusive due to the erratic movement of the magnet in this loosely constrained set-up. The magnet was embedded in the gel to improve the constraints. A challenge faced during implementation of this system in the gel was

the magnet-gel interface. Consider the following placement of magnet within the gel, with the axis orientation as stated.

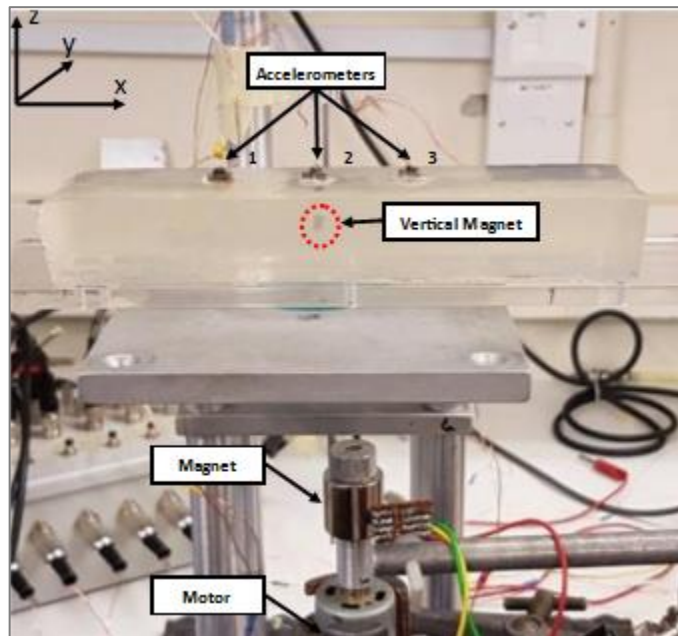


Figure 146: Gel with an embedded cylindrical magnet (length = 4mm, diameter = 3mm, 0.35kg pull strength), placed vertically above a rotating magnet (connected to a motor)

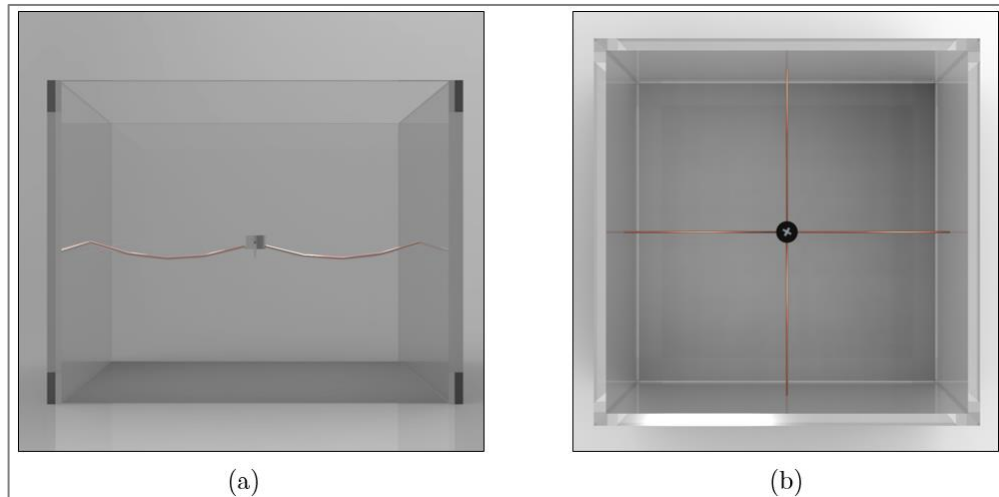


Figure 147: 3D model of the magnet test rig set-up, with a cylindrical magnet hanging in the middle with a set of nylon strings (a) Side view (b) Top view

If the external magnet induced a spin in the magnet along the y axis, the natural adhesion of the gel to the magnet would give away and the magnet would start spinning inside the gel which would not produce the desired conditions. If a spin was induced along the

x or z axis, the set-up performed better visually since the long edges allowed the magnet to be held in place. However, extra care had to be taken during this procedure, as with high voltage (high frequency oscillations) the magnet would induce large amount of force on the gel, hence compromising its integrity. Thereby, the effect of distance of the external magnet was controlled to prevent this from happening.

A cuboidal magnet was also investigated to avoid the spinning around y-axis. However, these experiments were conducted in the vegetarian gelatine which is stiffer and has a more rigid structure to it in comparison to the ultrasound gel. Hence, in the ultrasound gel, the magnet would have minimal constraints (due to its viscous nature) and once it starts to vibrate/oscillate at a higher frequency it will essentially spin freely and loosed any meaningful contact with the gel to transfer the vibrational energy. Therefore, this investigation was not continued further.

### 8.2.3. Platilon material properties

Basic Material			Polyurethane (Ester)		
Grade			2102 A	4100 D	U04/PE
Property	Standard/ Procedure	Unit			
Density	calculated	g/cm <sup>3</sup>	1,21 <sup>1)</sup>	1,21 <sup>1)</sup>	1,17 <sup>1)</sup>
Softening range	TMA Onset – Endset internal method	°C	150 - 175	155 - 175	—
Hardness	DIN 7619-1, DIN EN ISO 868 or ASTM D2240	Shore A	93 <sup>2)</sup>	94 <sup>2)</sup>	86 <sup>2)</sup>
Tensile stress at break	DIN EN ISO 527	MPa	70 <sup>3)</sup>	70 <sup>3)</sup>	55 <sup>3)</sup>
Tensile stress at 50% strain	DIN EN ISO 527	MPa	6 - 9	7 - 10	6 - 7
Tensile strain at break	DIN EN ISO 527	%	450 <sup>3)</sup>	450 <sup>3)</sup>	650 <sup>3)</sup>
Tear propagation resistance	DIN ISO 34-1, B	kN/m	75 <sup>3)</sup>	75 <sup>3)</sup>	70 <sup>3)</sup>
UV-stability	empirical	-	o	o	o
Hydrolysis resistance	empirical	-	o	o	o
Microbial resistance	empirical	-	o	o	o
Weldability	empirical	-	xx	xx	x
Thermoformability	empirical	-	xx	xx	x
Carrier film (PE)			no	no	yes

Figure 148: Typical properties of highly elastic polyurethane film - Platilon® (outlined in red) (Covestro, 2017)

#### 8.2.4. Fitting for the phantom

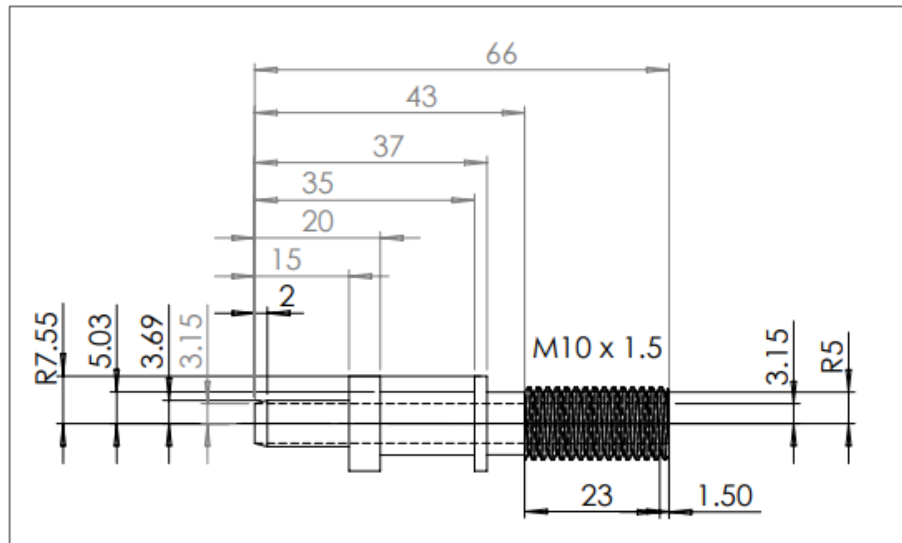


Figure 149: A 2-D drawing of the fittings used in the neck phantom. Left side shows a lip of 15mm over which the latex tube slides (all dimensions are in mm)

## 8.3. Appendix C

### 8.3.1. Microphone Study

#### Methods

An additional study is being conducted in collaboration with Prof. E. Drakakis and colleagues (Bio-inspired VSLI Circuits and Systems group, Department of Bioengineering, Imperial College) in which the possibility of using microphones placed on the skin surface to detect the murmurs resulting from flow disturbances in the underlying stenosed tube is being investigated. The study is currently in early stages, more details on its set-up and current outcomes can be found in.

For this study, four miniature SiSonic™ microphones (SPU1410LR5H-QB) (Knowles, 2013) were used were placed on the phantom's skin surface with their zone of maximum sensitivity directed towards the skin and the entire assembly was encased in a rubber surround to minimise the background noise. The set-up schematic is shown in Figure 150, where it can be seen that the MIC2, 3 and 4 were connected to the positive input of an op-amp (electronics designed and constructed by the Drakakis group). The negative inputs of the op-amps were connected together and to the output of MIC1, thus allowing this to act as a reference, so that common mode signals were rejected.

As shown in Figure 150, MIC 1 was fixed at a reference position (3cm upstream of the stenosis) while the others one recorded signals at various downstream positions (0cm, 1.5cm and 3cm). The 3cm upstream position was taken as the control position, in order to subtract any signals that were not associated with the post-stenotic disturbances.

The primary focus of this study was to investigate the effect of increasing mean flow rates, hence the experiments were limited to steady flow (at rates ranging from 0 to 357ml/min, with intervals of approximately 50ml/min) and the phantom used in this case contained a 75% axisymmetric stenosis. A 40:60 glycerine-water mixture was used to mimic the blood viscosity. Two additional flow rates were also used (511ml/min and 601ml/min) to enhance any signals of interest that might be present.

The output data (which were the difference between the signals from each of the measurement positions and the reference) were digitised using the PowerLab 16/35 equipment (detailed in section Figure 150) and the results are presented and discussed in section Figure 150.

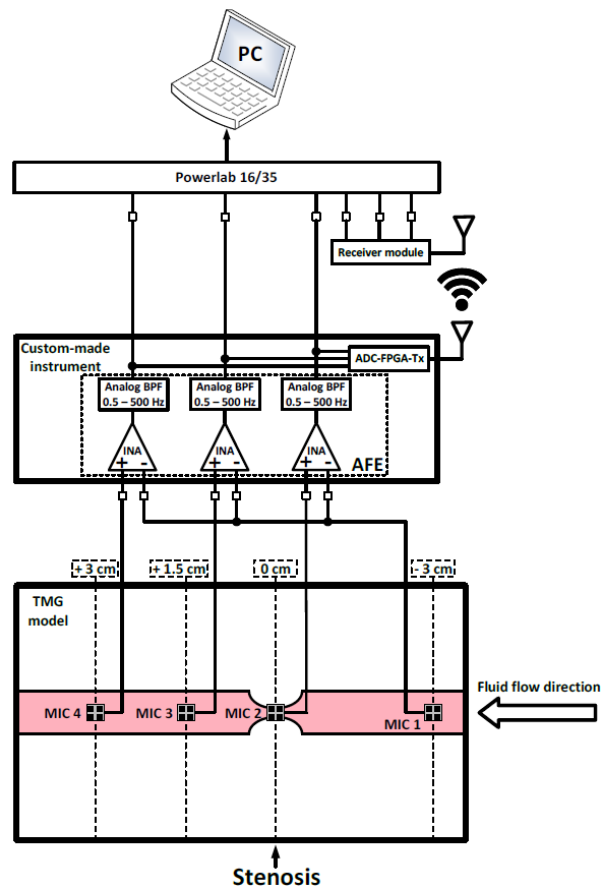


Figure 150: Schematic of the microphones set-up to detect disturbances in a 75% stenosed (embedded) tube (Drakakis Group)

A secondary aim of the microphone study was to investigate the possibility of using wireless techniques to record acoustic signals associated with stenosis without loss of critical information during data transfer. Hence, the data were recorded using both via wired connections as well as the wireless (using Zibgee protocol), to study any differences present. This aim, however, was beyond the scope of this project and differences in the wired vs. the wireless technology will not be discussed here.

## Results

A study was conducted, in collaboration with Drakakis Group, to detect the murmurs resulting from flow disturbances in the underlying stenosed tube. Results were obtained from both the wired and the wireless signal transmission between the op-amps and the data acquisition system and are presented in Figure 151. The results from both these methods were similar. However, the focus of discussion will be differences in the post-stenotic flow at increasing flow rates, and not the comparison between the wired and wireless set-up.

Figure 151 shows the area under the FFT curves obtained by processing the microphone signals from both, the reference position and another position of interest downstream of the stenosis. The area under the curve in the figure provide a comparison between the 0, +1.5cm & the +3cm positions for a range of flow rates.

A general trend that can be seen from all the flow rates in Figure 151 is that, within the first 150Hz, the area under the curve is highest at the stenosis then progressively lower at the +1.5cm and +3.0cm positions, although, in all cases the differences are small. At higher frequencies (i.e. 200-500Hz) it can be seen that the trend is reversed. The signal power at the +3cm position now has the maximum value, followed by the +1.5cm position and then the stenosis position.

In terms of the effect of flow rate, although the positional differences in the area are visible at all the flow rates, the numerical difference is small. No apparent change is seen in the areas up to flow rates of 259ml/min. Beyond that, little differences are seen for 302ml/min and 357ml/min around the 50-100 Hz and 400-450 Hz peaks where the area values have increased.

To further explore this, the areas under the two non-physiologically high flow rates were studied and the results are presented in Figure 152. On careful observation, it can be seen from the figure that at 511ml/min the highest peaks in 10-50 Hz and 350-400 Hz ranges are at  $2 \times 10^{-6}$  and just above  $1 \times 10^{-6}$  respectively while the same peaks for the 601ml/min flow rate lie at  $3 \times 10^{-6}$  and just above  $2 \times 10^{-6}$ .



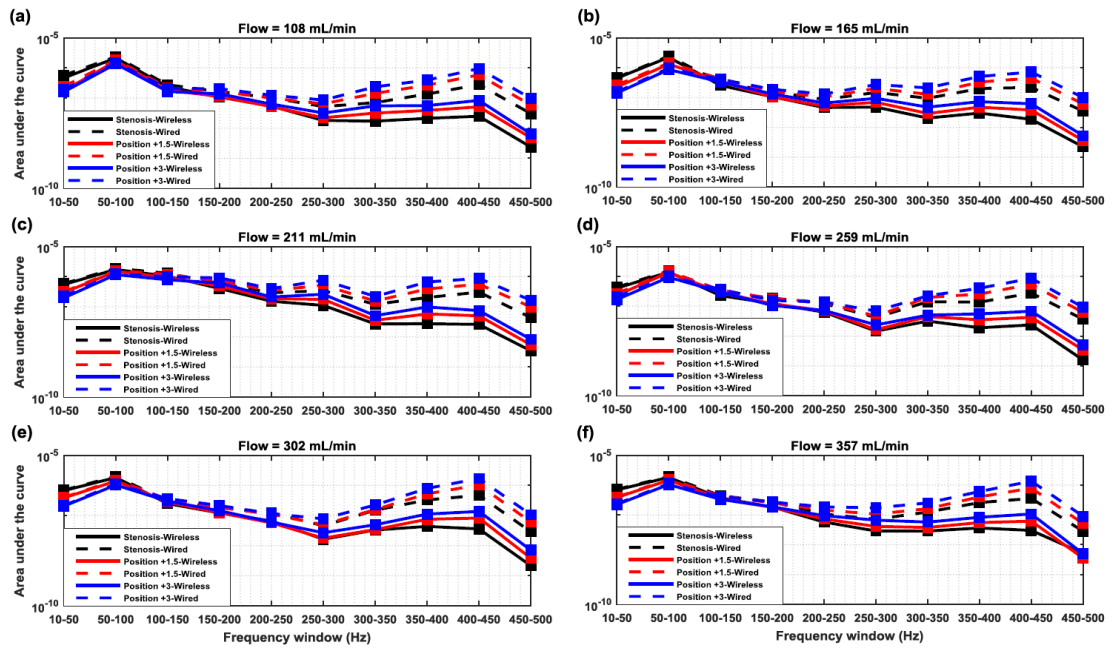


Figure 151: Areas under the power signal at stenosis (0cm), +1.5cm and +3cm for flow rates of (a) 108ml/min, (b) 165ml/min, (c) 211ml/min, (d) 259ml/min, (e) 302ml/min and (f) 357ml/min

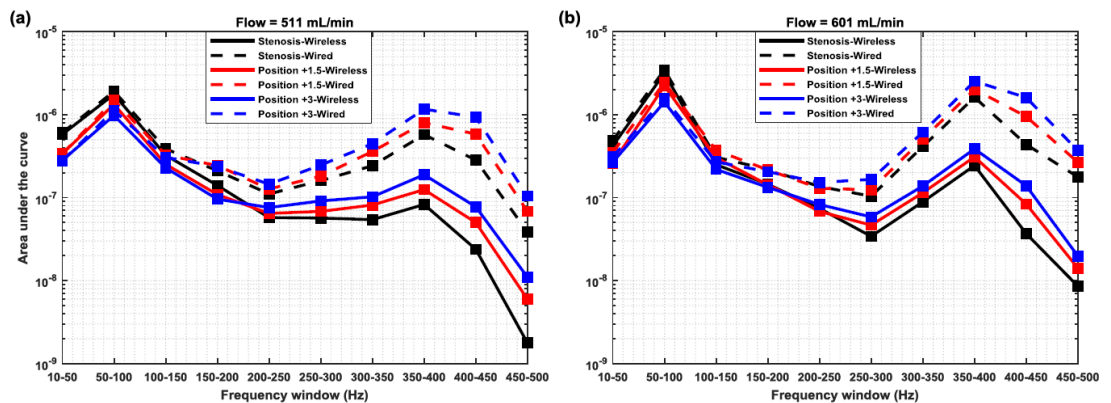


Figure 152: Area under the power signal at stenosis (0cm), +1.5cm and +3cm for flow rates of (a) 511ml/min and (b) 601ml/min

To clarify this effect further, a comparison of the flow rates is made (Figure 153) by means of the area ratios between the 0 & +1.5cm position and the +1.5cm & +3cm position at normal (0-360ml/min) and high (>500ml/min) flow rates. The first thing to be noted from Figure 153 is that generally the area ratios are higher for the >500ml/min flow rates than that <360ml/min ones and the largest differences in this case are seen in the 0 - 100Hz range, which was generally the case in the earlier LDV phantom experiments as well.

The second thing to be noted here is that the signal at the stenosis is higher than that at the +3cm downstream position for all flow rates, within that first 150Hz and that the trend is reversed at frequencies above 200-250Hz. This effect is not in general agreement with the bare tube and phantom experiments in which the surface movement was directly measured with accelerometers or the LDV as well as in the work of others, as the microphone data indicates strong disturbances at the stenosis location, at least at low frequencies.

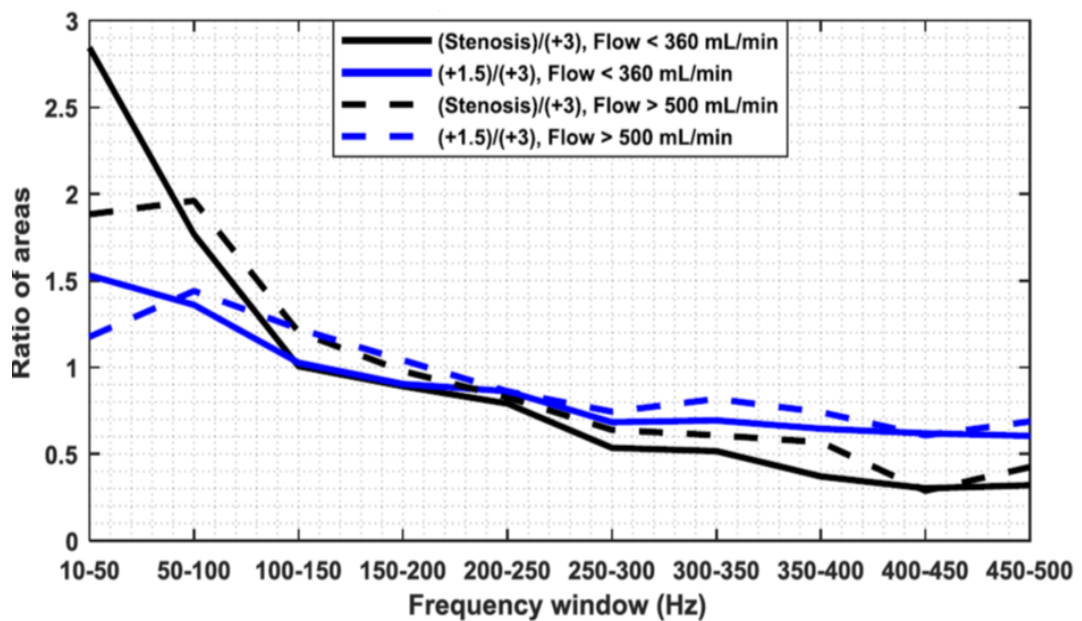


Figure 153: Positional comparison of area under the curve ratios for the normal (<360ml/min) and high (>500ml/min) flow rates

Currently, the microphone study is in its early stages (as a proof of concept) and several variables and parameters have not yet been investigated. For instance, the sensitivity of the microphone in terms of its omni-directional characteristics (it might be detecting signals from remains unknown). Moreover, the microphone mounting assembly has a small gap between the skin and the microphone and the wave characteristics in that small air pocket are unknown. Furthermore, the microphones are attached to the skin surface using adhesive tape, and despite the careful positioning, a small tilt in the microphone position might affect the collection of the signal.

Work on a flexible patch (with microphones mounted on it) is currently in progress. This will allow closer apposition to the skin surface. Further data on the microphone technique is needed before confirming this as a suitable method for measuring the murmurs produced by the post-stenotic disturbed flow.

### 8.3.2. Additional Duplex ultrasound scans from bare tube experiments

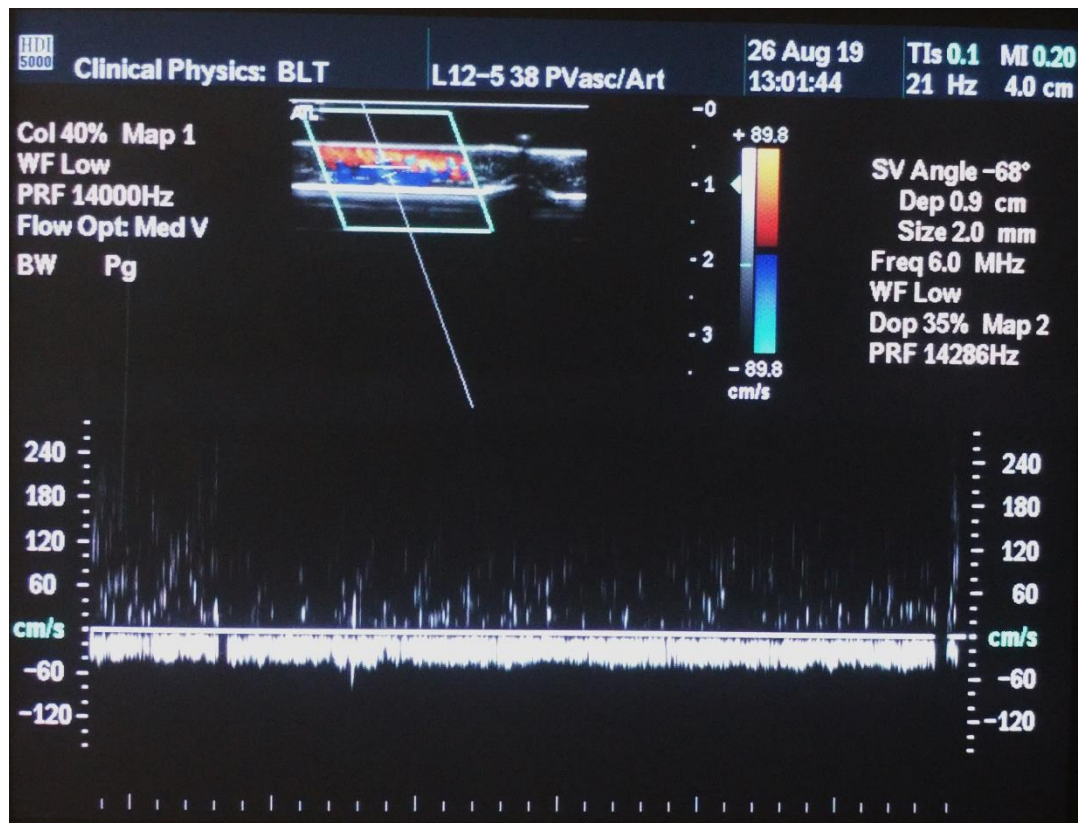


Figure 154: 90% Stenosis - 1.5cm position - Middle band of 2.0mm

### 8.3.3. Effect of flow rate

The following graphs show the effect of increasing flow rate, and a clear trend is seen in the 90% stenosed tube where the signal strength increases with the increasing flow rate.

#### 0% Stenosed case

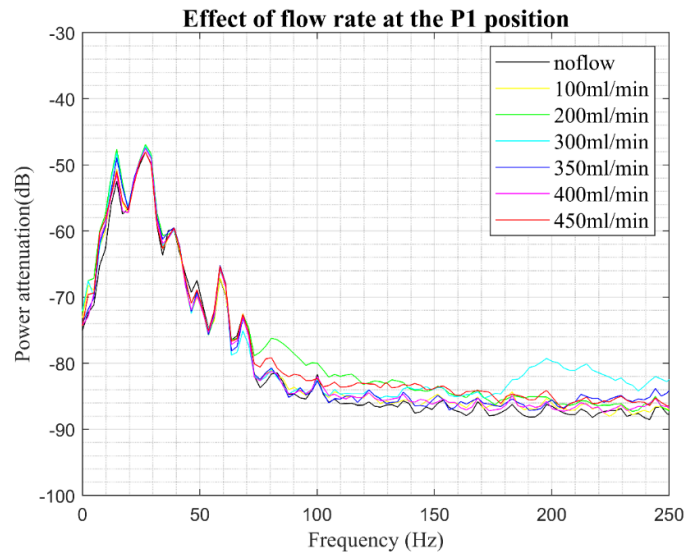


Figure 155: Effect of flow rate in a stenosed (embedded) tube in a 0% stenosed case at the P1 position (-3cm upstream of the stenosis)

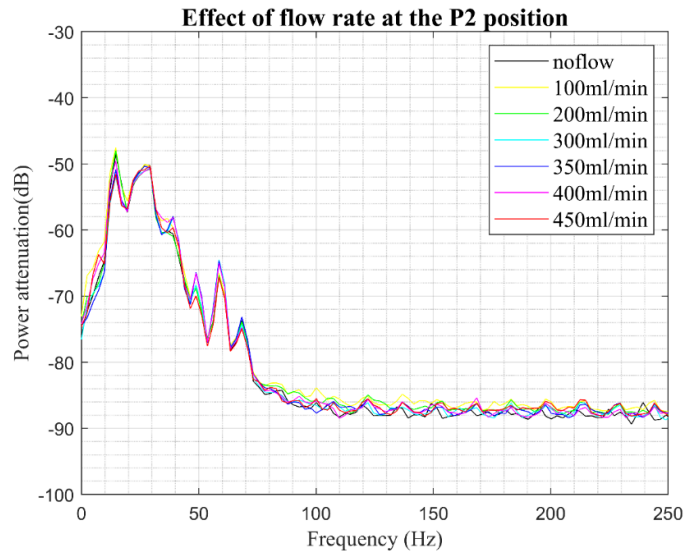


Figure 156: Effect of flow rate in a stenosed (embedded) tube in a 0% stenosed case at the P2 position (vertically above the stenosis)

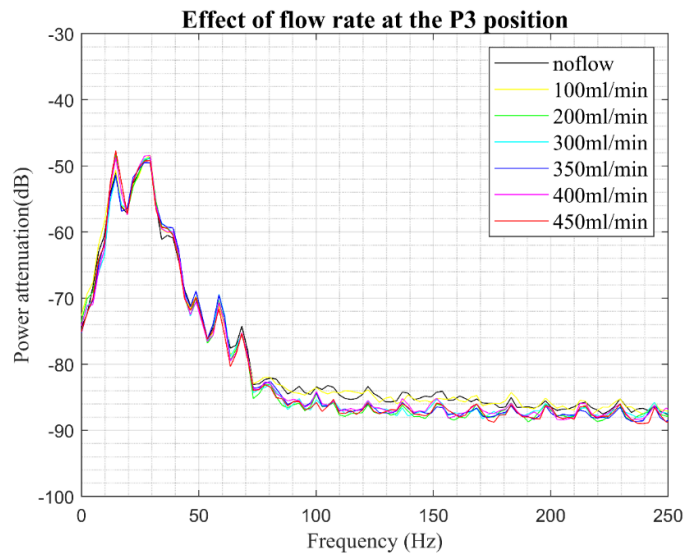


Figure 157: Effect of flow rate in a stenosed (embedded) tube in a 0% stenosed case at the P1 position P3 position (1.5cm downstream of the stenosis)

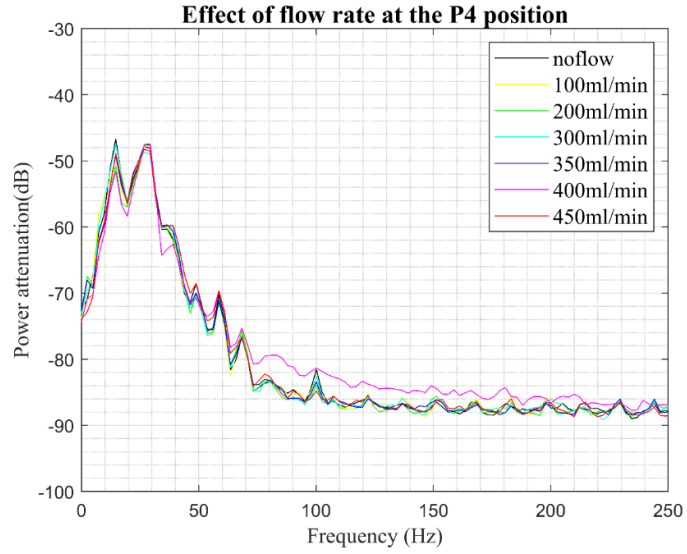


Figure 158: Effect of flow rate in a stenosed (embedded) tube in a 0% stenosed case at the P4 position (+3cm downstream of the stenosis)

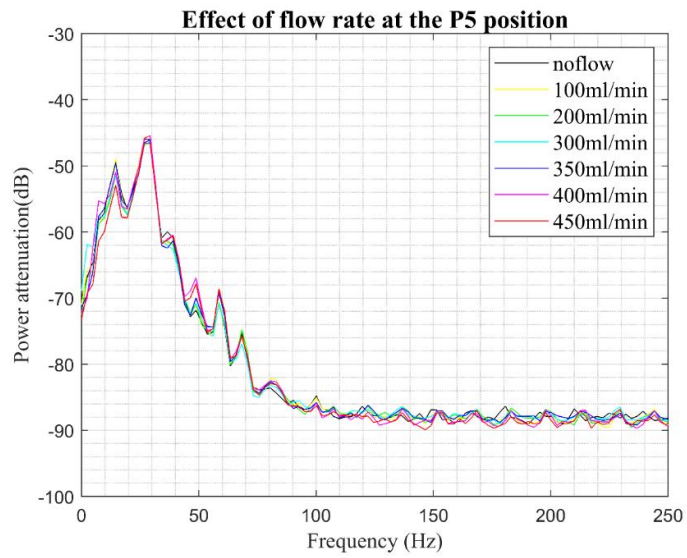


Figure 159: Effect of flow rate in a stenosed (embedded) tube in a 0% stenosed case at the P5 position (+6cm downstream of the stenosis)



## 60% Stenosed case

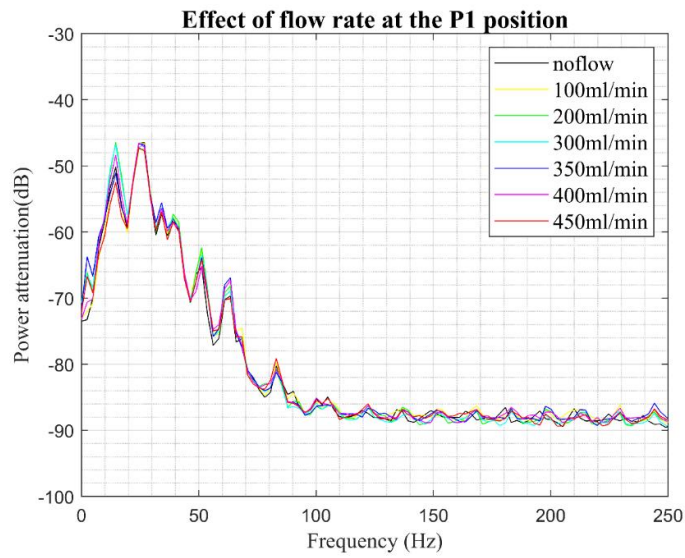


Figure 160: Effect of flow rate in a stenosed (embedded) tube in a 60% stenosed case at the P1 position (-3cm upstream of the stenosis)

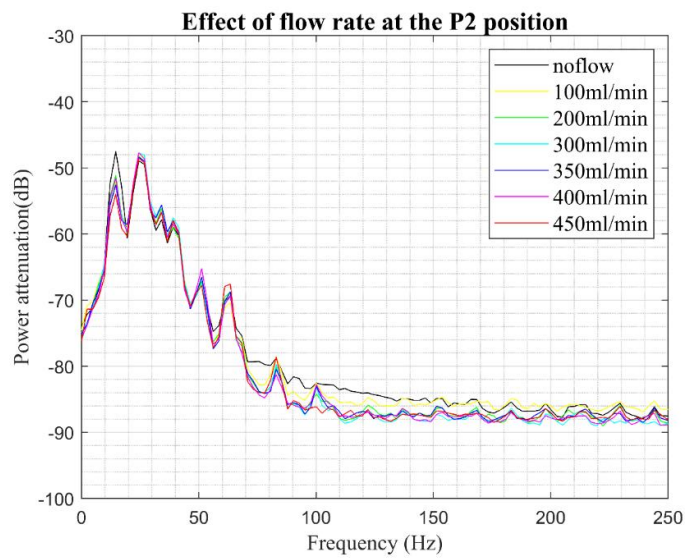


Figure 161: Effect of flow rate in a stenosed (embedded) tube in a 60% stenosed case at the P2 position (vertically above the stenosis)

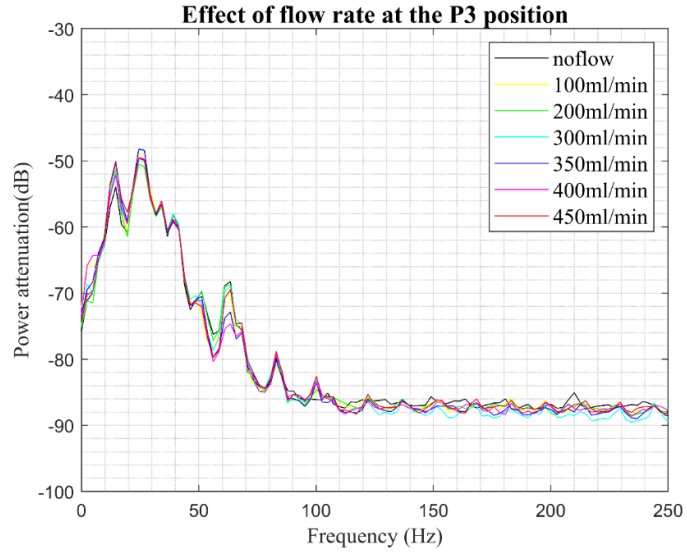


Figure 162: Effect of flow rate in a stenosed (embedded) tube in a 60% stenosed case at the P3 position (1.5cm downstream of the stenosis)

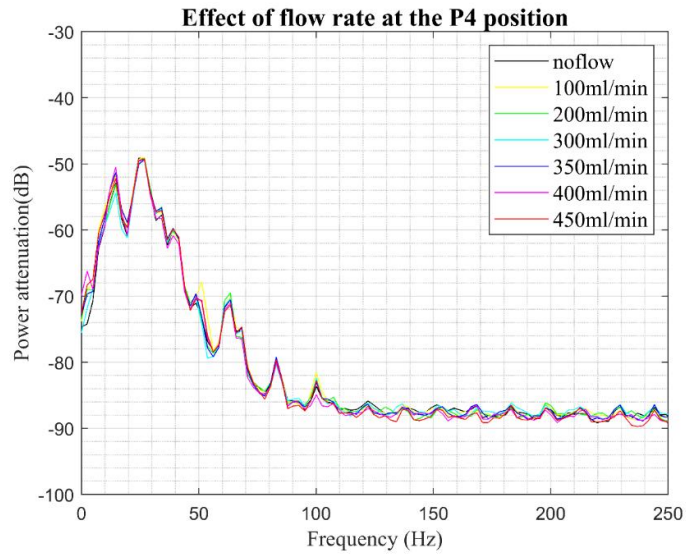


Figure 163: Effect of flow rate in a stenosed (embedded) tube in a 60% stenosed case at the P4 position (+3cm downstream of the stenosis)



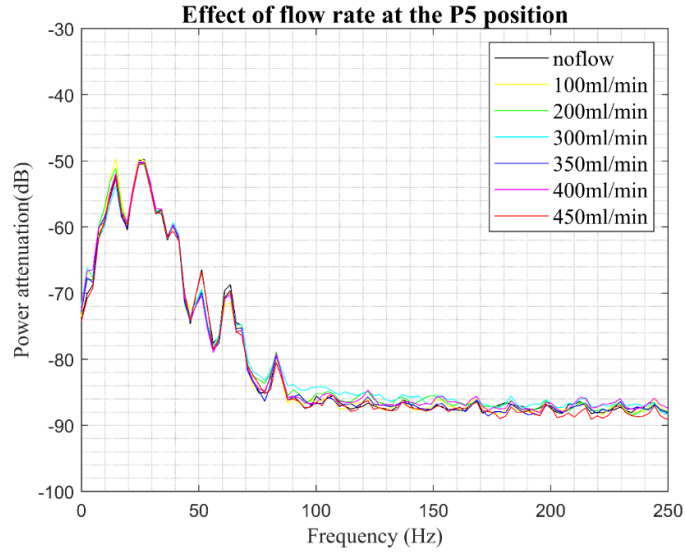


Figure 164: Effect of flow rate in a stenosed (embedded) tube in a 60% stenosed case at the P5 position (+6cm downstream of the stenosis)

### 75% Stenosed Case

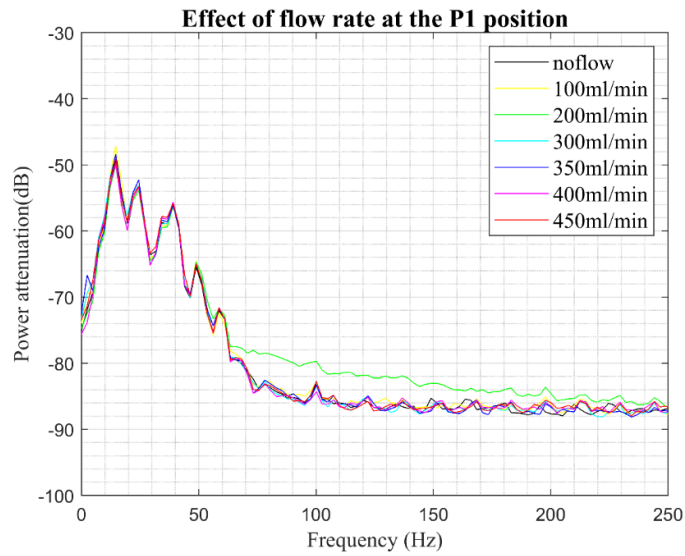


Figure 165: Effect of flow rate in a stenosed (embedded) tube in a 75% stenosed case at the P1 position (-3cm upstream of the stenosis)

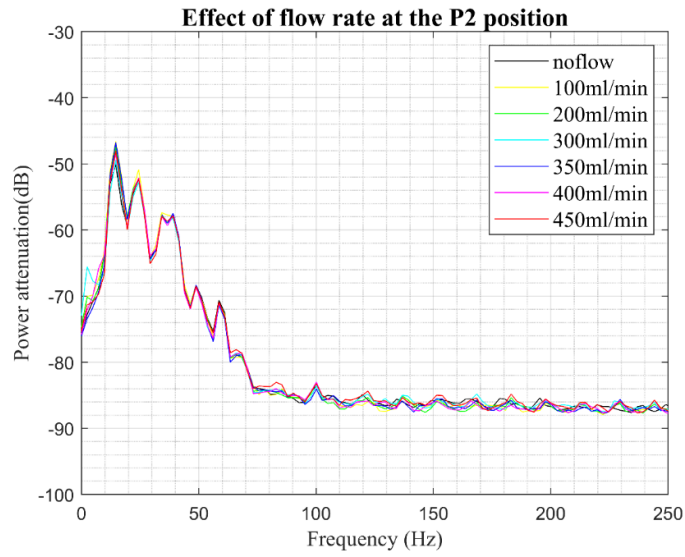


Figure 166: Effect of flow rate in a stenosed (embedded) tube in a 75% stenosed case at the P2 position (vertically above the stenosis)

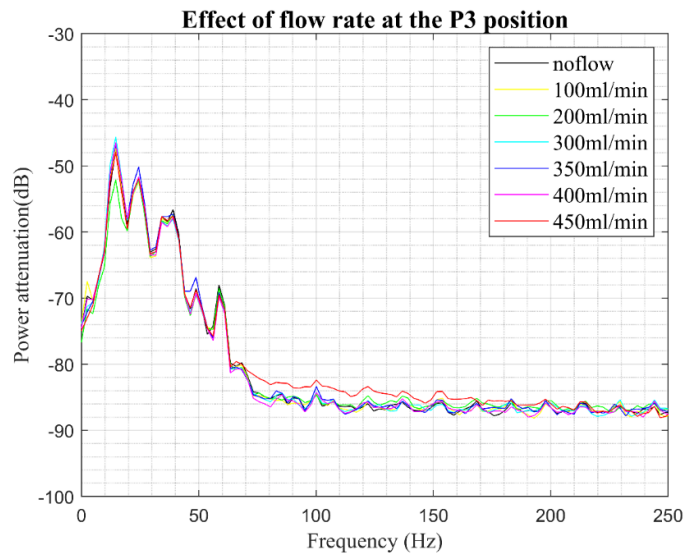


Figure 167: Effect of flow rate in a stenosed (embedded) tube in a 75% stenosed case at the P3 position (1.5cm downstream of the stenosis)

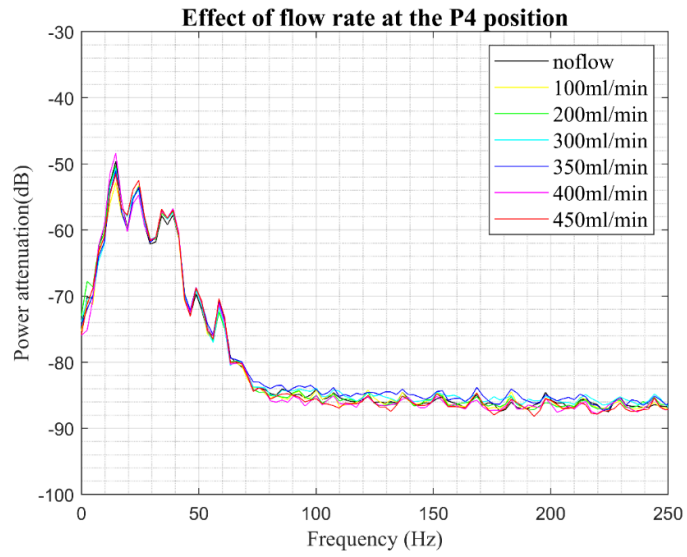


Figure 168: Effect of flow rate in a stenosed (embedded) tube in a 75% stenosed case at the P4 position (+3cm downstream of the stenosis)

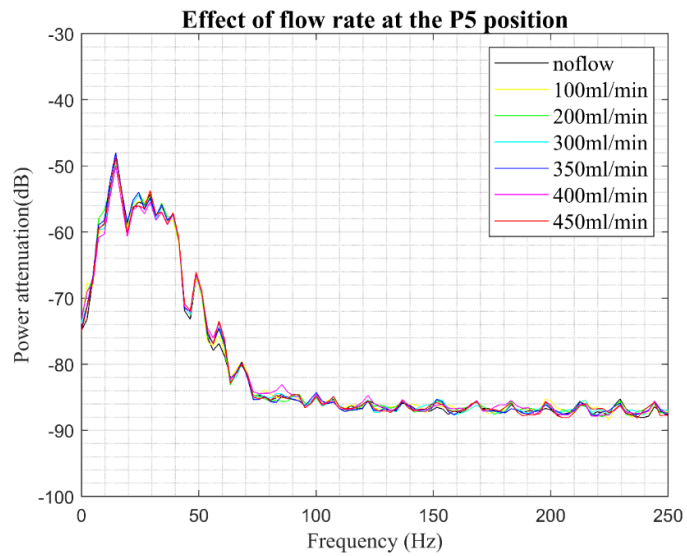


Figure 169: Effect of flow rate in a stenosed (embedded) tube in a 75% stenosed case at the P5 position (+6cm downstream of the stenosis)

### 90% Stenosed Case

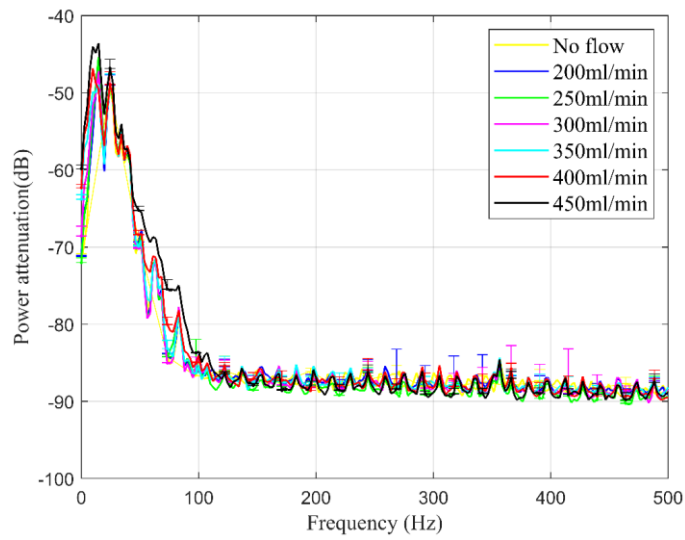


Figure 170: Effect of flow rate in a stenosed (embedded) tube in a 90% stenosed case at the P1 position (-3cm upstream of the stenosis)

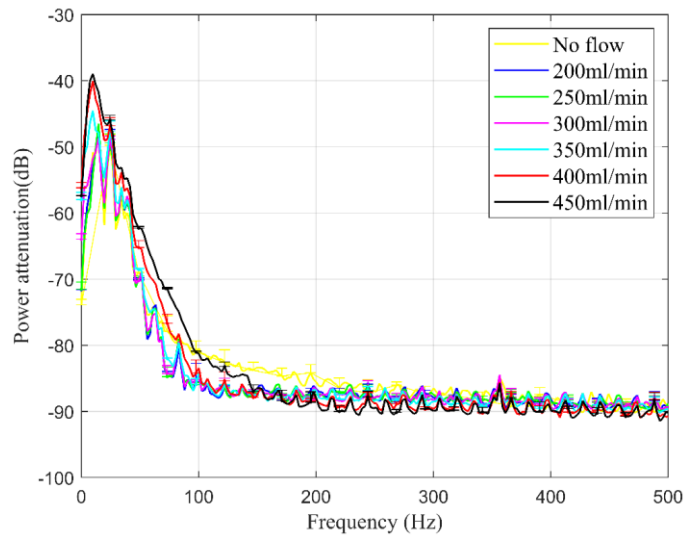


Figure 171: Effect of flow rate in a stenosed (embedded) tube in a 90% stenosed case at the P2 position (vertically above the stenosis)

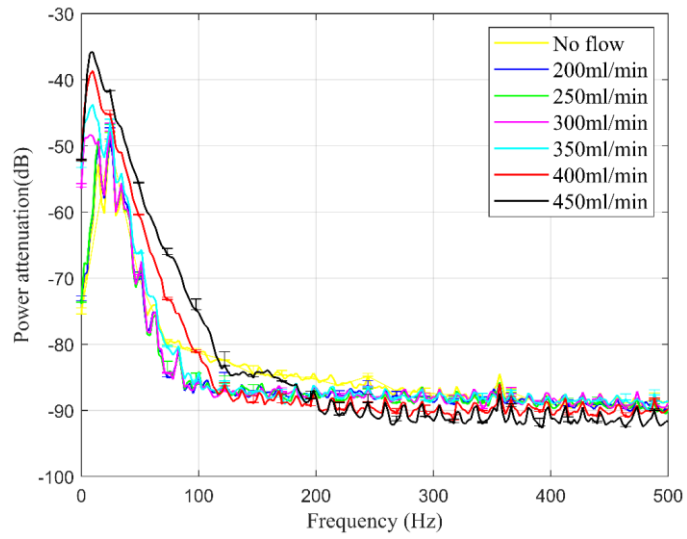


Figure 172: Effect of flow rate in a stenosed (embedded) tube in a 90% stenosed case at the P3 position (1.5cm downstream of the stenosis)

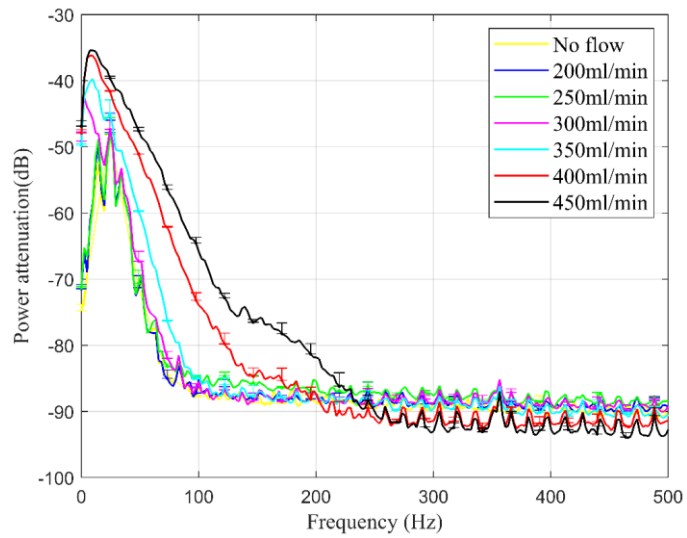


Figure 173: Effect of flow rate in a stenosed (embedded) tube in a 90% stenosed case at the P4 position (+3cm downstream of the stenosis)

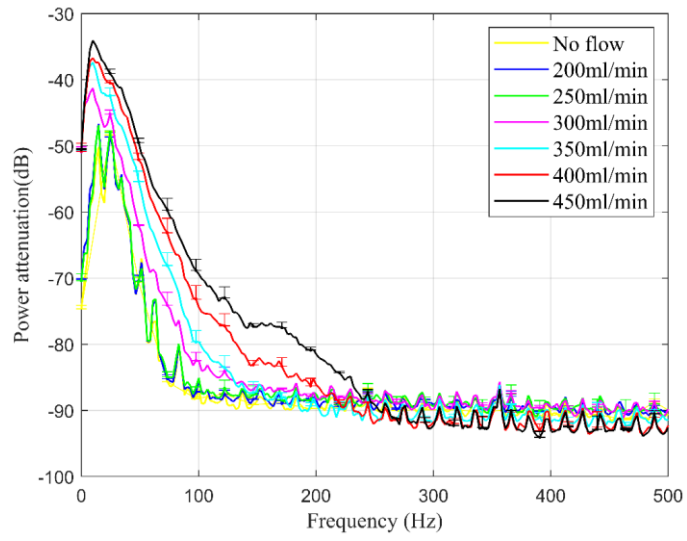


Figure 174: Effect of flow rate in a stenosed (embedded) tube in a 90% stenosed case at the P5 position (+6cm downstream of the stenosis)

8.3.4. Effect of flow rate (for steady flows) in 50-100Hz frequency range

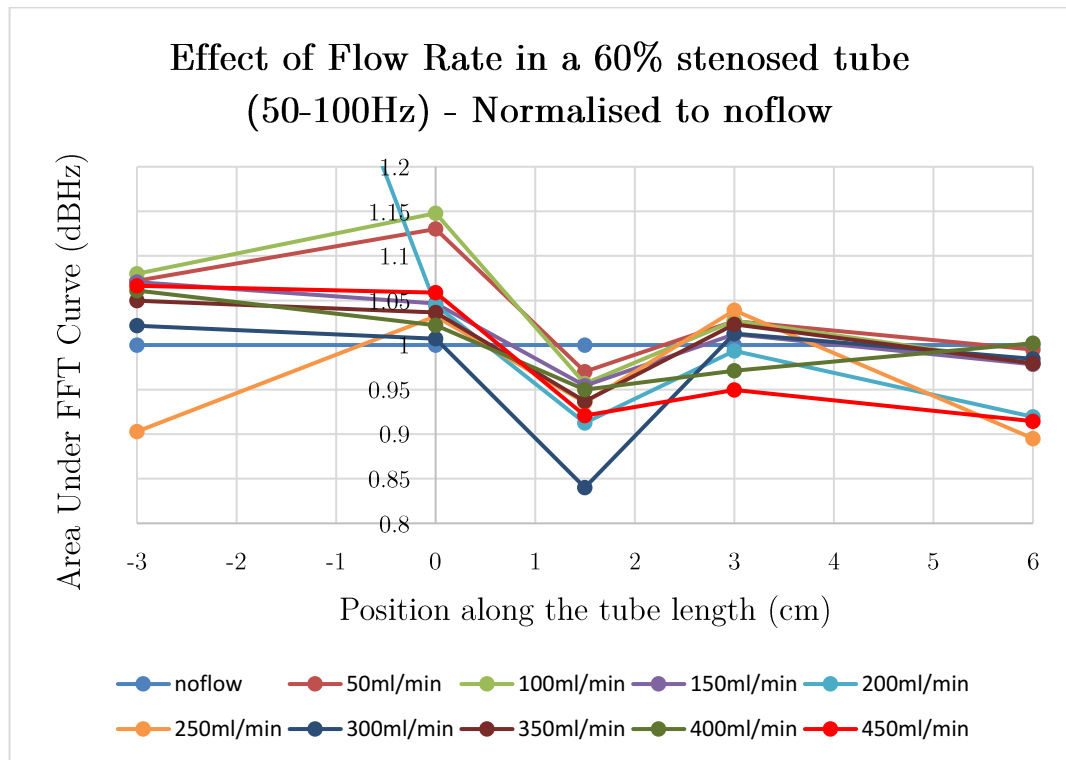


Figure 175: Effect of Flow Rate in a 60% stenosed tube embedded within a phantom (50-100Hz) - 200ml/min outlier at -3cm position filtered out on y-axis

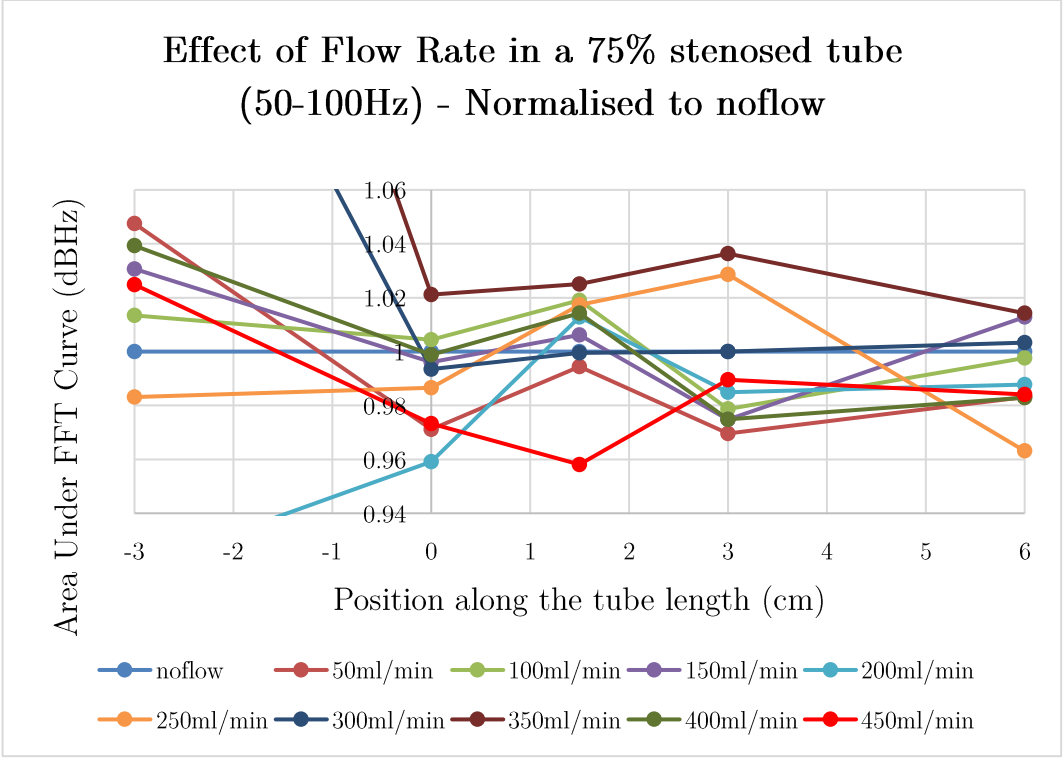


Figure 176: Effect of Flow Rate in a 75% stenosed tube embedded within a phantom (50-100Hz)